

**The South Indian Ocean –
Biogeochemical studies on water masses, nutrient and
stable isotope distribution, and particulate matter
in an oligotrophic ocean region**

Dissertation

zur Erlangung des Doktorgrades
an der Fakultät für Mathematik, Informatik und Naturwissenschaften
im Fachbereich Erdsystemwissenschaften der Universität Hamburg

vorgelegt von

Natalie Carina Harms

Hamburg

2020

Tag der Disputation: 03.02.2021

Folgende Personen begutachten die Dissertation:

Prof. Dr. Kay-Christian Emeis

Dr. Niko Lahajnar

Prüfungskommissionsmitglieder:

PD Dr. Thomas Pohlmann

Prof. Dr. Eva-Maria Pfeiffer

PD Dr. habil. Tim Rixen

Vorsitzender des Fachpromotionsausschusses Erdsystemwissenschaften:

Prof. Dr. Dirk Gajewski

Dekan der Fakultät MIN

Prof. Dr. Heinrich Graener

Abstract

The South Indian Ocean is predominantly influenced by the wind-driven ocean circulation of the subtropical gyre, one of the five extensive oligotrophic areas in the world's ocean. In contrast to subtropical gyres in the Atlantic and Pacific Ocean, the Indian Ocean subtropical gyre (IOSG) has been sparsely studied. This thesis provides new information on nitrogen (N) cycle processes and on the downward flux of sinking particulate matter to the seafloor, and the final organic carbon storage in deep-sea sediments. Together, the data illustrate a fundamental part of the organic carbon pump and thus of the global carbon (C) cycle.

First, I investigate the influence of the influx of preformed nutrients that regulate productivity in the sea surface and are injected into the IOSG by water masses originating from adjacent ocean regions of the Southern Ocean and the Arabian Sea. Basis for this study are water and nutrient samples (2° – 28° S, 67° – 77° E) collected during several ship cruises (2015–2019) that yield comprehensive data on the physical properties (e.g., temperature, salinity, density, oxygen concentration), nutrients, and stable isotopes of nitrate in the water column. I identify the convergence and mixing of water masses of Antarctic and Subantarctic origin with water masses from the southern equatorial Indian Ocean and the Arabian Sea that transport their specific nutrient and isotope signatures into the South Indian Ocean. The influx of the Subantarctic Mode Water (SAMW) from the Southern Ocean injects oxygen-saturated waters with preformed nutrients, reflecting partial N assimilation at high southern latitudes ($\delta^{15}\text{N} > 7\text{‰}$; $\delta^{18}\text{O} > 4\text{‰}$ at 26.6 – 26.7 kg m^{-3}). In the northern study area, a residue of nitrate affected by denitrification in the Arabian Sea is identified by an N deficit compared to phosphorus ($\text{N}^* \approx -1$ to $-4\text{ }\mu\text{mol L}^{-1}$) and elevated isotope ratios of nitrate ($\delta^{15}\text{N} > 7\text{‰}$, $\delta^{18}\text{O} > 3\text{‰}$) at intermediate and deep water masses ($> 27.0\text{ kg m}^{-3}$). Thus, the South Indian Ocean is supplied by preformed nutrients from the lateral influx of water masses from regions exhibiting distinctly different N cycle processes. Additionally, a contribution of dinitrogen (N_2) fixation at 20° – 24° S, documented by the deviations in the nitrate (NO_3^-) to phosphate (PO_4^{3-}) relationship from the Redfield-stoichiometry and by the dual isotope composition of nitrate, implies that at least 32–34 % of the nitrate in the upper ocean is provided from newly fixed N.

In a second step, I study the downward flux of sinking particulate matter collected by sediment traps and deployed during 2014 and 2019 in the central IOSG. This 5-year sediment trap experiment is the first in this region and provides basic information on the nature of and on the factors controlling particulate matter and organic carbon export fluxes. I can demonstrate that trap-averaged total mass fluxes of 9.8 – $10.6\text{ mg m}^{-2}\text{ day}^{-1}$, as well as particulate organic carbon (POC) fluxes of $\sim 0.5\text{ mg m}^{-2}\text{ day}^{-1}$ measured at 500–600 m above bottom (2600–3500 m water depth) are among the lowest fluxes on record worldwide. These low fluxes are the result of the strongly stratified and nutrient-depleted surface waters, leading to low primary production rates. Preliminary estimates indicate an average POC export efficiency of $\varepsilon \approx 0.02$ – 0.03 . Additionally, temporal and seasonal fluctuations in the IOSG are found to be minor. The lack of seasonality in POC fluxes is caused by intense organic matter degradation, variations in the ocean mixed

layer depth (OMLD), and impacts by physical mixing (surface wind stress, cyclonic eddies).

Furthermore, surface sediment samples collected during 2015 and 2018 reveal sedimentation rates of ~ 0.23 cm per 1000 years and provide new information on the final organic carbon storage in the pelagic sediments of the IOSG. A simple particulate organic carbon budget from the surface ocean, down to the ocean interior, and finally into the surface sediments indicates that only 4 % of the POC that reaches the seafloor accumulates there due to intense degradation at the sediment-water interface. Based on primary production rates of $7\text{--}10$ mol C m^{-2} year $^{-1}$ in surface waters, only ~ 0.01 % of the initial production in the euphotic zone, or in other words, only ~ 0.001 mol C m^{-2} year $^{-1}$ ($0.02\text{--}0.03$ mg m^{-2} day $^{-1}$ POC) accumulates in surface sediments. This is extremely low in a global comparison. Assuming that the IOSG, as well as comparable ocean regions, will expand under climate warming, it is of major importance to investigate POC export fluxes and its final carbon storage in the sediments in order to study the organic carbon pump and potential changes in the global C cycle.

Zusammenfassung

Der südliche Indische Ozean wird überwiegend durch die windgesteuerte Ozeanzirkulation des subtropischen Wirbels beeinflusst und gehört zu den fünf großen oligotrophen Regionen in den Weltozeanen. Im Gegensatz zu den subtropischen Wirbeln im Atlantischen und Pazifischen Ozean, ist der subtropische Wirbel im Indischen Ozean, der sogenannte „Indian Ocean Subtropical Gyre“ (IOSG), nur wenig erforscht. Diese Arbeit liefert neue Informationen über die Prozesse im Stickstoff(N)-Kreislauf und über das bis zum Meeresboden herabsinkende partikuläre Material und die damit verbundene endgültige Einbettung von organischem Kohlenstoff in das Tiefseesediment. Dies ist ein wichtiger Bestandteil der organischen Kohlenstoffpumpe und somit des globalen Kohlenstoff(C)-Kreislaufs.

Zunächst untersuche ich den Einfluss von Wassermassen und dessen Eintrag spezifischer Nährstoffs Signaturen aus den umliegenden Meeresregionen, hauptsächlich aus dem Südpolarmeer und dem Arabischen Meer. Grundlage dieser Studie sind Wasser- und Nährstoffproben, die während mehrerer Schiffsexpeditionen (2015–2019) genommen wurden (2° – 28° S, 67° – 77° E). Diese liefern umfassende Daten über die physikalischen Eigenschaften (z.B. Temperatur, Salzgehalt, Dichte, Sauerstoffkonzentration), Nährstoffe und über stabile Nitratisotope in der Wassersäule. Ich kann die Konvergenz und Mischung von Wassermassen antarktischen und subantarktischen Ursprungs mit Wassermassen aus dem äquatorialen südlichen Indischen Ozean und dem Arabischen Meer nachweisen, welche ihre spezifischen Nährstoff- und Isotopensignaturen in den südlichen Indischen Ozean transportieren. Der Zufluss des „Subantarctic Mode Water“ (SAMW) aus dem Südpolarmeer transportiert sauerstoffgesättigteres Wasser und spezifische Nährstoff- und Isotopensignaturen in den IOSG, welche die partielle N-Assimilation im Südpolarmeer widerspiegeln ($\delta^{15}\text{N} > 7 \text{‰}$; $\delta^{18}\text{O} > 4 \text{‰}$ bei $26,6$ – $26,7 \text{ kg m}^{-3}$). Das nördliche Untersuchungsgebiet ist beeinflusst durch den biologischen Prozess der Denitrifikation im Arabischen Meer und spiegelt sich durch ein N Defizit im Vergleich zu Phosphor ($\text{N}^* \approx -1$ bis -4 μmol L^{-1}) und durch erhöhte Isotopenverhältnisse im Nitrat wider ($\delta^{15}\text{N} > 7 \text{‰}$; $\delta^{18}\text{O} > 3 \text{‰}$), welche in die intermediären und tiefen Wassermassen ($> 27,0 \text{ kg m}^{-3}$) des südlichen Indischen Ozeans eingetragen werden. Somit ist der südliche Indische Ozean durch den lateralen Zufluss von Wassermassen aus den anliegenden Ozeanregionen mit ihren spezifischen Nährstoffs Signaturen stark beeinflusst und dokumentiert mit Hilfe der dualen Isotopenzusammensetzung im Nitrat die unterschiedlichen Prozesse im N-Kreislauf. Desweiteren weisen Änderungen im Nitrat (NO_3^-) zu Phosphat (PO_4^{3-}) Verhältnis und im Isotopenverhältnis von Nitrat auf Stickstofffixierung bei 20° – 24° S hin und ergeben, dass mindestens 32–34 % des assimilierten Nitrats im Oberflächenwasser aus neu fixiertem N stammen.

In einem zweiten Schritt untersuche ich herabsinkendes partikuläres Material (Sinkstoffe) in der Wassersäule, welches anhand von verankerten Sinkstofffallen zwischen 2014 und 2019 im zentralen IOSG gesammelt wurde. Diese 5-jährige Sinkstoffstudie ist die erste in dieser Region und liefert grundlegende Informationen über die Zusammensetzung und die Kontrollfaktoren des Exportes von partikulärem

Material und organischem Kohlenstoff. Ich kann zeigen, dass die gemittelten Gesamtmassenflüsse von $9,8\text{--}10,6 \text{ mg m}^{-2} \text{ day}^{-1}$, sowie die partikulären organischen Kohlenstoff(POC)-Flüsse von $\sim 0,5 \text{ mg m}^{-2} \text{ day}^{-1}$, die bei 500–600 m über dem Boden (2600–3500 m Wassertiefe) eingefangen wurden, zu den niedrigsten erfassten Stoffflüssen weltweit gehören. Dies ist das Ergebnis der mächtigen nährstoffarmen Oberflächenwasserschicht im IOSG, welche zu einer geringen Primärproduktion führt. Meine vorläufige Schätzung ergibt eine durchschnittliche POC-Exporteffizienz von $\varepsilon \approx 0,02\text{--}0,03$ im IOSG. Darüber hinaus zeigt sich nur eine geringe räumliche und zeitliche Variabilität im IOSG. Die Abwesenheit von saisonalen Schwankungen in den POC-Flüssen ist auf den intensiven Abbau organischer Substanzen, auf Unterschiede in der „ocean mixed layer depth“ (OMLD) und auf physikalische Faktoren (Oberflächenwinde, kleinskalige Oberflächen Verwirbelungen „Eddies“) zurück zu führen.

Desweiteren, ergeben die Oberflächensedimentenproben aus den Jahren 2015 bis 2018 eine Sedimentationsrate von $\sim 0,23 \text{ cm}$ pro 1000 Jahre und liefern zusätzliche Informationen über die endgültige Ablagerung von organischem Kohlenstoff in pelagischen Sedimenten des IOSG. Ein vereinfachtes Schema der POC-Flüsse von der Wasseroberfläche weiter durch die Wassersäule und bis hin zur Ablagerung im Oberflächensediment zeigt, dass nur 4 % des am Meeresboden ankommenden POC der Degradation an der Sediment-Wasser Grenzfläche im Oberflächensediment entgehen und abgelagert werden. Geht man von einer Primärproduktion von $7\text{--}10 \text{ mol C m}^{-2} \text{ year}^{-1}$ in der Euphotischen Zone aus, erreichen nur 0,01 % der Primärproduktion, oder anders ausgedrückt $\sim 0,001 \text{ mol C m}^{-2} \text{ year}^{-1}$ ($0,02\text{--}0,03 \text{ mg m}^{-2} \text{ day}^{-1}$ POC) das Oberflächensediment. Dies ist im globalen Vergleich extrem niedrig. Unter der Annahme, dass der IOSG, sowie vergleichbare Ozeanregionen sich unter der Klimaerwärmung ausdehnen, ist die Untersuchung von POC-Flüssen und die endgültige Speicherung von organischem Kohlenstoff in den Sedimenten von großer Bedeutung. Insbesondere im Hinblick auf die organische Kohlenstoffpumpe, und um mögliche Veränderungen im globalen C-Kreislauf fest zu stellen, sind langjährige Aufzeichnungen von Sinkstoffflüssen unerlässlich.

Table of contents

Abstract	iii
Zusammenfassung	v
Table of contents	vii
List of figures	xi
List of tables	xv
Chapter 1 – Introduction and thesis objective	1
1.1 Subtropical gyres	1
1.2 The Indian Ocean subtropical gyre (IOSG)	3
1.2.1 Regional setting	3
1.2.2 Biogeochemical setting	5
1.3 Research project and thesis outline	6
Chapter 2 – Cumulative Part I	9
2.1 Introduction	10
2.2 Materials and methods	13
2.2.1 CTD measurements and sample collection	13
2.2.2 Nutrient analysis	15
2.2.3 Measurements of N and O isotopes of nitrate	15
2.3 Results	16
2.3.1 Physical water column properties	16
2.3.2 Nutrient concentration	17
2.3.3 N and O isotopes of nitrate	18
2.4 Water mass distribution	20
2.4.1 Surface and thermocline water masses (<26.9 kg m ⁻³ ; <800 m).	20
2.4.2 Intermediate water masses (26.9–27.4 kg m ⁻³ ; 800–1000 m)	22
2.4.3 Deep water masses (>27.4 kg m ⁻³ ; >1000 m)	22
2.5 Nutrient distribution and N cycle processes	24
2.5.1 Nutrient supply in the oligotrophic gyre and lateral transfer across the gyre boundaries	24
2.5.2 Evidence for N ₂ fixation in the IOSG	31
2.6 Conclusion	35

Chapter 3 – Cumulative Part II	37
3.1 Introduction	38
3.2 Materials and methods	40
3.2.1 Sediment trap moorings	40
3.2.2 Sample collection	41
3.2.3 Analytical methods	43
3.3 Results	44
3.3.1 Particulate matter fluxes and particle composition	44
3.3.2 Particulate matter flux variability with depth at mooring 04-03	47
3.4 Discussion	49
3.4.1 Organic carbon fluxes in the IOSG compared to global data	49
3.4.2 Controlling factors of particulate matter fluxes in the IOSG	52
3.4.3 Spatial and temporal patterns in the IOSG	55
3.4.4 First estimates on the POC export efficiency	61
3.5 Summary and conclusion	62
Chapter 4 – Cumulative Part III	65
4.1 Introduction and regional setting	66
4.2 The use of nutrients and stable isotopes of nitrate	69
4.3 Water mass distribution in the South Indian Ocean	70
4.4 Nutrient distribution and N cycle processes in the IOSG	74
4.4.1 Lateral transfer of nutrients and nitrate isotope signals across the gyre boundaries	74
4.4.1.1 Influence from the North Indian Ocean on the nutrient distribution and nitrate composition of the IOSG	75
4.4.1.2 Influence from the Southern Ocean on the nutrient distribution and nitrate composition of the IOSG	78
4.4.2 External input of reactive nitrogen via N ₂ fixation in the IOSG	80
4.5 Conclusion	81
Chapter 5 – Cumulative Part IV	83
5.1 Introduction	84
5.2 Materials and methods	86
5.2.1 Use of sediment traps to collect sinking particulate matter	86
5.2.2 Sample preparation	88
5.2.2.1 Sinking particulate matter samples	88
5.2.2.2 Surface sediment samples	88
5.2.3 Analytical methods	88
5.3 Particulate matter in sediment traps	89
5.3.1 Total mass fluxes and main components	89
5.3.2 Organic carbon fluxes in a global comparison	91

5.3.3	Controlling factors of organic carbon export	93
5.3.4	Regional variability of POC fluxes in the IOSG	96
5.3.5	Seasonal variability of POC fluxes in the IOSG	97
5.4	Particulate matter in surface sediments	100
5.5	Conclusion and implications	104
Chapter 6 – Conclusion and outlook		107
6.1	Conclusion	107
6.2	Outlook	109
References		xvii
Used data and internet sources		liii
Appendix		lv
Appendix A1	Data of water column properties, nutrients, and stable nitrate isotopes collected during INDEX expeditions between 2015 and 2018	lv
Appendix A2	Data of sinking particulate matter collected during INDEX expeditions between 2015 and 2019	lxv
Appendix A3	Global data of sinking particulate organic carbon (POC) collected by sediment traps	lxxv
Appendix A4	The use of a Multiple Linear Regression Analysis (MLRA) to calculate the major ballast material enhancing the sinking speed of particles in the IOSG	lxxxv
Appendix A5	Calculation of the sinking speed of particulate matter to the deep IOSG	lxxxvii
Appendix A6	Data on surface sediments collected during INDEX expeditions between 2015 and 2018	xcii
Acknowledgement		xciii
List of Publications (Aus dieser Disserstation hervorgegangene Veröffentlichungen)		xcv

List of figures

Chapter 1 – Introduction and thesis objective

- Fig. 1.1 Map of the South Indian Ocean with schematic representation of deep-sea basins and surface/subsurface currents. 3

Chapter 2 – Cumulative Part I

- Fig. 2.1 Sampling location during the cruises *MSM 59/2* (INDEX 2016-2) and *SO 259* (INDEX 2017). 14
- Fig. 2.2 Profiles of salinity (a) and oxygen distribution (b) from CTD measurements during cruises *MSM 59/2* (2016) and *SO 259* (2017). 17
- Fig. 2.3 T-S diagram of CTD measurements during cruises *MSM 59/2* (2016) and *SO 259* (2017). 17
- Fig. 2.4 Profiles of nitrate (a) and phosphate concentrations (b), and $\delta^{15}\text{N-NO}_3^-$ (c) and $\delta^{18}\text{O-NO}_3^-$ (d) of seawater samples collected during cruises *MSM 59/2* (2016) and *SO 259* (2017). 20
- Fig. 2.5 Water mass properties represented as salinity vs. sigma-theta diagrams (a, b, c) and as oxygen vs. sigma-theta diagrams (d, e, f). 23
- Fig. 2.6 Water mass distribution model from 30°S to the equator. 24
- Fig. 2.7 Latitudinal profiles from S to N with an overlay of the water mass distribution in the South Indian Ocean of nitrate (a) and phosphate concentrations (b), $\text{NO}_3^-/\text{PO}_4^{3-}$ ratio (c), N^* (d), $\delta^{15}\text{N-NO}_3^-$ (e) and $\delta^{18}\text{O-NO}_3^-$ of nitrate (f), and nitrate $\Delta(15-18)$ (g). 25
- Fig. 2.8 Correlation of nitrate vs. phosphate concentrations in the IOSG (~14.56; $r^2 = 0.99$) and in the Arabian Sea (~12.81). 27
- Fig. 2.9 Nitrate concentrations vs. $\delta^{15}\text{N-NO}_3^-$ (a) and $\delta^{15}\text{N-NO}_3^-$ vs. $\ln(\text{NO}_3^-)$ (b) for CTD stations within the IOSG (20.36°–27.78°S). 30
- Fig. 2.10 $\text{NO}_3^-/\text{PO}_4^{3-}$ ratio vs. nitrate concentrations of seawater samples at 20.36°–23.91°S and 26.05°–27.78°S (a) and the portion of nitrate formed out of newly fixed N ($\text{NO}_3^-_{\text{new}}$) at 20.36°–23.91°S (b). 34

Chapter 3 – Cumulative Part II

- Fig. 3.1 Station map of sediment trap moorings deployed within the 12 clusters of the INDEX program during 2014 and 2018 in the IOSG. 41

Fig. 3.2	Average total mass flux ($\text{mg m}^{-2} \text{ day}^{-1}$) (a, b) and percentages (wt.-%) of the total mass flux of the individual components (c, d) of sediment traps deployed during 2014 and 2018 in the IOSG.	46
Fig. 3.3	Average percentages (wt.-%) and mass fluxes ($\text{mg m}^{-2} \text{ day}^{-1}$) of the major components CaCO_3 (a), biogenic opal (b), POC (c), and TN (d) of sediment traps deployed at 500–600 m.a.b. during 2014–2018.	47
Fig. 3.4	Particulate matter components given as mass fluxes ($\text{mg m}^{-2} \text{ day}^{-1}$) (a-d) and in percentages (wt.-%) (e-h) and the molar ratio POC/TN (i) vs. water depth for sediment trap of mooring 04-03 (traps <i>Shallow, Middle, and Deep</i>) deployed during 2017 and 2018.	49
Fig. 3.5	Global map of POC fluxes (a) normalized to 2000 m of sediment trap data from the literature extended by data in the IOSG.	51
Fig. 3.6	Latitudinal sections of sigma-theta (a), temperature (b), nitrate concentrations (c), and the distribution of $\text{NO}_3^-/\text{PO}_4^{3-}$ ratios on transects roughly along 71°E between 20°S and 29°S in the IOSG.	53
Fig. 3.7	Linear correlation of particulate organic carbon (POC) fluxes vs. CaCO_3 (a) and biogenic opal flux (b) averaged over the entire period of sediment trap deployments at 500–600 m.a.b..	55
Fig. 3.8	Distribution of the net primary production (NPP) for January (a) and July (b) during 2014–2018 in the South Indian Ocean.	57
Fig. 3.9	Nitrate concentrations, net primary production (NPP), ocean mixed layer depth (OMLD), and particulate organic carbon (POC) flux data along a meridional section from 20°S to 29°S for the INDEX region.	57
Fig. 3.10	Particulate organic carbon fluxes (POC) and seasonal fluctuations of net primary production (NPP) during 2014 and 2018.	59
Fig. 3.11	Temporal variations of the net primary production (NPP), sea surface temperature (SST), and ocean mixed layer depth (OMLD) for the time interval 2006–2019 (a) and 2014–2019 (b).	60
Chapter 4 – Cumulative Part III		
Fig. 4.1	Map of the South Indian Ocean with schematic representation of deep-sea basins and surface/subsurface currents.	66
Fig. 4.2	Latitudinal cross sections from 30°S to 0° for temperature (a), potential density (b), nitrate concentrations (c), and a scheme of the gyral deepening of isoclines in the IOSG and their upward lift towards the southern equatorial Indian Ocean (d) accompanied by chlorophyll- <i>a</i> concentration.	68
Fig. 4.3	Water mass properties from CTD measurements during 2015 and 2019 presented as temperature vs. sigma-theta (a, b, c, d), salinity vs. sigma-theta (e, f, g, h), and as oxygen vs. sigma-theta diagrams (I, j, k, l) for the different oceanic regimes.	72

Fig. 4.4	T-S diagram (a) of vertical profiles based on <i>Emery</i> (2001) with color coding of oxygen concentration. Latitudinal section of salinity distribution along water sampling stations from S to N with an overlay of oxygen concentrations (b). Schematic profile of the water mass distribution in the South Indian Ocean (c; <i>Harms et al.</i> , 2019)	74
Fig. 4.5	Latitudinal profiles from N to S with an overlay of the water mass distribution in the South Indian Ocean for nitrate (a) and phosphate (b) concentrations, $\text{NO}_3^-/\text{PO}_4^{3-}$ ratio (c), N^* (d), $\delta^{15}\text{N}-\text{NO}_3^-$ (e) and $\delta^{18}\text{O}-\text{NO}_3^-$ (f), and $\Delta(15-18)$ (g; <i>Harms et al.</i> , 2019).	76
Fig. 4.6	Correlation of nitrate vs. phosphate concentrations of the INDEX area and the Arabian sea compared to the Redfield ratio (a) and sigma-theta profiles vs. of oxygen concentration, N^* , $\delta^{15}\text{N}-\text{NO}_3^-$, and $\Delta(15-18)$ (b).	78
Fig. 4.7	NO_3^- concentrations vs. $\delta^{15}\text{N}-\text{NO}_3^-$ (a) and $\delta^{15}\text{N}-\text{NO}_3^-$ vs. $\ln(\text{NO}_3^-)$ (b) for water sampling stations within the IOSG (20.96°–27.80°S).	79
Fig. 4.8	Depth profiles of N^* , $\delta^{15}\text{N}-\text{NO}_3^-$, and $\Delta(15-18)$ of water sampling stations located at ~20°–24°S.	81

Chapter 5 – Cumulative Part IV

Fig. 5.1	Station map of particle flux and surface sediment sampling in the INDEX area (a) and surface chlorophyll- <i>a</i> concentrations averaged for 2014 to 2019 during January (b) and July(c).	85
Fig. 5.2	Schematic of a sediment trap mooring and a sediment trap (McLane Mark 7G-21) used during the INDEX program.	87
Fig. 5.3	Total mass fluxes and particle composition of the main components in wt.-% (a) and averaged composition in sinking particulate matter for sediment traps deployed during 2014 and 2019 at ~500–600 m.a.b. (b).	90
Fig. 5.4	Averaged total particulate matter flux (a), POC (b), and TN (c) given in percentages (wt.-%) and the elemental ratio POC/TN (d) are presented as depth profiles for sediment traps <i>Shallow</i> , <i>Middle</i> , and <i>Deep</i> of moorings 04-03 and 04-04 deployed in 2017–2019.	91
Fig. 5.5	Global data of POC fluxes normalized to 2000 m for sediment trap data collated from the literature extended by data from the IOSG collected during expeditions in 2014–2019 (a).	92
Fig. 5.6	Latitudinal section from 28°S to 21°S indicates nitrate, surface chlorophyll- <i>a</i> concentration, mixed layer depth, and POC fluxes averaged for each sediment trap except of traps <i>Shallow</i> and <i>Deep</i> of moorings 04-03 and 04-04.	97
Fig. 5.7	Time series of POC fluxes and chlorophyll- <i>a</i> concentrations (a) and combined POC fluxes for a one-year period accompanied by average chlorophyll- <i>a</i> concentrations during 2014 and 2019 (b).	98

Fig. 5.8	Fluctuations in chlorophyll- <i>a</i> concentration, sea surface temperature (SST), ocean mixed layer depth (OMLD), and surface wind speed between 2014 and 2019 (a) and chlorophyll- <i>a</i> concentration vs. SST (b) and OMLD (c).	99
Fig. 5.9	Particle compositions in surface sediments (0–1 cm) of push- and multicores taken during 2015, 2017, and 2018 in the INDEX area.	101
Fig. 5.10	Particulate organic carbon export (POC_{Export}) below the productive zone, its transfer ($POC_{Transfer}$) across the sediment trap depths of traps <i>Shallow</i> , <i>Middle</i> , and <i>Deep</i> of moorings 04-03 and 04-04, and its final burial (POC_{Burial}) in the deep-sea sediments (first centimeter).	105

List of tables

Chapter 2 – Cumulative Part I

Tab. 2.1	Average nitrate and phosphate concentrations and $\delta^{15}\text{N}\text{-NO}_3^-$ and $\delta^{18}\text{O}\text{-NO}_3^-$ values, defined along their density surfaces, separated into four latitudinal sections.	19
----------	--	----

Chapter 3 – Cumulative Part II

Tab. 3.1	Technical data on deployments and recoverys of sediment traps moored during November 2014 and September 2018 in the IOSG.	42
Tab. 3.2	Averaged values of total mass fluxes and percentages (wt.-%) of the individual components and the molar ratio POC/TN of sediment traps deployed during 2014 and 2018 in the oligotrophic IOSG.	45

Chapter 5 – Cumulative Part IV

Tab. 5.1	Technical Data on the deployments and recoverys of sediment traps moored during November 2014 and December 2019 in the IOSG.	86
----------	--	----

Appendix

Tab. A1.1	Location of CTD stations during <i>PE 405</i> (INDEX 2015), <i>MSM 59/2</i> (INDEX 2016), <i>SO 259</i> (INDEX 2017), and <i>PE 466</i> (INDEX 2018).	lv
Tab. A1.2	Results of CTD casts from cruise <i>PE 405</i> (2015).	lvi
Tab. A1.3	Results of CTD casts from cruise <i>MSM 59/2</i> (2016).	lvii
Tab. A1.4	Results of CTD casts from cruise <i>SO 259</i> (2017).	lx
Tab. A1.5	Results of CTD casts from cruise <i>PE 446</i> (2018).	lxiii
Tab. A2.1	Sediment trap data of annual fluxes and percentages of the individual particulate matter components during 2014–2019.	lxv
Tab. A3.1	Data on global sediment trap-based particulate organic carbon (POC) fluxes to depth and normalized to 2000 m water depth.	lxxv
Tab. A4.1	Statistical data of Multiple Linear Regression Analysis.	lxxxv
Tab. A5.1	Percentages and densities of the individual components contributing to the total mass flux at 500–600 m.a.b.	lxxxviii
Tab. A5.2	Values used to calculate sinking speeds and intermediate results of equations A2.2–A2.4.	lxxxix
Tab. A6.1	Data on the composition of surface sediments collected during INDEX expeditions in 2015, 2017, and 2018.	xcii

Chapter 1

Introduction and thesis objective

The South Indian Ocean, one of the least explored ocean regions, is dominated by the Indian Ocean subtropical gyre (IOSG), one of the five extensive oligotrophic areas in the world's ocean. This thesis comprises a comprehensive study on physical water column data (e.g., temperature, salinity, potential density) to identify and characterize major water masses, nutrient and stable isotope samples, sinking particulate matter samples, as well as surface sediment samples. The main goal is to understand the key processes of the nitrogen (N) and carbon (C) cycle within a sparsely investigated and underrepresented ocean region. Results presented here are the first provided for this ocean region and focus on the implications of water mass interfingering, on N sources and transformation processes (Chapter 2 and 4), on sediment trap-based sinking particle matter fluxes (Chapter 3 and 5), and on the final accumulation of pelagic sediments (Chapter 5) in the South Indian Ocean.

1.1 Subtropical gyres

Ocean and atmosphere circulation play an essential role in sustaining life by moderating climate over much of Earth's surface. An important part of the circulation of heat energy and other seawater components are ocean surface currents that help to form our weather over short and long timescales, impacting climate and environments for all life on Earth (*NASA Science: Nagaraja, 2020*). Subtropical gyres are the largest wind-driven circulation systems in the world's ocean and cover about 75 % of the ocean's surface (*McClain et al., 2004; Sarmiento and Gruber, 2006*). The five major subtropical gyres are located around 20°–30° latitude in the North and South Atlantic, the North and South Pacific, and the South Indian Ocean. In the Indian Ocean only one subtropical gyre is developed in the southern hemisphere due to the land-locked shape of the North Indian

Ocean. Gyres in the northern and southern hemispheres are similar except that they rotate in opposite directions, where subtropical gyres in the northern hemisphere rotate in a clockwise direction while southern hemisphere gyres rotate in a counter-clockwise direction (e.g., *Follows et al.*, 2002, *Williams and Follows*, 2003; *Sarmiento and Gruber*, 2006). This is caused by the Earth's rotation and the Coriolis force that acts to change the direction of a moving body (e.g., winds) to the right in the northern hemisphere and to the left in the southern hemisphere (*Persson*, 1998). Consequently, the circulation of the subtropical gyres is developed by the deflected westerly winds on the northern side of the gyre and easterly trade winds on the southern side.

The Ekman transport couples wind and surface water movements and leads to a net water movement of 90° to the right of the wind in the northern hemisphere and to the left in the southern hemisphere and is confined to the top 10 to 100 m of the water column (*Sarmiento and Gruber*, 2006). Regarding the subtropical gyre circulation, Ekman transport leads to the horizontal convergence of surface waters that move toward the central region of the subtropical gyre, piles up water in the center and thus creates large horizontal gradients, resulting in a high pressure zone in the upper ocean (*Williams and Follows*, 2003; *Sarmiento and Gruber*, 2006). The circulation around such a high pressure zone is referred to as anticyclonic and causes a broad mounding (elevation of the sea surface high; SSH) of water as high as one meter above mean sea level near the gyre center (*Williams and Follows*, 2003; *Sarmiento and Gruber*, 2006; *Baer et al.*, 2019). In response to the horizontal convergence, water moves from where the pressure is higher towards where the pressure is lower, that is, also downhill and thus induce downwelling in regions of convergent flow that is known as Ekman pumping (e.g., *Sarmiento and Gruber*, 2006). This leads to a depression of thermo- and pycnoclines that shoal towards the gyre margins (*McClain et al.*, 2004). The ocean mixed layer (OML; upper surface layer of uniform physical properties, such as density, temperature, and salinity/conductivity) and the nutricline follow these gradients (*Williams and Follows*, 1998; *Kantha and Clayson*, 2003; *Baer et al.*, 2019). Consequently, subtropical gyres are intensely stratified systems with strongly nutrient-depleted surface waters in the gyre region. Thus, subtropical gyres are extensive oligotrophic areas. However, due to their immense size, they contribute significantly to global N cycle budgets and to atmosphere-ocean carbon fluxes (*McClain et al.*, 2004).

1.2 The Indian Ocean subtropical gyre (IOSG)

1.2.1 Regional setting

The Indian Ocean subtropical gyre (IOSG) is one of the five large oligotrophic gyres that ranges approximately from 10°S to 35°S in the South Indian Ocean (Williams and Follows, 2003; Sarmiento and Gruber, 2006; Baer et al., 2019). Branches of several current systems drive the circulation of the IOSG. The South Equatorial Current (SEC), the South Indian Ocean Current (SIOC), and the West Australian Current (WAC) are the major currents that confine the counter-clockwise rotating IOSG (Figure 1.1).

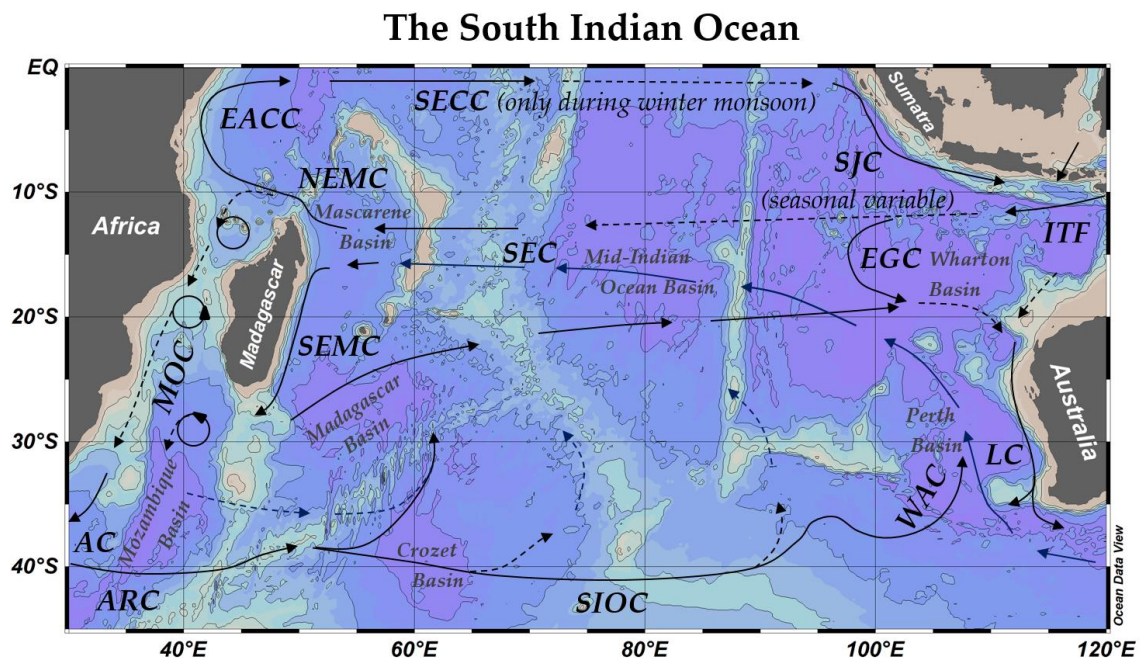


Figure 1.1. Map of the South Indian Ocean with schematic representation of deep-sea basins and surface/subsurface currents according to Stramma (1992), Stramma and Lutjeharms (1997), Schott and McCreary (2001), and Schott et al. (2009). Current branches are Agulhas Current (AC), Agulhas Return Current (ARC), East African Coastal Current (EACC), East Gyrat Current (EGC), Leeuwin Current (LC), Mozambique Current (MOC), Northeast Madagascar Current (NEMC), South Equatorial Current (SEC), South Equatorial Countercurrent (SECC), Southeast Madagascar Current (SEMS), South Indian Ocean Current (SIOC), South Java Current (SJC), West Australian Current (WAC), ITF indicates the Indonesian Throughflow.

The SEC is the northern boundary of the IOSG. This is a broad westward current roughly between 8°S to 20°S driven by the southeast trades and separates the IOSG from the clockwise, tropical gyre (cyclonic) in the southern equatorial Indian Ocean (Wyrтки, 1971; Godfrey and Golding, 1981; Pickard and Emery, 1982; Woodberry, 1989; Schott and McCreary, 2001). At about 10°–25°S, the SEC is in part fed by an external source from the Pacific Ocean, named Indonesian Throughflow (ITF) that injects fresh, less saline water into the South Indian Ocean (e.g., Wyrтки, 1971; Godfrey and Golding, 1981; Woodberry, 1989; You and Tomczak, 1993). At 50°–60°E the SEC splits into northward and southward branches, which are called the North East Madagascar Current (NEMC) and the South East Madagascar Current (SEMC; Schott and McCreary, 2001; Schott *et al.*, 2009). The western boundary current of the IOSG is the Agulhas Current along the east of South Africa fed by the SEMC and water throughflow from the Mozambique channel (Stramma and Lutjeharms, 1997). The southern boundary of the IOSG is marked by the South Indian Ocean Current (SIOC) and is located at the Subtropical Front (STF) at about 40°S (Deacon, 1933; Stramma, 1992).

A more detailed look on the IOSG reveals three main circulations: a basin wide circulation on time scales of years, a subgyre in the southwest Indian Ocean, and an intermediate circulation between these both (Heydorn *et al.*, 1978; Stramma and Lutjeharms, 1997), all with a pivot in the southwest corner (Wyrтки, 1971; Harris, 1972; Lutjeharms, 1976). The strongest flow rates are found in the southwest and central Indian Ocean (Stramma and Lutjeharms, 1997). Overall, the IOSG has a rather rectangular shape compared to the triangular shape of the South Atlantic subtropical gyre due to the ITF northeast of the IOSG (Stramma and Lutjeharms, 1997).

1.2.2 Biogeochemical setting

The specific physical conditions typical for subtropical gyres have a strong impact on the nutrient distribution, the particulate matter transport, and overall on the biogeochemical processes regarding the N and C cycles in the IOSG. As in all subtropical gyres, horizontal Ekman transport to the gyre center leads to a thick nutrient-depleted mixed layer. Here regeneration of organic matter and associated nutrients is efficient, while vertical mixing and the resulting influx of nutrients from deeper waters is reduced or absent (*Knox and McElroy, 1984; Sarmiento and Toggweiler, 1984; Siegenthaler and Wenk, 1984; Ito and Follows, 2005; Duteil et al., 2012; Rixen et al., 2019a*). Thus, the IOSG belongs to those extensive oligotrophic regions in the world's ocean, where the essential macronutrients, such as reactive N and phosphorus (P) are limited. Primary producers, i.e., the free-floating unicellular phytoplanktonic organisms that are responsible for photosynthesis in the ocean require and take up these elements (together with other macro- and micronutrients, e.g., carbon and iron) from the seawater in order to form organic matter (*Sarmiento and Gruber, 2006*) and couple the N and C cycles in the ocean. The IOSG has limited primary production in the biologically active zone (euphotic zone) that leads to low particulate matter production in surface waters and results in low sinking fluxes. However, due to their size, vast oligotrophic gyres account for half of the global organic carbon export to the ocean interior (*Emerson et al., 1997*). Thus, the particulate organic carbon (POC) export out of the euphotic zone, across the thermocline into the deep ocean, and into the sediments constitutes the organic carbon pump that is an essential part of the global C cycle (*Volk and Hoffert, 1985*). An effective organic carbon pump lowers the partial pressure of CO₂ in surface waters and thus enhances the ocean's ability to absorb CO₂ from the atmosphere (*Berger et al., 1989; Wefer and Fischer, 1991; Lutz et al., 2007*). Consequently, the organic pump controls the partitioning of carbon between the large reservoir in the deep ocean and the relatively small atmospheric reservoir (*Berger et al., 1989*).

1.3 Research project and thesis outline

The investigations in the South Indian Ocean are part of the environmental studies in the INDEX (Indian Ocean Exploration) program for marine resource exploration by the Federal Institute for Geosciences and Natural Resources (BGR), Germany, and the International Seabed Authority (ISA), Jamaica. The INDEX program bases on a 15-years contract between the BGR and the ISA and explores polymetallic sulfides on the seafloor for a potential future deep-sea mining in the German licence area, located along the Central Indian Ridge (CIR) and the Southeast Indian Ridge (SEIR). The aim of the accompanying environmental studies, to which the Universität Hamburg has been contributing since 2014, is to understand the processes driving and modulating productivity and sedimentation in order to be able to assess the potential environmental impacts of deep-sea mining activities.

Samples used for this thesis were collected during five ship expeditions during 2015 and 2019 and include water samples, sinking particulate matter samples collected by sediment traps, and surface sediment samples. The main goal was to understand the key processes of the N and C cycle within a sparsely investigated and underrepresented ocean region, where little is known on N cycle processes and primary production and no field data on the downward flux of sinking particles to the seafloor and its final carbon storage in the pelagic sediments are available.

This thesis is a cumulative work and consists of four scientific parts (Chapter 2 to 5). Each of these four main chapters is written in the style of journal publications, containing their own abstract, introduction, results and discussion section, and summary/conclusion. The individual Chapters can thus be read independently from each other. Chapter 2 depicts investigations on the relatively unknown hydrology and the hitherto unexplored distribution of nutrients and stable isotopes of nitrate to identify nutrient sources and N cycle processes within the IOSG towards the southern equatorial Indian Ocean. It is based on water column data and on analyses of water samples collected during INDEX expeditions in 2016 and 2017. This part has been published in the Journal Biogeosciences (*Harms et al.*, 2019, see the List of publications). Data presented and interpreted in Chapter 2 were collected and analyzed by myself. I wrote the draft and revised the manuscript during the review process.

Chapter 3 deals with the first data on sinking particulate matter collected during sediment trap experiments between 2014 and 2018. The results provide new information on the controlling factors of sinking POC and the seasonal and lateral gyre variability. This part is under revision for the Journal Deep-Sea Research II (*Harms et al.*, 2021; see the List of publications). Data presented and interpreted in Chapter 3 were collected and analyzed by myself. I wrote the draft and I revise the manuscript during the review process.

Chapter 4 extends the work on water mass distribution and N cycle processes, based on data from INDEX expeditions in 2018 and 2019. Chapter 5 extends the sinking particulate matter study in Chapter 3 by new data of sediment trap experiments between 2018 and 2019 and surface sediment data collected between 2015 and 2018. The Chapters 4 and 5 were submitted to Springer Nature as book chapters 19 and 20 as part of a comprehensive report that include all disciplines contributing to the INDEX program (preliminary book title: Marine Metal Exploration: The INDEX Project – Prospecting the Seafloor for Polymetallic Sulphides, see the List of publications). Data presented and interpreted in the Chapters 4 and 5 were collected and analyzed by myself. I wrote the drafts and I will revise the manuscripts during the review processes. In Chapter 6, I summarize the findings of this thesis and draw the main conclusions. Furthermore, I give an outlook on possible future research.

Technical remark

This Introduction (Chapter 1) and Conclusion (Chapter 6) are written in the first person, whereas the main Chapters 2, 3, 4, and 5 are the individual cumulative parts I to IV and are written in the first person plural.

Chapter 2 – Cumulative Part I

Nutrient distribution and nitrogen and oxygen isotopic composition of nitrate in water masses of the subtropical South Indian Ocean

(Published in Biogeosciences, DOI: 10.5194/bg-16-2715-2019)

Natalie C. Harms¹, Niko Lahajnar¹, Birgit Gaye¹, Tim Rixen^{1,2}, Kirstin Dähnke³, Markus Ankele³, Ulrich Schwarz-Schampera⁴, and Kay-Christian Emeis^{1,3}

¹Institute of Geology, Universität Hamburg, Hamburg, 20146, Germany.

²Leibniz-Centre for Tropical Marine Research, Bremen, 28359, Germany.

³Helmholtz-Zentrum Geesthacht (HZG), Institute for Coastal Research, Geesthacht, 21502, Germany.

⁴Federal Institute for Geosciences and Natural Resources (BGR), Hannover, 30655, Germany.

Correspondence to: Natalie C. Harms (natalie.harms@uni-hamburg.de)

Abstract. The Indian Ocean subtropical gyre (IOSG) is one of five extensive subtropical gyres in the world's ocean. In contrast to those of the Atlantic and Pacific Ocean, the IOSG has been sparsely studied. We investigate the water mass distributions based on T/S and oxygen data, concentrations of water column nutrients, and stable isotope composition of nitrate, using waters samples from two expeditions in 2016 (*MSM 59/2*) and 2017 (*SO 259*), collected between ~30°S and the equator. Our results are the first in this ocean region and provide new information on nitrogen sources and transformation processes. We identify the thick layer of nutrient-depleted surface waters of the oligotrophic IOSG with nitrate (NO_3^-) and phosphate (PO_4^{3-}) concentrations of $<3 \mu\text{mol L}^{-1}$ and

$<0.3 \mu\text{mol L}^{-1}$, respectively ($<300 \text{ m}$; $\sigma <26.4 \text{ kg m}^{-3}$). Increased nutrient concentrations towards the equator represent the northern limb of the gyre, characterized by typical strong horizontal gradients of the outcropping nutriclines. The influx of the Subantarctic Mode Water (SAMW) from the Southern Ocean injects oxygen-saturated waters with preformed nutrients, indicated by increased nitrogen (N) and oxygen (O) isotope composition of nitrate ($\delta^{15}\text{N} >7 \text{ ‰}$; $\delta^{18}\text{O} >4 \text{ ‰}$) at $400\text{--}500 \text{ m}$ ($26.6\text{--}26.7 \text{ kg m}^{-3}$), into the Subtropical thermocline. These values reflect partial N assimilation in the Southern Ocean. Moreover, in the northern study area, a residue of nitrate affected by denitrification in the Arabian Sea is imported into intermediate and deep water masses ($>27.0 \text{ kg m}^{-3}$) of the gyre, indicated by an N deficit ($\text{N}^* \approx -1$ to $-4 \mu\text{mol L}^{-1}$) and by elevated isotopic ratios of nitrate ($\delta^{15}\text{N} >7 \text{ ‰}$; $\delta^{18}\text{O} >3 \text{ ‰}$). Remineralisation of partial-assimilated organic matter, produced in the Subantarctic, leads to a decoupling of N and O isotopes in nitrate and results in relatively low $\Delta(15\text{--}18)$ of $<3 \text{ ‰}$ within the SAMW. In contrast, remineralisation of ^{15}N -enriched organic matter originated in the Arabian Sea indicates higher $\Delta(15\text{--}18)$ values of $>4 \text{ ‰}$ within the Red Sea-Persian Gulf Intermediate Water (RSPGIW). Thus, the subtropical South Indian Ocean is supplied by preformed nitrate from the lateral influx of water masses from regions exhibiting distinctly different N cycle processes documented in the dual isotope composition of nitrate. Additionally, a significant contribution of N_2 fixation between $20.36^\circ\text{--}23.91^\circ\text{S}$ is inferred from reduced $\delta^{15}\text{N}\text{-NO}_3^-$ values towards surface waters (upward decrease of $\delta^{15}\text{N} \approx 2.4 \text{ ‰}$), N^* values of $>2 \mu\text{mol L}^{-1}$ and a relatively low $\Delta(15\text{--}18)$ of $<3 \text{ ‰}$. A mass and isotope budget implies that at least 32–34 % of the nitrate in the upper ocean between $20.36^\circ\text{--}23.91^\circ\text{S}$ is provided from newly fixed N, whereas N_2 fixation appears to be limited by iron or temperature south of 26°S .

2.1 Introduction

The South Indian Ocean is dominated by a subtropical anticyclonic gyre (*Williams and Follows, 2003; Sarmiento and Gruber, 2006*), the Indian Ocean Subtropical Gyre (IOSG), one of the major five subtropical gyres in the world's ocean. In contrast to those of the Atlantic and Pacific Oceans, where subtropical gyres occur north and south of the equator, the Indian Ocean developed only one subtropical gyre south of the equator. In comparison to other subtropical gyres, the IOSG has been sparsely investigated. Between $10^\circ\text{--}20^\circ\text{S}$, the South Equatorial Current (SEC)

marks the northern limb of the IOSG (*Duing, 1970; Pickard and Emery, 1982; Woodberry et al., 1989*) and separates the subtropical gyre of the South Indian Ocean from the southern equatorial Indian Ocean. In the center of the subtropical gyre, Ekman transport leads to an intensive downwelling (*Williams and Follows, 1998*), which results in a deepening of thermo-, pycno-, and nutriclines. These layers shoal towards the fringe of the IOSG causing steep horizontal gradients (*McClain et al., 2004*). Due to the intense downwelling and the resulting deepening of nutriclines, subtropical gyres form extensive oligotrophic regions, which occupy ~40 % of the Earth's surface (*McClain et al., 2004*). Since the biological productivity within these oligotrophic regions is relatively low they are often referred to as "oceanic deserts" (*Clark et al., 2008*). However, due to their immense size they contribute significantly to atmosphere-ocean carbon fluxes (*McClain et al., 2004*).

Future global warming is assumed to strengthen stratification in low-latitude oceans and to expand the low productive subtropical gyres, accompanied by a decrease of the net primary production (*Behrenfeld et al., 2006*). This might have crucial impact on the marine nitrogen (N) cycle. To study the marine N cycle, we use nitrate and phosphate concentrations, as well as the isotopic signature of nitrate (*Gruber and Sarmiento, 1997; Deutsch et al., 2001; Lehmann et al., 2005; Sigman et al., 2005; Deutsch et al., 2007*). The dominant source and sink of fixed, reactive N in the ocean are diazotrophic dinitrogen (N₂) fixation and heterotrophic denitrification (*Deutsch et al., 2001*). N₂ fixation by diazotrophs, such as *Trichodesmium*, is observed over much of the tropical and oligotrophic subtropical oceans (*Karl et al., 1995; Michaels et al., 1996; Capone et al., 1997; Emerson et al., 2001*). N₂ fixation compensates the loss of reactive N during the heterotrophic denitrification if the ocean's marine N cycle is in a steady state (*Deutsch et al., 2001*).

The inputs of N through N₂ fixation are detached from inputs of phosphorus (P), leading to a decoupling of the nitrate (NO₃⁻) and phosphate (PO₄³⁻) pool. Deviations in the NO₃⁻ to PO₄³⁻ relationship from the Redfield-stoichiometry are used to study rates of both, N₂ fixation and denitrification (*Gruber and Sarmiento, 1997; Sigman et al., 2005*). Therefore, the tracer N* is used as an indicator for excesses and deficits in NO₃⁻ relative to the global NO₃⁻/PO₄³⁻ ratio and is expressed by the formula $N^* = [NO_3^-] - 16 \times [PO_4^{3-}] + 2.9 \mu\text{mol L}^{-1}$. The concept of N* has been discussed in detail by *Gruber and Sarmiento (1997)* and slightly modified by *Deutsch et al. (2001)*. The concentration of 2.9 $\mu\text{mol L}^{-1}$ was added to bring the

global mean of N^* to about zero (*Sarmiento and Gruber, 2006*). However, the use of N^* has limitations. First, the deviation from the Redfield-stoichiometry may not always be a result of N inputs or outputs (N_2 fixation and denitrification) but may reflect also variations of uptake and remineralisation processes (*Sigman et al., 2005*). Second, input and losses partially overprint each other when they occur simultaneously in the same water body.

We use stable isotopes of nitrate (N and O) to overcome the weakness associated with the N^* approach and distinguish between sources and sinks of fixed N to study transfer processes in the N cycle (e.g., N assimilation, denitrification, nitrification, N_2 fixation), also when they occur simultaneously. Isotope ratios are reported in per mil (‰) using the δ -notation ($\delta^{15}N = [(^{15}N/^{14}N_{\text{sample}})/(^{15}N/^{14}N_{\text{atm.N}_2}) - 1] \times 1000$; $\delta^{18}O = [(^{18}O/^{16}O_{\text{sample}})/(^{18}O/^{16}O_{\text{VSMOW}}) - 1] \times 1000$, with air N_2 and VSMOW as reference for $^{15}N/^{14}N$ and $^{18}O/^{16}O$, respectively). During consumption processes of nitrate, e.g., N assimilation or denitrification, lighter isotopes are preferentially assimilated, leaving the substrate enriched in ^{15}N and ^{18}O according to its isotope effect ($^{15}\epsilon$ and $^{18}\epsilon$, e.g., $^{15}\epsilon$ is defined as $^{14}k/^{15}k - 1$, where ^{14}k and ^{15}k are the rate coefficients of the reactions for the ^{14}N - and ^{15}N -bearing forms of nitrate). Several culture experiments indicate that $\delta^{15}N$ and $\delta^{18}O$ of the residual nitrate pool rise equally as consumption proceeds, consequently the O-to-N isotope effect ($^{18}\epsilon:^{15}\epsilon$) is close to 1 (*Sigman et al., 2003; Granger et al., 2004; Sigman et al., 2005; Rafter et al., 2013*).

While nitrate consumption processes such as N assimilation and denitrification lead to indistinguishable imprints on N and O isotope compositions, nitrate production processes (nitrification and N_2 fixation) have very different effects on the N and O isotopes of nitrate (*Sigman et al., 2005; Rafter et al., 2013*). Whereas almost all of the ammonium generated from organic N is oxidized to nitrate in oxic subsurface waters of the open ocean, the N isotope effect associated with ammonium production and nitrification do not affect the $\delta^{15}N\text{-NO}_3^-$. Therefore, the N isotope effect depends more on the biomass being remineralized (*Sigman et al., 2005; Rafter et al., 2013*). In contrast, the $\delta^{18}O$ of newly nitrified nitrate is independent of the isotopic composition of the organic matter and leads to a counteracting behaviour of $\delta^{15}N$ and $\delta^{18}O$. Consequently, the decoupling of N and O isotopes provide a better understanding of nitrate assimilation and regeneration processes in marine environments (*Sigman et al., 2005; Wankel et al., 2007; Casciotti et al., 2008; Sigman et al., 2009; DiFiore et al., 2010*).

Our investigations in the South Indian Ocean are part of environmental studies in the INDEX (Indian Ocean Exploration) program for marine resource exploration by the federal Institute for Geosciences and Natural Resources (BGR), Germany, and the International Seabed Authority (ISA). We use CTD measurements and analyse seawater samples to determine nutrient concentrations and stable isotopes of nitrate ($\delta^{15}\text{N}$ and $\delta^{18}\text{O}$) along a transect from the IOSG to the southern equatorial Indian Ocean. The main goal of this study is to investigate the relatively unknown hydrology and the unexplored distribution of nutrients and stable isotopes of nitrate to identify N cycle processes within the IOSG towards the equatorial South Indian Ocean. First, we identify the water masses and their provenance by their unique characteristic physical properties and establish the first water mass distribution model for this ocean region. In a second step, we use new nutrient and stable isotope data to determine nutrient sources to the IOSG and their role in the marine N cycle. Furthermore, we demonstrate the influence of water masses on the nutrient distribution and the isotopic composition of water column nitrate by the influx of preformed nutrients. Our results of nutrient and isotope measurements are the first in the IOSG and bridge the gap between several investigations in the Arabian Sea (e.g., Brandes *et al.*, 1998; Gaye-Haake *et al.*, 2005; Ward *et al.*, 2009; Gaye *et al.*, 2013) and in the Indian section of the Southern Ocean (e.g., Bianchi *et al.*, 1997; Sigman *et al.*, 1999, 2000; DiFiore *et al.*, 2006; DiFiore *et al.*, 2010).

2.2 Materials and methods

2.2.1 CTD measurements and sample collection

In total, 313 seawater samples were collected at 15 CTD stations (Figure 2.1) during two expeditions with the R/V *Maria S. Merian* (MSM 59/2 “INDEX 2016-2”; November–December 2016) and the R/V *Sonne* (SO 259 “INDEX 2017”; August–October 2017, see station list in Table A1.1 in the Appendix A1). The compiled data is available at the DataBase PANGAEA at <https://doi.pangaea.de/10.1594/PANGAEA.897503> and <https://doi.pangaea.de/10.1594/PANGAEA.897504> (see Harms *et al.*, 2019). The CTD was equipped with sensors to determine density, temperature, salinity, and oxygen at overall 17 CTD stations from the surface down to the seafloor. No water samples were collected at stations 07 and 11.

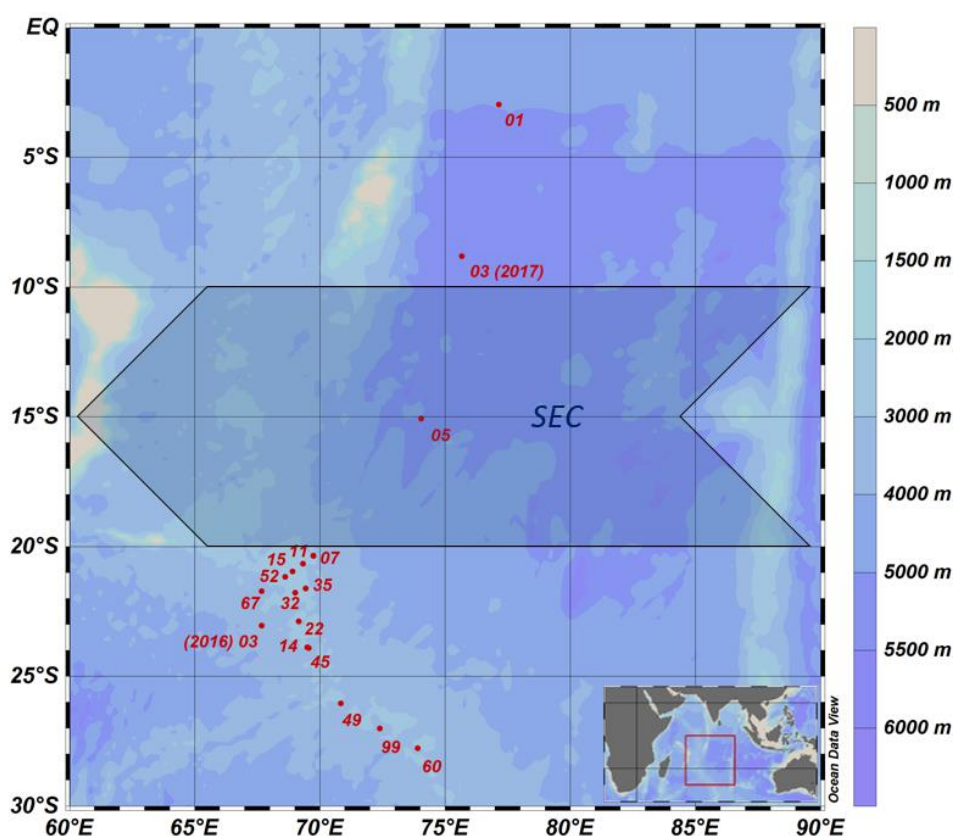


Figure 2.1. Sampling location during the cruises *MSM 59/2* (INDEX 2016-2) and *SO 259* (INDEX 2017). For station numbers (red) see Table A1.1 in the Appendix A1. Shaded arrow represents the westward-directed, broad South Equatorial Current (SEC) after Woodberry (1989) from 10°–20°S. Colours denote water depths.

The study area covers the region of the IOSG from 30°S, across the SEC at 10°–20°S and towards the equator. Fourteen CTD stations are located within the IOSG from 20.36°S to 27.78°S and 67.07°E to 73.92°E. CTD 05 is located in the region of the SEC (15.08°S, 74.05°E) and at the northern end of the IOSG. The northernmost CTD stations (CTD 01, 03; 2017) at 8.81°S, 75.67°E and 2.98°S, 77.16°E are positioned in the southern equatorial Indian Ocean, north of the SEC. Seawater samples were collected for measurements of nutrients and stable isotopes of nitrate. Samples were filtered through a Nucleopore polycarbonate filter (0.4 μm) with a metal- and silicon-free Nalgene filtration unit. The filtered water was bottled in Falcon PE tubes (45 ml) and immediately stored at -20°C during the cruise. The samples were shipped as frozen airfreight (-20°C) to Germany. Nutrient concentrations and stable isotopes of nitrate (N and O) were determined in the home lab immediately after arrival.

2.2.2 Nutrient analysis

Nutrient concentrations (NO_x , NO_2^- , NH_4^+ , PO_4^{3-}) were measured with a SEAL AutoAnalyzer3HR with standard colourimetric methods (Grasshoff *et al.*, 2009). Ammonia (NH_4^+) and nitrite (NO_2^-) concentrations were below detection limit. Nitrate determination included reduction of nitrate to nitrite with a cadmium reduction column. Nitrite ions reacted with sulphanilamide to form a diazo compound, followed by a reaction to an azo dye with N-(1-naphthyl)-ethylenediamine (NEDD) and was measured at 520–560 nm. Phosphate determination followed the method of Murphy and Riley (1962). Under acid conditions a phosphomolybdic complex was formed of ortho-phosphate, antimony and molybdate ion (Wurl, 2009). Followed by reduction of ascorbic acid, the blue colour complex was measured at 880 nm. The relative error of duplicate sample measurements was below 1.5 % for nitrate and phosphate concentrations and detection limit was $<0.5 \mu\text{mol L}^{-1}$ for NO_x , and $>0.1 \mu\text{mol L}^{-1}$ for PO_4^{3-} .

2.2.3 Measurements of N and O isotopes of nitrate

Isotope measurements were only conducted for samples with nitrate concentrations $>1.7 \mu\text{mol L}^{-1}$. Stable isotopes of nitrate ($\delta^{15}\text{N}$ and $\delta^{18}\text{O}$) were determined using the “denitrifier” method (Sigman and Casciotti, 2001; Casciotti *et al.*, 2002). Nitrate was converted to N_2O gas using denitrifying bacteria (*Pseudomonas aureofaciens*). Based on nitrate concentrations, sample volumes were adjusted to yield 10 nmoles N_2O and were injected into suspensions of *Pseudomonas aureofaciens* (ATCC#13985) for combined analysis of $\delta^{15}\text{N}$ and $\delta^{18}\text{O}$. The resulting N_2O gas in headspace was purged into a GasBench II (ThermoFinnigan) and analysed in a Delta V Advantage and a Delta V Plus mass spectrometer. The results were calibrated using IAEA-N3 ($\delta^{15}\text{N-NO}_3^- = +4.7 \text{‰}$ and $\delta^{18}\text{O-NO}_3^- = +25.6 \text{‰}$) and USGS-34 ($\delta^{15}\text{N-NO}_3^- = -1.8 \text{‰}$ and $\delta^{18}\text{O-NO}_3^- = -27.9 \text{‰}$) (Böhlke *et al.*, 2003). A further internal potassium nitrate standard (KBI) was analysed within each run for quality assurance ($\delta^{15}\text{N-NO}_3^- = +7.1 \text{‰}$). Isotope values were corrected using the “bracketing scheme” from Sigman *et al.*, (2009) for $\delta^{18}\text{O-NO}_3^-$ and a two-point correction referred to IAEA-N3 and USGS-34 for $\delta^{15}\text{N-NO}_3^-$ and $\delta^{18}\text{O-NO}_3^-$. The standard deviation for IAEA-N3 was better than 0.2 ‰ for $\delta^{15}\text{N-NO}_3^-$ and 0.3 ‰ for $\delta^{18}\text{O-NO}_3^-$, which is within the same

specification for $\delta^{15}\text{N}\text{-NO}_3^-$ and $\delta^{18}\text{O}\text{-NO}_3^-$ for at least duplicate measurements of the samples.

2.3 Results

2.3.1 Physical water column properties

South of 25°S the upper 170 m are characterized by an intense salinity maximum with values of >35.5 PSU and temperatures above 15°C (Figure 2.2a, Figure 2.3). The salinity maximum is carried northwards and is subducted underneath the surface layer within a temperature range of 22–15°C and with a core density of $\sigma = 25.5 \text{ kg m}^{-3}$ (~250 m). Further north (CTD 03, 2017; 8.81°S) at the same density level, the salinity is significantly lower and reveals values of 35.2 PSU. The northernmost station (CTD 01, 2017; 2.89°S) indicates again a slight increase in salinity (>35.3 PSU). Between 22°S and 10°S, less saline surface water (<35.1 PSU) lies above the density level of the salinity maximum with temperatures of >23°C and densities above 24.0 kg m^{-3} (<150 m). South of 15°S, directly underneath the salinity maximum an oxygen maximum with values of >4.7 mL L⁻¹ occurs at a density range of $26.4\text{--}26.9 \text{ kg m}^{-3}$ (250–750 m; Figure 2.2b) and temperatures between 8°C and 15°C (Figure 2.3). The lower limit of the oxygen maximum coincides with a temperature level of 8–9°C at $\sigma = 26.9\text{--}27.0 \text{ kg m}^{-3}$ and marks the permanent thermocline at a depth of ~750 m in the south and at a depth of ~500 m in the north. Oxygen concentrations decrease towards the north and fall below 2 mL L⁻¹ at the northernmost stations (CTD 01, CTD 03; 2017; Figure 2.2b, Figure 2.3). Below the permanent thermocline (<9°C), an absolute salinity minimum with values less than 34.6 PSU is found in the southern region (Figure 2.2a, Figure 2.3), within a density range of $26.9\text{--}27.4 \text{ kg m}^{-3}$ (core density $\sigma = 27.2 \text{ kg m}^{-3}$), which is strongly diluted further north and temperatures are below 8°C (Figure 2.3). In the southern equatorial Indian Ocean at CTD 01, an increase in salinity (>34.9 PSU; $\sigma = 27.2 \text{ kg m}^{-3}$) corresponds with reduced oxygen concentrations of <1.1 mL L⁻¹. Overall, low oxygen concentrations dominate the northern study area and extend to deeper water masses at the southernmost stations (<3.5 mL L⁻¹; Figure 2.2b, Figure 2.3).

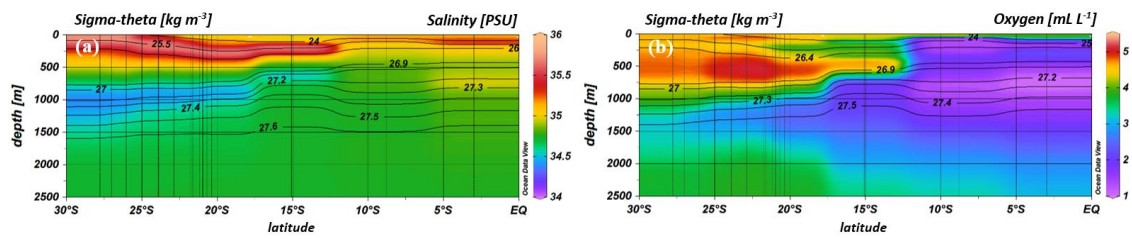


Figure 2.2. Profiles of salinity (a) and oxygen distribution (b) from CTD measurements during cruises *MSM 59/2* (2016) and *SO 259* (2017). Contour lines indicate the potential density sigma-theta in kg m^{-3} .

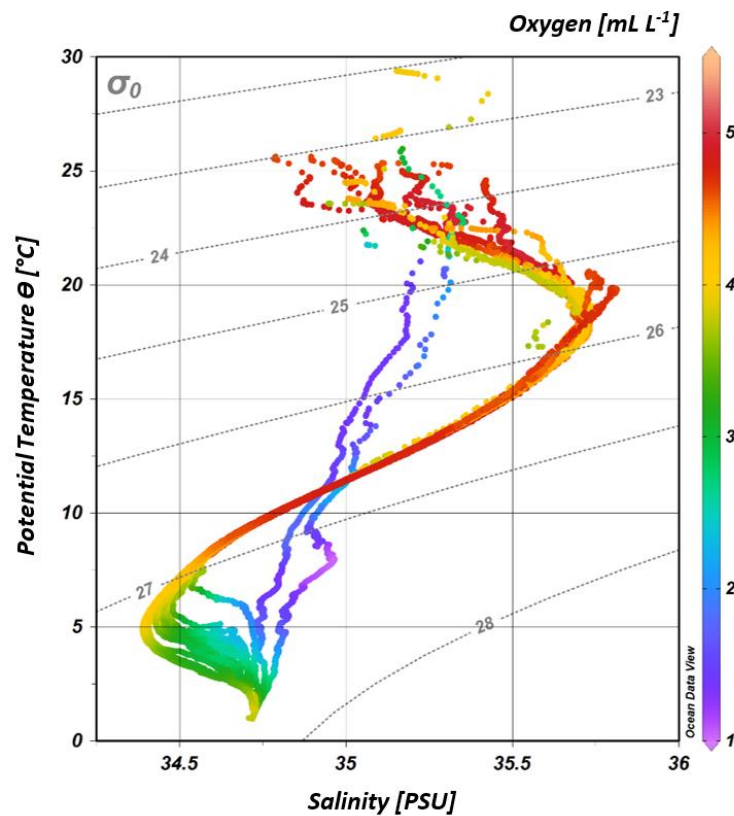


Figure 2.3. T-S diagram (potential temperature vs. salinity) from CTD measurements during cruises *MSM 59/2* (2016) and *SO 259* (2017). The colour bar indicates oxygen concentrations and grey, dotted lines represent density surfaces in sigma-theta (kg m^{-3}). The northernmost CTD stations (CTD 01, CTD 03; 2017) are characterized by low oxygen concentrations ($<2 \text{ mL L}^{-1}$) and less variations in the salinity distribution, while the water column profiles in the IOSG indicate a distinct salinity maximum and minimum, respectively.

2.3.2 Nutrient concentration

Within the subtropical gyre, the upper 100 m are strongly depleted in nitrate and phosphate with concentrations less than $1 \mu\text{mol L}^{-1}$ of nitrate and less than $0.1 \mu\text{mol L}^{-1}$ of phosphate (Figure 2.4a, b, Table 2.1). Within the depth range of the salinity maximum ($24.9\text{--}26.4 \text{ kg m}^{-3}$; $<300 \text{ m}$), nutrient concentrations are still minor with NO_3^- and PO_4^{3-} values of $<3 \mu\text{mol L}^{-1}$ and $<0.3 \mu\text{mol L}^{-1}$, respectively (Table 2.1). Nutrient concentrations rise within the depth range of the oxygen maximum ($\sigma = 26.4\text{--}26.9 \text{ kg m}^{-3}$), where we observe concentrations of $\sim 11 \mu\text{mol L}^{-1} \text{ NO}_3^-$ and $<0.9 \mu\text{mol L}^{-1} \text{ PO}_4^{3-}$ before they reach typical deep-sea values of $>30 \mu\text{mol L}^{-1}$ and $>2 \mu\text{mol L}^{-1}$ (Sarmiento and Gruber, 2006) within intermediate waters ($>26.9 \text{ kg m}^{-3}$; $>750 \text{ m}$). Across the northern fringe of the gyre at surface waters, (CTD 05, 2017; 15.08°S) nutrient concentrations slightly increase (Figure 2.4a, b).

Further north, at stations CTD 01 and 03 ($2.98^\circ\text{--}8.81^\circ\text{S}$), nutrient concentrations in the upper water column reach values typical for open ocean areas that are unaffected by gyral downwelling or high biological production (Figure 2.4a, b). At 90 m water depth, concentrations were $\sim 11 \mu\text{mol L}^{-1}$ for nitrate and $\sim 1 \mu\text{mol L}^{-1}$ for phosphate. Within the thermocline ($23.0\text{--}27.0 \text{ kg m}^{-3}$; $<550 \text{ m}$), nutrient concentrations attain values of $>20 \mu\text{mol L}^{-1}$ for nitrate and $>1.5 \mu\text{mol L}^{-1}$ for phosphate, before they level out at values of $>35 \mu\text{mol L}^{-1}$ for nitrate and $>2.5 \mu\text{mol L}^{-1}$ for phosphate at greater depth (Table 2.1).

2.3.3 N and O isotopes of nitrate

In the upper 750 m ($<26.9 \text{ kg m}^{-3}$), distinct N and O isotope maxima with $\delta^{15}\text{N}$ of $>7.0 \text{ ‰}$ and $\delta^{18}\text{O}$ of $>4.0 \text{ ‰}$ are found at latitudes $27.78^\circ\text{--}15.08^\circ\text{S}$ (Table 2.1, Figure 2.4c, d). N and O isotope maxima are observed at $\sim 400\text{--}500 \text{ m}$ ($26.6\text{--}26.7 \text{ kg m}^{-3}$) and correlate with the oxygen maximum of $>4.7 \text{ mL L}^{-1}$. At latitudes $23.91^\circ\text{--}20.96^\circ\text{S}$, the N isotope maximum is found at 400 m, whereas the O isotope maximum is observed at 500 m. Consequently, N and O isotope maxima indicates an offset of $\sim 100 \text{ m}$ (see Table A1.3 and Table A1.4 in the Appendix A1). Above the isotopic maxima, both $\delta^{15}\text{N}$ and $\delta^{18}\text{O}$ decrease to values of $\sim 5.4 \text{ ‰}$ and $\sim 2.1 \text{ ‰}$, respectively, in the upper 300 m; an exception are the southernmost stations (CTD 49, 60, 99; 2017), where elevated $\delta^{15}\text{N}$ values extend up to the surface (Figure 2.4c). In surface waters further north ($<250 \text{ m}$), $\delta^{15}\text{N}$ and $\delta^{18}\text{O}$

increase to values of >7.0 ‰ and >4 ‰, respectively, at the northernmost station (CTD 01, 2017; Figure 2.4c, d). Underneath this surface layer, N and O isotope ratios slightly decrease at ~ 180 m, before $\delta^{15}\text{N}$ and $\delta^{18}\text{O}$ again rise to >7.0 ‰ and >3.0 ‰, with an extended maximum in the depth interval from 300 m to 900 m (<27.3 kg m $^{-3}$) that coincides with elevated salinities. Below the isotopic maxima in the southern region at ~ 400 – 500 m and below the depth interval with high δ -values in the northernmost CTD station, $\delta^{15}\text{N}$ and $\delta^{18}\text{O}$ decrease towards deeper waters and have average values of 5.8 ‰ and 2.3 ‰ (Figure 2.4c, d).

Table 2.1. Average nitrate and phosphate concentrations and average $\delta^{15}\text{N}\text{-NO}_3^-$ and $\delta^{18}\text{O}\text{-NO}_3^-$ values within water masses of the South Indian Ocean, defined along their potential density surfaces (sigma-theta) and separated into four latitudinal sections (27.78° – 26.05°S , 23.91° – 20.36°S , 15.08°S , 8.81° – 2.98°S). Water mass abbreviations as followed: Indonesian Upper Water (IUW), Subtropical Surface Water (SSW), Subantarctic Mode Water (SAMW), Indian Equatorial Water (IEW), Antarctic Intermediate Water (AAIW), Indonesian Intermediate Water (IIW), Red Sea-Persian Gulf Intermediate Water (RSPGIW), Indian Deep Water (IDW), and Circumpolar Deep Water (CDW).

Latitude [°S]	Sigma-theta [kg m $^{-3}$]	Water masses	NO_3^- [$\mu\text{mol L}^{-1} \pm$ 1 D.A.]	PO_4^{3-} [$\mu\text{mol L}^{-1} \pm$ 1 D.A.]	$\delta^{15}\text{N}\text{-NO}_3^-$ [‰ \pm 1 D.A.] ^a	$\delta^{18}\text{O}\text{-NO}_3^-$ [‰ \pm 1 D.A.] ^b
27.78– 26.05	<26.4	SSW	1.67 ± 1.59	0.24 ± 0.15	7.62 ± 0.30	2.94 ± 0.47
	26.4–26.9	SAMW	11.43 ± 4.01	0.88 ± 0.24	7.25 ± 0.31	4.34 ± 0.52
	26.9–27.4	AAIW	28.71 ± 5.24	2.05 ± 0.32	6.28 ± 0.16	2.95 ± 0.40
	>27.4	Deep Water Masses	34.55 ± 1.02	2.48 ± 0.07	5.68 ± 0.29	2.17 ± 0.26
23.91– 20.36	<24.9	Surface Water/IUW	0.37 ± 0.26	0.08 ± 0.03	N/D	N/D
	24.9–26.4	SSW	2.85 ± 0.98	0.29 ± 0.08	5.41 ± 0.54	2.07 ± 0.44
	26.4–26.9	SAMW	11.04 ± 2.76	0.82 ± 0.17	7.35 ± 0.25	4.60 ± 0.29
	26.9–27.4	AAIW	28.57 ± 3.23	1.99 ± 0.23	6.22 ± 0.13	2.21 ± 0.32
	>27.4	Deep Water Masses	32.72 ± 2.54	2.34 ± 0.16	5.45 ± 0.30	1.62 ± 0.32
15.08	<24.3	IUW	1.69 ± 1.15	0.30 ± 0.06	N/D	N/D
	24.3–26.6	SSW	4.42 ± 3.27	0.37 ± 0.15	N/D	N/D
	26.6–26.9	SAMW	15.19 ± 2.70	1.11 ± 0.16	7.19 ± 0.26	4.01 ± 0.40
	26.9–27.2	AAIW/IIW	30.74 ± 3.30	2.18 ± 0.26	6.68 ± 0.05	2.94 ± 0.08
	>27.2	Deep Water Masses	36.28 ± 0.89	2.58 ± 0.15	6.06 ± 0.49	3.03 ± 0.45
8.81– 2.98	<23.0	Surface Water	0.61 ± 0.26	0.17 ± 0.04	6.66 ± 0.41	3.77 ± 0.55
	23.0–27.0	IEW	22.84 ± 5.85	1.57 ± 0.34	6.96 ± 0.07	2.86 ± 0.14
	27.0–27.3	RSPGIW	32.77 ± 3.23	2.35 ± 0.19	7.03 ± 0.09	2.85 ± 0.23
	27.3–27.7	IDW	34.21 ± 4.59	2.48 ± 0.23	6.56 ± 0.19	2.72 ± 0.36
	>27.7	CDW	35.92 ± 0.48	2.41 ± 0.05	5.32 ± 0.24	2.07 ± 0.13

Note: ^a $\delta^{15}\text{N}\text{-NO}_3^-$ in ‰ versus air and ^b $\delta^{18}\text{O}\text{-NO}_3^-$ in ‰ versus VSMOW; D.A. = deviation from the average value; N/D = not detectable due to insufficient nitrate concentrations.

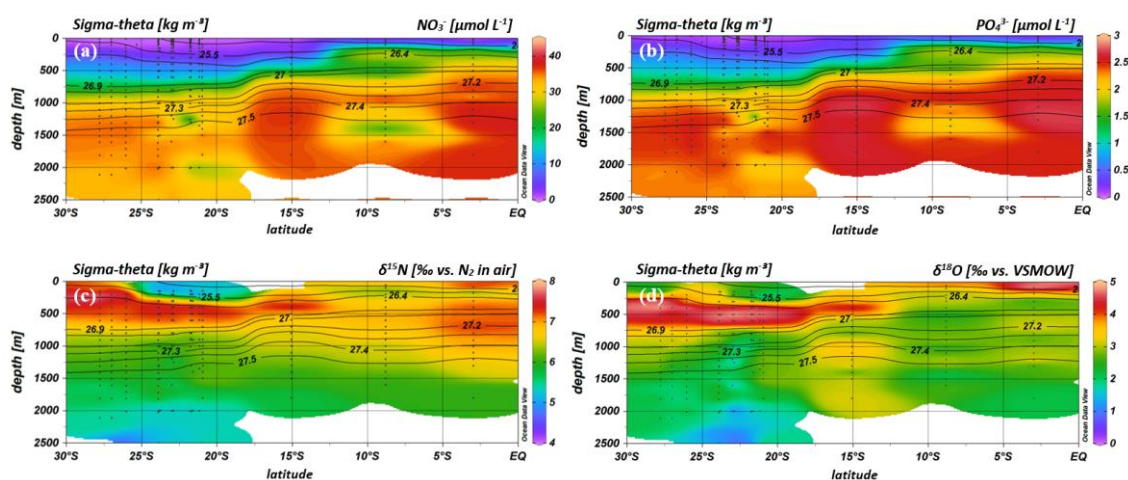


Figure 2.4. Profiles of nitrate (a) and phosphate concentrations (b) and $\delta^{15}\text{N}$ - NO_3^- (c) and $\delta^{18}\text{O}$ - NO_3^- (d) of seawater samples collected during cruises *MSM 59/2* (2016) and *SO 259* (2017). Contour lines indicate the potential density sigma-theta in kg m^{-3} .

2.4 Water mass distribution

Water masses in the study area are well discernible by their temperatures, densities, salinities, and oxygen concentrations (Figure 2.5). In accordance with definitions from the literature, we identified water masses from the IOSG towards the southern equatorial Indian Ocean and established the first water mass distribution model for this ocean region (Figure 2.6). To generate the water mass distribution model, we use salinity and oxygen distributions along sigma-theta surfaces. We separate our study area into three latitudinal sections, which demonstrate the alteration of water masses along the latitudinal transect and between the different ocean regimes (Figure 2.5). We present the provenance of water masses of Antarctic and Subantarctic origin converging and mixing with water masses from the southern equatorial Indian Ocean and the Arabian Sea. The water mass distribution model serves as a basis for the understanding of our nutrient and coupled N and O isotope measurements of nitrate.

2.4.1 Surface and thermocline water masses ($<26.9 \text{ kg m}^{-3}$; $<800 \text{ m}$)

A high salinity surface layer ($>35.5 \text{ PSU}$) centered at $\sim 25.5 \text{ kg m}^{-3}$ (Figure 2.5a) is described in several studies. It has been termed “southern subtropical surface water” by *Muromtsev* (1959), “subtropical surface water” by *Wyrтки* (1973) and “subtropical subsurface water” (SSW) by *Schott and McCreary* (2001). For further

descriptions, we adopt the definition of *Wyrtki* (1973) and use the abbreviation SSW. The SSW is formed in the subtropical gyre of the southern hemisphere by excess of evaporation over precipitation (*Schott and McCreary, 2001*) at latitudes 25°–35°S (*Baumgartner and Reichel, 1975*). It is subducted into the thermocline of the subtropical gyre (*Schott and McCreary, 2001*), is detectable as far north as 15.08°S at CTD 05 (Figure 2.5b) and not discernable further north in the southern equatorial Indian Ocean (Figure 2.5c, Figure 2.6).

Less saline surface water (<35.1 PSU) occurs above the density level of the salinity maximum (>23°C; <24.0 kg m⁻³; Figure 2.5b) and is described by *Wyrtki* (1971) and *Warren* (1981). These low salinity values reflect an excess of precipitation over evaporation at latitudes 0°–10°S (*Baumgartner and Reichel, 1975*) accompanied by the influx of low salinity water (34.0–34.5 PSU) from the Pacific Ocean through the Indonesian Archipelago, called “Indonesian Throughflow” (ITF). The ITF carries less saline water westwards by the SEC within the entire thermocline (*Wyrtki, 1971; You and Tomczak, 1993*). *Emery* (2001) named this less saline surface water (34.4–35.0 PSU) “Indonesian Upper Water” (IUW; Figure 2.6).

The oxygen maximum south of 20°S in a density range of 26.4–26.9 kg m⁻³ (250–750 m; Figure 2.5d) corresponds with the “Subantarctic Mode Water” (SAMW; Figure 2.5, Figure 2.6), described by *McCartney* (1977). It is formed at latitudes 40°–50°S and injects oxygen-saturated waters at a temperature range of 6–14°C into the subtropical gyre. The SAMW in the South Indian Ocean can be separated into three modes by slightly different density distributions (*Herraiz-Borreguero and Rintoul, 2011*), which are originated in different ocean regions. For example, a lighter mode of the SAMW is formed in the western Indian basins and is limited to the southwest portion of the subtropical gyre, while the denser mode is found south off Australia and is carried further north by the outer portion of the subtropical gyre and ventilate a larger fraction of the gyre interior (*Herraiz-Borreguero and Rintoul, 2011*). However, for our purposes we assume the SAMW as one homogenous water mass flowing above the density surface of 26.9 kg m⁻³. On its transition to the north, the oxygen concentrations rapidly decrease from >4.6 mL L⁻¹ (CTD 05; Figure 2.5e) to <1.9 mL L⁻¹ (CTD 01, 03; Figure 2.5f) because of respiration and the absence of effective ventilation in the North Indian Ocean. The reduced vertical changes in salinity north of ~15°S mark the “Indian Equatorial Water” (IEW; Figure 2.6). This is described by *Sharma* (1976), *Warren* (1981), *Quadfasel and Schott* (1982), *You and Tomczak* (1993), and *Schott and*

McCreary (2001) as a mixture of thermocline water masses from the North and South Indian Ocean.

2.4.2 Intermediate water masses (26.9–27.4 kg m⁻³; 800–1000 m)

The salinity minimum (<34.6 PSU) south of 15°S, in a density range of 26.9–27.4 kg m⁻³ (core density $\sigma = 27.2$ kg m⁻³; Figure 2.5a) is associated with the “Antarctic Intermediate Water” (AAIW; Figure 2.4; Deacon, 1933; Wyrтки, 1973; Warren, 1981; Fine, 1993; Toole and Warren, 1993; You, 1998; Bindoff and McDougall, 2000; Schott and McCreary, 2001). It is transported eastwards by the “Antarctic Circumpolar Current” (ACC), penetrates into all three oceans and extends towards the equator to feed the intermediate waters (Wüst, 1935; Sverdrup *et al.*, 1942; McCartney, 1977; Reid, 1986, 1989; Piola and Gordon, 1989; Fine, 1993; Talley, 1996). The salinity minimum (<34.6 PSU) observed at station CTD 05 (15.08°S; Figure 2.5b) has a slightly divergent core density (27.0 kg m⁻³) compared to the AAIW (Figure 2.5a). This implies a further source to the salinity minimum of the AAIW. A low salinity water mass (~34.8 PSU) flows along 10°–15°S (Wyrтки, 1971; You and Tomczak, 1993; Schott and McCreary, 2001) and originates from the ITF. At intermediate depths it has been called “Indonesian Intermediate Water” (IIW; Figure 2.6) by Emery and Meincke (1986) and Emery (2001).

The increase in salinity (>34.9 PSU; Figure 2.5c) further north, at the same density level as the AAIW, is caused by the inflow of saline water from the Arabian Sea, mainly from the Red Sea outflow (Warren, 1981) and is additionally fed by the outflow of the Persian Gulf (Emery and Meincke, 1986). Therefore, this water mass is called “Red Sea-Persian Gulf Intermediate Water” (RSPGIW; Figure 2.6). The RSPGIW is transported towards the equator and beyond to as far south as 10°S (You, 1998), recirculates in the tropical gyre, and creates the absolute oxygen minimum (<1.1 mL L⁻¹) caused by biogeochemical processes in the Arabian Sea (see section 2.5.1).

2.4.3 Deep water masses (>27.4 kg m⁻³; >1000 m)

Overall, low oxygen concentrations in the northern study area underneath the AAIW (>27.4 kg m⁻³; Figure 2.5f) are caused by in situ consumption (Wyrтки, 1962) and reduced ventilation in the North Indian Ocean. The deep oxygen minimum extends towards the south (~3.0 mL L⁻¹) and is associated with the water mass of

the “Indian Deep Water” (IDW). The IDW has higher salinities than the overlying AAIW (Mantyla and Reid, 1995; Bindoff and McDougall, 2000; Schott and McCreary, 2001; Talley, 2013) with values of >34.6 PSU below the density range of the AAIW (Figure 2.5a). The IDW ($\sigma \approx 27.5 \text{ kg m}^{-3}$) flows in the density range just above the “Circumpolar Deep Water” (CDW; Figure 2.6) and a further increase in salinity (34.62–34.73 PSU) and in the oxygen concentration at the 2°C temperature level (Emery, 2001) mark the transition between the IDW and the underlying CDW.

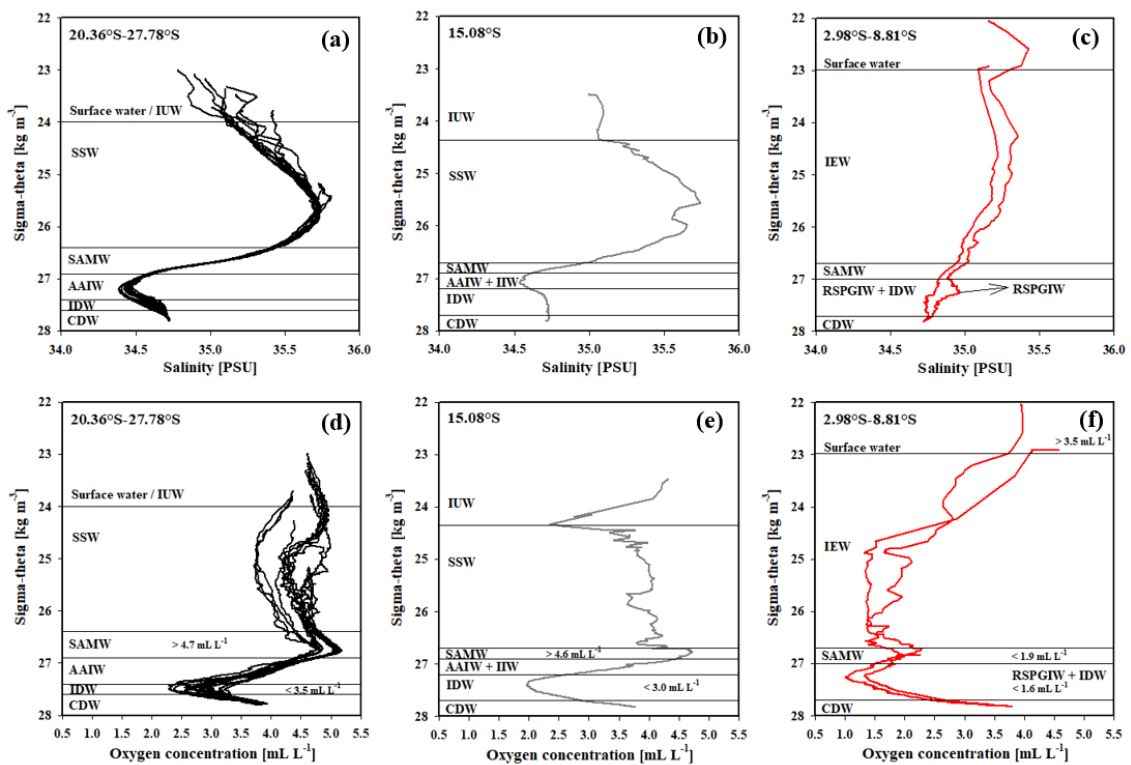


Figure 2.5. Water mass properties represented as salinity vs. sigma-theta diagrams (a, b, c) and as oxygen vs. sigma-theta diagrams (d, e, f) for CTD stations at latitudes 20.36° – 27.78°S , 15.08°S , and 2.98° – 8.81°S . For water mass abbreviations see Table 2.1.

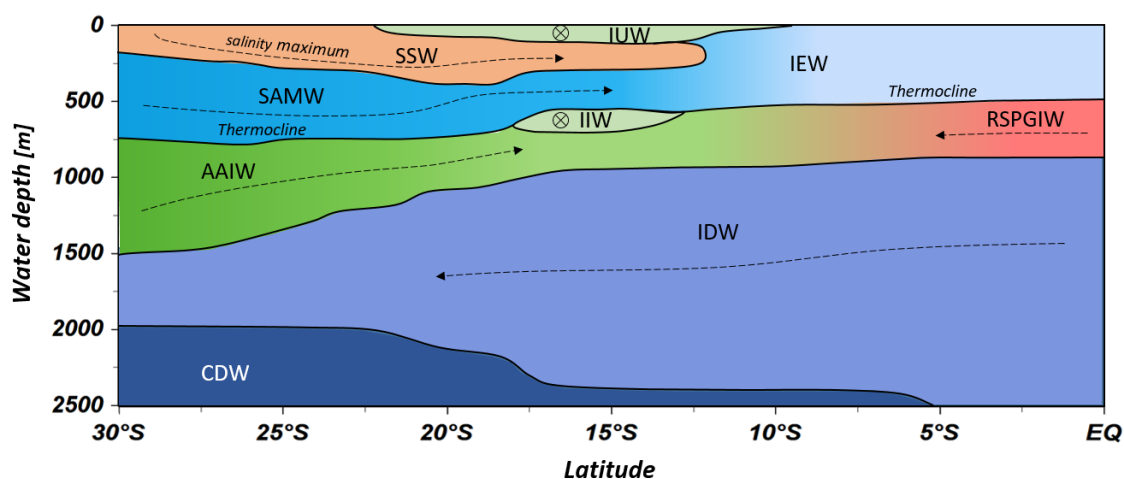


Figure 2.6. Water mass distribution model from 30°S to the equator. The CTD stations taken into account for this transect ranged between 67.07°E and 77.16°E. Dotted lines represent N-S current directions and circled crosses indicate latitudinal directions from E to W. For water mass abbreviations see Table 2.1.

2.5 Nutrient distribution and N cycle processes

2.5.1 Nutrient supply in the oligotrophic gyre and lateral transfer across the gyre boundaries

Intense downwelling in the center of the IOSG is induced by the convergence of horizontal Ekman volume flux (*Williams and Follows, 2003*) and creates the thick layer of nutrient-depleted surface waters within the IUW and SSW (Figure 2.7a, b, Table 2.1), and also within the underlying SAMW. The northward increase in nutrients at ~15°S (CTD 05; 2017) marks the northern boundary of the subtropical gyre and the maximum extension of the IUW, SSW, and SAMW (Table 2.1). Further increase in nutrient concentrations within the IEW indicate the transition from the subtropical gyre towards the southern equatorial Indian Ocean identified by the characteristic shoaling of the nutricline at the northern fringe of the gyre (Table 2.1, Figure 2.7a, b). The IEW is not a well-defined water mass, but rather a mixture of thermocline waters from the South Indian Ocean and from the nutrient-enriched North Indian Ocean. Therefore, just below the upper 100 m nutrient concentrations increase up to ~23 $\mu\text{mol L}^{-1}$ nitrate and ~1.6 $\mu\text{mol L}^{-1}$ phosphate (Table 2.1) at the northernmost stations (CTD 01, 03; 2017) and indicate the increasing influence of the nutrient-enriched North Indian Ocean (*Gaye et al., 2013*). This increased northern influence is also reflected by the $\text{NO}_3^-/\text{PO}_4^{3-}$ ratios, which exhibit values of less than 8 in the upper 200 m of the subtropical gyre, but

increase towards the southern equatorial Indian Ocean, tracking the outcropping nutriclines (Figure 2.7c). Low $\text{NO}_3^-/\text{PO}_4^{3-}$ ratios are typical in surface waters of oligotrophic regions because nitrate commonly becomes depleted prior to phosphate (Sarmiento and Gruber, 2006; Deutsch et al., 2007). Due to the intense downwelling in the center of the IOSG, the supply of nutrients by vertical mixing is reduced or absent in the gyre (Williams and Follows, 1998). Thus, lateral transfer across the gyre boundaries and biologically N_2 fixation are major processes supplying nutrients to the euphotic zone of the subtropical gyre.

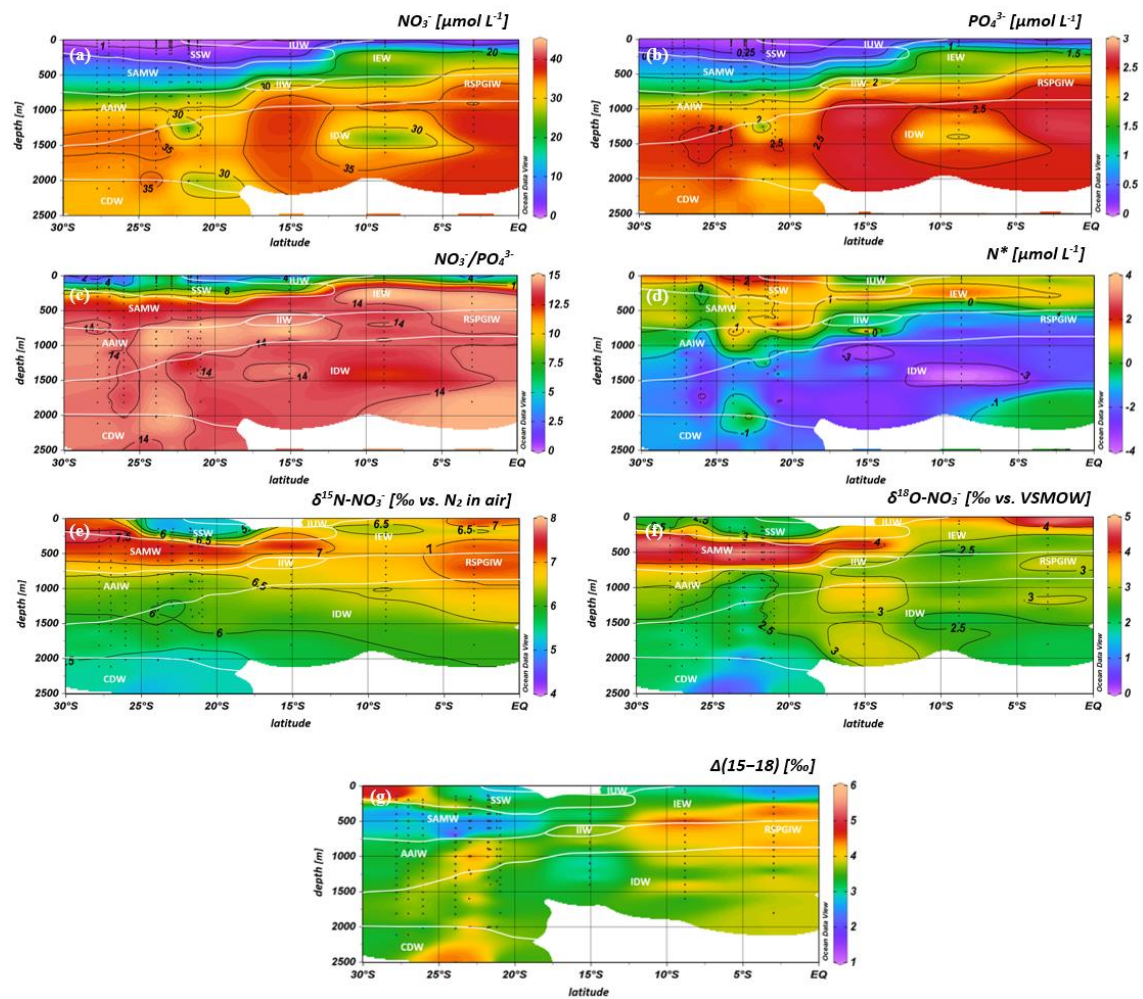


Figure 2.7. Latitudinal profiles from south to north with an overlay of the water mass distribution model (white contour lines) in the South Indian Ocean of nitrate (a) and phosphate concentrations (b), $\text{NO}_3^-/\text{PO}_4^{3-}$ ratio (c), N^* (d), $\delta^{15}\text{N}-\text{NO}_3^-$ (e) and $\delta^{18}\text{O}-\text{NO}_3^-$ of nitrate (f), and nitrate $\Delta(15-18)$ (g) as the difference between $\delta^{15}\text{N}-\text{NO}_3^-$ and $\delta^{18}\text{O}-\text{NO}_3^-$. For water mass abbreviations see Table 2.1.

The water masses entering the study area from the Southern Ocean and from the North Indian Ocean have characteristic nutrient concentrations and isotope fingerprints of reactive N, so that some of the water masses are clearly discernible by the distribution of nutrients and the isotopic composition of nitrate within the IOSG. Our samples show $\text{NO}_3^-/\text{PO}_4^{3-}$ ratios of 14.56 on average (Figure 2.8). These $\text{NO}_3^-/\text{PO}_4^{3-}$ ratios are lower than the global ocean mean of 16:1 (Redfield, 1934, 1963). Furthermore, measurements in the Arabian Sea reveal typical $\text{NO}_3^-/\text{PO}_4^{3-}$ ratios of 12.81 (Codispoti *et al.*, 2001), even lower than our detected $\text{NO}_3^-/\text{PO}_4^{3-}$ ratios. Consequently, the average $\text{NO}_3^-/\text{PO}_4^{3-}$ ratio of 14.56 falls between the global ocean mean of 16:1 (Redfield, 1934, 1963) and the typical ratio in the Arabian Sea of 12.81 (Codispoti *et al.*, 2001). This alone indicates the mixing of water masses of North and South Indian Ocean origin.

The deviation from the Redfield stoichiometry (Redfield, 1934, 1963) is quantified by the tracer N^* . The analytical error on N^* estimate based on the relative error for nitrate and phosphate analysis was below 1.5 % for duplicate sample measurements. The Arabian Sea is characterized by an extensive oxygen deficit zone (ODZ) that induces denitrification in mid-water depths (150–400 m) (Gaye *et al.*, 2013) and leads to an N deficit and therefore to negative N^* values (e.g., Bange *et al.*, 2005; Rixen *et al.*, 2005; Gaye *et al.*, 2013). Our data set reveals values of about $-1 \mu\text{mol L}^{-1}$ within the RSPGIW and values lower than $-4 \mu\text{mol L}^{-1}$ within the IDW (Figure 2.7d), which coincide with the oxygen minimum (see section 2.4). Consequently, negative N^* values are a result of the influx of water masses from the Arabian Sea, which are affected by denitrification. To strengthen this assumption and to compensate the limitations of the N^* approach mentioned before, we use stable isotope measurements.

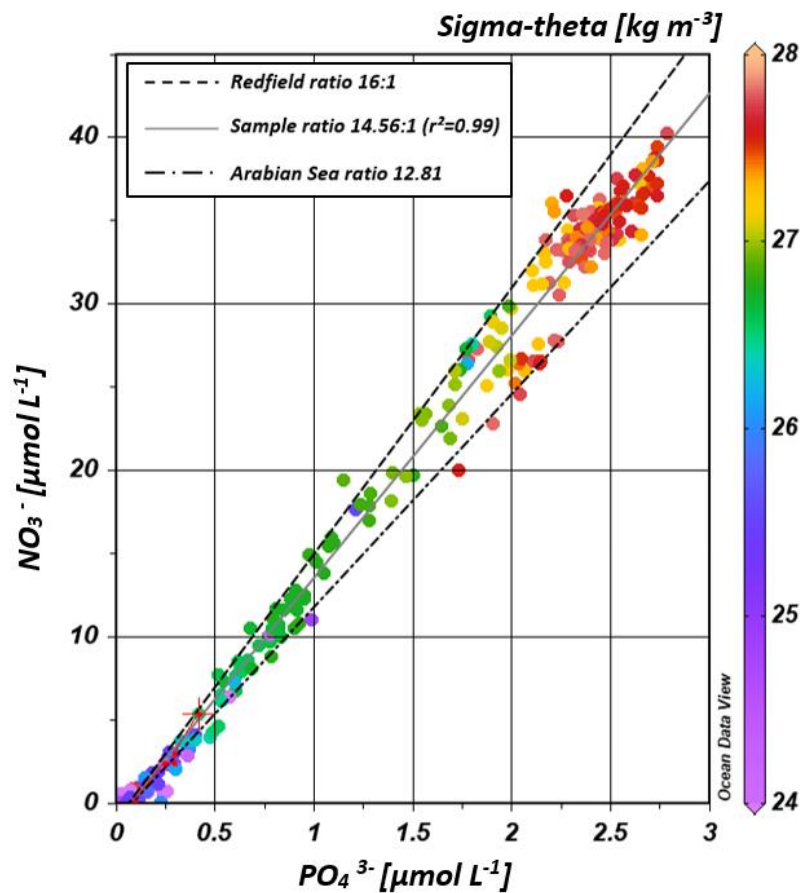


Figure 2.8. Correlation of nitrate (NO_3^-) versus phosphate (PO_4^{3-}) concentrations. Regression line of the sample pool (solid, grey line) indicates a ratio of ~ 14.56 ($r^2 = 0.99$), intermediate between the Redfield ratio of 16:1 (black, dashes line) and the mean ratio in the Arabian Sea with a slope of ~ 12.81 (grey, dotted-dashed line) after *Codispoti et al.* (2001). Colour-coding of dots indicates the potential density sigma-theta in kg m^{-3} .

We observe elevated $\delta^{15}\text{N}\text{-NO}_3^-$ and $\delta^{18}\text{O}\text{-NO}_3^-$ values of $>7\text{‰}$ and $>3\text{‰}$ within the RSPGIW at CTD 01 and 03 (Table 2.1, Figure 2.7e, f) accompanied by nitrate concentrations of $>30\ \mu\text{mol L}^{-1}$ (Figure 2.7a). Denitrification discriminates against the heavier isotope of nitrate (^{15}N , ^{18}O) and raises $\delta^{15}\text{N}\text{-NO}_3^-$, as well as $\delta^{18}\text{O}\text{-NO}_3^-$. In the Arabian Sea average $\delta^{15}\text{N}\text{-NO}_3^-$ and $\delta^{18}\text{O}\text{-NO}_3^-$ values of $>20\text{‰}$ and $>15\text{‰}$, respectively, are observed in mid-water depth (150–400 m), within the oxygen minimum zone (*Gaye et al.*, 2013; *Martin and Casciotti*, 2017). The significant progressive reduction of $\delta^{15}\text{N}\text{-NO}_3^-$ and $\delta^{18}\text{O}\text{-NO}_3^-$ towards the South Indian Ocean is a result of mixing with subtropical thermocline water masses and remineralisation/N assimilation processes along the flow path.

Within the RSPGIW and the lower IEW, we observe a deviation from the O-to-N isotope effect of $^{18}\epsilon:^{15}\epsilon \approx 1$ that is typical for consumption processes like denitrification (*Sigman et al.*, 2003; *Granger et al.*, 2004; *Sigman et al.*, 2005; *Rafter et*

al., 2013). The difference between N and O isotopes ($\delta^{15}\text{N}$, $\delta^{18}\text{O}$) can be quantified by the tracer $\Delta(15-18)$ that indicates values of >4 ‰ within the RSPGIW and the lower IEW (Figure 2.7g). The RSPGIW injects nitrate that is remineralized from ^{15}N -enriched organic matter, originated in a region of strong denitrification. During remineralisation of organic matter, the N isotope effect associated with ammonium production and nitrification does not affect the $\delta^{15}\text{N-NO}_3^-$ but depends on the biomass being remineralized (*Rafter et al.*, 2013). In contrast, the $\delta^{18}\text{O}$ of newly nitrified nitrate is independent of the isotopic composition of the organic matter. However, $\delta^{18}\text{O-NO}_3^-$ depends on the isotope effect during NH_4^+ and NO_2^- oxidation, water incorporation ($\delta^{18}\text{O-H}_2\text{O}$ of ~ 0 ‰), and the exchange of oxygen atoms with water that should generate a $\delta^{18}\text{O}$ of newly produced NO_3^- between -8 and -1 ‰ (*Buchwald and Casciotti*, 2010; *Casciotti et al.*, 2010). Therefore, the RSPGIW adds nitrate that is enhanced in $\delta^{15}\text{N}$ compared to the ambient water and has a relative lower $\delta^{18}\text{O}$, thus drives the decoupling of N and O isotopes. Furthermore, the source nitrate for N assimilation in the lower IEW is this regenerated nitrate and results also in the decoupling of N and O isotopes in this depth range. Consequently, the elevated $\Delta(15-18)$ can be explained by a remineralisation/N assimilation cycle and by the lateral influx of ^{15}N -enriched nitrate induced by strong denitrification in the oxygen minimum zone of the Arabian Sea. Furthermore, alteration processes within the oxygen minimum zone have the possibility to modify the $\Delta(15-18)$. However, it is still unclear how this signal is preserved along the flow path and we suggest that the dominant mechanism that elevates $\Delta(15-18)$ values is because of the influx of ^{15}N -enriched nitrate due to denitrification.

In the IOSG, we observe elevated $\delta^{15}\text{N-NO}_3^-$ and $\delta^{18}\text{O-NO}_3^-$ values of >7 ‰ and >4 ‰ (Table 2.1, Figure 2.7e, f) within the SAMW (400–500 m) that is originated in the Subantarctic thermocline of the Southern Ocean. In general, N assimilation has an isotopic effect of about 5–10 ‰ (*Montoya and McCarthy*, 1995; *Waser et al.*, 1998; *Sigman et al.*, 2005) and produces biomass that is relatively depleted in ^{15}N and ^{18}O in comparison to the nitrate source. Consequently, this drives the elevation in $\delta^{15}\text{N}$ and $\delta^{18}\text{O}$ of the remaining nitrate as uptake proceeds. However, in oligotrophic waters, such as in the IOSG, this isotopic effect is not observable (*Montoya et al.*, 2002) as nitrate is typically drawn down to the limit of detection by complete N assimilation. Nitrate in surface waters of the Southern Ocean is only partially assimilated due to light limitation and less iron availability (*Sigman et al.*, 1999; *Boyd et al.*, 2000; *Hutchins et al.*, 2001; *DiFiore et al.*, 2006; *DiFiore et al.*, 2010) and leads to $\delta^{15}\text{N-NO}_3^-$ values of up to ~ 13 ‰ (*Sigman et al.*, 1999, 2000;

DiFiore et al., 2006). Seasonal mixing and remineralisation processes result in $\delta^{15}\text{N}\text{-NO}_3^-$ values of 5–9 ‰ within Subantarctic thermocline waters (*McCartney, 1977; Sigman et al., 1999*). On its flow path towards the north, this isotope trace of incomplete assimilation causes the elevated isotope values within the SAMW that enters the subtropical Indian Ocean thermocline with $\delta^{15}\text{N}\text{-NO}_3^-$ values of >7 ‰ (Table 2.1, Figure 2.4c, Figure 2.7e, Figure 2.9a).

Because Subantarctic thermocline waters are the source water of the SAMW and the underlying AAIW in the IOSG, we compare the nitrate isotope properties of Subantarctic thermocline waters with our results. *Sigman et al.* (1999, 2000) and *DiFiore et al.* (2006) use the correlation of $\delta^{15}\text{N}\text{-NO}_3^-$ and the fraction of nitrate remaining – $\ln(\text{NO}_3^-)$ – to quantify the isotope fractionation effect during N assimilation in the Antarctic and Subantarctic region. If N assimilation occurs with a constant effect and no new nitrate is added to the surface ocean, then the uptake process can be described in terms of Rayleigh fractionation kinetics (*Mariotti et al., 1981*). To fulfil the conditions of Rayleigh fractionation, the nitrate samples plot along a straight line in $\delta^{15}\text{N}/\ln(\text{NO}_3)$ space, where the slope of the line represents the isotope effect of N-uptake or mixing of different nitrate pools. *Sigman et al.* (1999, 2000) and *DiFiore et al.* (2006) compare the theoretically Rayleigh utilization trend of $\delta^{15}\text{N}/\ln(\text{NO}_3) = 5$ ‰ with their measured nitrate utilisation trend within the Subantarctic thermocline, where *Sigman et al.*, (1999, 2000) determined a slope of $\delta^{15}\text{N}/\ln(\text{NO}_3) = 1.3$ ‰ (Figure 2.9b). Our results reveal a similar, but even shallower slope of $\delta^{15}\text{N}/\ln(\text{NO}_3) = 0.93$ ‰ (Figure 2.9b). It is clearly a mixing signal that causes the moderate slopes of $\delta^{15}\text{N}/\ln(\text{NO}_3)$ in both the gyre region and in the Subantarctic because biological utilisation of nitrate is unlikely at this depth range. The explanation for the slightly shallower slope in our data set compared to the results in the Subantarctic is vertical mixing with the overlying SSW that has lower $\delta^{15}\text{N}\text{-NO}_3^-$ values (<6 ‰) with nitrate concentrations of <5 $\mu\text{mol L}^{-1}$. This process does not fulfil conditions of Rayleigh fractionation because of fundamentally different formation background (Table 2.1, Figure 2.9a; see section 2.5.2). Deep-water nitrate concentrations vary little and $\delta^{15}\text{N}\text{-NO}_3^-$ increases towards shallower water depths and the nitrate signal slightly differ from that of the Southern Ocean due to the influence of the IDW, originated in the North Indian Ocean.

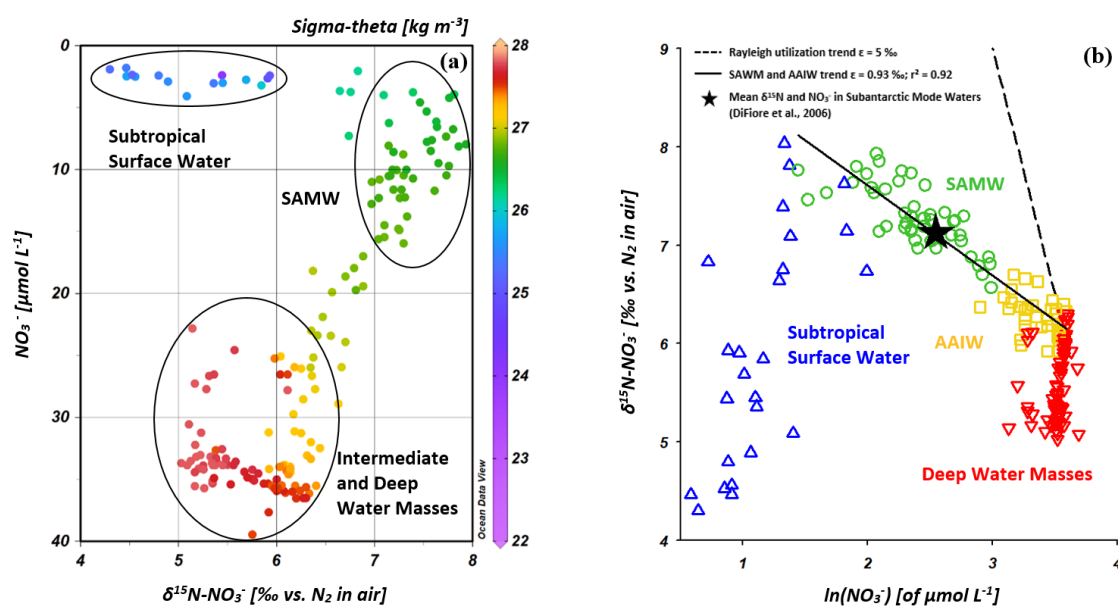


Figure 2.9. Nitrate concentrations versus $\delta^{15}\text{N-NO}_3^-$ (a) and $\delta^{15}\text{N-NO}_3^-$ versus $\ln(\text{NO}_3^-)$ (b) for CTD stations within the IOSG (20.36° – 27.78°S). Colour-code of dots in panel a indicates the potential density sigma-theta (kg m^{-3}). In panel b, data is grouped for the subtropical surface water (blue), SAMW (green), AAIW (yellow), and deep water masses (red).

Within the isotope maxima of the SAMW (~ 500 m), the uniform evolution of N and O isotopes of nitrate breaks down and reveals an offset of about 100 m between the N and O isotopic maxima at 23.91° – 20.36°S (Figure 2.4c, d; see Table A1.3 and Table A1.4 in the Appendix A1). Both, $\delta^{15}\text{N-NO}_3^-$ and $\delta^{18}\text{O-NO}_3^-$, are elevated within the SAMW, but $\delta^{15}\text{N-NO}_3^-$ is less elevated than $\delta^{18}\text{O-NO}_3^-$. The decoupling of N and O isotopes leads to low $\Delta(15-18)$ values of $<3 \text{ ‰}$ (Figure 2.7g) within the SAMW, that is originated in the partially assimilated Subantarctic region. Isotope fractionation during the initial phase of partial N assimilation leads to sinking organic matter that is more depleted in ^{15}N than the source nitrate (Sigman et al., 1999; Rafter et al., 2013). The influx of the SAMW into the subtropical gyre injects ^{15}N depleted organic matter and its remineralisation adds nitrate that lowers the $\delta^{15}\text{N}$ of the ambient nitrate and thus leads to low $\Delta(15-18)$ in subtropical thermocline waters (Figure 2.7g). To conclude, remineralisation of organic matter produced by partial N assimilation in the Southern Ocean is reflected in lower $\Delta(15-18)$ and leads to the deviation of the isotope maxima with an offset of 100 m within the depth range of the SAMW. However, the remineralisation of ^{15}N -depleted organic matter formed out of newly fixed N from N_2 fixation in surface waters may also influence the decrease of $\Delta(15-18)$ (see the following section 2.5.2).

2.5.2 Evidence for N₂ fixation in the IOSG

The mixing of source water signals from the lateral influx of the neighbouring North Indian Ocean and Southern Ocean significantly affects the nutrient distribution and isotopic composition of nitrate in the gyre region. However, N* and $\delta^{15}\text{N}-\text{NO}_3^-$ suggest that N₂ fixation introduces new nitrate into the surface waters of the IOSG. The increase in N* up to 2 $\mu\text{mol L}^{-1}$ at 60–200 m indicates a positive deviation of the $\text{NO}_3^-/\text{PO}_4^{3-}$ ratio from the Redfield stoichiometry (Redfield, 1934, 1963; Gruber and Sarmiento, 1997) and is an evidence for the input of newly fixed N into the surface water. Studies in the South-West Pacific Ocean also indicate positive N* anomalies of $\sim 2 \mu\text{mol L}^{-1}$ in the productive layer reflecting diazotrophic N₂ fixation (Fumenia et al., 2018). Although N₂ fixation is the first-order driver of positive N* (Monteiro and Follows, 2006; Bourbonnais et al., 2009), other processes, for instance atmospheric deposition or the preferential remineralisation of N over P, may also be responsible for excess N and result in an overestimation of N*-based N₂ fixation (Monteiro and Follows, 2006; Bourbonnais et al., 2009). However, the South Indian Ocean is less affected by the influx of nutrient enriched mineral aerosols from atmospheric deposition (Duce and Tindale, 1991; Duce et al., 2008) and we neglect this factor in our further discussion. Furthermore, we use $\delta^{15}\text{N}$ and $\delta^{18}\text{O}$ of nitrate, as well as $\Delta(15-18)$, as additional indicators of N sources to overcome the weakness associated with the N* approach.

Diazotrophic N₂ fixation produces organic matter that has a low $\delta^{15}\text{N}-\text{NO}_3^-$ relative to average oceanic combined N (Wada and Hattori, 1976; Minagawa and Wada, 1986; Carpenter et al., 1997; Montoya et al., 2002). Within the upper 200 m of the IOSG (20.36°–23.91°S), the $\delta^{15}\text{N}$ of nitrate varies between 4.3 ‰ and 5.9 ‰ with a mean of ~ 5.0 ‰ (Figure 2.7e, Figure 2.9a, b). These values are higher compared to other regions of intense N₂ fixation, such as in the subtropical NE Atlantic, where values of 2–5 ‰ occur in surface waters (Bourbonnais et al., 2009). At first sight, the high values of surface waters in the IOSG do not speak for significant N₂ fixation in surface waters. However, considering that SAMW is the source of nitrate with elevated $\delta^{15}\text{N}-\text{NO}_3^-$ values of 7.4 ‰ on average (20.36°–23.91°S) and highest values of 7.9 ‰ (Figure 2.9a, b; see also Table A1.3 and Table A1.4 in the Appendix A1), the $\delta^{15}\text{N}-\text{NO}_3^-$ in surface waters (4.3–5.9 ‰) is lowered by ~ 2.4 ‰. This is similar to the decrease of ~ 3 ‰ in surface waters of the north Atlantic, where N₂ fixation is verified (Knapp et al., 2008; Bourbonnais et al., 2009). Therefore, N₂ fixation is most likely the main driver in the upward

decrease of $\delta^{15}\text{N-NO}_3^-$ in surface waters and adds isotopically light N from the atmosphere into the gyre region. To prove this, we take the nitrate $\delta^{18}\text{O}$ into account, which exhibits values of $<3\text{‰}$ and shows a minor decrease compared to $\delta^{15}\text{N}$. The resulting decoupling of N and O isotopes of nitrate leads to smaller differences between $\delta^{15}\text{N}$ and $\delta^{18}\text{O}$ and reveals a $\Delta(15-18)$ of $<3\text{‰}$ (Figure 2.7g). To conclude, positive N^* values, distinct upward decrease of $\delta^{15}\text{N-NO}_3^-$, reduced $\Delta(15-18)$ and the distance from any external nitrate sources are unambiguous evidences of diazotrophic activity within the surface layer.

To estimate the supply of newly fixed N to the nitrate pool within the IOSG, we can calculate the fraction of nitrate coming from atmospheric N_2 fixation and the fraction that is added from the underlying source water by using the observed $\delta^{15}\text{N-NO}_3^-$ within the upper 200 m using the following equation modified after *Bourbonnais et al.* (2009, 2013):

$$\delta^{15}N_{\text{surface}} = (\delta^{15}N_{\text{fix}} \times a) + (\delta^{15}N_{\text{source}} \times b), \quad (2.1)$$

where " $\delta^{15}N_{\text{surface}}$ " is the detected $\delta^{15}\text{N-NO}_3^-$, which shows an average of $\sim 5.0\text{‰}$ in the upper 200 m (range: $4.3\text{--}5.9\text{‰}$) at latitude $20.36^\circ\text{--}23.91^\circ\text{S}$. The " $\delta^{15}N_{\text{fix}}$ " is the isotope value of atmospheric N_2 , assumed to be about 0‰ and the factor " a " is the percentage of nitrate coming from atmospheric N_2 fixation. The $\delta^{15}\text{N-NO}_3^-$ of the source water, which is the SAMW, with values about 7.4‰ , is represented by " $\delta^{15}N_{\text{source}}$ " and " b " is the corresponding percentage.

In this equation, we neglect the point of isotope fractionation via N assimilation due to the fact that in oligotrophic environments a complete N assimilation takes place (*Montoya et al.*, 2002). Thus, no net expression of the isotope fractionation occurs. Consequently, the produced organic matter that is again being remineralized also has a similar isotope signal as the assimilated nitrate. This assimilated nitrate is the mixing product of newly fixed N from the atmosphere and the input from the underlying SAMW, which is expressed by Eq. 2.1. We resolve the equation to $a (= 1-b)$ and $b (= \delta^{15}N_{\text{surface}}/\delta^{15}N_{\text{source}})$ and hence we calculate that about 32 % of the assimilated nitrate is provided from newly fixed N by N_2 fixation.

To prove this first approach, indicating that about 32 % of the assimilated nitrate results from atmospheric N input by N_2 fixation, we can calculate the $\text{NO}_3^-/\text{PO}_4^{3-}$ ratio resulting from nutrient assimilation without any external N input by N_2 fixation and compare this with our measured $\text{NO}_3^-/\text{PO}_4^{3-}$ ratio within surface

waters. To provide an estimate of the excess N in surface waters supplied by the remineralisation of cyanobacterial biomass, we use the following equations:

$$NO_3^-/PO_4^{3-}{}_{cal} = NO_3^-{}_{sample} / \left(\frac{NO_3^-{}_{in}}{NO_3^-/PO_4^{3-}{}_{in}} - \frac{NO_3^-{}_{ass}}{NO_3^-/PO_4^{3-}{}_{ass}} \right) \quad (2.2)$$

with “ $NO_3^-{}_{in}$ ” as initial nitrate concentration of the source water (SAMW within the IOSG), “ $NO_3^-{}_{ass}$ ” denoting the assimilated nitrate ($NO_3^-{}_{in} - NO_3^-{}_{sample}$) and “ $NO_3^-{}_{sample}$ ” being the sample concentrations. The initial nitrate to phosphate pool $NO_3^-/PO_4^{3-}{}_{in}$ is defined as mean ratio of the source water. For the region of the IOSG, we presume that the mean ratio within the SAMW is 13.25. For the general N assimilation in the euphotic zone, we assume Redfield conditions of $NO_3^-/PO_4^{3-}{}_{ass} = 16$. To calculate the residual nitrate, we multiply the calculated nitrate to phosphate ratio ($NO_3^-/PO_4^{3-}{}_{cal}$) with the measured phosphate concentrations:

$$NO_3^-{}_{cal} = NO_3^-/PO_4^{3-}{}_{cal} \times PO_4^{3-}{}_{sample} \quad (2.3)$$

The difference of “ $NO_3^-{}_{sample}$ ” and “ $NO_3^-{}_{cal}$ ” represents the portion of the nitrate supplied by nitrification out of newly fixed N. At latitude 20.36°–23.91°S, our samples indicate elevated NO_3^-/PO_4^{3-} ratios and a resulting positive deviation from the calculated line of N assimilation at nitrate concentrations of $<10 \mu\text{mol L}^{-1}$ (Figure 2.10a), that indicates an external input of N into the surface waters of the IOSG. We presume that N_2 fixation leads to the local elevation in NO_3^-/PO_4^{3-} ratios due to the input of new N and coincide with the decrease of $\delta^{15}\text{N-NO}_3^-$ and the decoupling of N and O isotopes, leading to low $\Delta(15-18)$. The quantity of newly fixed nitrate ($NO_3^-{}_{new}$) is given by the formula

$$NO_3^-{}_{new} [in \%] = \frac{(NO_3^-{}_{sample} - NO_3^-{}_{cal})}{NO_3^-{}_{sample}} \times 100, \quad (2.4)$$

which is presented in Figure 2.10b, indicating a distinct upward increase in the upper 200 m at 20.36°–23.91°S with an average portion of fixed nitrate of about 34 %. Consequently, our first approach that suggests that 32 % of the nitrate measured in the upper 200 m is derived from newly fixed N hence agrees quite well with the 34 % calculated by using NO_3^-/PO_4^{3-} ratios. *Bourbonnais et al.* (2009) stated that N_2 fixation accounts for ~40 % of newly supplied nitrate in the subtropical North Atlantic. This is slightly higher than our assumption for the subtropical South Indian Ocean. However, in the subtropical North Atlantic higher N^* values ($3.5 \mu\text{mol L}^{-1}$), a slightly stronger upward decrease of $\delta^{15}\text{N-NO}_3^-$

and a stronger decoupling of N and O isotopes are observed in surface waters, suggesting higher fixation rates.

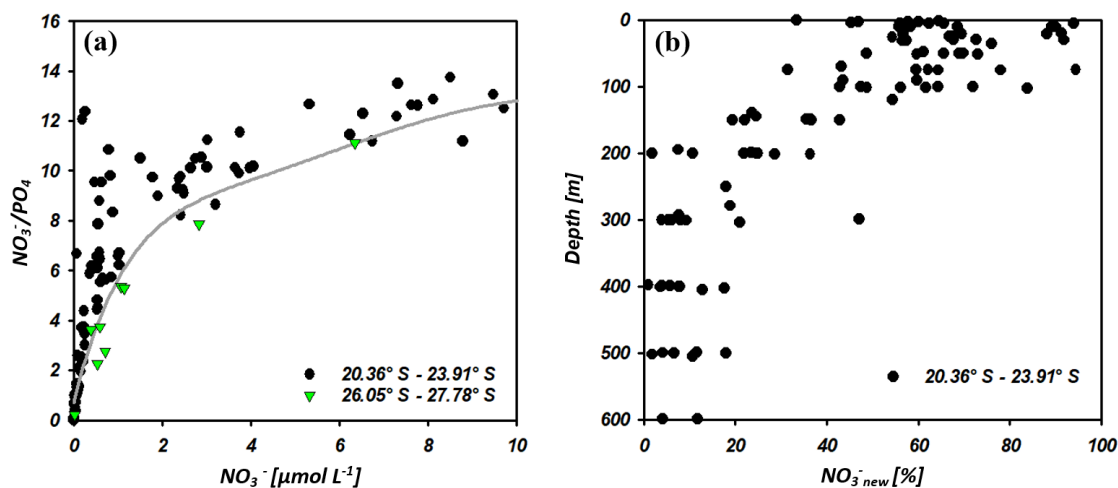


Figure 2.10. $\text{NO}_3^-/\text{PO}_4^{3-}$ ratio versus nitrate concentrations of seawater samples at 20.36°S – 23.91°S and 26.05°S – 27.78°S (a). The grey solid line indicates the calculated N assimilation ($\text{NO}_3^-_{\text{cal}}$ vs. $\text{NO}_3^-/\text{PO}_4^{3-}_{\text{cal}}$) with a preformed $\text{NO}_3^-/\text{PO}_4^{3-}_{\text{in}}$ ratio of 13.25 for the region of the IOSG and 14.25 for the southern equatorial Indian Ocean and progressive nutrient assimilation with a Redfield ratio of 16 ($\text{NO}_3^-/\text{PO}_4^{3-}_{\text{ass}}$). In Figure 2.10b we present the portion of nitrate formed out of newly fixed N ($\text{NO}_3^-_{\text{new}}$) versus depth at latitudes 20.36°S – 23.91°S .

Further south at 26.05°S – 27.78°S , samples plot close to the line of N assimilation and no significant input of fixed nitrate is indicated (Figure 2.10a). This agrees with the $\delta^{15}\text{N}\text{-NO}_3^-$ values in surface waters, which demonstrate an abrupt increase at about 26°S to similar values as in the underlying SAMW ($>7\text{‰}$), while $\delta^{18}\text{O}\text{-NO}_3^-$ shows still low values of $<3\text{‰}$. Consequently, N and O isotopes reveal a counteracting behaviour that differs from the region at 20.36°S – 23.91°S , resulting in high $\Delta(15\text{--}18)$ of $>4.5\text{‰}$ (Figure 2.7g). This is a strong indication for the absence of N_2 fixation in this region but also leads to the assumption that $\delta^{18}\text{O}$ remains low due to ongoing nitrate production by nitrification. This sudden termination of N_2 fixation may be due to a temperature-limiting factor, mentioned by Capone *et al.* (1997) and Breitbarth *et al.* (2007). They argue that N_2 fixation by *Trichodesmium*, which is the dominant N-fixing cyanobacteria in subtropical oligotrophic waters (Paerl *et al.*, 1994; Berman-Frank *et al.*, 2001), decreases dramatically at seawater temperatures below 22°C (Berman-Frank *et al.*, 2001). Modelling N_2 fixation with this assumption thus resulted in very low fixation rates south of about 25°S in the Indian Ocean (Paulsen *et al.*, 2017). However, N_2 fixation by other diazotrophs (e.g., unicellular diazotrophic

cyanobacteria) has been shown to occur at higher latitudes than *Trichodesmium* (Moisander *et al.*, 2010). Another reason for the decline of N₂ fixation south of 26°S may be the limited availability of iron and other micronutrients. Atmospheric iron deposition is low in the southern hemisphere oceans and iron availability gradually decreases towards high southern latitudes (Duce and Tindale, 1991; Boyd *et al.*, 2000; Duce *et al.*, 2008). Reduced iron availability is suggested to limit the growth of N-fixing organisms in regions of already limited iron availability (Sanudo-Wilhelmy *et al.*, 2001). Berman-Frank *et al.* (2001) calculated the potential of N₂ fixation by *Trichodesmium* and suggested that in 75 % of the global ocean, iron availability limits N₂ fixation. However, until now no concrete studies on iron and other micronutrient availability and N₂ fixation have been conducted within the South Indian Ocean.

2.6 Conclusion

The IOSG of the South Indian Ocean is the only oligotrophic gyre in the Indian Ocean due to the land-locked nature of the North Indian Ocean. Compared to the Atlantic and Pacific Ocean gyres the IOSG is less explored and is poorly understood in terms of nutrient distribution and isotopic composition of nitrate.

This work compiles the general distribution of water masses from 30°S, within the IOSG, across the South Equatorial Current (SEC), and towards the southern equatorial Indian Ocean. We established the first water mass distribution model in this ocean region that provides a basis for the identification of nutrient sources and the isotopic signatures of nitrate. Water masses in our study area are diverse and originate in two fundamentally different ocean regimes: the Southern Ocean (SAMW and AAIW) and the North Indian Ocean (RSPGIW and IDW). These different water masses have a major influence on the nutrient distribution and stable isotope composition of nitrate in the IOSG.

Our nutrient and isotopic data, which are one of the first reported for the subtropical South Indian Ocean, demonstrate the lateral influx from the Arabian Sea, characterized by strong denitrification in mid-water depths that leads to an N deficit in intermediate and deep waters accompanied by elevated isotope ratios of nitrate within the RSPGIW. The lateral influx from the Southern Ocean is via the oxygen-saturated SAMW, with characteristically elevated isotope ratios of nitrate due to partial N assimilation in high southern latitudes. Additionally, our data mirror an external input of N by N₂ fixation that is indicated by positive N*

and low $\Delta(15-18)$ values in surface waters. In the upper 200 m in the region of 20.36° – 23.91° S, we calculate that approximately 32–34 % of the nitrate consumed by N assimilation is provided from newly fixed N.

The IOSG has been sparsely investigated and is an area representing those oceanic oligotrophic regions that are likely to adjust to continued warming by deepening stratification, reduced upward nutrient supply across the thermocline, and decreasing biological production. Whether this will be offset by enhanced N_2 fixation in warming layers remains as an open question that needs dedicated follow-up studies, i.e., in terms of experimental approaches, time series observation, remote sensing, and biogeochemical modelling.

Chapter 3 – Cumulative Part II

Sediment trap-derived particulate matter fluxes in the oligotrophic subtropical gyre of the South Indian Ocean

(Published in Deep-Sea Research II: Topical Studies in Oceanography, DOI: 10.1016/j.dsr2.2020.104924)

Natalie C. Harms¹, Niko Lahajnar¹, Birgit Gaye¹, Tim Rixen^{1,2}, Ulrich Schwarz-Schampera³, and Kay-Christian Emeis^{1,4}

¹Institute of Geology, Universität Hamburg, Hamburg, 20146, Germany.

²Leibniz-Centre for Tropical Marine Research, Bremen, 28359, Germany.

³Federal Institute for Geosciences and Natural Resources (BGR), Hannover, 30655, Germany.

⁴Helmholtz-Zentrum Geesthacht (HZG), Institute for Coastal Research, Geesthacht, 21502, Germany.

Correspondence to: Natalie C. Harms (natalie.harms@uni-hamburg.de)

Abstract. Oligotrophic areas cover about 75 % of the ocean's surface, and these ocean regions are predicted to expand under global warming scenarios. To evaluate impacts on global marine biogeochemical cycles and changes in ocean-atmosphere carbon fluxes, it is essential to understand particulate matter fluxes and determine the amount of organic carbon that is exported to the ocean's interior. The oligotrophic Indian Ocean subtropical gyre (IOSG) is one of the least explored ocean regions in terms of particulate matter fluxes. Sediment trap-based particulate matter fluxes determined during a 4-year time series provide new information on the nature of export fluxes, their controlling factors, and on the

spatial and temporal variability of oceanic processes in the IOSG. Trap-averaged total mass fluxes ($\sim 9.8 \pm 3.7 \text{ mg m}^{-2} \text{ day}^{-1}$), as well as particulate organic carbon (POC) fluxes ($0.49 \pm 0.15 \text{ mg m}^{-2} \text{ day}^{-1}$) measured at 500–600 m above bottom (2600–3500 m water depth) are among the lowest fluxes recorded worldwide. These low flux values are a result of strongly stratified and nutrient-depleted upper waters in the gyre. Such oligotrophic conditions lead to low primary production rates in a relatively homogeneous and isolated ocean region. Consequently, we observe an almost constant rain of POC fluxes in space and time, although minor variations in the net primary production (NPP) and in the sea surface temperature (SST) are seen in satellite surveys and model estimations. Factors contributing to the lack of seasonality in the POC fluxes are intense organic matter degradation, variations in the ocean mixed layer depth (OMLD), and impacts of physical mixing (surface wind stress, cyclonic eddies). Preliminary estimates indicate that the average POC export efficiency ($\varepsilon = 0.03 \pm 0.01$) is extremely low in the IOSG. Assuming that the IOSG, as well as comparable ocean regions, will expand under climate warming conditions, it is of major importance to investigate POC export fluxes to the deep ocean in order to predict changes in the global carbon cycle during the next decades.

3.1 Introduction

Primary production and particulate organic carbon (POC) export out of the productive (euphotic) zone across the thermocline into the deep ocean and into the sediments drive the organic carbon pump and are essential parts of the global carbon cycle (*Volk and Hoffert, 1985*). An effective organic carbon pump lowers the partial pressure of CO_2 in surface waters and thus enhances the ocean's ability to absorb CO_2 from the atmosphere (*Berger et al., 1989; Wefer and Fischer, 1991; Lutz et al., 2007*). Consequently, ocean productivity and the export of organic carbon control the partitioning of carbon between the large sub-thermocline ocean reservoir and the relatively small atmospheric reservoir (*Berger et al., 1989*). The export and respiration of organic carbon below the biologically active surface layer are often described as a simple function of primary production and water depth (*Suess, 1980; Betzer et al., 1984; Pace et al., 1987*), but many processes involved are not well understood or quantitatively constrained. There is limited field data on primary production and organic carbon export fluxes in the Indian Ocean, although it has been suggested that the Indian Ocean accounts for 15–

20 % of the global ocean net primary production (NPP; *Behrenfeld and Falkowski, 1997; Baer et al., 2019*). Less is known about the biogeochemical processes in the subtropical region ($\sim 15^{\circ}$ – 35° N, $\sim 15^{\circ}$ – 35° S) of the South Indian Ocean and no field data are available on particulate matter export fluxes in the Indian Ocean subtropical gyre (IOSG). Sediment traps are considered as a reliable tool to monitor the quantity and quality of sinking particulate matter (*Honjo et al., 1995; Wong et al., 1998; Buesseler et al., 2000; Rixen et al., 2019a, 2019b*). Here, we present data on sinking particulate matter collected during a 4-year time series of sediment trap deployments in the IOSG. Furthermore, we provide new information on POC fluxes, their controlling factors, internal and seasonal gyre variabilities, and POC export efficiency.

Particulate matter fluxes at depth in the ocean are directly linked to upper ocean processes (*Eppley and Peterson, 1979; Suess, 1980; Betzer et al., 1984; Lampitt and Antia, 1997*), and sediment trap data suggest that there is often a positive correlation between particulate matter fluxes and the rate of primary production (*Betzer et al., 1984*). The rate of primary production and its transfer as sinking POC through the thermocline and further into the deep ocean is controlled by multiple factors, e.g., light, availability of nutrients, water column stratification, availability of ballast material, and organic matter degradation (*Lampitt and Antia, 1997; Cram et al., 2018; Rixen et al., 2019a*). The IOSG is part of the extensive oligotrophic areas that cover about 75 % of the ocean's surface. The anticyclonic and counter-clockwise gyre of the South Indian Ocean (*Williams and Follows, 2003; Sarmiento and Gruber, 2006*) extends approximately from 10° S to 30° S and from 50° E to 100° E (*McClain et al., 2004; Baer et al., 2019*). Ekman transport to the gyre center leads to a thick nutrient-depleted ocean mixed layer (OML; zone of equal physical properties), where regeneration of organic matter and associated nutrients is efficient, while vertical mixing and the resulting influx of nutrients from deeper waters is reduced or absent (*Knox and McElroy, 1984; Sarmiento and Toggweiler, 1984; Siegenthaler and Wenk, 1984; Ito and Follows, 2005; Duteil et al., 2012; Harms et al., 2019; Rixen et al., 2019a*). As a result, the POC export out of the euphotic zone is low compared to other open ocean regions (*Sarmiento and Gruber, 2006*), but the vast oligotrophic gyres account for half of the global POC export to the ocean interior (*Emerson et al., 1997*). Precisely these ocean regions will most likely expand in future warmer times (*Behrenfeld et al., 2006*) and there are indications that CO₂ uptake via the organic carbon pump responds to climate change (e.g., *Riebesell et al., 2007; Duce et al., 2008; DeVries and Deutsch, 2014; Laufkötter et al., 2017*). Consequently, these areas will become even more

important on a global scale during the next decades and are of major importance in terms of global carbon budgets.

3.2 Materials and methods

3.2.1 Sediment trap moorings

Sediment trap moorings are used to investigate the vertical flux of particles in a water column and consist of multiple tools, with the sediment trap as the central part. In this work, we used Kiel K/MT 234 and McLane Mark 7G-21 sediment traps. Other important parts are float modules, acoustic releases, anchors, as well as a variety of wires and shackles. A sufficient number of floats is important to stabilize the mooring in the water column during the deployment and for the uplift during recovery. The anchor weight moors the system on the ground, while the acoustic release disconnects the anchor from the remaining system for recovery. Sediment traps consist of a funnel, which collects the sinking particles and has a slope angle of 34° and an aperture size of 0.5 m^2 . A lattice grid baffle is used to cover the funnel. This serves as a current stabilizer, reduces washout, and prevents large swimmers from entering the funnel. A rotation platform is placed under the funnel's orifice and is loaded with 20 HDPE (high-density polyethylene) trap cups (400 ml for Kiel K/MT 234 traps and 250 ml for the McLane Mark 7 trap), where sinking particles were stored after a pre-programmed timetable. The corresponding control unit is equipped with a microprocessor for programming the rotation steps and serves as the power supply for the drive unit. Prior to deployment, the trap cups were filled with filtered deep-sea water, from the respective location and depth where the sediment trap will be moored. To this water-filled trap cup, 35 g NaCl (analytical grade) was added to create a brine solution of $\sim 70 \text{ g L}^{-1}$ NaCl that reduces diffusion out of the cups during the deployment. In addition, 3.3 g L^{-1} HgCl_2 (analytical grade) was added to the brine solution to suppress organic matter degradation by bacterial or microbial activities. All trap cups that are not directly placed under the funnel's orifice are sealed against the outer seawater medium.

3.2.2 Sample collection

The investigations in the South Indian Ocean are part of environmental studies in the INDEX (Indian Ocean Exploration) program for marine resource exploration by the Federal Institute for Geosciences and Natural Resources (BGR), Germany, and the International Seabed Authority (ISA), Jamaica. During several ship cruises between November 2014 and September 2018 involving various vessels, sediment trap moorings were deployed and recovered at seven sites (cluster areas of the INDEX program) in the oligotrophic subtropical gyre of the South Indian Ocean (21.25°–27.80°S, 68.59°–73.89°E; Figure 3.1, Table 3.1).

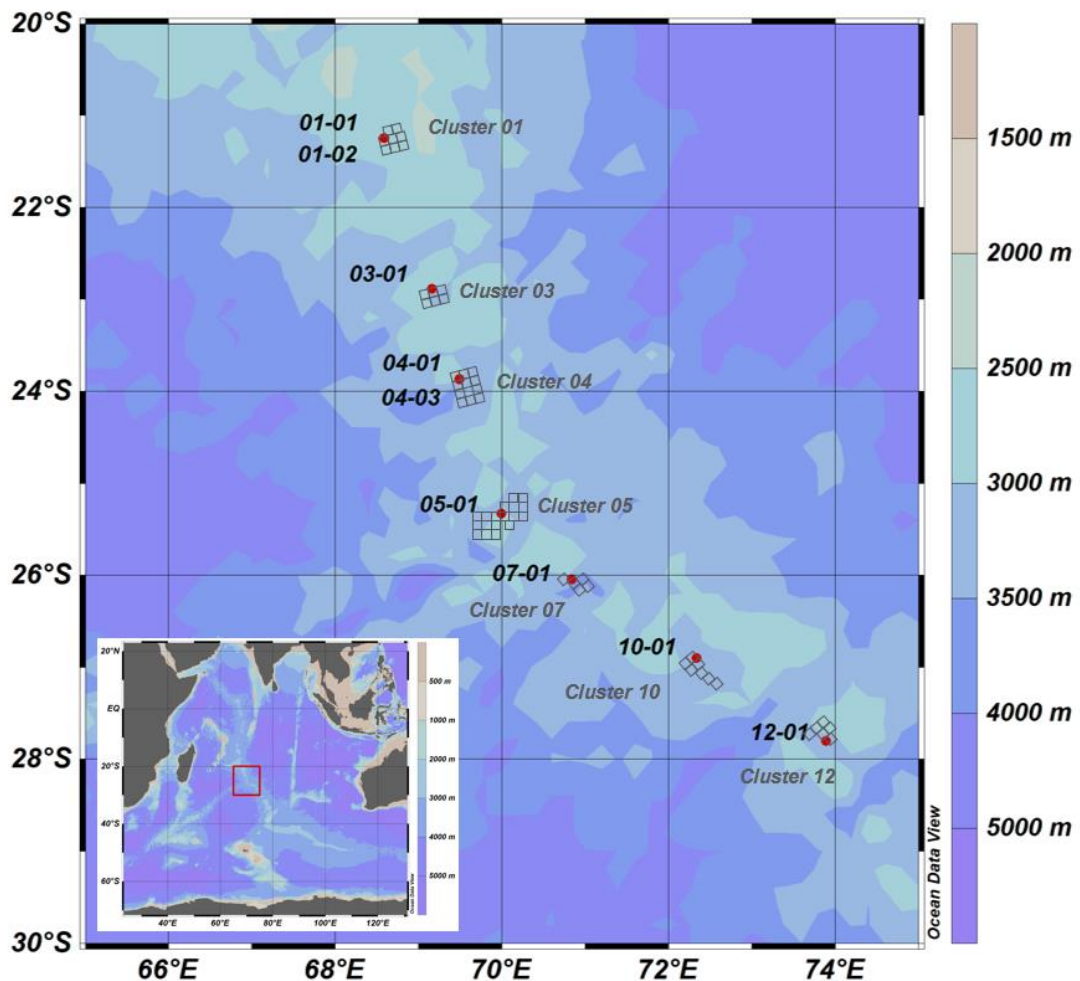


Figure 3.1. Station map of sediment trap moorings deployed within the 12 clusters of the INDEX program during November 2014 and September 2018 in the oligotrophic IOSG. Each INDEX cluster is subdivided into 10×10 km blocks (grey rectangles). Trap IDs represent the cluster number (first two digits) and the number of deployments at this site (second two digits).

Table 3.1. Technical data on the deployment and recovery of sediment traps moored during November 2014 and September 2018 in the INDEX area within the IOSG listed in temporal sequence.

Trap ID	Lat.	Long.	Water depth [m]	Trap depth		Deployment period	Filled cups [of 20]	Expeditions with research vessels [Deployment/ Recovery]
	[°S]	[°E]		[m.b.s.] ^a	[m.a.b.] ^b			
05-01	25.330	70.000	3110	2579	531	10.11.14–06.11.15	15	<i>PE 394/PE 405</i>
04-01	23.869	69.496	3493	2962	531	28.11.15–04.11.16	13	<i>PE 405/MSM 59-2</i>
01-01	21.247	68.591	3145	2614	531	20.12.16–12.09.17	16	<i>MSM 59-2/SO 259</i>
03-01	22.885	69.162	3700	3169	531	20.12.16–12.09.17	4	<i>MSM 59-2/SO 259</i>
01-02	21.248	68.589	3145	2614	531	03.10.17–10.09.18	20	<i>SO 259/PE 446</i>
04-03 <i>Shallow</i>	23.864	69.495	3493	695	2798	03.10.17–10.09.18	18	<i>SO 259/PE 446</i>
04-03 <i>Middle</i>	23.864	69.495	3493	2931	562	03.10.17–10.09.18	20	<i>SO 259/PE 446</i>
04-03 <i>Deep</i>	23.864	69.495	3493	3465	28	03.10.17–10.09.18	18	<i>SO 259/PE 446</i>
07-01	26.046	70.845	4010	3479	531	03.10.17–10.09.18	20	<i>SO 259/PE 446</i>
10-01	26.899	72.341	3400	2869	531	03.10.17–10.09.18	1	<i>SO 259/PE 446</i>
12-01	27.804	73.889	3970	3439	531	03.10.17–10.09.18	4	<i>SO 259/PE 446</i>

Note: ^ameter below surface; ^bmeter above bottom; *PE*: R/V *Pelagia*; *MSM*: R/V *Maria S. Merian*; *SO*: R/V *Sonne*.

In total, nine sediment trap moorings with eleven sediment traps were deployed for 1-year periods, and 150 particulate matter flux samples were successfully recovered. The sampling intervals of sediment trap cups range between 14 and 19 days (see Appendix A2, Table A2.1). Only four, one, and four filled cups were retrieved from sediment traps 03-01, 10-01, and 12-01, respectively, due to instrumental malfunction of the microprocessor or stepper motor. However, the last filled cups of sediment traps 03-01 and 12-01 collected particles during the remaining time interval and were used to calculate the annual mean mass fluxes (see Table 3.2). To collect the undisturbed vertical particle flux to the deep sea, with minimal influence of resuspended material from the seafloor, sediment traps were generally deployed at 500–600 m above bottom (m.a.b.). This corresponds to water deployment depths of ~2600–3500 m (Table 3.1), ensuring good comparability of data sets across multiple sites, and intercomparison studies suggest that the trapping efficiency of sediment traps deployed deeper than 1500 m is close to 100 % (Yu *et al.*, 2001). Sediment trap mooring 04-03 (cluster 04) was equipped with additional sediment traps, one above (*Shallow*) and one below (*Deep*) the general deployment depth of 500–600 m.a.b. (04-03 *Middle*). Trap 04-03 *Shallow* was located at 694 m water depth, trap 04-03 *Middle* was located at 2931 m water depth (563 m.a.b.), and trap 04-03 *Deep* was located close to the seafloor at 3465 m water depth (28 m.a.b.; Table 3.1). The deployment depth of trap 04-03 *Deep* was chosen in order to understand processes in the benthic nepheloid layer and other issues within the INDEX program regarding potential deep-sea mining activities (not discussed in this study). To compare our

particulate matter fluxes to primary production rates in sections 4.3 and 4.4, we used net primary production (NPP) data from the Ocean Productivity DataBase (<http://sites.science.oregonstate.edu/ocean.productivity/index.php>). The NPP bases on the standard VGPM (Vertically Generalized Production Model; *Behrenfeld and Falkowski, 1997*) algorithm, using MODIS chlorophyll-*a* concentration, sea surface temperature (SST), SeaWiFS Photosynthetically Available Radiation (PAR), and estimates of euphotic zone depth after *Morel and Berthon (1989)*.

3.2.3 Analytical methods

A visual inspection of the collected particles and measurements on chemical changes (salinity, pH, oxygen concentrations) in the supernatant of the trap cups was conducted on board and indicated no changes in closed or open cups throughout the year of deployment. The samples were then sieved to separate the particles into fractions of >1 mm and <1 mm. The latter fraction is regarded as the true particulate matter flux and was filtered through a pre-weighed Nucleopore polycarbonate filter (pore size: 0.4 μm) and rinsed with Milli-Q water charged with 0.002 g L⁻¹ Na₂B₄O₇ (sodium tetraborate, analytical grade) to avoid destruction of carbonate tests. The loaded filters were dried at ~40°C for 2 days and stored in a dark and dry environment. The dried filters were weighed in the home lab to determine the total particulate mass flux (mg m⁻² day⁻¹). Afterward, the particulate matter was mechanically removed from the filter and homogenized in a mortar. Concentrations of total carbon (TC), total nitrogen (TN), and organic carbon (POC) were analyzed using a EuroVector EA-3000 CHNSO Elemental Analyzer, which works with an analytical precision of 0.05 % for carbon and 0.005 % for nitrogen. Organic carbon was determined after the removal of carbonate with HCl (1N). Calcium carbonate (CaCO₃) is calculated by $\text{CaCO}_3 \text{ (wt.\-%)} = (\text{TC} - \text{POC}) / 0.12$. Biogenic opal was analyzed with the modified wet alkaline extraction method, according to *DeMaster (1981)* and *Mortlock and Froelich (1989)*. For biogenic opal, the relative error on duplicate sample measurements was generally below 5 % (for detailed data, see Appendix A2, Table A2.1). Particulate organic matter (POM) is calculated by the formula: $\text{POM (wt.\-%)} = \text{POC} \times 1.8$ (*Anderson, 1995; Francois et al., 2002*). The lithogenic matter was determined by subtracting the sum of POM, CaCO₃, and biogenic opal from 100 %. Particulate matter fluxes of all components were calculated by using the total mass flux. Traps 05-01, 03-01, 04-01, 04-03 *Shallow*, 04-03 *Deep*, and 12-01

stopped prior to the end of the deployment period at cup #15, #4, #13, #18, #18, and #4 respectively, and were recovered with open cups. However, no changes in the chemical parameters of the supernatant in trap cups were observed so that these samples are chemically comparable to the other cups. Thus, the particulate matter caught in the open cups was used for the reconstruction of the annual mass flux. In contrast, cups #16 of 01-01 (2016–2017) and #2 of 10-01 (2017–2018) had salinity values close to the seawater and low particle load, which indicated water mixing and potential loss of particulate matter. These cups were not used to extrapolate the total particulate matter flux and annual mass fluxes.

3.3 Results

3.3.1 Particulate matter fluxes and particle composition

Data on average total mass fluxes, the individual components CaCO_3 , biogenic opal, POM, POC, TN, and lithogenic matter as mass fluxes ($\text{mg m}^{-2} \text{day}^{-1}$) and percentages (wt.-%) and the molar ratio POC/TN, are listed in Table 3.2. Total mass fluxes of sinking particulate matter, collected by the traps deployed at 500–600 m.a.b. (2600–3500 m) range between $4.27 \text{ mg m}^{-2} \text{day}^{-1}$ (01-02) and $16.34 \text{ mg m}^{-2} \text{day}^{-1}$ (04-01) with an average mass flux of $9.8 \pm 3.7 \text{ mg m}^{-2} \text{day}^{-1}$ (Figure 3.2a). Total mass fluxes were relatively high in the *Shallow* and *Deep* traps of mooring 04-03 (Figure 3.2b; for details, see section 3.2). In the following description of the individual components, the *Shallow* and *Deep* traps of mooring 04-03 are excluded due to different deployment depths and are discussed separately in comparison with trap 04-03 *Middle* in section 3.2.

CaCO_3 is the main component of the total mass flux (62.7–72.4 wt.-%; Figure 3.2c, Figure 3.3a), which corresponds to our visual inspection, showing numerous foraminifera and pteropods. The high percentages of >60 wt.-% CaCO_3 in all traps are typical for the tropical and subtropical regions of the open ocean, which are largely unaffected by chemical solution (Kolla *et al.*, 1976; Lyle, 2014). In the region of 20°–30°S in the Indian Ocean, the carbonate compensation depth (CCD) for calcite is located between 4600–4800 m depth (Kolla *et al.*, 1976). All sediment traps are deployed above 3479 m along the Central Indian Ridge and the Southeast Indian Ridge. Thus, we can exclude the possibility of significant dissolution of CaCO_3 components in the intercepted sinking particulate matter. Berger (1978) mentioned that the aragonite compensation depth (ACD) has

typical depths of 500–1500 m in the Indian Ocean. In all traps, we found several fragments of pteropods, even in the deepest deployed trap 07-01 (3479 m depth), and observed no significant dissolution of aragonite components.

Biogenic opal is the second main component ranging from 11.64 to 17.42 wt.-% (Figure 3.2c, Figure 3.3b). Slightly lower percentages than biogenic opal are observed for POM that contributes between 8.20–11.01 wt.-% (Table 3.2, Figure 3.2c) to the total mass flux. The corresponding individual components POC and TN have percentages of 4.56–6.45 wt.-% and 0.49–0.69 wt.-%, respectively, and result in POC/TN ratios between 9.44–11.11 (Table 3.2, Figure 3.3c, d). Overall, the individual components CaCO₃, biogenic opal, POC, TN, and lithogenic matter vary little in total mass fluxes (Figure 3.2a, Figure 3.3a–d).

Table 3.2. Averaged values of total mass fluxes (mg m⁻² day⁻¹) and composition (wt.-%) of the total mass flux of individual components CaCO₃, biogenic opal (bOpal), POM, POC, TN, and lithogenic matter (LM) and molar ratio POC/TN of sediment traps deployed during November 2014 and September 2018 in the oligotrophic IOSG.

	Sediment traps deployed during November 2014 and September 2018 in the IOSG										
	05-01	04-01	01-01	03-01 ^a	01-02	04-03	04-03	04-03	07-01	10-01 ^b	12-01 ^c
						<i>Shallow</i>	<i>Middle</i>	<i>Deep</i>			
Mass fluxes [mg m ⁻² d ⁻¹]											
Total	9.94	16.34	8.38	13.01	4.27	16.57	5.41	14.32	12.22	6.68	12.20
CaCO ₃	7.24	10.89	5.69	8.59	3.42	10.98	3.60	9.20	8.00	4.19	7.70
bOpal	1.14	2.78	1.43	2.17	0.97	1.64	0.83	2.54	1.86	0.96	1.57
POM	0.88	1.33	0.75	1.17	0.52	2.79	0.52	1.29	0.95	0.74	1.10
POC	0.49	0.74	0.42	0.65	0.29	1.55	0.29	0.57	0.53	0.41	0.61
TN	0.058	0.092	0.052	0.063	0.030	0.223	0.034	0.067	0.066	0.044	0.070
LM	0.69	1.39	0.51	1.09	0.78	1.15	0.50	1.72	1.41	0.80	1.83
wt.-% of the total mass flux											
CaCO ₃	72.35	66.98	66.69	65.87	62.65	66.22	65.68	61.80	65.15	62.70	63.14
bOpal	11.64	16.43	17.42	16.69	14.50	9.61	15.26	15.02	15.08	14.32	12.90
POM	8.45	8.20	9.29	9.01	11.62	17.30	10.60	7.32	8.40	11.01	9.01
POC	4.94	4.56	5.16	5.00	6.45	9.61	5.89	4.07	4.67	6.12	5.00
TN	0.57	0.56	0.64	0.49	0.65	1.38	0.69	0.47	0.58	0.66	0.57
LM	7.11	8.39	6.61	8.43	11.21	6.87	10.12	15.86	11.37	11.98	14.96
Molar ratio											
POC/TN	9.79	9.58	9.50	12.02	11.11	8.20	10.08	10.10	9.44	10.90	10.17

Note: Sediment traps 03-01, 10-01, and 12-01 were retrieved with only four samples (^a), one sample (^b), and four samples (^c), respectively.

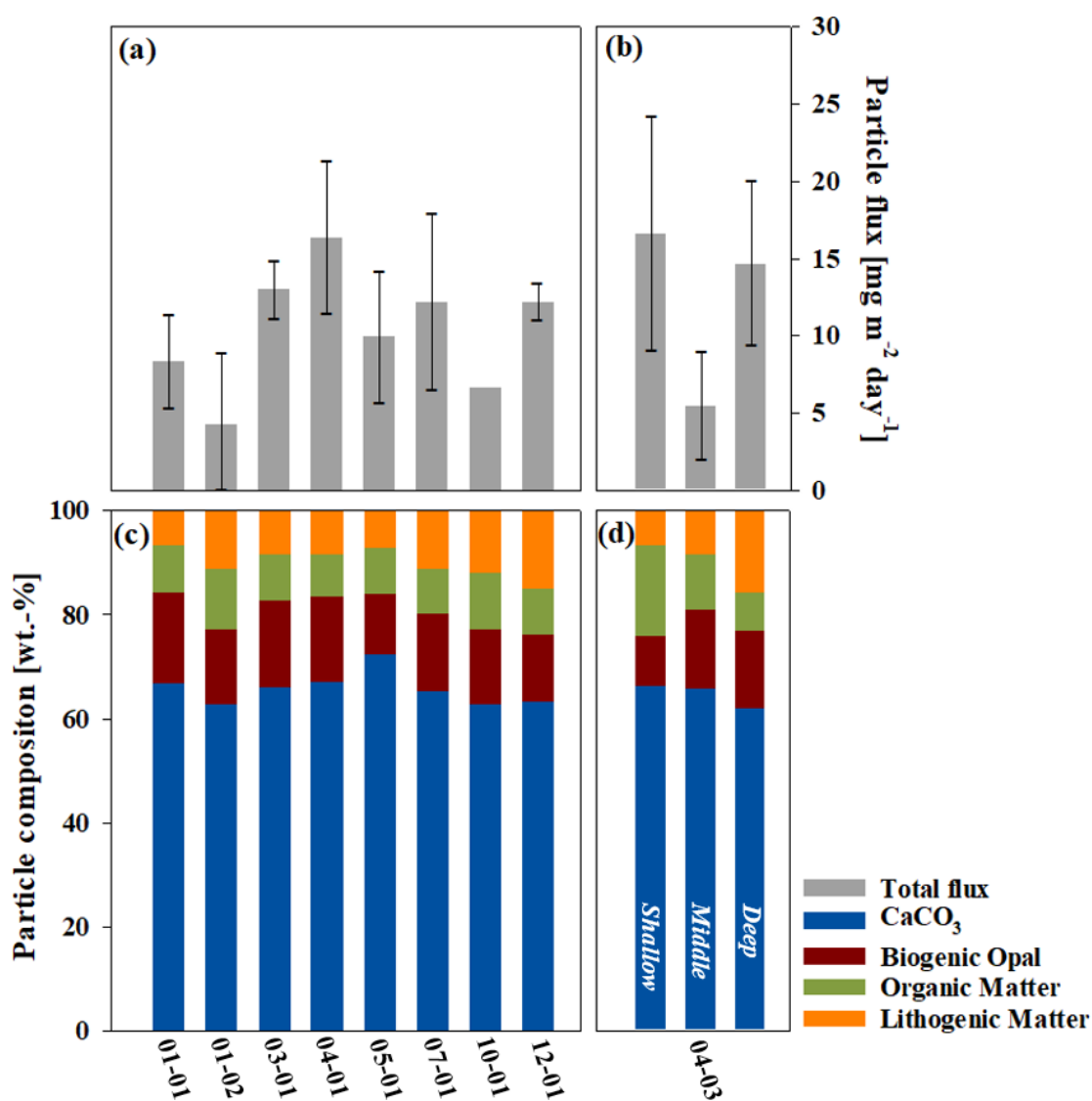


Figure 3.2. Average total mass fluxes ($\text{mg m}^{-2} \text{ day}^{-1}$) (a, b) and percentages (wt.-%) of the individual components CaCO_3 , biogenic opal, POM, and lithogenic matter (c, d) of sediment traps deployed during November 2014 to September 2018 in the oligotrophic IOSG by latitude. Standard deviations are indicated for total mass fluxes. For trap 10-01, no standard deviation was determined (only one sample).

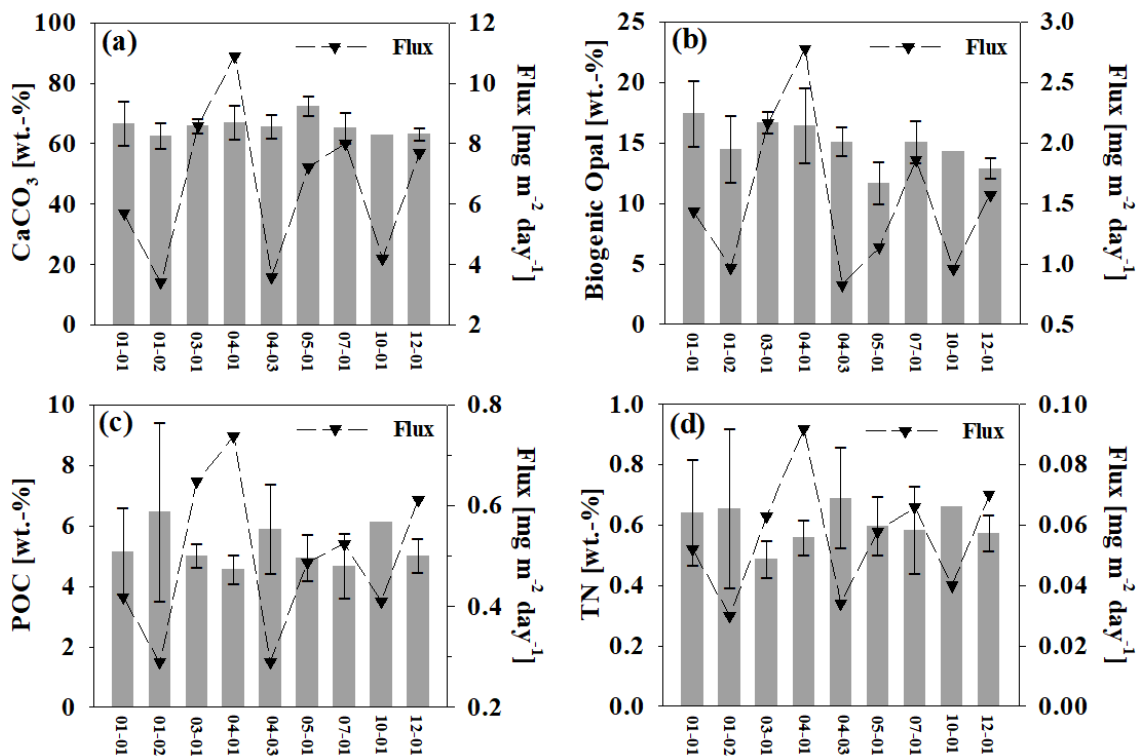


Figure 3.3. Average percentages (wt.-%) and mass fluxes (mg m⁻² day⁻¹) of the major components CaCO₃ (a), biogenic opal (b), POC (c), and TN (d) of sediment traps deployed at 500–600 m above bottom (2600–3500 m) during November 2014 and September 2018. Standard deviations are indicated for the average percentages of the individual components. For trap 10-01, no standard deviation was determined (only one sample).

3.3.2 Particulate matter flux variability with depth at mooring 04-03

Three sediment traps were deployed at mooring 04-03 to collect particles at various depths (*Shallow*, *Middle*, and *Deep*). Total particulate matter fluxes are highest in the trap 04-03 *Shallow* (16.57 mg m⁻² day⁻¹), which was deployed closest to the sea surface but below the upper ocean layer of active diurnal vertical migration, so that we collect only the passive particle flux (Table 3.1, Figure 3.2b). Total fluxes decreased to trap 04-03 *Middle* (5.41 mg m⁻² day⁻¹) that was deployed at the same distance to the sea floor as the sediment traps of the other moorings and intercepted the virtually undisturbed vertical particle flux to the deep sea, with minimal influence of resuspended material from the seafloor. In contrast, trap 04-03 *Deep* was deployed close to the seafloor (28 m.a.b.). The influx of particles from rebound processes at the seafloor or horizontal influx due to a

rough and steep seafloor topography at the mooring site is reflected in higher mass fluxes of $14.32 \text{ mg m}^{-2} \text{ day}^{-1}$ compared to trap 04-03 *Middle*. Indeed, higher contents of lithogenic matter in trap 04-03 *Deep* (15.86 wt.-%) compared to trap *Middle* (10.12 wt.-%) and trap *Shallow* (6.87 %) are an indicator for the influence of resuspended material from the seafloor (Table 3.1).

Mass fluxes of the individual components CaCO_3 , POC, and TN follow the distribution of the total mass flux with lowest fluxes in trap 04-03 *Middle* and higher fluxes in traps 04-03 *Shallow* and *Deep* (Figure 3.2d, Figure 3.4a–d). CaCO_3 has constant proportions in traps *Shallow* and *Middle*, while trap *Deep* has lower percentages most likely because of the proportionally higher lithogenic matter contents (Figure 3.4e, Table 3.2). Biogenic opal shows a clear increase from low values (9.61 wt.-% in trap 04-03 *Shallow*) towards higher values (of >15 %) in traps 04-03 *Middle* and *Deep* (Figure 3.4f). In contrast, POC and TN gradually decrease with depth and have highest percentages in trap 04-03 *Shallow* (9.61 wt.-% POC; 1.38 wt.-% TN), moderate percentages in 04-03 *Middle* (5.89 wt.-% POC; 0.69 wt.-% TN), and low percentages in 04-03 *Deep* (4.07 wt.-% POC; 0.47 wt.-% TN) (Figure 3.4g, h). This reflects the typical progressive degradation of organic matter components with depth (Sarmiento and Gruber, 2006; Henson et al., 2019). TN indicates a stronger decline than POC between traps 04-03 *Shallow* and *Middle* and thus leads to the typical downward increase of POC/TN ratios reflecting preferential degradation of TN (Figure 3.4i; Knauer et al., 1979; Martin et al., 1987). The POC/TN ratio indicates little changes between traps *Middle* and *Deep* and demonstrates a decline in organic matter degradation in the deeper water column. It is important to note that POC and TN contents in trap 04-03 *Deep* may be biased by the influx of resuspended matter from the seafloor with significantly lower POC and TN contents (first centimetre of short sediment cores: 0.40 wt.-% POC; 0.053 wt.-% TN; Harms et al., submitted). These bottom processes can lead to an underestimation of organic matter contents and relatively higher shares of inorganic components.

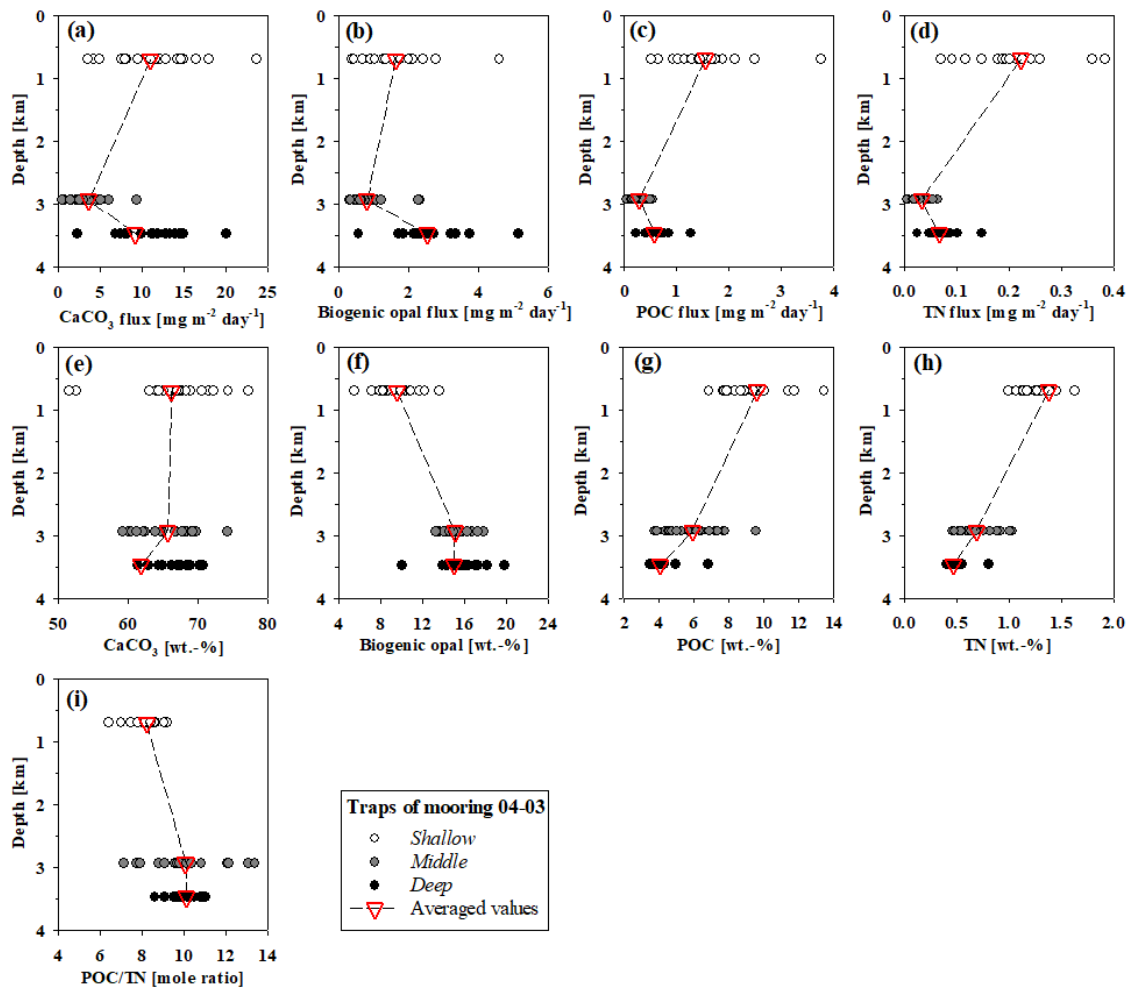


Figure 3.4. Particulate matter components CaCO_3 , biogenic opal, POC, and TN given as mass fluxes ($\text{mg m}^{-2} \text{day}^{-1}$) (a-d) and in percentages (wt.-%) (e-h) and the molar ratio POC/TN (i) versus water depth for sediment traps of mooring 04-03, deployed at 695 m (*Shallow*), 2931 m (*Middle*), and 3465 m (*Deep*) during October 2017 to September 2018.

3.4 Discussion

3.4.1 Organic carbon fluxes in the IOSG compared to global data

First data on particulate matter fluxes in the IOSG reveal average POC fluxes of $0.49 \pm 0.15 \text{ mg m}^{-2} \text{day}^{-1}$ for sediment traps deployed in the deep ocean at about 500–600 m.a.b. (Table 3.1), which is roughly 5 % of the total mass flux. To put our data into a larger context and to evaluate upper ocean processes and the transfer of sinking POC to the deep IOSG, we compare our measured POC fluxes with global POC data previously collated from the literature (e.g., *Lampitt and Antia, 1997; Lutz et al., 2007; Honjo et al., 2008*; see data and references in the Appendix

A3, Table A3.1). For comparison, we adjusted POC flux data to a water depth of 2000 m using the equation of *Martin et al.* (1987):

$$POC_{2000} = POC_{TD} \times (2000/TD)^b, \quad (3.1)$$

where “ POC_{2000} ” is the normalized particulate organic carbon flux at a water depth of 2000 m (in $\text{mg m}^{-2} \text{day}^{-1}$), and “ POC_{TD} ” denotes the particulate organic carbon flux measured at trap depth (TD). The exponent “ b ” indicates the “best fit” for the log-log slope representing the decrease of POC fluxes with water depth. This equation is commonly used to reference oceanic POC fluxes to a uniform deployment depth (*Lampitt and Antia, 1997; Sarmiento et al., 1998; Hedges et al., 1999; Buesseler et al., 2000; Fischer et al., 2000; Lutz et al., 2007*). Due to limited observational data on depth-integrated POC fluxes for the IOSG, we use the “best fit” of the *Martin et al.* (1987) power function ($b = -0.858$) that is based on sediment trap data collected in the low- and mid-latitudes of the Pacific Ocean, which is closest to biogeochemical patterns in our study area and has been used previously to depth-normalized global POC fluxes (*Lampitt and Antia, 1997; Lutz et al., 2007*).

The resulting global map of normalized POC fluxes reveals that the IOSG is among the areas of lowest POC fluxes worldwide (Figure 3.5a, b). Comparing POC fluxes to other subtropical gyres shows that fluxes measured in the IOSG are also lower than fluxes detected in the northern hemisphere gyres of the Pacific (NPSG) and Atlantic Ocean (NASG; Figure 3.5c). Very little data is available for the southern hemisphere gyres of the Pacific (SPSG) and Atlantic Ocean (SASG), but suggest that POC fluxes there are either in the range of those in the IOSG or higher (Figure 3.5a, c). Thus, POC flux data in the IOSG depict one of the lowest fluxes recorded worldwide. Nevertheless, more field data are needed to verify whether the IOSG has significantly lower POC fluxes than all other subtropical gyres of the world’s ocean, or if southern hemisphere gyres are generally characterized by lower POC fluxes compared to northern hemisphere gyres.

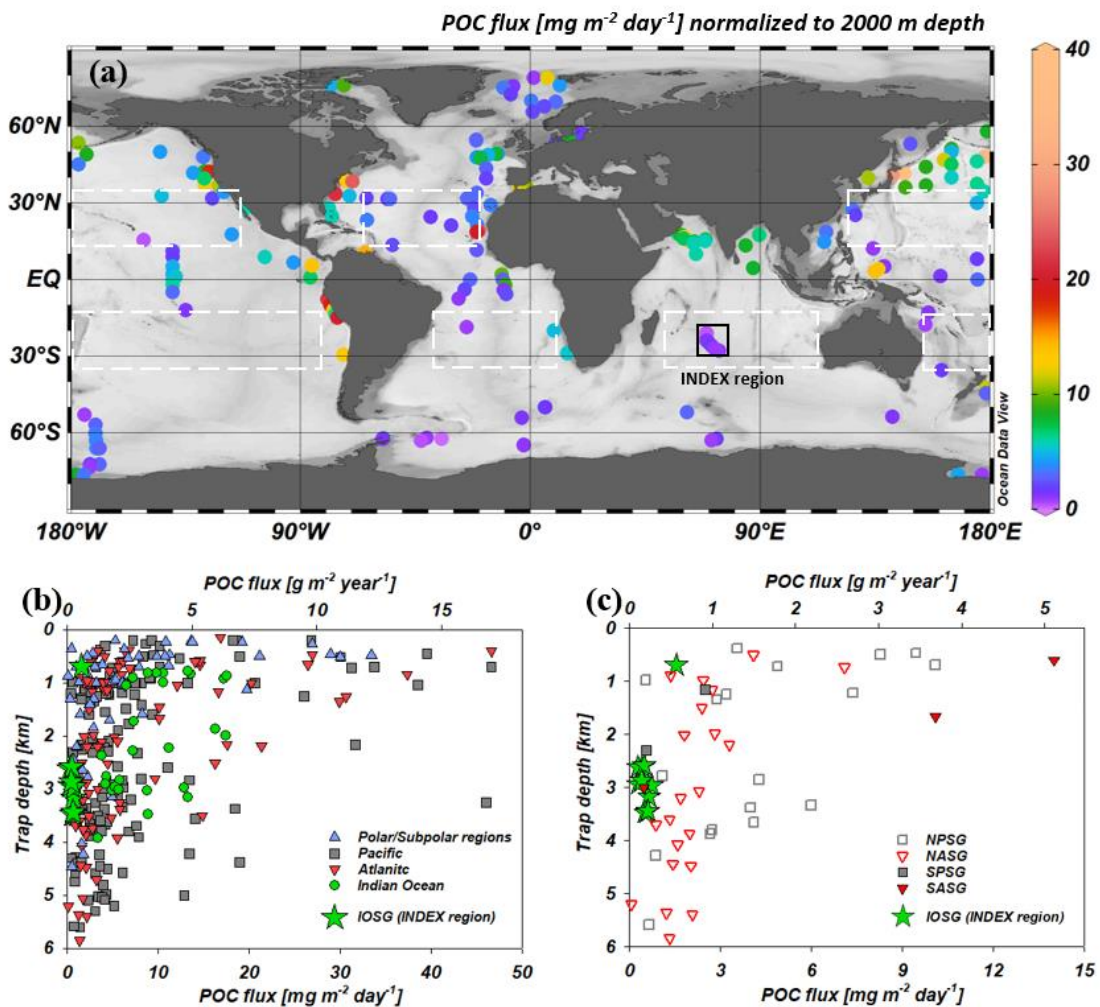


Figure 3.5. Global map of sediment trap POC fluxes compiled from the literature normalized to 2000 m water depth (see data and the corresponding references in the Appendix A3, Table A3.1) extended by data from the IOSG (this study; black rectangle) (a). Absolute data of global POC fluxes (b) are plotted against trap depths for the Polar/Subpolar regions (blue), Pacific (grey), Atlantic (red), and Indian Ocean (green); green stars denote the INDEX region (our data). Panel c shows POC fluxes plotted against trap depths for the subtropical gyres in the Atlantic, Pacific and Indian Ocean, defined by the white dashed rectangles (15° – 35° N, 15° – 35° S) in the global map (NPSG: North Pacific subtropical gyre, NASG: North Atlantic subtropical gyre, SPSG: South Pacific subtropical gyre, SASG: South Atlantic subtropical gyre).

3.4.2 Controlling factors of particulate matter fluxes in the IOSG

Particulate matter fluxes are first-order linked to surface primary production (Eppley and Peterson, 1979; Suess, 1980; Betzer et al., 1984; Lampitt and Antia, 1997). The extremely low POC fluxes in the IOSG compared to global data clearly reflect the oligotrophic conditions and the specific physical properties of the IOSG. Particulate organic matter sampling took place in the western part ($\sim 68^{\circ}$ – 74° E) of the subtropical gyre between $\sim 21^{\circ}$ – 28° S (Figure 3.1). In the southern part of our study area, pycno- and thermoclines are depressed due to overturning circulation that causes downwelling, reflected by steep horizontal gradients and outcropping density surfaces at the gyre margins (Figure 3.6a, b; Williams and Follows, 1998; Lee, 2004; McClain et al., 2004; Baer et al., 2019; Harms et al., 2019).

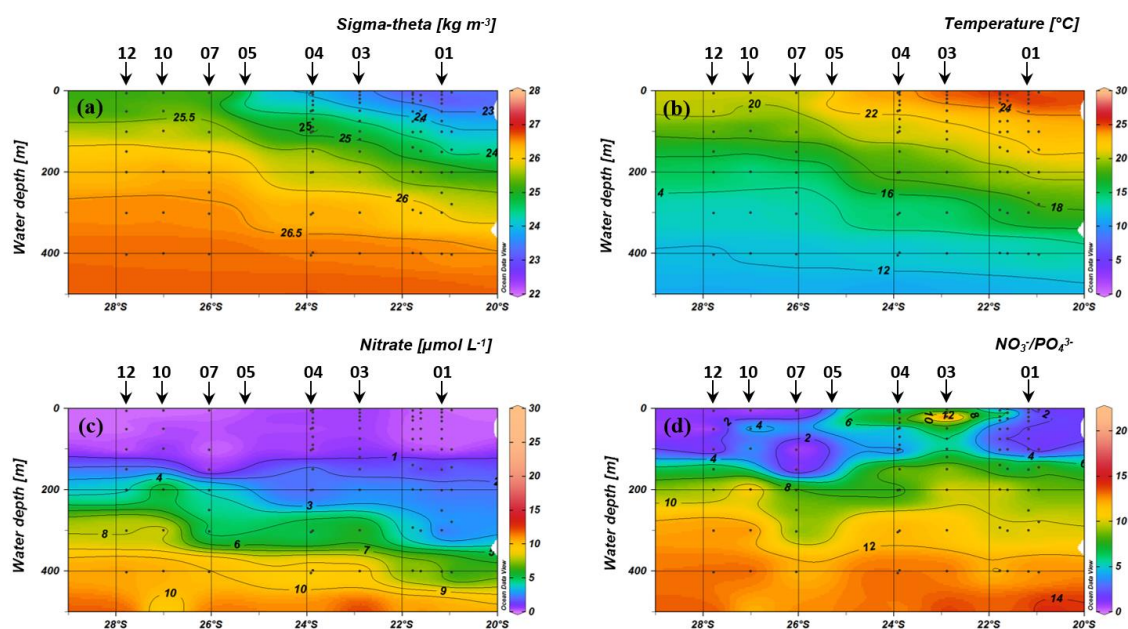


Figure 3.6. Latitudinal sections of sigma-theta (in kg m^{-3}) (a), temperature ($^{\circ}\text{C}$) (b), nitrate concentrations ($\mu\text{mol L}^{-1}$) (c), and the distribution of $\text{NO}_3^-/\text{PO}_4^{3-}$ ratios on transects roughly along 71°E between 20°S and 29°S in the IOSG (data available at the <https://doi.pangaea.de/10.1594/PANGAEA.897503> and <https://doi.pangaea.de/10.1594/PANGAEA.897504>, see Harms et al., 2019). Black arrows mark the locations of sediment trap deployments and numbers above are the corresponding cluster numbers.

The northern part of the study area is characterized by high sea surface temperatures ($>24^{\circ}\text{C}$ in the upper 50 m; Figure 3.6b) due to local surface heating. In accordance with the depression of pycnoclines, the nutriclines and the ocean mixed layer (OML; $\Delta T \approx 0.5^{\circ}\text{C}$, $\Delta\text{sigma-theta} \approx 0.125 \text{ kg m}^{-3}$) deepen towards the center of the IOSG (Williams and Follows, 1998; Kantha and Clayson, 2003; Baer et

al., 2019; *Harms et al.*, 2019). This leads to strongly nutrient-depleted upper waters (<100 m with <1 $\mu\text{mol L}^{-1} \text{NO}_3^-$; Figure 3.6c; *Harms et al.*, 2019) and relatively low diffusive nutrient input fluxes from deeper waters (*Baer et al.*, 2019). This is illustrated by the very low dissolved $\text{NO}_3^-/\text{PO}_4^{3-}$ ratios of <4 in the surface layer (<100 m; Figure 3.6d) and results in a strongly N limited ocean region with low phytoplankton productivity (*Baer et al.*, 2019; *Harms et al.*, 2019).

Primary production in the IOSG is most likely co-limited by iron, due to the absence of significant dust deposition (*Mahowald et al.*, 2005; *Grand et al.*, 2015). Limited iron availability might impede dinitrogen fixation and therefore enhances N stress. Until now, dinitrogen fixation was found only locally ($\sim 20^\circ$ – 24°S) in nitrate isotope composition and $\text{NO}_3^-/\text{PO}_4^{3-}$ ratios (>6, <100 m; Figure 3.6d; *Harms et al.*, 2019). Higher primary production rates and higher POC fluxes in the northern hemisphere subtropical gyre of the Atlantic Ocean (NASG) (Figure 3.5c) are most likely due to a higher dust supply via atmospheric deposition leading to extensive dinitrogen fixation (*Mahowald et al.*, 2005; *Bourbonnais et al.*, 2009; *Pabortsava et al.*, 2017). Furthermore, the input of lithogenic matter (dust) leads to a more efficient ballast effect that enhances POC export fluxes (*Jickells and Spokes*, 2001; *Baker et al.*, 2003). To conclude, the absence of vertical nutrient input due to a strong stratified surface layer and external nutrient input via atmospheric deposition resulting in low rates of dinitrogen fixation limit primary production in the IOSG (e.g., *Donaghay et al.*, 1978; *Goldman*, 1980). Indeed, *Baer et al.* (2019) registered extremely low primary production rates of 0.12–4.6 $\text{nmol C L}^{-1} \text{h}^{-1}$ in surface waters (upper 20 m), lower than the primary production rates measured in other oligotrophic gyres (>20 $\text{nmol C L}^{-1} \text{h}^{-1}$; e.g., *Williams et al.*, 2013).

In warm and carbonate dominated regions such as the IOSG, complex food webs lead to an enhanced regeneration of organic components and exponentially decreasing fluxes of particulate organic matter in the upper water column observed by sediment trap experiments (*Suess*, 1980; *Martin et al.*, 1987). Therefore, POC undergoes intense degradation before being exported into the ocean's interior (*Francois et al.*, 2002; *Sarmiento and Gruber*, 2006; *Rixen et al.*, 2019b). We use the equation of *Martin et al.* (1987, Eq. 3.1 with $b = -0.858$) to calculate the POC flux that is exported out of the productive zone. For this, we normalized our POC flux data to the lower limit of the euphotic zone that is approximately 130 m in the IOSG (based on model data from the NASA Earth DataBase Giovanni: MODIS-A, Lee algorithm; *Lee et al.*, 2007). The calculation

yields an area-averaged $\text{POC}_{\text{export flux}}$ of $7.4 \pm 2.4 \text{ mg m}^{-2} \text{ day}^{-1}$. Comparing this estimate with POC fluxes in trap 04-03 *Shallow* ($1.6 \pm 0.7 \text{ mg m}^{-2} \text{ day}^{-1}$), only ~22 % of the POC that was exported below the euphotic zone reaches a water depth of ~700 m. From that depth downwards to trap 04-03 *Middle* (~3000 m), we find a further loss of 39 % POC contents between 700 m (9.61 wt.-%) and 3000 m (5.89 wt.-%), while another 31 % are lost between 3000 m and ~3500 m (trap 04-03 *Deep*: 4.07 wt.-%; Figure 3.4g). This implies that most water column remineralization occurs at depths less than 700 m, and most of the POC passing 700 m reaches the ocean floor in agreement with previous observations of exponentially decreasing POC fluxes in the upper water column and a more linear decline in the deep sea (Suess, 1980; Armstrong *et al.*, 2002).

One decisive factor that promotes the transport of POC from the base of the euphotic zone to the ocean interior is the availability of ballast material. The effective aggregation of smaller particles – individually having an insignificant role in vertical mass flux – transforms them into fast sinking aggregates (>100 m per day) by increasing their specific density (Schrader, 1971; McCave, 1975; Shanks and Trent, 1980; Suess, 1980; Rixen *et al.*, 2019b). Moreover, the increase of the sinking speeds shortens the residence time of particulate matter in the biologically active zone, lowers organic matter degradation within the OML and sub-thermocline, and thus enhances the downward flux (Haake and Ittekkot, 1990; Ramaswamy *et al.*, 1991; Armstrong *et al.*, 2002; Hamm, 2002; Klaas and Archer, 2002). In the IOSG, CaCO_3 (~65 wt.-%; $6.6 \text{ mg m}^{-2} \text{ day}^{-1}$), biogenic opal (~15 %; $1.5 \text{ mg m}^{-2} \text{ day}^{-1}$) or lithogenic matter (~10 %; $1.0 \text{ mg m}^{-2} \text{ day}^{-1}$) might act as the relevant ballast material. We use a multiple linear regression analysis (MLRA) from Honda and Watanabe (2010) (initial formula: $\text{POC}_{\text{total flux}} = \text{POC}_{\text{CaCO}_3} + \text{POC}_{\text{Opal}} + \text{POC}_{\text{lith. matter}}$), to evaluate how these potentially relevant components contribute to the total POC flux. We found positive correlations between POC fluxes and all components (CaCO_3 , biogenic opal, lithogenic matter), but with different magnitudes (“carrying coefficients”= CCs; Honda and Watanabe, 2010) and significances (p) (for detail see Appendix A4). CaCO_3 has the highest relevance (CC = 0.48) followed by biogenic opal (CC = 0.39), both revealing a high significance ($p < 0.001$). This agrees with simple linear regressions between POC and CaCO_3 ($r^2 = 0.93$; Figure 3.7a) and POC and biogenic opal fluxes ($r^2 = 0.82$) (Figure 3.7b). In contrast, the lithogenic matter is insignificant in promoting sinking POC fluxes (CC = 0.12). In fact, lithogenic matter fluxes at open ocean sites in the IOSG are too small to have a significant impact (Francois *et al.*, 2002;

Rixen *et al.*, 2019b) despite the generally higher densities of lithogenic matter ($\rho = 1.4\text{--}2.8 \text{ g cm}^{-3}$) compared to CaCO_3 ($\rho = 1.55\text{--}1.7 \text{ g cm}^{-3}$; Winter and Siesser, 1994; Schiebel and Hemleben, 2000; Schiebel *et al.*, 2007; Osipov, 2012; Rixen *et al.*, 2019b).

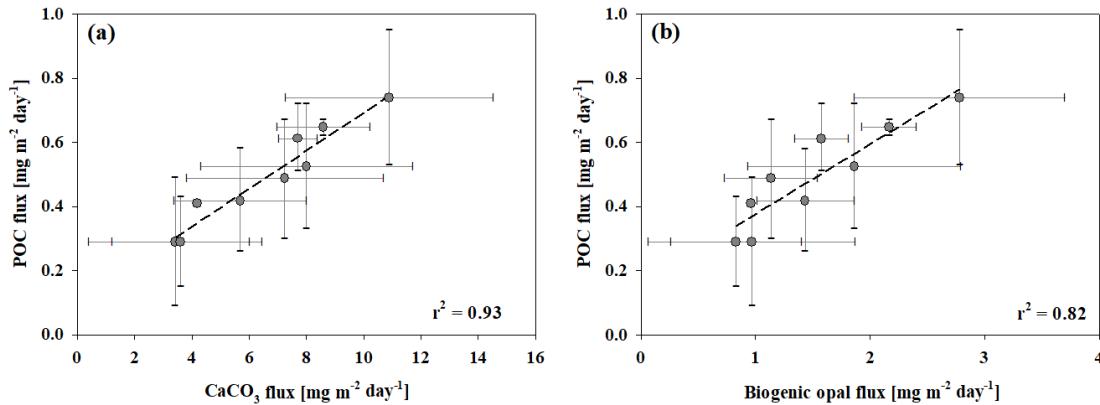


Figure 3.7. Linear correlation of particulate organic carbon (POC) fluxes versus calcium carbonate (CaCO_3) (a) and biogenic opal flux (b) averaged over the entire period of sediment trap deployments at 500–600 m.a.b. (traps 04-03 *Shallow* and *Deep* are excluded) with standard deviations. Dashed regression lines illustrate the positive linear relationships with correlation coefficients of $r^2 = 0.93$ for POC vs. CaCO_3 and $r^2 = 0.82$ for POC vs. biogenic opal.

3.4.3 Spatial and temporal patterns in the IOSG

Subtropical gyres, like the IOSG, are relatively isolated and spatially homogenous ocean regions with muted seasonality compared to other open ocean regions (McClain *et al.*, 2004; Sarmiento and Gruber, 2006; Henson *et al.*, 2019). However, there are minor regional and seasonal fluctuations in the nutrient concentrations, SST and consequently in the NPP. In the following, we use data of NPP based on the standard VGPM (Vertically Generalized Production Model) algorithm (Behrenfeld and Falkowski, 1997), using MODIS chlorophyll-*a* concentration, SST, SeaWiFS PAR, and estimates of euphotic zone depth after Morel and Berthon (1989) to analyze the regional and seasonal fluctuations in our POC flux data. The maximum expansion of oligotrophic areas and the corresponding lowest NPP rates in the southern hemisphere gyres, such as the IOSG, occur during austral summer (January; Figure 3.8a), while oligotrophic areas shrink during austral winter (July, Figure 3.8b) and have maximum NPP rates. The IOSG extends from 12°S to 28°S, and our study area (~21°–28°S) covers

the central IOSG towards its southern margin and during both seasons, it is situated in an area close to perennially lowest NPP rates (Figure 3.8a, b).

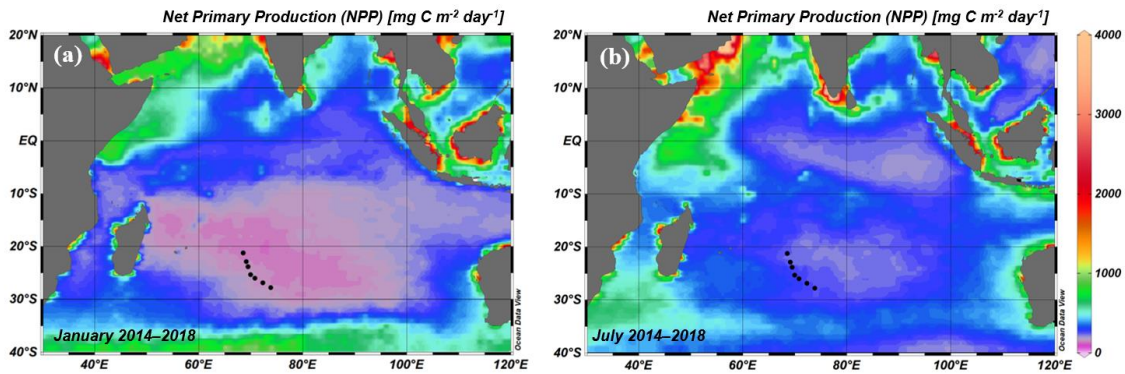


Figure 3.8. Distribution of the net primary production (NPP in $\text{mg C m}^{-2} \text{ day}^{-1}$) based on the standard VGPM algorithm (Behrenfeld and Falkowski, 1997) using data of MODIS chlorophyll-*a* concentrations, sea surface temperature (SST), SeaWiFS PAR, and estimates of euphotic zone depth from a model developed by Morel and Berthon (1989). Data was extracted from global monthly grids (original resolution: 1080×2160 ; <http://sites.science.oregonstate.edu/ocean.productivity/index.php>) for January (a) and July (b; time-averaged for 2014–2018). Black dots present the sediment trap locations in the INDEX area.

Regarding the regional patterns, we observe a minor trend of increasing NPP rates towards our southern study area that corresponds to the rise of nitrate concentrations (>200 m) and to a shallower OML caused by the convergence horizontal Ekman volume flux and the resulting shoaling of density surfaces towards the southern gyre margin (Figure 3.9). Although, no significant differences in the nitrate concentrations were observed in the euphotic zone (~ 130 m, see above), NPP follows this trend. This discrepancy likely arises from different times covered by the data sets, whereas nitrate concentrations are from samples collected during austral summer (lowest nitrate concentrations, lowest NPP rates) and NPP data were averaged over the entire time period of sediment trap deployments (2014–2018), including winter seasons. Higher nitrate concentrations in winter lead to the slight increase in NPP towards the gyre margin in the multi-year analysis. Additionally, Figure 3.9 presents average POC fluxes, normalized to a water depth of 2000 m, that tend to increase towards the south (except in traps 03-01 and 04-01) with a correlation coefficient of $r^2 = 0.56$ between POC and degree of latitude. On the other hand, the spatial distribution of POC fluxes reveals similar standard deviations ($\pm 0.14 \text{ mg m}^{-2} \text{ day}^{-1}$) as the temporal fluctuation during the deployment intervals ($\pm 0.10\text{--}0.19 \text{ mg m}^{-2} \text{ day}^{-1}$).

Thus, a statistical significance of increasing POC fluxes towards the southern gyre margin is questionable. Furthermore, a MLRA indicate that POC fluxes have no significant correlation with variations in either nitrate distribution, NPP, or OMLD. Thus, there is no robust trend of increasing fluxes towards the south, and the spatial pattern of POC export to the deep ocean is homogeneous in the working area, in agreement with previous investigations in the IOSG (*McClain et al.*, 2004; *Sarmiento and Gruber*, 2006; *Henson et al.*, 2019).

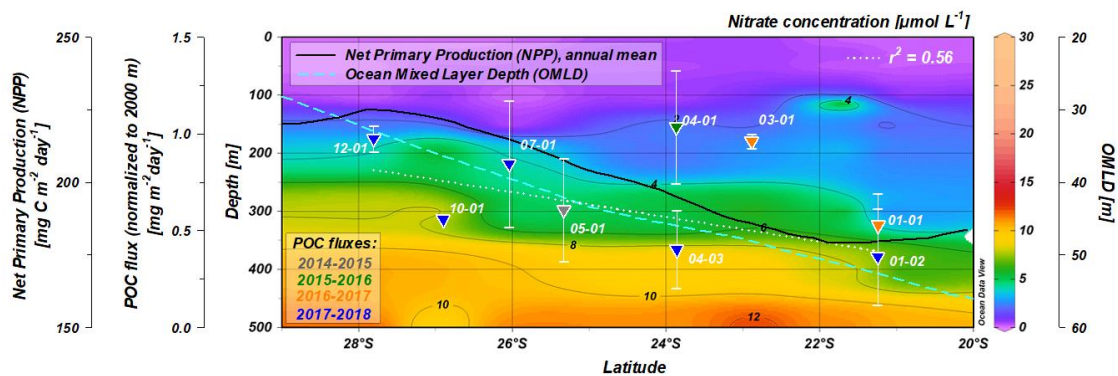


Figure 3.9. Nitrate concentrations in $\mu\text{mol L}^{-1}$ (color code), net primary production (NPP in $\text{mg C m}^{-2} \text{ day}^{-1}$; solid black line), ocean mixed layer depth (OMLD, blue dashed line), and particulate organic carbon (POC) flux data (triangles) with standard deviations along a meridional section from 20°S to 29°S for the INDEX region. Nitrate data is available at <https://doi.pangaea.de/10.1594/PANGAEA.897503> and <https://doi.pangaea.de/10.1594/PANGAEA.897504> (*Harms et al.*, 2019). Data on the NPP is from the Ocean Productivity DataBase (see figure caption Figure 3.8) and was interpolated as annual mean for the time period between 2014 and 2018 (monthly resolution) and as zonal mean averaged over 67° – 75°E (original resolution: 1080×2160 global monthly grids). Data on the OMLD were taken from the NASA Earth DataBase Giovanni (<https://10.5067/BHCFDIICI0U5>; monthly from January 2014–December 2015; 68° – 74°S ; resolution $0.67 \times 1.25^{\circ}$; *Gregg and Rousseaux*, 2017). Average POC fluxes were normalized to 2000 m for sediment traps deployed at 500–600 m.a.b. (2600–3500 m). The white dotted line presents the correlation between POC fluxes and latitude—correlation coefficient of $r^2 = 0.56$.

Regarding the seasonal fluctuations in the IOSG, Figure 3.10 compares POC fluxes and NPP rates at the different cluster sites during the deployment periods. A seasonal cycle in the NPP can be observed at all mooring stations with maximum values in austral winter and minimum values in austral summer. In addition, minor differences in the magnitude and in the inter-seasonal variability of the NPP among the different sites are apparent. Generally, POC fluxes to depth

are positively correlated to primary production (*Betzer et al.*, 1984), however we observe a rather constant rain of POC flux throughout the year (Figure 3.10).

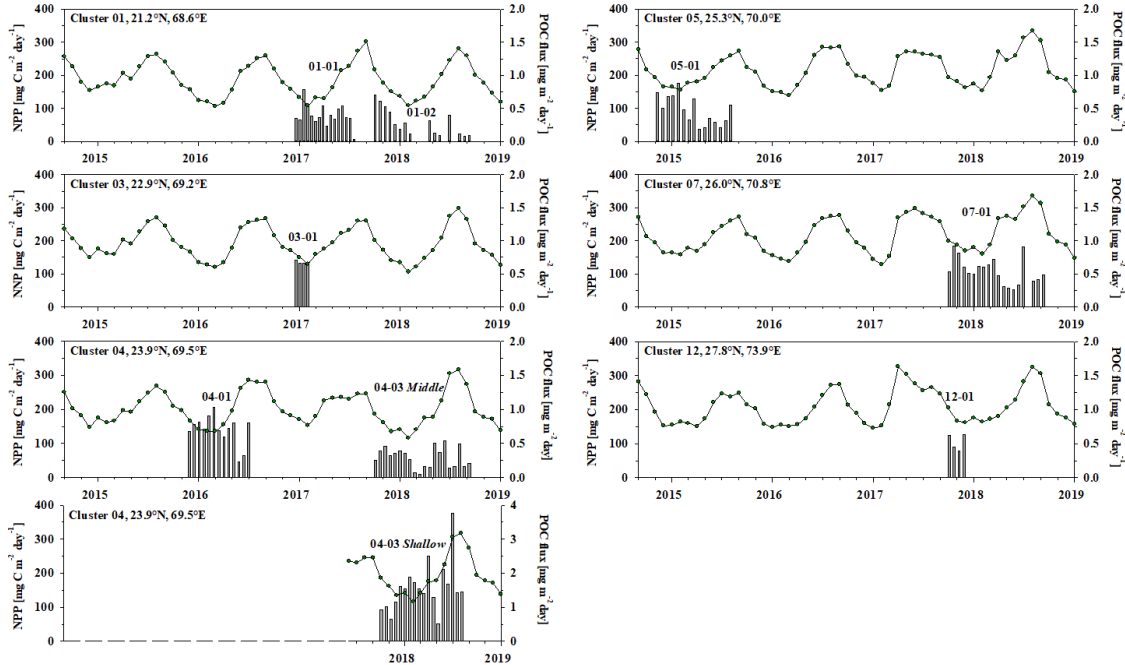


Figure 3.10. Particulate organic carbon fluxes (POC; grey bars) and seasonal fluctuations of net primary production (NPP in $\text{mg C m}^{-2} \text{ day}^{-1}$; line plot; available at the Ocean Productivity DataBase, see figure caption Figure 3.8). NPP data are interpolated as global monthly grids (original resolution: 1080×2160) averaged for each respective cluster site. Sediment trap 04-03 *Deep* is excluded due to potentially high influx of resuspended material.

One factor that might mask a correlation of POC fluxes and NPP rates is the time lag between surface production and the arrival of particulate organic matter to the ocean interior. As stated above, CaCO_3 is the relevant and effective ballast material that enhances the sinking speed of organic components. Stokes' law was used by several authors (e.g., *Lal and Lerman*, 1975; *McCave*, 1975; *Engel et al.*, 2009; *Miklasz and Denny*, 2010; *Rixen et al.*, 2019b) to calculate sinking speeds of particulate matter. Taking into account previous estimates on particle size, fluid viscosity (η), and particle porosity (*Rixen et al.*, 2019b) and considering the particle composition and density of particulate matter in the IOSG (our results), we estimate sinking speeds between $153 \pm 65 \text{ m day}^{-1}$ and $179 \pm 33 \text{ m day}^{-1}$ (for the detailed calculation see Appendix A5). This is lower than estimates for the North Indian Ocean ($224 \pm 33 \text{ m day}^{-1}$ or $230 \pm 72 \text{ m day}^{-1}$), where high LM contents ($\sim 14\text{--}60 \text{ wt.}\%$) accelerate the sinking speed (*Berelson*, 2001; *Rixen et al.*, 2019b). A sinking speed of $\sim 153\text{--}179 \text{ m day}^{-1}$ causes a time lag of $\sim 15\text{--}23$ days

(2600–3500 m) between surface production and arrival at trap depth and is roughly equal to one cup opening interval (see Appendix A2, Table A2.1). Thus, this time shift is most likely not the driving factor leading to the incoherence between POC fluxes and NPP.

Other factors that impede the transmission of seasonal primary production signals and act on the particle transfer to the deep sea are organic matter degradation, variations of the OML, and physical mixing due to enhanced wind stress and eddy diffusion processes (Siegel *et al.*, 1990; Asper *et al.*, 1992; Delman *et al.*, 2018; Rixen *et al.*, 2019a). These mechanisms likely smooth the primary production signals, especially in regions of low particulate matter production and low seasonal variability, and lead to a constant rain of particulate matter to the deep ocean (Michaels *et al.*, 1994). Figure 3.11 compares POC fluxes with seasonal data on SST, NPP, OMLD, and sea surface wind speed. The SST is highest during austral summer, promotes a strong stratification and, thus, impedes primary production, leading to an anti-correlation with NPP (Figure 3.11a, b). Furthermore, high temperatures in the upper ocean layer tend to enhance zooplankton/bacteria respiration rates, resulting in higher degradation rates of POC. These two effects should promote a positive correlation between NPP and POC fluxes at low SST. However, this is not observed in the IOSG, most likely due to the strong organic matter degradation in low production areas (Francois *et al.*, 2002; Sarmiento and Gruber, 2006; Rixen *et al.*, 2019a). Furthermore, the OML and nutricline in the IOSG have considerably different depth intervals in the gyre region (Baer *et al.*, 2019), and a deeper OML (max. 60 m) will not trigger a significant nutrient input from subsurface waters and does not favor NPP. Instead, a deep OML will lead to enhanced organic matter degradation and reduce POC fluxes below the euphotic zone. Thus, variations in NPP and OMLD might have counteracting effects on the POC export flux in the IOSG, thereby explaining the opposite trends between NPP and POC fluxes in traps 04-01, 05-01, and 07-01. On the other hand, the depth range of the OML increases is only between ~30 and ~60 m, and it is questionable if this is significant for POC degradation. Nevertheless, the decrease in POC flux is exponential in the upper water column (Martin curve), and small variations in the OML might have crucial impacts on the final POC export.

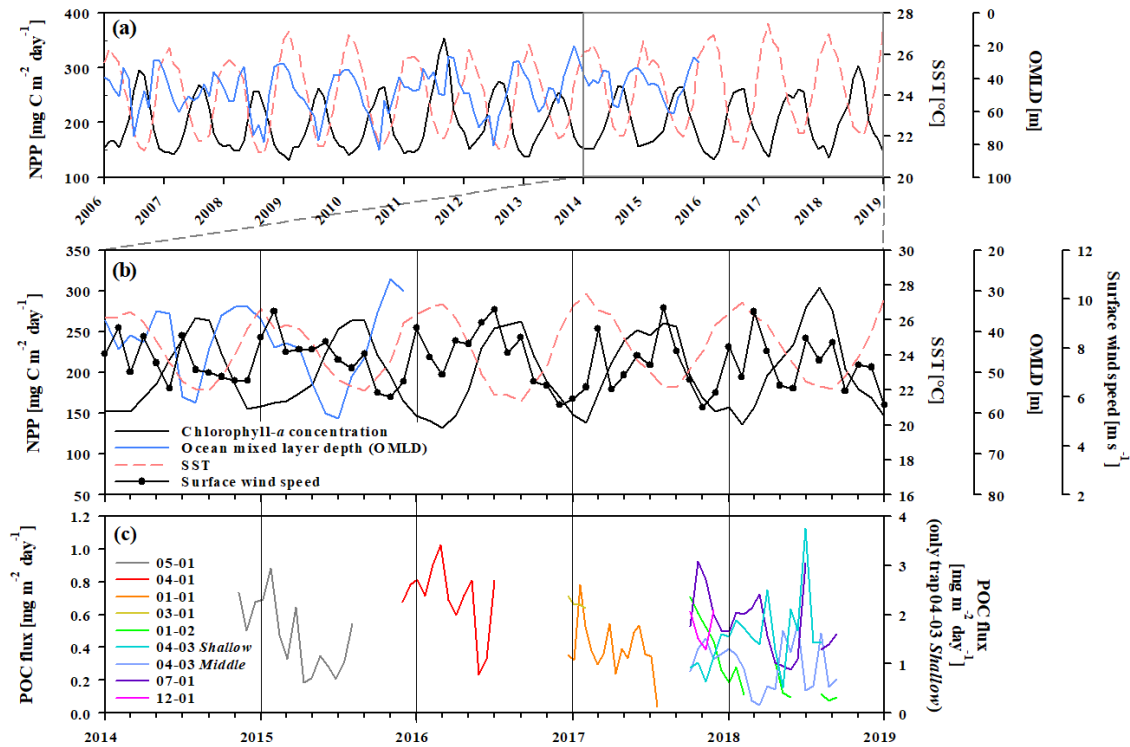


Figure 3.11. Temporal variations of the net primary production (NPP in $\text{mg C m}^{-2} \text{ day}^{-1}$, black solid line; averaged over 20° – 29°S ; 67° – 75° , see figure caption of Figure 3.8) sea surface temperature (SST in $^{\circ}\text{C}$; red dashed line; <https://oceancolor.gsfc.nasa.gov/citations/>) and ocean mixed layer depth (OMLD; solid blue line; <https://10.5067/BHCFDIICIU5>) for the time interval 2006–2019 (a) and 2014–2019 (b). Panel b also depicts fluctuations in surface wind speeds (black solid-dotted line; <https://10.5067/0JRLVL8YV2Y4>). Data are area-averaged over 20° – 29°S and 67° – 75°E . Data on OMLD was available only until December 2015. Panel c depicts the temporal variation in POC fluxes of sediment traps deployed during 2014 and 2019 in the IOSG.

Additionally, physical forcing, such as changes in surface wind velocities, might influence the export of POC (*Delman et al., 2018; Rixen et al., 2019a*). Enhanced mixing in the upper ocean waters leads to increases in surface nutrient supply and might trigger regional POC export production. Elevated wind speeds correspond to elevated POC fluxes in traps 05-01, 04-01, and 07-01 during February, December–July, and February–May, respectively (Figure 3.11b, c). However, until now, little is known about the link between surface wind speed and particulate matter fluxes in the IOSG. Even less is known about the overall seasonal fluctuations in the gyre strength and the volume transport of in- and outflows (*McMonigal et al., 2018*) and about variations in the dynamics of cyclonic eddies in the IOSG and their effects on biogeochemical processes and particulate matter fluxes. Enhanced cyclonic eddy-activities are observed between Australia and Madagascar in a wide band from $\sim 20^{\circ}\text{S}$ to 30°S , propagating westwards

across our study area (*Delman et al., 2018*) and might well influence particulate matter export. In the subtropical western North Pacific Ocean, cyclonic eddies are assumed to be an important mechanism for the nutrient supply to the euphotic zone and, thus, might lead to enhanced particulate matter export production (*Honda et al., 2018*).

3.4.4 First estimates on the POC export efficiency

Subtropical gyres generally have a very low POC export efficiency in addition to low productivity and particulate matter export fluxes (*Sarmiento and Gruber, 2006; Henson et al., 2019*). The concept of the export efficiency is based on *Eppley and Peterson (1979)* and has been developed further by various authors (*Murray et al., 1989; Laws et al., 2000; Ducklow et al., 2001; Francois et al., 2002; Sarmiento and Gruber, 2006; Henson et al., 2019*). The export efficiency (ε) is defined as the POC export flux divided by the NPP and expressed by the following formula:

$$\varepsilon = POC_{export\ flux}/NPP \quad (3.2)$$

Several studies have described the general patterns of export efficiency in the global oceans (e.g., *Francois et al., 2002; Henson et al., 2019*). Subtropical gyres are considered as “low primary production and low export efficiency regions” (LP-LE-region; *Sarmiento and Gruber, 2006; Henson et al., 2019*), where the food web in the OML favors the effective recycling of organic matter and leads to low particulate matter export fluxes. Because we did not measure organic matter degradation rates directly, we can only assume that this holds true for the IOSG, leading to the observed low and constant rain of particulate organic matter to the deep ocean with little seasonality. Taking into account our area-averaged POC export flux of $7.4 \pm 2.4 \text{ mg m}^{-2} \text{ day}^{-1}$ ($0.23 \pm 0.07 \text{ mol C m}^{-2} \text{ year}^{-1}$) at 130 m (normalized by using the Martin equation Eq. 3.1) and NPP rates of $224 \pm 19 \text{ mg C m}^{-2} \text{ day}^{-1}$ ($\sim 7 \text{ mol C m}^{-2} \text{ year}^{-1}$; annual mean, area-averaged over 20° – 29° S; 67° – 75° E based on the standard VGPM algorithm (*Behrenfeld and Falkowski, 1997*, see figure caption of Figure 3.8), we calculate an export efficiency of $\varepsilon = 0.03 \pm 0.01$. This is even lower than the estimate of *Sarmiento and Gruber (2006)* with $\varepsilon \approx 0.05$ for the IOSG, calculated by the chlorophyll and temperature-based empirical algorithm of *Dunne et al. (2005)*. Therefore, our data in the IOSG reveal one of the lowest export efficiencies reported in the global ocean and is even lower than previously assumed in model estimations.

3.5 Summary and conclusion

Sediment trap derived total mass fluxes ($\sim 9.8 \pm 3.7 \text{ mg m}^{-2} \text{ day}^{-1}$) and particulate organic carbon (POC) fluxes ($0.49 \pm 0.15 \text{ mg m}^{-2} \text{ day}^{-1}$) measured at 500–600 m.a.b. (2600–3500 m) in the Indian Ocean subtropical gyre (IOSG) are among the lowest fluxes globally. This reflects the overall low primary production in the spatially homogeneous, strongly stratified, and nutrient-depleted upper ocean waters. Although sea surface temperatures (SSTs) and net primary production (NPP) rates vary in space and time in the IOSG, the interaction of several factors, such as organic matter degradation, variations in the ocean mixed layer depth (OMLD), and physical mixing (surface wind stress, cyclonic eddies) smooth seasonal fluctuations in the POC export below the euphotic zone. Consequently, POC flux data reveal a locally and temporally constant rain of sinking particulate matter below the euphotic zone that is transported to the deep sea with CaCO_3 as the relevant ballasting material. The fraction of the POC produced in the upper ocean that reach the deep ocean is extremely low, and the first quantitative estimate of the export efficiency is $\varepsilon = 0.03 \pm 0.01$ for the IOSG, even lower than previously assumed from model estimations. Assuming that all subtropical gyres are characterized by similarly low export efficiencies (as has been postulated for the oligotrophic North Atlantic; *Henson et al.*, 2019), and considering that these enormous ocean areas are likely to expand further under climate warming, this might weaken the organic carbon pump and reduce the transfer of organic carbon to the deep oceans. As yet, the decrease in baseline fluxes and extent of the areas affected by gyre expansion are unknown, and possible adaptations in food webs, biological community structure, or potential adaptations of global or regional circulation patterns to a warmer climate are still under debate. Thus, the magnitude and even the direction of impacts of changing climate on the biogeochemistry of oligotrophic ocean areas, including its biological carbon pump, are uncertain (*Passow and Carlson*, 2012; *Laufkötter et al.*, 2017; *Laufkötter and Gruber*, 2018). Furthermore, other regions (e.g., the Southern Ocean, the eastern upwelling systems) might compensate changes in organic carbon export fluxes in the subtropical gyres under global warming conditions (*Laufkötter and Gruber*, 2018). Clearly, more interdisciplinary research is needed to understand how these extensive oligotrophic regions will change under global warming conditions and how they contribute to global carbon budgets. To make better and more reliable assumptions for the IOSG, we need more observational data on POC fluxes and direct measurements of NPP. Furthermore, the impact of

variations in the gyre strength and of eddy diffusion processes on the nutrient supply and NPP, resulting in higher particulate matter fluxes, should be investigated in detail.

Chapter 4 – Cumulative Part III

Water masses and nutrient cycling in the subtropical South Indian Ocean

(submitted in 2020 as book chapter 19 in “Marine Metal Exploration: The INDEX Project – Prospecting the Seafloor for Polymetallic Sulphides” to Springer Nature)

Natalie C. Harms¹, Niko Lahajnar¹, Birgit Gaye¹, and Kay-Christian Emeis^{1,2}

¹Institute of Geology, Universität Hamburg, Hamburg, 20146, Germany.

²Helmholtz-Zentrum Geesthacht (HZG), Institute for Coastal Research, Geesthacht, 21502, Germany.

Abstract. The South Indian Ocean, one of the least explored ocean regions, is dominated by the Indian Ocean subtropical gyre (IOSG), one of five extensive oligotrophic areas in the world’s ocean. During INDEX expeditions between 2015 and 2019, we collected vertical profiles of data on water properties and took water samples in an area from ~3°S to ~28°S. Our detailed water mass analyses in the South Indian Ocean demonstrate the convergence and mixing of water masses of Antarctic and Subantarctic origin with water masses from the North Indian Ocean. This detailed characterization of water masses and their provenance helps to understand nitrogen sources and cycling processes utilizing nutrient concentrations and dual isotope signals of nitrate. In addition to injection of preformed nutrients from the Subantarctic and the Arabian Sea, N₂ fixation evidently accounts for a significant proportion of primary production. Based on stable isotopes of nitrate, we calculated that ~32–34 % of the nitrified nitrate is contributed by dinitrogen (N₂) fixation in surface waters of the IOSG (~20°–24°S).

4.1 Introduction and regional setting

Measurements of water mass properties and collection of water samples during INDEX expeditions between 2015 and 2019 were conducted at several stations from $\sim 3^\circ$ to $\sim 28^\circ\text{S}$ (Figure 4.1) in order to understand major water mass pathways and key processes of the nitrogen (N) cycle in the South Indian Ocean (SIO). The SIO is a sparsely investigated and underrepresented ocean region, especially in terms of biogeochemical element cycling. To study the N cycle and to shed light on the different N cycle processes, we extend our previous work, published in *Harms et al. (2019)*, with new data from INDEX expeditions in 2018 and 2019 (only data of vertical profiles on physical water column properties). First, we characterize major water masses in the SIO and their provenance, and in addition, we describe nitrate (NO_3^-) and phosphate (PO_4^{3-}) concentrations and the isotopic signature of nitrate.

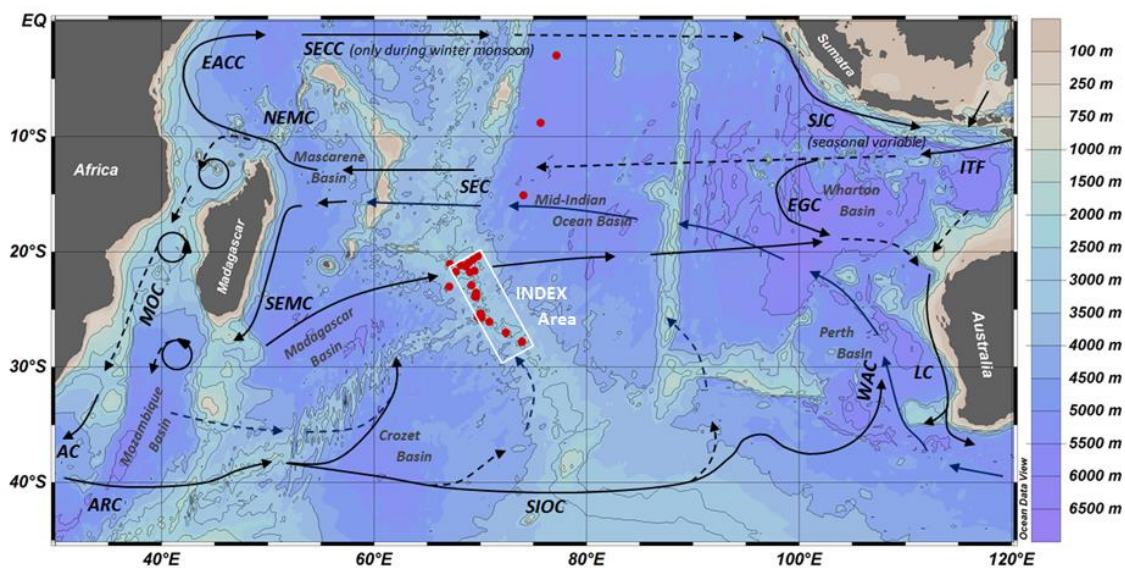


Figure 4.1. Map of the South Indian Ocean with schematic representation of deep-sea basins and surface/subsurface currents according to *Stramma (1992)*, *Stramma and Lutjeharms (1997)*, *Schott and McCreary (2001)*, and *Schott et al. (2009)*. Red dots indicate water sampling stations during INDEX expeditions between 2015 and 2019. The white rectangle marks the INDEX license area. Current branches are Agulhas Current (AC), Agulhas Return Current (ARG), East African Coastal Current (EACC), East Gyral Current (EGC), Leeuwin Current (LC), Mozambique Current (MOC), Northeast Madagascar Current (NEMC), South Equatorial Current (SEC), South Equatorial Countercurrent (SECC), Southeast Madagascar Current (SEMS), South Indian Ocean Current (SIOC), South Java Current (SJC), West Australian Current (WAC), ITF indicates the Indonesian Throughflow.

The INDEX license area is located in the Indian Ocean subtropical gyre (IOSG) and is one of the major five subtropical gyres in the world's ocean. In contrast to the Atlantic and Pacific Oceans, the Indian Ocean is land-locked to the north and thus developed only one subtropical gyre south of the equator. The IOSG is an anticyclonic and counter-clockwise gyre that ranges approximately from 10°S to 30°S (*Williams and Follows, 2003; Sarmiento and Gruber, 2006; Baer et al., 2019*). The circulation of the IOSG is bordered by branches of several current systems. The northern boundary of the IOSG is the South Equatorial Current (SEC) and separates the IOSG from the southern equatorial Indian Ocean (*Duing, 1970; Pickard and Emery, 1982; Woodberry et al., 1989*). The SEC is a broad westward current roughly from 8°S to 20°S (*Wyrтки, 1971; Godfrey and Golding, 1981; Pickard and Emery, 1982*) with a maximum transport at 12°–15°S (*Woodberry, 1989*). The SEC is in part fed by a water mass from the Pacific Ocean (Indonesian Throughflow – ITF) at about 10°–25°S and injects low salinity water into the SIO (e.g., *Wyrтки, 1971; Godfrey and Golding, 1981; Woodberry, 1989; You and Tomczak, 1993*). The southern boundary of the IOSG is marked by the South Indian Ocean Current (SIOC) and is located at the Subtropical Front (STF) at about 40°S (*Deacon, 1933; Stramma, 1992*). Together with the Agulhas Current (AC), the South East Madagascar Current (SEMC), and the West Australian Current (WAC), the SEC and the SIOC limit the IOSG and restrict its counter-clockwise rotation. The gyre circulation results in a center-directed (convergent) horizontal Ekman volume flux and leads to an intense downwelling of water in the gyre center. Consequences are a deepening of thermo-, pycnocline and nutriclines, which shoal upwards the gyre margins (*McClain et al., 2004; Figure 4.2a–d*).

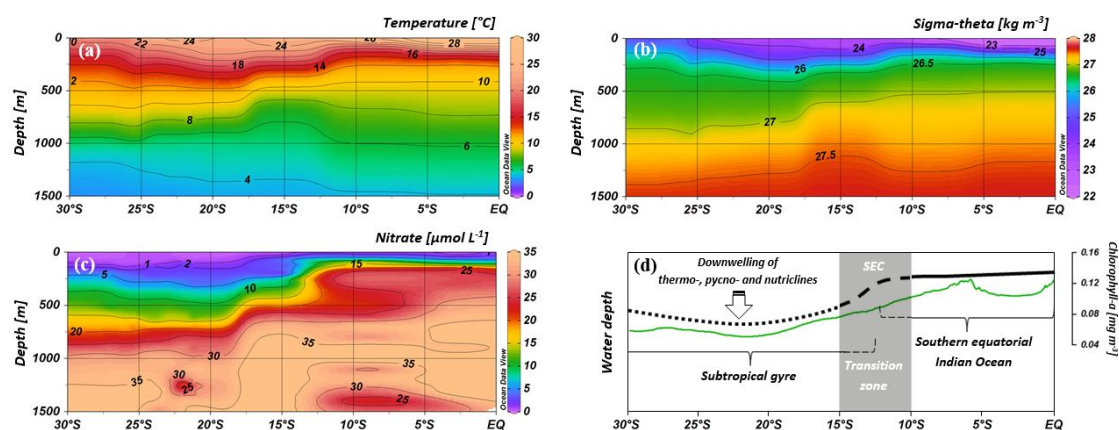


Figure 4.2. Latitudinal cross sections from 30°S towards the equator along sampling stations (Figure 4.1) for temperature (a), potential density (sigma-theta in kg m^{-3}) (b), and nitrate concentrations (c). The bottom panel presents the deepening of isoclines in the IOSG and their upward lift towards the southern equatorial Indian Ocean accompanied by chlorophyll-*a* concentration (d). Water column and nutrient data is available at the PANGAEA DataBase at <https://doi.pangaea.de/10.1594/PANGAEA.897503> and <https://doi.pangaea.de/10.1594/PANGAEA.897504> (see *Harms et al.*, 2019).

As in all subtropical gyres, surface waters are strongly depleted in nutrients and the IOSG is an extensive oligotrophic (low nutrient) region with overall low primary production rates indicated by low chlorophyll-*a* concentrations (Figure 4.2d). The five oligotrophic gyres account for ~75 % of the global ocean's surface and they contribute significantly to global N cycle budgets despite their low concentrations of reactive N and subdued biological productivity (*McClain et al.*, 2004). Future global warming is assumed to expand these low productivity areas globally and to strengthen stratification in low-latitude oceans, which will lead to a further decrease of the net primary production possibly accompanied by changes in picoplankton community structure, possibly favoring more extensive dinitrogen (N_2) fixation (*Behrenfeld et al.*, 2006; *Signorini et al.*, 2015). Our investigations on water masses, nutrient distributions, and stable isotopes of nitrate in the IOSG contribute a nowcast for this understudied ocean region and for subtropical gyres in general. It is a starting point to track the course of N cycle processes and budgets in a changing climate over the coming years under the INDEX project.

4.2 The use of nutrients and stable isotopes of nitrate

Water samples were taken for biogeochemical analyses of nutrients and stable isotopes of nitrate (N and O) during INDEX 2015 and 2018 (see overview and data in Table A1.1–Table A1.5 in the Appendix A1). Sample preparation and the analytical methods for determining NO_3^- and PO_4^{3-} concentrations, as well as the stable isotope ratios relative to a reference standard ($\delta^{15}\text{N}$ and $\delta^{18}\text{O}$) are given in detail in *Harms et al.* (2019). Nutrient concentrations and nitrate isotope ratios are useful indicators for N cycle processes and help to distinguish between different N sources and sinks.

The dominant source and sink of reactive N in the ocean are atmospheric N_2 fixation and heterotrophic denitrification, respectively (*Deutsch et al.*, 2001). N_2 fixation by cyanobacteria i.e., diazotrophs such as *Trichodesmium*, is observed over much of the tropical and oligotrophic subtropical oceans (*Karl et al.*, 1995; *Michaels et al.*, 1996; *Capone et al.*, 1997; *Emerson et al.*, 2001) and compensates for the loss of reactive N during heterotrophic denitrification if the ocean's marine N cycle is in a steady state (*Deutsch et al.*, 2001). The inputs of N through N_2 fixation are detached from inputs of phosphorus (P), which have their major source on land, leading to a decoupling between the NO_3^- and PO_4^{3-} pools. Deviations in the NO_3^- to PO_4^{3-} relationship from the Redfield stoichiometry (16:1; *Redfield*, 1934, 1963) are used to study rates of both N_2 fixation and denitrification (*Gruber and Sarmiento*, 1997; *Sigman et al.*, 2005). For a better quantification, the tracer N^* was established (see *Gruber and Sarmiento*, 1997; *Deutsch et al.*, 2001) and is used as an indicator for excesses or deficits in NO_3^- relative to the global $\text{NO}_3^-/\text{PO}_4^{3-}$ ratio. N^* is expressed by the formula:

$$\text{N}^* = [\text{NO}_3^-] - 16 \times [\text{PO}_4^{3-}] + 2.9 \mu\text{mol L}^{-1} \quad (4.1)$$

However, the use of N^* has limitations. First, the deviation from the Redfield stoichiometry may not always be a result of N inputs or outputs (N_2 fixation and denitrification), but may also reflect variations of uptake and remineralisation processes (*Sigman et al.*, 2005). Second, input and losses partially overprint each other, when they occur simultaneously in the same water body. Stable isotopes of nitrate are used to overcome the weakness associated with the N^* approach and distinguish between sources and sinks of fixed N to study transfer processes in the N cycle (e.g., N assimilation, denitrification, nitrification, N_2 fixation), also

when they occur simultaneously. Isotope ratios are reported in per mil (‰) using the δ -notation:

$$\delta^{15}\text{N} = \left[\left(\frac{{}^{15}\text{N}/{}^{14}\text{N}_{\text{sample}}}{{}^{15}\text{N}/{}^{14}\text{N}_{\text{atm.N}_2}} \right) - 1 \right] \times 1000 \quad (4.2)$$

$$\delta^{18}\text{O} = \left[\left(\frac{{}^{18}\text{O}/{}^{16}\text{O}_{\text{sample}}}{{}^{18}\text{O}/{}^{16}\text{O}_{\text{VSMOW}}} \right) - 1 \right] \times 1000. \quad (4.3)$$

The “ ${}^{15}\text{N}/{}^{14}\text{N}_{\text{atm.N}_2}$ ” and “ ${}^{18}\text{O}/{}^{16}\text{O}_{\text{VSMOW}}$ ” serve as reference for N and O isotope ratios, respectively. During consumption processes of nitrate (e.g., N assimilation and denitrification), lighter isotopes are preferred, leaving the substrate enriched in ${}^{15}\text{N}$ and ${}^{18}\text{O}$ according to intrinsic isotope effects. Several culture experiments indicate that $\delta^{15}\text{N}$ and $\delta^{18}\text{O}$ of the residual nitrate pool rise equally as consumption proceeds. Consequently, the O-to-N isotope effect (${}^{18}\epsilon: {}^{15}\epsilon$) is close to 1 (Sigman *et al.*, 2003; Granger *et al.*, 2004; Sigman *et al.*, 2005; Rafter *et al.*, 2013).

Nitrate consumption processes thus shift N and O isotope compositions in a nitrate pool in parallel, but nitrate production processes (N_2 fixation and nitrification) have very different effects and decouple N and O isotope compositions (Sigman *et al.*, 2005; Rafter *et al.*, 2013). In oxygenated environments, almost all of the ammonium generated from organic N is oxidized to nitrate. Thus, the isotope effect is negligible and the $\delta^{15}\text{N}\text{-NO}_3^-$ depends solely on the biomass being remineralized (Sigman *et al.*, 2005; Rafter *et al.*, 2013). In contrast, the $\delta^{18}\text{O}$ of newly nitrified nitrate is independent of the isotopic composition of the mineralised organic matter. Significant addition to a nitrate pool by nitrification are marked by deviating values of $\delta^{15}\text{N}$ and $\delta^{18}\text{O}$. The tracer $\Delta(15-18)$ calculated as

$$\Delta(15 - 18) = \delta^{15}\text{N} - \delta^{18}\text{O} \quad (4.4)$$

keeps track of the difference between N and O isotope ratios in the nitrate pool (Rafter *et al.*, 2013) and quantifies of nitrate assimilation and regeneration processes in marine environments (Casciotti *et al.*, 2002; Sigman *et al.*, 2005; Wankel *et al.*, 2007; Sigman *et al.*, 2009; Casciotti *et al.*, 2010; DiFiore *et al.*, 2010).

4.3 Water mass distribution in the South Indian Ocean

Water masses in the SIO are diverse and have specific physical properties (potential density, temperature, salinity, oxygen concentration). Temperature-Salinity (T-S) diagrams, accompanied by an overlay of potential density surfaces

(sigma-theta in kg m^{-3}), are typically used by oceanographers to identify water masses in a region of complex water mass interfingering. The study area can be subdivided into four latitudinal sections that represent different oceanic regimes: the southern limb of the IOSG (25.66° – 27.80°S), the central IOSG (20.36° – 25.42°S), the northern boundary of the IOSG (15.08°S), and the southern equatorial Indian Ocean (2.98° – 8.81°S). For each latitudinal section, we plot individual diagrams for the variables temperature (Figure 4.3a–d), salinity (Figure 4.3e–h), and oxygen concentrations (Figure 4.3i–l) relative to their sigma-theta surfaces, to identify the occurrence of different water masses and their flow paths along the latitudinal transect. The T-S diagram in Figure 4.4a summarises all water masses in the INDEX area.

Overall, water masses in the SIO can be subdivided into surface water masses (covered by a thin surface layer that is mainly affected by seasonal variations and weather conditions), thermocline water masses, intermediate water masses, and deep water masses. Surface waters in subtropical regions of the southern hemisphere are characterized by strong evaporation rates that exceed precipitation (*Schott and McCreary, 2001*) and are often called “Subtropical Surface Waters” (SSW; see *Muromtsev, 1959; Wyrski, 1973; Schott and McCreary, 2001*). The SSW of the IOSG is formed at latitudes between 25° – 35°S (*Baumgartner and Reichel, 1975*) and is marked by highest salinities (Figure 4.3e–g, Figure 4.4b). The SSW follows the typical gyral depression of pycnoclines and is detectable as far as $\sim 15^{\circ}\text{S}$ (*Harms et al., 2019*). Less saline water is found above the SSW at the transition from the central IOSG and its northern end and can be traced back to the “Indonesian Upper Water” (IUW) that is injected via the ITF from the Pacific Ocean into the gyre region (*Emery, 2001*). Moderate vertical changes in salinity are found in surface waters of the southern equatorial Indian Ocean (Figure 4.3d, h, Figure 4.4b, c) related to the “Indian Equatorial Water” (IEW). It is a mixture of subsurface water masses from the SIO (SSW) with subsurface and thermocline waters from the Arabian Sea (*Sharma, 1976; Warren, 1981; Quadfasel and Schott, 1982; You and Tomczak, 1993; Schott and McCreary, 2001*). Thermocline waters of the SIO are ventilated south of the IOSG at 32°S by mode waters observed between surface waters (seasonally mixed and approximately isohaline) and intermediate waters (salinity minimum; *McDonagh et al., 2005*). These mode waters were named “Subantarctic Mode Water” (SAMW) by *McCartney (1977, 1982)* and formed at latitudes between 40°S and 50°S . The SAMW injects oxygen-saturated waters into all subtropical gyres of the southern hemisphere (*McCartney, 1977*), as well as into the thermocline of the IOSG, where temperature

and salinity vary monotonically with depth (Figure 4.3a–c, Figure 4.3e, f, Figure 4.4b, c). On its transition to the north, oxygen concentrations rapidly decrease due to respiration and the absence of effective ventilation in the North Indian Ocean (Figure 4.3i–k; *Harms et al.*, 2019).

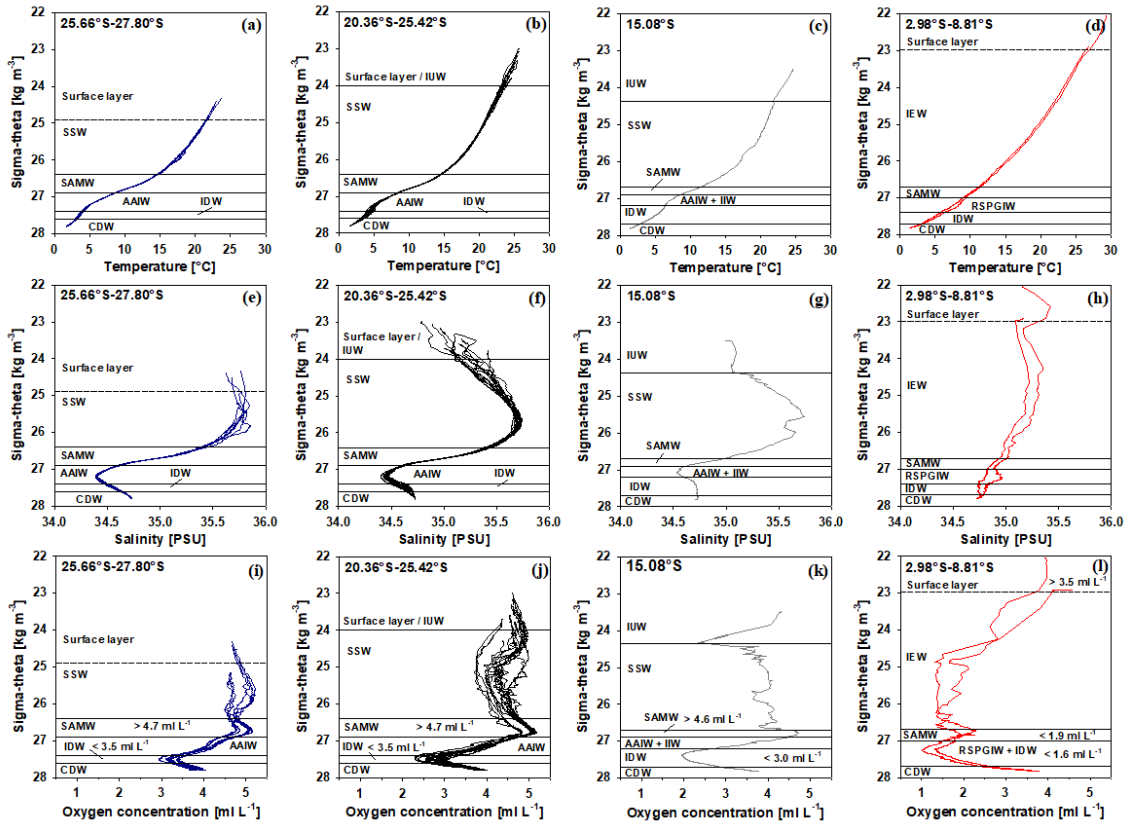


Figure 4.3. Water mass properties from CTD measurements during the INDEX program between 2015 and 2019 presented as temperature vs. sigma-theta (a–d), salinity vs. sigma-theta (e–h), and as oxygen vs. sigma-theta diagrams (i–l) for the different oceanic regimes: the southern limb of the IOSG (25.66°–27.80°S), the central IOSG (20.36°–25.42°S), the northern boundary of the IOSG (15.08°S), and the southern equatorial Indian Ocean (2.98°–8.81°S). Figure is modified from *Harms et al.* (2019). Water masses are Indonesian Upper Water (IUW), Indian Equatorial Water (IEW), Subtropical Surface Water (SSW), Subantarctic Mode Water (SAMW), Red Sea-Persian Gulf Intermediate Water (RSPGIW), Indonesian Intermediate Water (IIW), Antarctic Intermediate Water (AAIW), Indian Deep Water (IDW), and Circumpolar Deep Water (CDW).

At intermediate water depths, a distinct salinity minimum (Figure 4.3e, f, Figure 4.4b, c) is associated with the “Antarctic Intermediate Water” (AAIW) mentioned by several authors (*Deacon, 1933; Wyrcki, 1973; Warren, 1981; Fine, 1993; Toole and Warren, 1993; You, 1998; Bindoff and McDougall, 2000; Schott and McCreary, 2001*). The AAIW originates in surface waters of the Antarctic Ocean, is then transported eastwards by the Antarctic Circumpolar Current (ACC) and penetrates into of all three oceans. In the SIO, the AAIW flows along a core density of 27.2 kg m^{-3} and extends towards the equator (*Wüst, 1935; Sverdrup et al., 1942; McCartney, 1977; Reid, 1986, 1989; Piola and Gordon, 1989; Fine, 1993; Talley, 1996*). At $\sim 15^\circ\text{S}$ a slightly divergent core density of the salinity minimum compared to the AAIW implies an additional inflow of less saline water. It is injected from the ITF into intermediate waters (*Harms et al., 2019*) and is called the “Indonesian Intermediate Water” (IIW; *Emery and Meincke, 1986; Emery, 2001*), which flows westwards between 10°S and 15°S (*Wyrcki, 1971; You and Tomczak, 1993; Schott and McCreary, 2001*).

Higher saline waters in thermocline waters of the southern equatorial Indian Ocean mark the inflow of saline water from the Arabian Sea, mainly from the Red Sea and Persian Gulf outflow. This water mass is mentioned as “Red Sea-Persian Gulf Intermediate Water” (RSPGIW; *Warren, 1981; Emery and Meincke, 1986*) and transports oxygen-depleted water from the oxygen minimum zone in the Arabian Sea (see section 4.4.1.) towards the equator and beyond $\sim 10^\circ\text{S}$ (*You, 1998*). A further transport of this oxygen-depleted water into the central and southern IOSG is triggered by the “Indian Deep Water” (IDW; Figure 4.3i, j). It originates in the northern basin of Arabian Sea comprising the “Circumpolar Deep Water” (CDW) and the overlying RSPGIW (*Talley, 2013*) and flows southwards just below the density level of the AAIW. The CDW is a mixture of the “North Atlantic Deep Water” (NADW) and the “Antarctic Bottom Water” (AABW) and enters the Indian Ocean passing the Agulhas Basin, the Crozet Basin, and the southern Australian Basin (*Toole and Warren, 1993; Emery, 2001*).

To conclude, data from INDEX expeditions 2015 to 2019 across the INDEX area permit a detailed analyses of the water masses in the SIO from $\sim 3^\circ\text{S}$ to 28°S . We illustrate the provenance of water masses of Antarctic and Subantarctic origin that converge and mix with water masses from the southern equatorial Indian Ocean and the Arabian Sea (*Harms et al., 2019*). In addition, Pacific waters from the ITF are injected into surface and intermediate depths of the SIO. A complete profile of the water mass distribution in the SIO is shown in Figure 4.4c that is

based on our previous work (*Harms et al., 2019*), amended with data from the INDEX expeditions in 2018 and 2019.

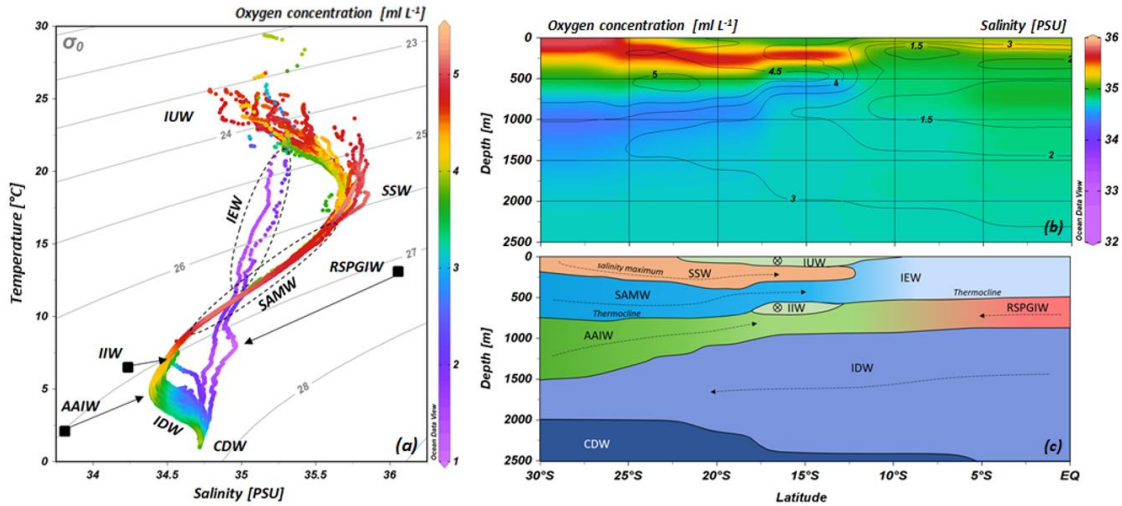


Figure 4.4. T-S diagram of vertical profiles (source properties of water masses based on *Emery (2001)*) accompanied by oxygen concentration in mL L^{-1} (color coding) (a), salinity distribution as latitudinal section from south to north with an overlay of oxygen concentrations (contour lines) based on data collected during the INDEX expeditions between 2015 and 2019 (b). Panel c presents an overview of the water mass distribution in the South Indian Ocean from 30°S towards the equator (reproduced from *Harms et al., 2019*); for water mass abbreviations see Figure 4.3.

4.4 Nutrient distribution and N cycle processes in the IOSG

4.4.1 Lateral transfer of nutrients and nitrate isotope signals across the gyre boundaries

The distinct water masses entering the study area from the Southern Ocean and from the North Indian Ocean have characteristic nutrient concentrations and isotope fingerprints of reactive N. Based on the water mass distribution, we are able to reconstruct the main factors that lead to the observed nutrient distribution and to the detected fluctuations in the stable isotopes of nitrate. Therefore, the NO_3^- and PO_4^{3-} , the stable isotope ratios $\delta^{15}\text{N}$ and $\delta^{18}\text{O}$, the parameters $\text{NO}_3^-/\text{PO}_4^{3-}$, N^* , and $\Delta(15-18)$ are presented in Figure 4.5 as latitudinal sections with an overlay of the water mass distribution from Figure 4.4c.

The nutrient distribution in the IOSG predominantly reflects by the typical architecture of subtropical gyres expressed in sloping nutriclines towards the center of thick layer (~300 m) of nutrient-depleted surface waters made up by the IUW and the SSW (Harms *et al.*, 2019; Figure 4.5a, b). Low nutrient concentrations are also found in the underlying SAMW. Consequently, the supply of nutrients to the euphotic layer by vertical mixing is reduced or absent in the gyre (Williams and Follows, 1998) and the external input of nutrients via lateral transfer across the gyre boundaries is a major nutrient source.

4.4.1.1 Influence from the North Indian Ocean on the nutrient distribution and nitrate isotopic composition of the IOSG

Towards the northern limb of the IOSG, the isoclines shoal upward and increase nitrate and phosphate concentrations in the upper 500 m. This shoaling marks the transition from subsurface waters of the IOSG to the IEW of the southern equatorial Indian Ocean and restricts the northward flow of the IUW, SSW and the SAMW (Figure 4.5a, b). Surface waters in the gyre region have low $\text{NO}_3^-/\text{PO}_4^{3-}$ ratios because nitrate commonly becomes depleted prior to phosphate in oligotrophic regions (Sarmiento and Gruber, 2006; Deutsch *et al.*, 2007; Harms *et al.*, 2019). Furthermore, the $\text{NO}_3^-/\text{PO}_4^{3-}$ ratios track the outcropping nutriclines from low values within the SSW towards high ratios at the northern gyre boundary and further north within the IEW (Figure 4.5c).

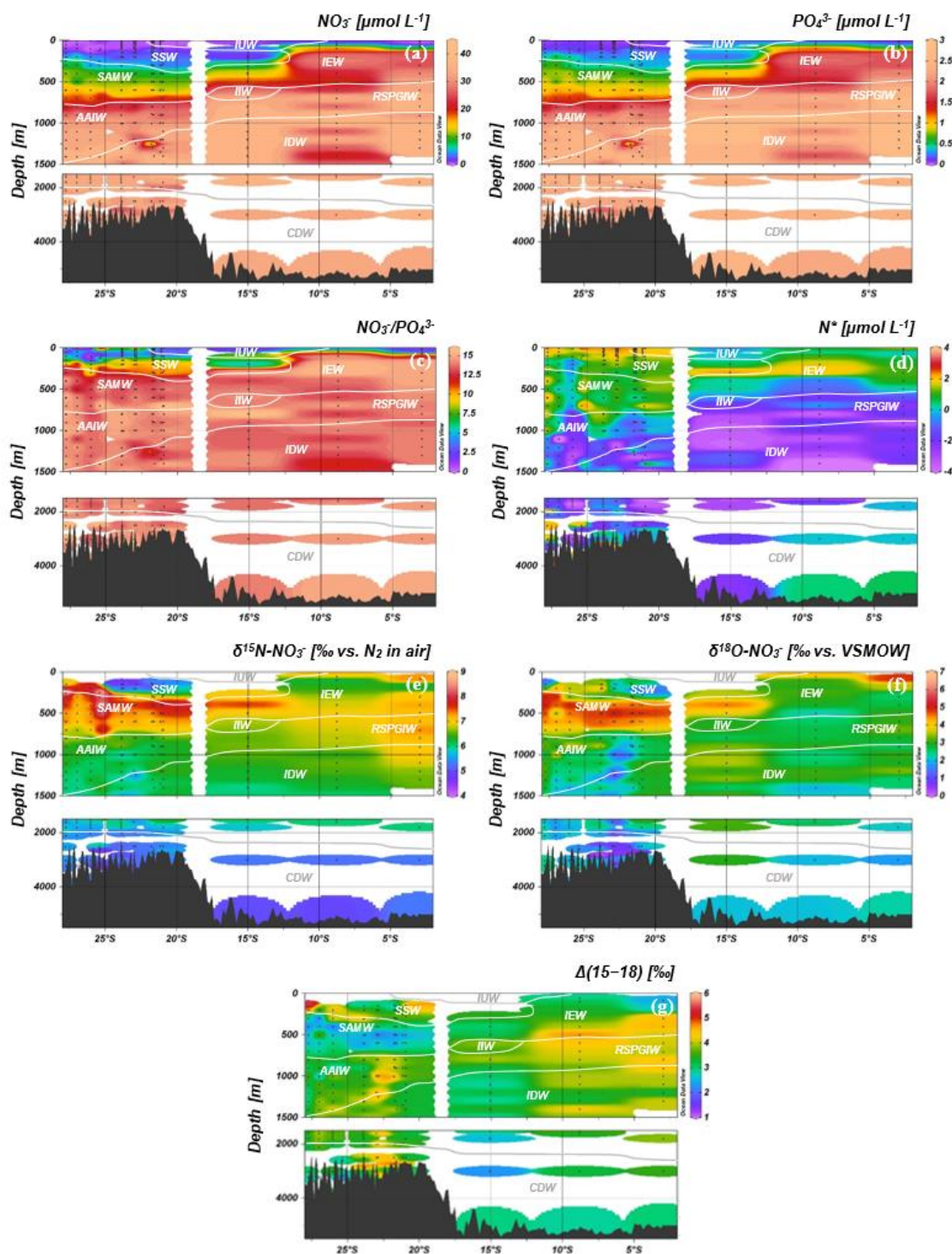


Figure 4.5. Latitudinal profiles from south to north along the INDEX licence area with an overlay of the water mass distribution (white lines; see Figure 4.4c) in the South Indian Ocean for nitrate (a), phosphate (b), $\text{NO}_3/\text{PO}_4^{3-}$ ratio (c), N^* (d), stable isotopes $\delta^{15}\text{N-NO}_3^-$ (e) and $\delta^{18}\text{O-NO}_3^-$ (f), and $\Delta(15-18)$ (difference between $\delta^{15}\text{N-NO}_3^-$ and $\delta^{18}\text{O-NO}_3^-$) (g). Data is available at the PANGAEA DataBase at <https://doi.pangaea.de/10.1594/PANGAEA.897503> and <https://doi.pangaea.de/10.1594/PANGAEA.897504> (see Harms *et al.*, 2019). For water mass abbreviations see Figure 4.3.

An average $\text{NO}_3^-/\text{PO}_4^{3-}$ ratio of 14.7 is calculated for the entire water column (Figure 4.6a). This value is lower than the global ocean mean of 16 (Redfield, 1934, 1963) and marks the mixing of water masses of South and North Indian Ocean origin and is one indication that the Arabian Sea influences the nutrient distribution in the SIO. Typical $\text{NO}_3^-/\text{PO}_4^{3-}$ ratios in the Arabian Sea are 12.81 (Codispoti *et al.*, 2001), thus the ratio in the SIO falls between the global ocean mean and the ratio in the Arabian Sea (Harms *et al.*, 2019). The second indication is the tracer N^* that marks NO_3^- deficits and excesses relative to phosphate in the nutrient pools. The Arabian Sea is characterized by an extensive oxygen deficit zone (ODZ) that induces denitrification in mid-water depths there (150–400 m; Gaye *et al.*, 2013), causing negative N^* values. This Arabian N deficit imported by the observed tongue of oxygen-depleted waters transported by the RSPGIW and IDW into the IOSG, can be observed in the SIO (Figure 4.3i–l, Figure 4.5d, Figure 4.6b). Denitrification is a biologically induced process associated with isotope fractionation and thus affects the $\delta^{15}\text{N}-\text{NO}_3^-$. Because lighter isotopes are preferentially removed during denitrification, the residual nitrate is enriched in ^{15}N as seen in $\delta^{15}\text{N}-\text{NO}_3^-$ within the RSPGIW (Figure 4.5e), in conjunction with elevated N^* values and low oxygen concentrations (Figure 4.6b). High $\Delta(15-18)$ values in the RSPGIW and maximum values in the SAMW are induced by the decoupling of N and O isotopes in the nitrate pool when nitrate from remineralisation is added (Figure 4.5e–g). The nitrate advected from the Arabian Sea is progressively replenished by ongoing organic matter respiration that brings the $\delta^{18}\text{O}-\text{NO}_3^-$ value close to the oceanic average of $\sim 2\text{‰}$, while retaining the original elevated $\delta^{15}\text{N}-\text{NO}_3^-$ values (Harms *et al.*, 2019).

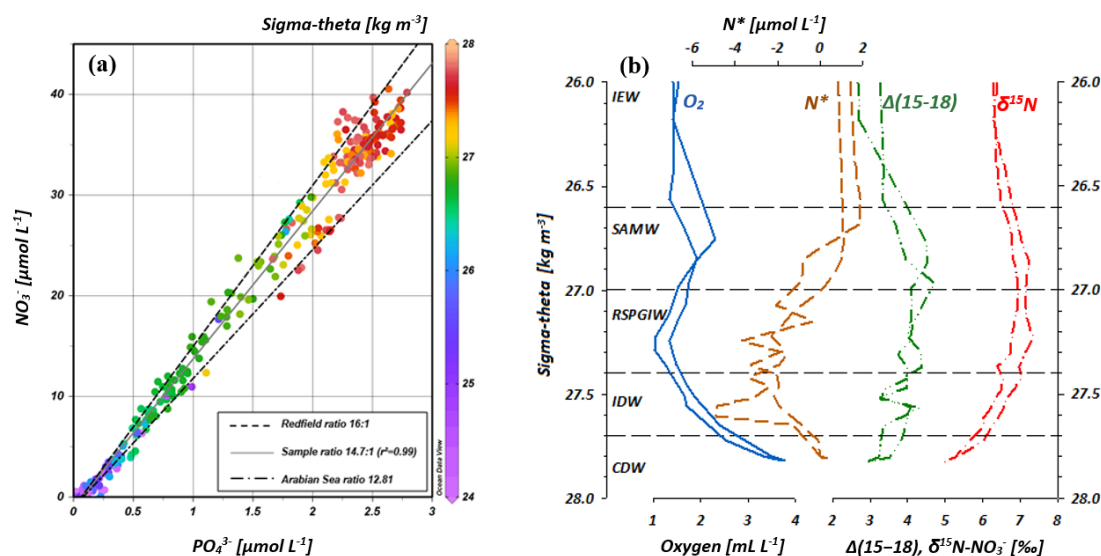


Figure 4.6. Nitrate vs. phosphate concentrations (a); the regression line of the sample data (solid, grey line) indicates a ratio of ~ 14.7 ($r^2 = 0.99$) that is intermediate between the Redfield ratio of (16:1; black, dashes line) and the mean ratio in the Arabian Sea with a slope of ~ 12.8 (grey, dotted-dashed line from *Codispoti et al.*, 2001); color-coding of dots indicates the potential density (sigma-theta; color scale). Panel b shows sigma-theta profiles of oxygen concentration, N^* , $\delta^{15}\text{N}\text{-NO}_3^-$, and $\Delta(15-18)$ that depict the denitrification signal from the Arabian Sea in the water column profiles of the south equatorial Indian Ocean (stations at $\sim 3^\circ\text{S}$ and $\sim 9^\circ\text{S}$; see Figure 4.1). Water mass boundaries are given for the IEW, SAMW, RSPGIW, IDW, and CDW (for water mass abbreviations see Figure 4.3).

4.4.1.2 Influence from the Southern Ocean on the nutrient distribution and nitrate isotopic composition of the IOSG

Elevated $\delta^{15}\text{N}\text{-NO}_3^-$ and $\delta^{18}\text{O}\text{-NO}_3^-$ values within the SAMW (Figure 4.5e, f, Figure 4.7a) are the consequence of incomplete (partial) N assimilation in the Subantarctic thermocline of the Southern Ocean (*Harms et al.*, 2019). In general, N assimilation can induce an isotope effect of about 5–10 ‰ (*Montoya and McCarthy*, 1995; *Waser et al.*, 1998; *Sigman et al.*, 2005) and produces biomass that is depleted in ^{15}N . However, in oligotrophic waters such as the IOSG, this isotopic fractionation is not expressed (*Montoya et al.*, 2002) due to complete N assimilation that also depresses nitrate concentrations to the limit of detection. Thus, elevated isotope ratios must be produced by partial N assimilation that takes place in the Southern Ocean, where light limitation and low iron availability limit primary productivity (*Sigman et al.*, 1999; *Boyd et al.*, 2000; *Hutchins et al.*, 2001; *DiFiore et al.*, 2006, 2010). *McCartney* (1977) and *Sigman et al.*

(1999) observed $\delta^{15}\text{N-NO}_3^-$ values of 5–9 ‰ within the Subantarctic thermocline waters of the Southern Ocean. These thermocline waters are then injected as SAMW into the IOSG, where we observe nitrate with high $\delta^{15}\text{N-NO}_3^-$ and $\delta^{18}\text{O-NO}_3^-$ (Figure 4.5e, f).

As further evidence for water mass transport from the Southern Ocean into the IOSG thermocline, the NO_3^- and $\delta^{15}\text{N-NO}_3^-$ relationship in Subantarctic thermocline waters can be compared to IOSG thermocline waters (for details see *Harms et al.*, 2019). Using the correlation of $\delta^{15}\text{N-NO}_3^-$ and the fraction that remains from N assimilation ($\ln(\text{NO}_3^-)$), the isotope fractionation effect during N assimilation can be quantified (*Sigman et al.*, 1999, 2000; *DiFiore et al.*, 2006). The isotope effect can then be displayed as a slope angle of a linear line in $\ln(\text{NO}_3^-)/\delta^{15}\text{N-NO}_3^-$ space (Figure 4.7b). Comparing the isotope effect (slope angle) calculated for the IOSG thermocline (0.93 ‰; *Harms et al.*, 2019) with the isotope effect detected for the Subantarctic thermocline (1.3 ‰; *Sigman et al.*, 1999, 2000) reveals a similar trend. The slight less steep slope in the IOSG thermocline can be explained by vertical mixing with the overlying SSW (*Harms et al.*, 2019), which has a fundamentally different formation background (N_2 fixation, see section 4.4.2).

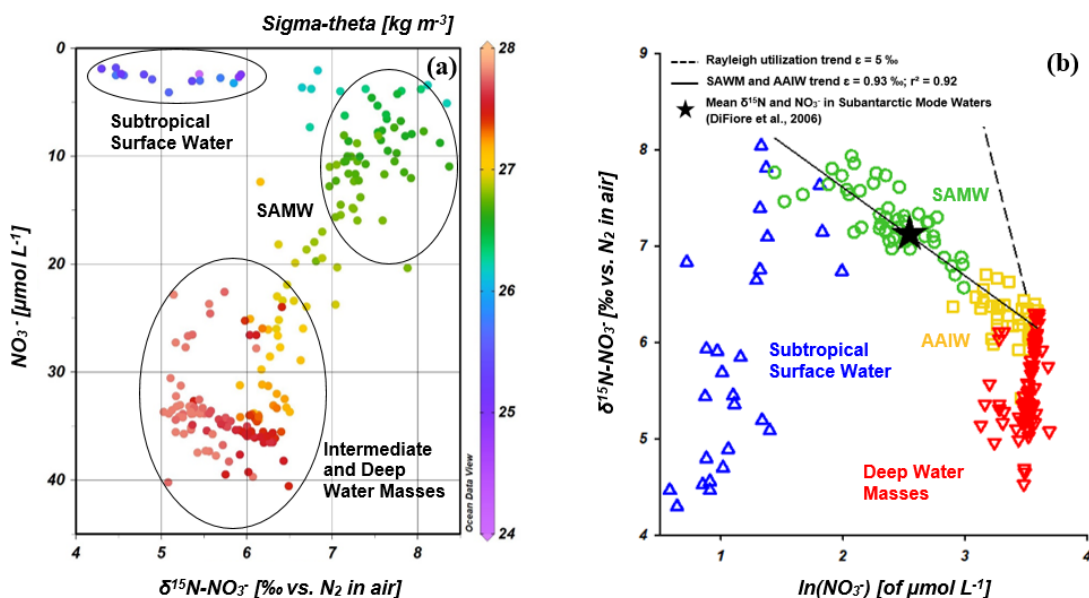


Figure 4.7. NO_3^- concentrations vs. $\delta^{15}\text{N-NO}_3^-$ (a) and $\delta^{15}\text{N-NO}_3^-$ vs. $\ln(\text{NO}_3^-)$ (b) for water sampling stations within the IOSG (20.96°–27.80°S); color code of dots indicates the potential density sigma-theta (kg m^{-3}). In panel b, data are grouped for the SSW (blue), SAMW (green), AAIW (yellow) and deep water masses (red). Figures are modified after *Harms et al.* (2019).

4.4.2 External input of reactive nitrogen via N₂ fixation in the IOSG

In addition to the imprint from the North Indian Ocean and the Southern Ocean on the nutrient distribution and isotopic composition, the parameter N*, $\delta^{15}\text{N-NO}_3^-$, and $\Delta(15-18)$ suggest an additional nitrate source from N₂ fixation in surface waters of the IOSG (Harms *et al.*, 2019). Increasingly positive N* values in the upper 300 m at ~20°–24°S indicate a positive deviation of the NO₃⁻/PO₄³⁻ ratio from the Redfield stoichiometry (Figure 4.5d; Figure 4.8) and thus an additional input of N to the system decoupled from P (Redfield, 1934, 1963; Gruber and Sarmiento, 1997). Due to the fact that the SIO is little affected by the influx of nutrient-enriched mineral aerosols from atmospheric deposition (Duce and Tindale, 1991; Duce *et al.*, 2008), airborne input is an unlikely source for external N. Instead, diazotrophic N₂ fixation is indicated as the origin for the new N, similar to the situation in the southwestern Pacific Ocean where positive N* anomalies of 2 $\mu\text{mol L}^{-1}$ in the mixed layer reflect diazotrophic N₂ fixation (Fumenia *et al.*, 2018).

The isotopic composition of nitrate is an unequivocal indicator of external atmospheric N sources by N₂ fixation. Because atmospheric N is assimilated by fixation, the $\delta^{15}\text{N}$ of biomass thus produced is around ~0 ‰ and the nitrification of this isotopically light N in diazotrophic biomass lowers the $\delta^{15}\text{N-NO}_3^-$ in surface waters relative to the average oceanic NO₃⁻. Consequently, the decrease in $\delta^{15}\text{N-NO}_3^-$ from elevated values in the SAMW (>7 ‰) to values less than 5 ‰ is clear evidence for N₂ fixation (Figure 4.7a, Figure 4.8). Similar upward decreases were found in the North Atlantic, where N₂ fixation was verified (Knapp *et al.*, 2008; Bourbonnais *et al.*, 2009). While the $\delta^{15}\text{N-NO}_3^-$ is lowered by N₂ fixation, the $\delta^{18}\text{O-NO}_3^-$ is less affected and leads to the decoupling of N and O isotopes (Wada and Hattori, 1976; Minagawa and Wada, 1986; Carpenter *et al.*, 1997; Montoya *et al.*, 2002). Therefore, the slight upward decrease in $\Delta(15-18)$ (Figure 4.8) is a further indication for N₂ fixation in the surface waters of the IOSG at ~20°–24°S.

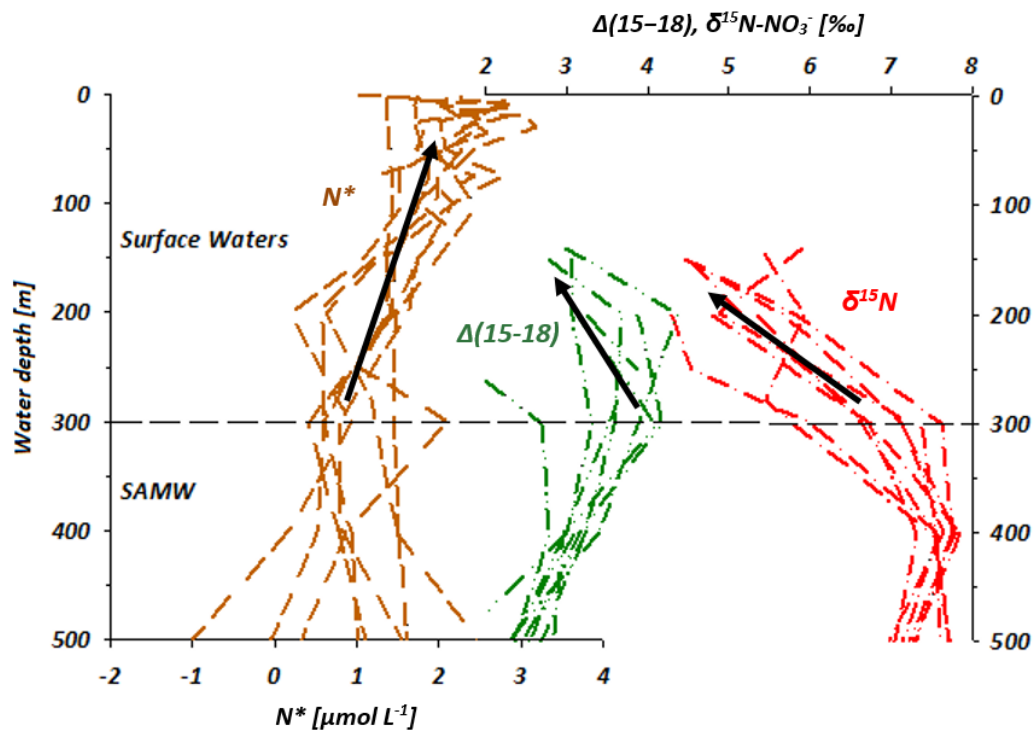


Figure 4.8. Depth profiles of N^* , $\delta^{15}\text{N-NO}_3^-$, and $\Delta(15-18)$ of water sampling stations located at $\sim 20^\circ\text{--}24^\circ\text{S}$ indicate an external input of new nitrogen via N_2 fixation in the upper 300 m. Black arrows illustrate the upward increase of N^* and the decrease of $\delta^{15}\text{N-NO}_3^-$ and $\Delta(15-18)$ in the upper 300 m water depth. SAMW represents the Subantarctic Mode Water.

Harms et al. (2019) calculated that $\sim 32\text{--}34\%$ of the assimilated NO_3^- present in the upper 200 m at $\sim 20^\circ\text{--}24^\circ\text{S}$ is provided by newly fixed N via N_2 fixation. For the subtropical North Atlantic, *Bourbonnais et al.* (2009) stated that N_2 fixation accounts for $\sim 40\%$ of newly supplied nitrate. This is slightly higher than our fixation input to the subtropical SIO. As the subtropical North Atlantic is characterized by higher N^* values, a slightly stronger upward decrease of $\delta^{15}\text{N-NO}_3^-$ and a stronger decoupling of N and O isotopes in surface waters, even higher fixation rates are very likely.

4.5 Conclusion

The oligotrophic Indian Ocean subtropical gyre (IOSG) is among the extensive oligotrophic areas that cover about 75 % of the global ocean's surface. These ocean regions are assumed to expand in future ocean warming (*Behrenfeld et al.*, 2006) and thus become more important on a global scale over the next decades. In order to improve the understanding of biogeochemical processes in the IOSG

and to be able to better predict possible consequences of warming on the global marine N cycle, we investigated water column properties to map water mass distribution and analysed water samples for nutrients and stable isotopes of nitrate.

Nutrient distribution in the IOSG is predominantly influenced by the typical circulation pattern of subtropical gyres leading to specific physical conditions. In the center, intense downwelling is induced by the convergence of horizontal Ekman volume flux (*Williams and Follows, 2003*) leading to deep thermo-, pycno- and nutriclines, which shoal towards the gyre margins and thus form strongly stratified and nutrient-depleted surface waters. Consequently, the supply of nutrients to the euphotic zone by vertical mixing is reduced or absent in the gyre and accordingly, the external input via the lateral transfer across the gyre boundaries acts as the major nutrient source. Indeed, we can illustrate that nutrient distribution and isotopic composition of nitrate are affected by the influx of different water masses of different origin, based on our water mass analysis. The nutrient and isotopic data reported in *Harms et al. (2019)* and amended here are among the first for the subtropical SIO. We demonstrate the lateral influx of water masses from the Arabian Sea, imprinted by strong denitrification at mid-water depths, leading to nitrate deficits and elevated N and O isotope ratios in intermediate and deep waters of the IOSG. Furthermore, oxygen-saturated mode waters characterized by preformed nutrients and distinctly elevated nitrate isotope composition formed by partial N assimilation at high southern latitude are injected from the Southern Ocean. As an additional nitrate source, our data mirror an external input of atmospheric N via N₂ fixation. First estimates in the upper 200 m (~20°–24°S) revealed that approximately 32–34 % of the nitrate consumed by N assimilation is provided from newly fixed N.

Chapter 5 – Cumulative Part IV

Biogeochemistry of particulate matter fluxes and sediment composition in the Indian Ocean subtropical gyre

(submitted in 2020 as book chapter 20 in “Marine Metal Exploration: The INDEX Project – Prospecting the Seafloor for Polymetallic Sulphides Title” to Springer Nature)

Natalie C. Harms¹, Niko Lahajnar¹, and Kay-Christian Emeis^{1,2}

¹Institute of Geology, Universität Hamburg, Hamburg, 20146, Germany.

²Helmholtz-Zentrum Geesthacht (HZG), Institute for Coastal Research, Geesthacht, 21502, Germany.

Abstract. The Indian Ocean subtropical gyre (IOSG) is one of the five extensive oligotrophic areas characterized by low primary production rates and hence very low sinking particulate matter fluxes. Sinking particulate matter were sampled during 5-year sediment trap deployments between 2014 and 2019 as part of the INDEX program and were accompanied by surface sediment investigations to determine the final burial of particles at the seafloor. Comparing particulate organic carbon (POC) fluxes to global data, the IOSG reveals lowest fluxes worldwide, even compared to other oligotrophic areas. We provide new information on the major factors that control the POC export out of the biologically active zone, its transfer into the ocean’s interior and its final accumulation in surface sediments. Furthermore, we present data on spatial and seasonal variabilities of particle fluxes in the IOSG. We found a bulk sedimentation rate of 0.23 cm per 1000 years within the IOSG. Translated to sediment burial of carbon, mineralization in the water column and low sedimentation rate attenuate the burial rates to the point that only 0.17 % of the

POC produced at the sea surface reaches the seafloor, and $<0.01\%$ ($\sim 0.02 \text{ mg POC m}^{-2} \text{ d}^{-1}$) accumulates in surface sediments.

5.1 Introduction

The downward flux of sinking particles transports particulate organic carbon (POC) out of the surface layer into the ocean's interior and into the sediments. This drives the organic carbon pump and is an essential component of the global carbon cycle (*Volk and Hoffert, 1985*). Furthermore, an efficient organic carbon pump lowers the partial pressure of dissolved CO_2 in surface waters, thereby enhancing the ocean's ability to absorb CO_2 from the atmosphere (*Berger et al., 1989; Wefer and Fischer, 1991; Lutz et al., 2007*). Consequently, the organic pump controls the partitioning of carbon between the large sub-thermocline ocean reservoir and the relatively small atmospheric reservoir (*Berger et al., 1989*). There is limited field data on POC fluxes in the Indian Ocean and virtually nothing is known on sinking particulate matter fluxes in the Indian Ocean subtropical gyre (IOSG). The IOSG is one of the extensive oligotrophic areas that cover about 75 % of the ocean's surface. These oligotrophic regions are characterized by extremely low primary production and organic matter export rates (*Sarmiento and Gruber, 2006; Williams et al., 2013; Baer et al., 2019*). However, they are assumed to account for half of the global POC export to the ocean interior (*Emerson et al., 1997*).

A reliable tool to monitor the quantity, quality, and the temporal variability of sinking POC are sediment trap moorings (e.g., *Honjo et al., 1995; Wong et al., 1998; Buesseler et al., 2000; Rixen et al., 2019a*). To investigate the particle export to the deep ocean and finally the accumulation of particulate matter in deep-sea sediments, we collected sinking particulate matter and surface sediments in the INDEX licence area (Figure 5.1a). Our study bases on a 4-year time series of sediment trap deployments during INDEX expeditions from 2014 to 2018 (*Harms et al., 2021*) and is here extended by sediment trap investigations between 2018 and 2019. Sampling stations are located in a region with lowest annual chlorophyll-*a* concentrations, with only small seasonal variations (Figure 5.1b, c). Particulate matter fluxes to the deep ocean are directly linked to surface water processes (*Eppley and Peterson, 1979; Suess, 1980; Betzer et al., 1984; Lampitt and Antia, 1997; Cram et al., 2018*) and particulate matter fluxes collected by sediment traps often reveal a positive correlation with surface primary production (*Betzer et al., 1984*). The rate of primary production is controlled by various factors, such

as light, available nutrients, and water column stratification (*Sarmiento and Gruber, 2006*). The efficiency of the transfer of organic matter via sinking particles through the thermocline and further into the deep ocean depends on numerous parameters like particle size, water temperature, oxygen concentrations, the availability of ballast material acting on particle aggregation (ballast effect), and organic matter degradation (*Lampitt and Antia, 1997; Cram et al., 2018; Rixen et al., 2019b*). These effects on sedimentation processes are being studied in the IOSG using sediment trap-derived particulate matter fluxes, surface sediment samples, and additional information on surface chlorophyll-*a* concentrations and nutrient data (*Harms et al., 2019*).

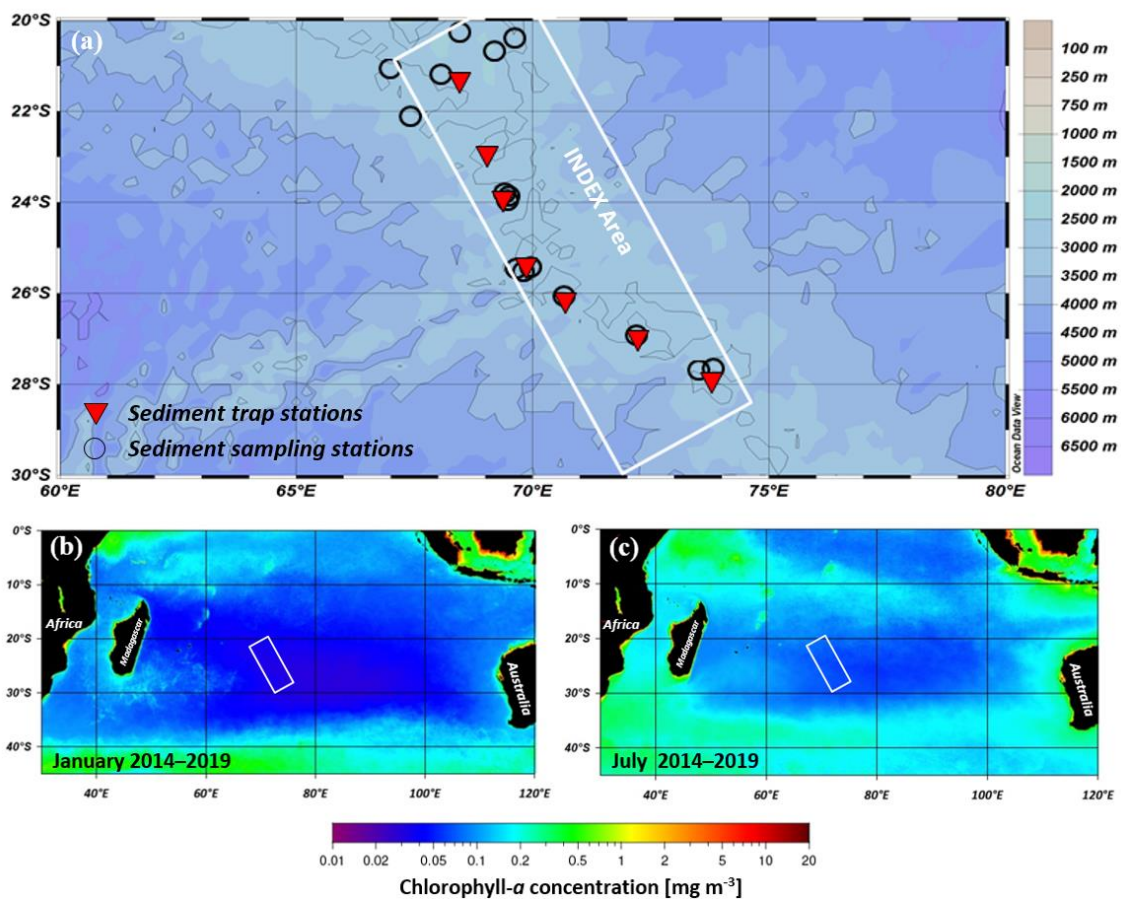


Figure 5.1. Station map of particle flux and surface sediment sampling in the INDEX area (white rectangle) (a) and chlorophyll-*a* concentrations as an indicator for primary production averaged over the time period from 2014 to 2019 during austral summer (January; b) and austral winter (July; c). Chlorophyll-*a* data was downloaded from the NASA Ocean Color DataBase (<https://oceancolor.gsfc.nasa.gov/l3/>; MODIS-Aqua; monthly climatology time-series; 4 km area-averaged, OCI Algorithm; *Werdell and Bailey (2002)*).

5.2 Materials and methods

5.2.1 Use of sediment traps to collect sinking particulate matter

Sediment trap moorings were deployed for one-year periods at seven sites in the clusters of the INDEX licence area between November 2014 and October 2019 (Figure 5.1a, Table 5.1, see detailed data in Table A2.1 in the Appendix A2). Sediment traps were moored at ~500–600 m above bottom (m.a.b.) (2600–3500 m water depth), to collect the undisturbed vertical (“true”) particulate matter flux to the deep-sea and avoid influence of resuspended material from the seafloor. An exception were sediment trap moorings in cluster 04 (04-03, 04-04), where additionally one trap was installed above (*Shallow* at ~695 m water depth) and one below (*Deep* at 3465 m water depth, i.e., ~30 m.a.b.) the trap moored at ~560 m.a.b. (*Middle*). This provides additional information on flux composition and degradation rates of sinking particles.

Table 5.1. Technical data on the deployment and recovery of sediment traps moored during November 2014 and December 2019 in the oligotrophic IOSG.

Trap ID	Latitude	Longitude	Water depth [m]	Trap depth		Sampling interval
				[m.b.s.] ^a	[m.a.b.] ^b	
05-01	25°19.81'S	070°00.00'E	3110	2579	531	10.11.14-06.11.15 ^(1,2)
04-01	23°52.16'S	069°29.75'E	3493	2962	531	28.11.15-04.11.16 ^(2,4)
01-01	21°14.80'S	068°35.47'E	3145	2614	531	20.12.16-12.09.17 ^(4,5)
03-01	22°53.11'S	069°09.70'E	3700	3169	531	20.12.16-12.09.17 ^(4,5)
01-02	21°14.88'S	068°35.33'E	3145	2614	531	03.10.17-10.09.18 ^(5,3)
04-03 <i>Shallow</i>	23°51.86'S	069°29.71'E	3493	695	2798	03.10.17-10.09.18 ^(5,3)
04-03 <i>Middle</i>	23°51.86'S	069°29.71'E	3493	2931	562	03.10.17-10.09.18 ^(5,3)
04-03 <i>Deep</i>	23°51.86'S	069°29.71'E	3493	3465	28	03.10.17-10.09.18 ^(5,3)
07-01	26°02.78'S	070°50.67'E	4010	3479	531	03.10.17-10.09.18 ^(5,3)
10-01	26°53.95'S	072°20.48'E	3400	2869	531	03.10.17-10.09.18 ^(5,3)
12-01	27°48.24'S	073°53.35'E	3970	3439	531	03.10.17-10.09.18 ^(5,3)
01-03	21°14.88'S	068°35.15'E	3146	2614	531	07.11.18-02.11.19 ^(3,6)
04-04 <i>Shallow</i>	23°51.98'S	069°29.48'E	3493	714	2778	07.11.18-10.11.19 ^(3,6)
04-04 <i>Middle</i>	23°51.98'S	069°29.48'E	3493	2930	563	07.11.18-10.11.19 ^(3,6)
04-04 <i>Deep</i>	23°51.98'S	069°29.48'E	3493	3464	29	07.11.18-10.11.19 ^(3,6)
07-02	26°02.68'S	070°50.53'E	4010	3479	531	07.11.18-02.11.19 ^(3,6)
10-02	26°53.72'S	072°20.37'E	3400	2869	531	07.11.18-04.12.19 ^(3,6)
12-02	27°48.50'S	073°53.33'E	3820	3289	531	19.11.18-05.12.19 ^(3,6)

Note: ^ameter below surface; ^bmeter above bottom; numbers in parentheses behind sampling intervals denote the deployment and recovery of sediment trap moorings during ship expeditions with *R/V Pelagia*: PE 394⁽¹⁾, PE 405⁽²⁾, PE 446⁽³⁾, *R/V Maria S. Merian*: MSM 59-2⁽⁴⁾ and *R/V Sonne* SO 259⁽⁵⁾, and SO 271⁽⁶⁾.

A typical sediment trap mooring consists of different tools with the sediment trap as the central part. Other important parts are float modules, acoustic releases, anchors, as well as a variety of wires and shackles. For our investigations we use

Kiel K/MT 234 and McLane Mark 7G-21 sediment traps. A representative sediment trap mooring is shown in Figure 5.2. The anchor weight moors the system on the ground. A sufficient number of floats is important to stabilize the mooring in the water column during the deployment and for the uplift during recovery. The acoustic release disconnects the anchor from the remaining system.

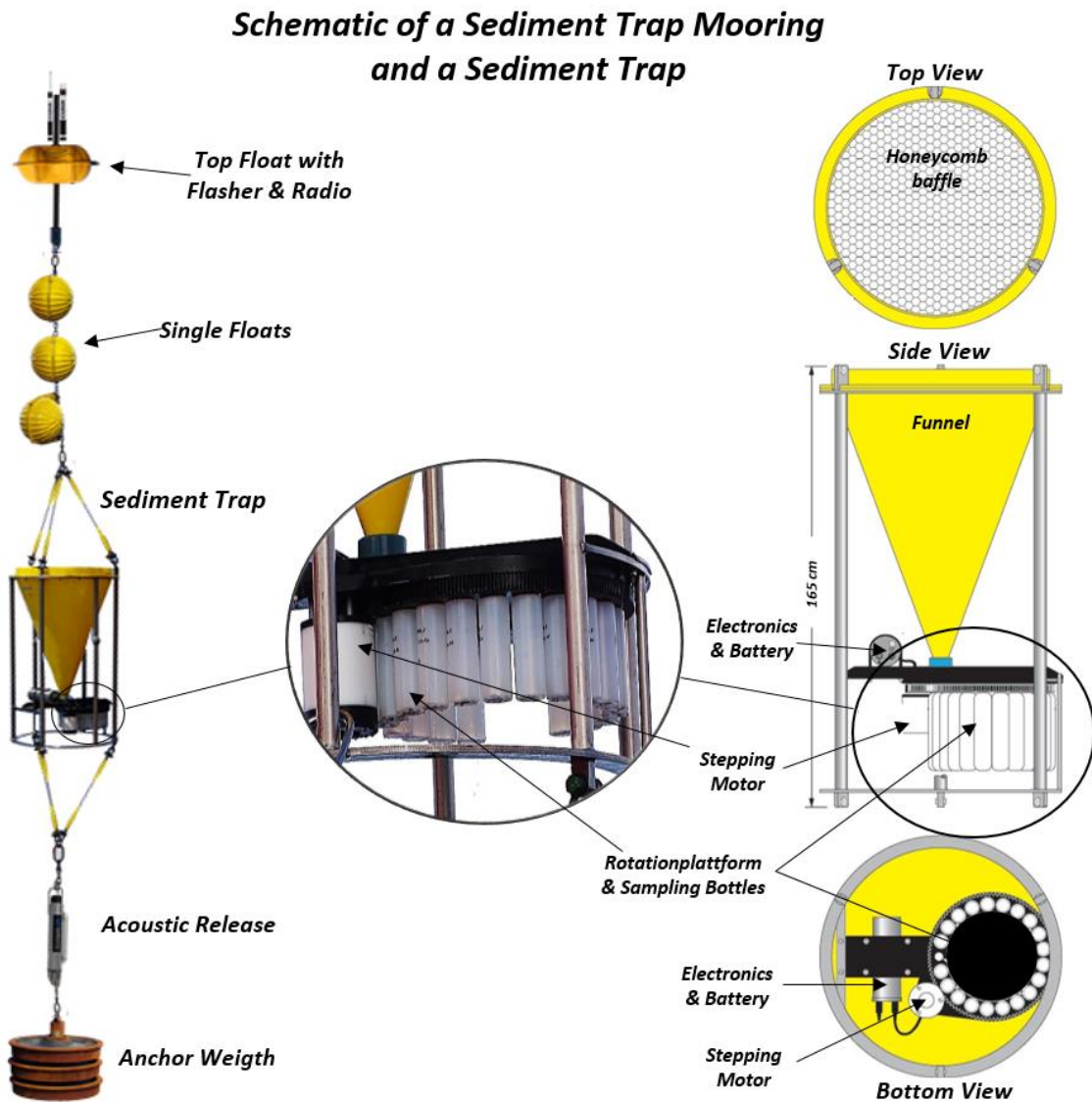


Figure 5.2. Schematic of a sediment trap mooring and a sediment trap (McLane Mark 7G-21) used during the INDEX program. Source: Woods Hole Oceanographic Institution (<https://www.whoi.edu/what-we-do/explore/instruments/instruments-sensors-samplers/sediment-trap/>).

The sediment trap consists of a funnel (aperture size 0.5 m²; slope angle 34°), which intercepts the vertical particle flux. A hexagonal “honeycomb” lattice covers the funnel. This serves as a current stabilizer, reduces washout and

prevents large swimmers to enter the funnel. The control unit is equipped with a microprocessor for programming the rotation steps and serves as the power supply for the stepping motor. The rotation platform is placed under the funnel's orifice and is loaded with 20 HDPE (high-density polyethylene) bottles (250 ml for McLane Mark 7G-21 trap and 400 ml for Kiel K/MT 234 trap).

5.2.2 Sample preparation

5.2.2.1 Sinking particulate matter samples

Prior to deployment, sediment trap bottles were filled with filtered deep-seawater and NaCl (35 g; analytical grade) was added in order to create a brine solution ($\sim 70 \text{ g L}^{-1}$ NaCl) that reduces diffusion out of the bottles during deployment. In addition, 3.3 g L^{-1} HgCl₂ (analytical grade) was added to suppress organic matter degradation by bacterial or microbial activities. After recovery, samples were sieved and divided into fraction of $>1 \text{ mm}$ and $<1 \text{ mm}$. The latter fraction represents the “true” particulate matter flux and was filtered through a pre-weighed Nucleopore polycarbonate filter ($0.4 \mu\text{m}$) and rinsed with Milli-Q water charged with 0.002 g L^{-1} Na₂B₄O₇ (sodium tetraborate, analytical grade) to avoid destruction of carbonate tests. The loaded filters were dried ($\sim 40^\circ\text{C}$) for two days and weighed in the home lab to determine the total particulate mass flux (in $\text{mg m}^{-2} \text{ d}^{-1}$).

5.2.2.2 Surface sediment samples

Surface sediment cores with a length of up to 26 cm were collected by push-cores installed on a ROV (remotely operated underwater vehicle) or by a multicorer during INDEX expeditions between 2015 and 2018. In the ship labs the cores were cut into one centimeter slices and stored at -20°C until they were freeze-dried in the home lab.

5.2.3 Analytical methods

Sinking particulate matter and surface sediment samples were homogenized in a mortar. The concentrations of total carbon (TC), total nitrogen (TN), and organic carbon (C_{org} , POC) were analysed by flash combustion using a EuroVector EA-3000 CHNSO Elemental Analyzer, which works with an analytical precisions of

0.05 % for carbon and 0.005 % for nitrogen. Organic carbon concentration was determined after removal of carbonate from tared subsamples with HCl (1N). Calcium carbonate (CaCO_3) was calculated by the formula: CaCO_3 (wt.-%) = $(\text{TC} - \text{POC})/0.12$. Biogenic opal (bOpal) was analyzed with the modified wet alkaline extraction method according to *DeMaster* (1981) and *Mortlock and Froelich* (1989). For bOpal, the relative error of duplicate measurements was generally below 5 %. Particulate organic matter (POM) was calculated by the formula: POM (wt.-%) = $\text{POC} \times 1.8$ (*Anderson*, 1995; *Francois et al.*, 2002). Lithogenic matter (LM) was calculated using the formula: LM (wt.-%) = $100 - (\text{POM} + \text{CaCO}_3 + \text{bOpal})$. For trap samples, individual component fluxes were calculated from the total mass flux <1 mm.

5.3 Particulate matter in sediment traps

5.3.1 Total mass fluxes and main components

Total mass fluxes of sinking particulate matter, collected by sediment traps deployed at ~500–600 m.a.b. range between 2.3 and 22.2 $\text{mg m}^{-2} \text{d}^{-1}$ (Ø 10.6 $\text{mg m}^{-2} \text{d}^{-1}$; Figure 5.3a). In general, sinking particulate matter in the open ocean and the resultant pelagic sediments consist mainly of the products generated by planktic and nektic organisms in surface waters (*Hüneke and Henrich*, 2011). Primary producers like free-floating phytoplanktonic organisms (e.g., coccolithophores and diatoms) are the basis of the marine food web and control the biological productivity of the entire marine community by converting inorganic substances into OM by photosynthesis (*Hüneke and Henrich*, 2011; *Turner*, 2015). Major consumers are zooplankton such as planktic foraminifera and pteropods (*Turner*, 2015). POM sinking out of the productive zone is generally composed of combinations of fecal pellets from zooplankton and fish, organic aggregates known as "marine snow" and phytodetritus from sinking phytoplankton (*Turner*, 2015). Several phyto- and zooplanktonic organisms generate mineralised tests consisting of carbonate (planktic foraminifera, coccolithophores) or silicate (diatoms, radiolarians) (*Lyle*, 2014). This agrees with our observations in the IOSG, where the dominant components of the total mass flux are CaCO_3 (~66 wt.-%) and bOpal (~14 wt.-%), followed by minor percentages of POM (~9.9 wt.-%) and LM (~9.6 wt.-%; Figure 5.3a, b). Overall, the distribution of the individual components CaCO_3 , bOpal, POM, and LM is relatively constant in all sediment trap moorings (Figure 5.3a).

The high percentages of CaCO_3 in all traps are typical for the tropical and subtropical regions of the open Indian Ocean (Kolla *et al.*, 1976; Lyle, 2014). The carbonate compensation depth (CCD) is at 4600–4800 m depth (Kolla *et al.*, 1976) between 20°–30°S in the Indian Ocean so that an extensive solution of CaCO_3 components in sinking particulate matter and sediments can be excluded.

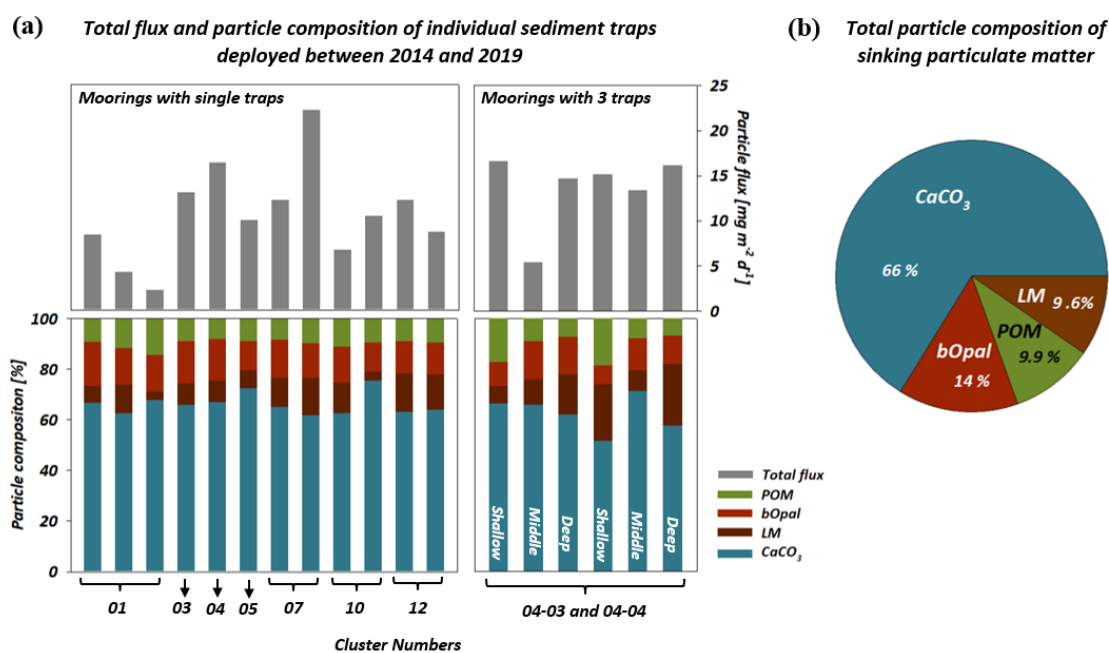


Figure 5.3. Total mass fluxes and particle composition of the main components calcium carbonate (CaCO_3), particulate organic matter (POM), biogenic opal (bOpal), and lithogenic matter (LM) in wt.-% of individual sediment traps deployed during INDEX expeditions between 2014 and 2019 (a). Panel a is divided into sediment trap moorings, deployed with a single sediment trap and one with a system of three sediment traps (mooring 04-03 and 04-04). The overall averaged composition in sinking particulate matter for traps deployed at ~500–600 m.a.b. is presented in panel (b).

At sediment trap moorings 04-03 and 04-04, three traps were deployed to collect particles at different depths (see section 5.2.1). Traps *Shallow* intercepted the particle flux that was directly exported out of the photic (low nutrient) zone. Active daily zooplankton migration extends to this depth and fluxes were higher compared to traps *Middle* (deployment depth is equal to single-sediment trap moorings; Figure 5.3a, Figure 5.4a). Traps *Deep* reveal increasing total fluxes compared to traps *Middle* due to the influx of particles from resuspension and rebound-processes (Figure 5.3a, Figure 5.4a). These benthic nepheloid layer processes are crucial for the understanding of potential deep-sea mining activities. Additionally, the mooring systems of three sediment traps in row allow us to decipher degradation processes of particles on their way through the

water column. The CaCO_3 content is similar to the amount in the other sediment traps and there are minor differences between Traps *Shallow*, *Middle* and *Deep* (Figure 5.3a). POC and TN gradually decrease with depth (Figure 5.4b, c), reflecting the typical progressive degradation of organic components on their way down towards the ocean's interior (Sarmiento and Gruber, 2006; Henson et al., 2019). The bOpal and LM contents both increase with depth, except of trap 04-04 *Shallow* indicating higher LM contents compared to trap *Middle* (Figure 5.3a).

The gradual decrease of POC and TN between traps *Shallow* and *Middle* is more pronounced than between traps *Middle* and *Deep* (Figure 5.4b, c). In total, we can calculate that less than a half of the POC and TN trapped in the upper most traps reached the near-bottom traps. Moreover, TN indicates a stronger downward decrease compared to POC, leading to a downward increase of POC/TN ratios (Figure 5.4d) due to a preferential degradation of TN compared to POC (Knauer et al., 1979; Martin et al., 1987).

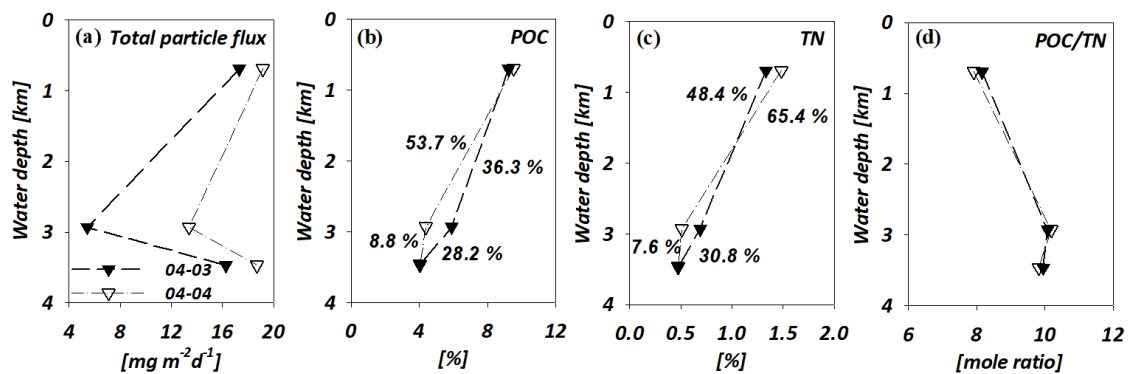


Figure 5.4. Averaged total particulate matter flux (a), particulate organic carbon (POC) (b), total nitrogen (TN) (c) given in percentages (wt.-%) and the elemental ratio POC/TN (d) are presented as depth profiles for sediment traps *Shallow* (~695 m), *Middle* (~2930 m), and *Deep* (~3465 m and ~30 m a.b.) of moorings 04-03 (black triangles) and 04-04 (open triangles) deployed between 2017 and 2019 in the INDEX licence area. Percentages next to line plots in panel b and c show the relative reduction in % of POC and TN percentages (wt.-%).

5.3.2 Organic carbon fluxes in a global comparison

Our data reveal POC fluxes of $0.52 \pm 0.18 \text{ mg m}^{-2} \text{ d}^{-1}$ on average and range between 0.2 to $0.9 \text{ mg m}^{-2} \text{ d}^{-1}$ for sediment traps deployed at ~500–600 m a.b., which is roughly 5 % of the total mass flux. Organic carbon export out of the biologically active zone, across the thermocline into the deep ocean and its final

storage in sediments drives the organic carbon pump and is thus an essential part of the global carbon cycle (*Volk and Hoffert, 1985*). To evaluate the efficiency of the organic carbon pump and the role of the IOSG in carbon sequestration on an ocean-wide scale, we compare our POC flux data with global data previously collated from the literature (e.g., *Lampitt and Antia, 1997; Lutz et al., 2007; Honjo et al., 2008; Harms et al., 2021*, see compiled data in Table A3.1 in the Appendix A3). For comparison, we normalize POC flux data to a water depth of 2000 m by using the equation of *Martin et al. (1987)*:

$$POC_{2000} = POC_{TD} \times (2000/TD)^{-0.858} \quad (5.1)$$

This equation is commonly used (see *Lampitt and Antia, 1997; Sarmiento et al., 1998; Hedges et al., 1999; Buesseler et al., 2000; Fischer et al., 2000; Lutz et al., 2007; Harms et al., 2021*), where “ POC_{2000} ” ($\text{mg m}^{-2} \text{d}^{-1}$) is the particulate organic carbon flux normalized to a water depth of 2000 m and “ POC_{TD} ” is the particulate organic carbon flux measured at trap depth “ TD ”. The resulting global map of normalized POC fluxes shows that fluxes in the IOSG are extremely low compared to global data (Figure 5.5a). Furthermore, the IOSG has among the lowest fluxes compared to other subtropical gyres in the Atlantic and Pacific Oceans (Figure 5.5b).

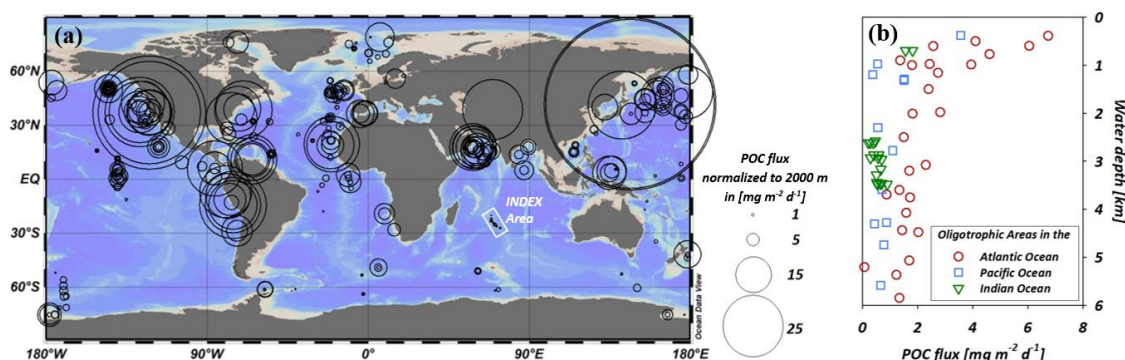


Figure 5.5. Global map of particulate organic carbon (POC) fluxes in $\text{mg m}^{-2} \text{d}^{-1}$ for sediment trap data collated from the literature (*Harms et al., 2021*; see Table A3.1 in the Appendix A3) are extended by sediment trap samples in the IOSG collected during INDEX expeditions between 2014 and 2019 (a). All POC flux data were normalized to 2000 m. Panel b shows POC flux data for the oligotrophic gyres (15° – 35°N , 15° – 35°S) against trap depths, grouped for the Pacific Ocean (grey), Atlantic Ocean (red), and Indian Ocean (green).

5.3.3 Controlling factors of organic carbon export

The formation of sinking particulate matter is to a first-order driven by primary production (*Eppley and Peterson, 1979; Suess, 1980; Betzer et al., 1984; Lampitt and Antia, 1997*). The rate of primary production (rate of CO₂ uptake via phytoplankton photosynthesis) and the transfer as sinking POC through the thermocline and further into the deep ocean is controlled by various factors (*Lampitt and Antia, 1997; Cram et al., 2018; Rixen et al., 2019b*). Major factors controlling primary production are light, available nutrients, and water column stability (*Lampitt and Antia, 1997; Rixen et al., 2019b*). The IOSG is a strongly stratified system with highly nutrient-depleted surface waters down to ~500 m (*Harms et al., 2019*). This is supported by the elevated POC/TN ratios of ~10 in particulate matter (*Harms et al., 2021*), which are higher than the Redfield ratio (~6.63; *Redfield, 1934, 1963*) and indicate strong phytoplankton nutrient limitation (e.g., *Donaghay et al., 1978; Goldman, 1980*). In subtropical gyres like the IOSG, the ocean mixed layer depth (OMLD) increases towards the center via depression of the pycnocline (*Sarmiento and Gruber, 2006; Baer et al., 2019*). However, the zone of significant nutrient increase is well below the OMLD in the gyre center and does not favor nutrient input by vertical mixing. Consequently, primary production in the IOSG is nutrient limited at extremely low primary production rates of 0.12–12.4 nmol C L⁻¹ h⁻¹ (*Baer et al., 2019*). These rates are lower than those measured in other oligotrophic gyres (>20 nmol C L⁻¹ h⁻¹; e.g., *Williams et al., 2013*). Thus, lowest oceanic POC fluxes worldwide (as known so far), detected in our sediment trap experiments are consequence of low primary production rates in the sea surface mixed layer.

The amount of the particle fraction exported from the productive layer can be expressed by the export efficiency ε (*Murray et al., 1989; Laws et al., 2000; Ducklow et al., 2001; Francois et al., 2002; Sarmiento and Gruber, 2006; Henson et al., 2019*), while the transport below the productive zone towards the deep ocean is referred to the transfer efficiency (T_{eff} ; *Cram et al., 2018*). Various factors such as water temperature, oxygen concentrations, particle size (particle aggregation), and the sinking speed (ballast effect), play a significant role for the final burial of POM at the seafloor. Temperature and particle size appear to have the strongest influence on the export/transfer efficiency and positive correlations between particle export efficiency, particle size, and the ballast effect have been observed (*Weber et al., 2016; Cram et al., 2018*). Ballast material enhances the vertical flux by promoting the aggregation of small particles that have individually an insignificant role in

the vertical mass flux and transform them into fast sinking aggregates ($>100 \text{ m d}^{-1}$) by increasing their specific density (Schrader, 1971; McCave, 1975; Shanks and Trent, 1980; Suess, 1980; Rixen et al., 2019b). The increase of the sinking speeds shortens the residence time of particulate matter in the biologically active zone, lowers organic matter regeneration within the OML and sub-thermocline and thus enhances the downward flux (Haake and Ittekkot, 1990; Ramaswamy et al., 1991; Armstrong et al., 2002; Hamm, 2002; Klaas and Archer, 2002).

The composition of the sinking material and the respective densities of the bulk components needs to be known to evaluate the ballast effect in terms of organic carbon out of the productive zone. Sinking particulate matter in the IOSG is dominated by CaCO_3 and bOpal, which together account for ~80 wt.-% of the total mass flux. Coccolithophores and foraminifera tests mainly contribute to CaCO_3 fluxes and have densities of 1.55 g cm^{-3} (Winter and Siesser, 1994) up to 1.7 g cm^{-3} (Schiebel and Hemleben, 2000; Schiebel et al., 2007). The density of diatom frustules, which are the main components of bOpal, varies between 1.46 and 2.0 g cm^{-3} (Csögör et al., 1999; DeMaster, 2003). The density of LM depends on its mineral composition but is generally higher than that of CaCO_3 and bOpal with average values of 2.7 g cm^{-3} (Rixen et al., 2019b) and is a relevant ballast material. However, LM makes up $<10 \%$ of the total mass flux in the IOSG and its contribution to total flux is too low to have a significant impact on the ballast effect (Francois et al., 2002; Rixen et al., 2019b). A multiple linear regression analysis (MLRA) confirmed the insignificant contribution of LM to the POC flux and indicates that instead CaCO_3 is highly correlated with POC fluxes (Harms et al., 2021; see details in the Appendix A4). Thus, CaCO_3 is the relevant ballast material in the IOSG that promotes the downwards flux of POC. However, in regions of higher LM fluxes outside the IOSG, a more effective transport of POC towards the ocean interior can be observed due to generally higher densities of LM than CaCO_3 and bOpal. For example, the Atlantic Ocean is characterized by a significant external input of LM via atmospheric dust supply from the Sahara that triggers the effective particulate matter export to depth (Ratmeyer et al., 1999). On the other hand, in warm and carbonate dominated regions like the IOSG, complex food webs lead to an enhanced regeneration of organic components in the upper ocean (Francois et al., 2002; Sarmiento and Gruber, 2006; Rixen et al., 2019b). Consequently, POC undergoes intense degradation before being exported into the deeper ocean. Thus, we do not only observe low POC fluxes, but also a very low POC export efficiency. This agrees with previous work on subtropical gyres (Sarmiento and Gruber, 2006; Cram et al., 2018; Henson et al., 2019).

To quantify the export efficiency or “ ε -ratio” we use the well-established concept of *Eppley and Peterson (1979)* with the formula:

$$\varepsilon = POC_{export\ flux} / Primary\ Production \quad (5.2)$$

used in numerous studies (*Murray et al., 1989; Laws et al., 2000; Ducklow et al., 2001; Francois et al., 2002; Sarmiento and Gruber, 2006; Henson et al., 2019*). We first normalized our POC flux data to a depth of 130 m (equation of *Martin et al., 1987; Eq. 5.1*), which is roughly the lower limit of the euphotic zone in our study area (NASA DataBase Giovanni, MODIS-A, Lee algorithm; *Lee et al., 2007*) and calculated an area-averaged $POC_{export\ flux}$ of $7.63\ mg\ m^{-2}\ d^{-1}$ ($0.23\ mol\ C\ m^{-2}\ yr^{-1}$). Additionally, we adopted the depth-integrated primary production estimates for the euphotic zone based on the SeaWiFS 4-year monthly chlorophyll climatology, which was converted to productivity using the average of three separate productivity algorithms in *Dunne et al. (2005)* (for details see *Sarmiento and Gruber, 2006*). A primary production rate of $\sim 10\ mol\ C\ m^{-2}\ yr^{-1}$ was calculated for the IOSG region. According to this, we determine an export efficiency of $\varepsilon = 0.023$ (Eq. 5.2), which means that only 2.3 % of the produced organic carbon is exported below the biologically active zone. This is even lower than estimates of *Sarmiento and Gruber (2006)* for the IOSG, who used the chlorophyll-*a* concentration and temperature based empirical algorithm of *Dunne et al. (2005)* and estimated $\varepsilon = 0.05$. However, the empirical algorithm of *Dunne et al. (2005)* is limited to export efficiencies between 0.04 and 0.72, which may be inadequate for estimating the export efficiency in subtropical gyres in general and in the IOSG in particular. This highlights the need of more observational data on particulate matter fluxes and primary production in low production areas, especially in the IOSG.

While the ε -ratio quantifies the POC fraction that is exported out of the productive layer, the transfer efficiency (T_{eff}) denotes the fraction of POC transferred from the base of the productive zone into the deep waters, bypassing remineralization in the mesopelagic zone (100–1000 m; *Francois et al., 2002*). Several studies suggested that T_{eff} is inversely related to the ε -ratio, resulting in highest T_{eff} in low latitude oligotrophic regions (*Francois et al., 2002; Lam et al., 2011; Guidi et al., 2015; Mouw et al., 2016; Henson et al., 2019*). However, other recent studies indicate the opposite, where T_{eff} is highest in high latitudes, intermediate in the tropics and lowest in the subtropical gyre regions (*Buesseler et al., 2007; DeVries and Deutsch, 2014; Marsay et al., 2015; Weber et al., 2016*).

Sediment trap moorings 04-03 and 04-04 allow a first estimate of the POC fraction that is transferred to the deep ocean. Our calculations show that approximately 20 % of the POC exported out of the productive zone (base of the productive zone ~130 m, see above) reaches a water depth of ~700 m (trap *Shallow*). The percentages further decrease towards ~2900 m (trap *Middle*; 10 %) and ~3500 m water depth (trap *Deep*; 7.4 %).

To conclude, the strongest decline in the POC content takes place within the surface layer (2.3 %, $\varepsilon = 0.023$), while the reduction is less pronounced below 700 m water depth. This matches previous observations that POC fluxes typically decrease exponentially in the upper water column and decline almost linearly towards the deep-sea (Suess, 1980; Armstrong *et al.*, 2002). Most water-column remineralization thus occurs at depths less than 1000 m and most of the POC passing 1000 m water depth in fact reach the ocean floor (Armstrong *et al.*, 2002). In summary, only 0.17 % of the POC produced in the biologically active zone reach the seafloor in the IOSG. This is in accordance with combined sediment trap studies in the open ocean where <1 % of surficial productivity reach depths of 4000 m (Suess, 1980; Martin *et al.*, 1987). Assuming that primary production generates $10 \text{ mol C m}^{-2} \text{ yr}^{-1}$ in the surface layer, we estimate that approximately $0.02 \text{ mol C m}^{-2} \text{ yr}^{-1}$ is transferred to the seabed. At the sediment-water interface further remineralisation/degradation or transport processes strongly diminish the POC that is finally accumulated in pelagic sediments (see section 5.4.).

5.3.4 Regional variability of POC fluxes in the IOSG

Subtropical gyres are often considered as relatively closed ocean regions with a high internal homogeneity (McClain *et al.*, 2004; Sarmiento and Gruber, 2006; Henson *et al.*, 2019). However, latitudinal variations in nitrate and chlorophyll-*a* concentrations, as well as in the POC flux of sinking particulate matter and OMLD, can be observed in the IOSG (Figure 5.6). Subsurface nitrate concentrations show a slight increase from north to south in the IOSG mirrored by a slight increase in chlorophyll-*a* concentration in surface waters. The OMLD corresponds to this trend and rises gradually from the northern study area towards the southern part. Variations of the OMLD generally affect the nutrient supply to the biologically active zone (Rixen *et al.*, 2019a), as a deeper OMLD entrains nutrient-enriched subsurface waters into the surface layer, leading to increases in primary production and generally to elevated particulate matter

export. Average POC fluxes, normalized to a water depth of 2000 m tend to increase towards the south. However, a statistical significance by using a multiple linear regression analyses (MLRA) of increasing POC fluxes towards the southern gyre margin was not found in *Harms et al.* (2021). Thus, there is no robust trend of increasing fluxes towards the south, and the spatial pattern of POC export to the deep ocean is homogeneous in the working area, in agreement with previous investigations in the IOSG (*McClain et al.*, 2004; *Sarmiento and Gruber*, 2006; *Henson et al.*, 2019).

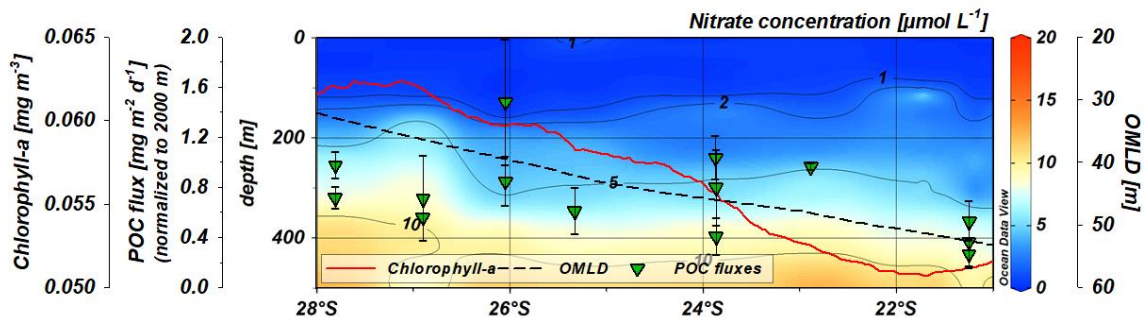


Figure 5.6. Latitudinal section from 28°S to 21°S. Colors and thin contour lines represent nitrate concentration ($\mu\text{mol L}^{-1}$) from INDEX expeditions between 2015 and 2019 (Figure 5.5a). Surface chlorophyll-*a* concentrations (thick red line; in mg m^{-3}) were taken from MODIS-Aqua (MODISA_L3m_CHLv2018; source: <https://giovanni.gsfc.nasa.gov/giovanni/>) as a zonal mean (monthly 4 km) during 2014–2019 within a region of 20°–30°S, 68°–74°E. Data on the ocean mixed layer depth (OMLD; black dashed line) are from the NOBM model (NORM-MONvR2017 h; source: <https://giovanni.gsfc.nasa.gov/giovanni/>) as a zonal mean over the time period from 2001–2019 within a region of 20°–30°S, 68°–74°E. Particulate organic carbon (POC) fluxes are normalized to 2000 m water depth and are shown as green triangles with standard deviation averaged for each sediment trap (except of traps *Shallow* and *Deep* of moorings 04-03 and 04-04).

5.3.5 Seasonal variability of POC fluxes in the IOSG

The maximum expansion of oligotrophic areas and thus lowest chlorophyll-*a* concentrations are observed during austral summer (January), while higher chlorophyll-*a* concentrations occur in austral winter (July; *McClain et al.*, 2004; Figure 5.1b, c). Subtropical gyres are in general regions of muted seasonality compared to other open ocean regions and have perennially low primary production rates (*Williams et al.*, 2013; *Baer et al.*, 2019; *Henson et al.*, 2019; Figure 5.1). As sediment trap data are often related to surface primary production (*Betzer*

et al., 1984), we would assume coherence between POC fluxes and chlorophyll-*a* concentrations. However, a comparison of our sediment trap data (2014–2019) with chlorophyll-*a* data (NASA Earth DataBase Giovanni) yields no positive correlation but rather a slightly negative relationship (Figure 5.7a). Averaging our 5-year data, there is no clearly discernible relationship between POC fluxes and chlorophyll-*a* concentrations (Figure 5.7b).

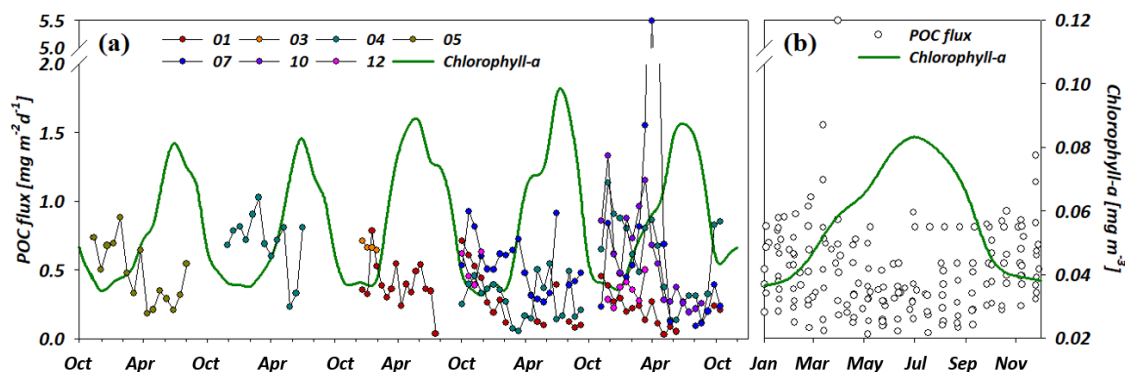


Figure 5.7. Time series data of particulate organic carbon (POC) fluxes and chlorophyll-*a* concentrations during sediment trap investigation between 2014 and 2019 in the INDEX area (a) and combined POC fluxes for a one-year period accompanied by average chlorophyll-*a* concentrations for the period 2014–2019 (b). Legend of panel a presents the cluster numbers of the INDEX area (see Figure 5.1). Chlorophyll-*a* concentrations were taken from MODIS-Aqua (MODISA_L3m_CHLv2018; NASA Earth DataBase Giovanni: <https://giovanni.gsfc.nasa.gov/giovanni/>) as monthly time series, area-averaged over 4 km during 01.12.2013–01.01.2020 within a region of 21°–28°S, 68°–74°E.

Major factors that interfere with the transmission of seasonally induced surface production signals are transformation and regeneration processes, ocean circulation and physical mixing due to enhanced wind stress, and variations in the OMLD (Siegel *et al.*, 1990; Asper *et al.*, 1992; Rixen *et al.*, 2019a). Especially in regions of low primary production and low seasonal variability, these mechanisms possibly alter surface production signals and temporal variations in the deep ocean biogeochemistry (Michaels *et al.*, 1994). To determine a potential interplay of processes that modify the export of POC in the IOSG, we compare the temporal variations in chlorophyll-*a* concentration, sea surface temperature (SST), OMLD, and sea surface wind speed (Figure 5.8a).

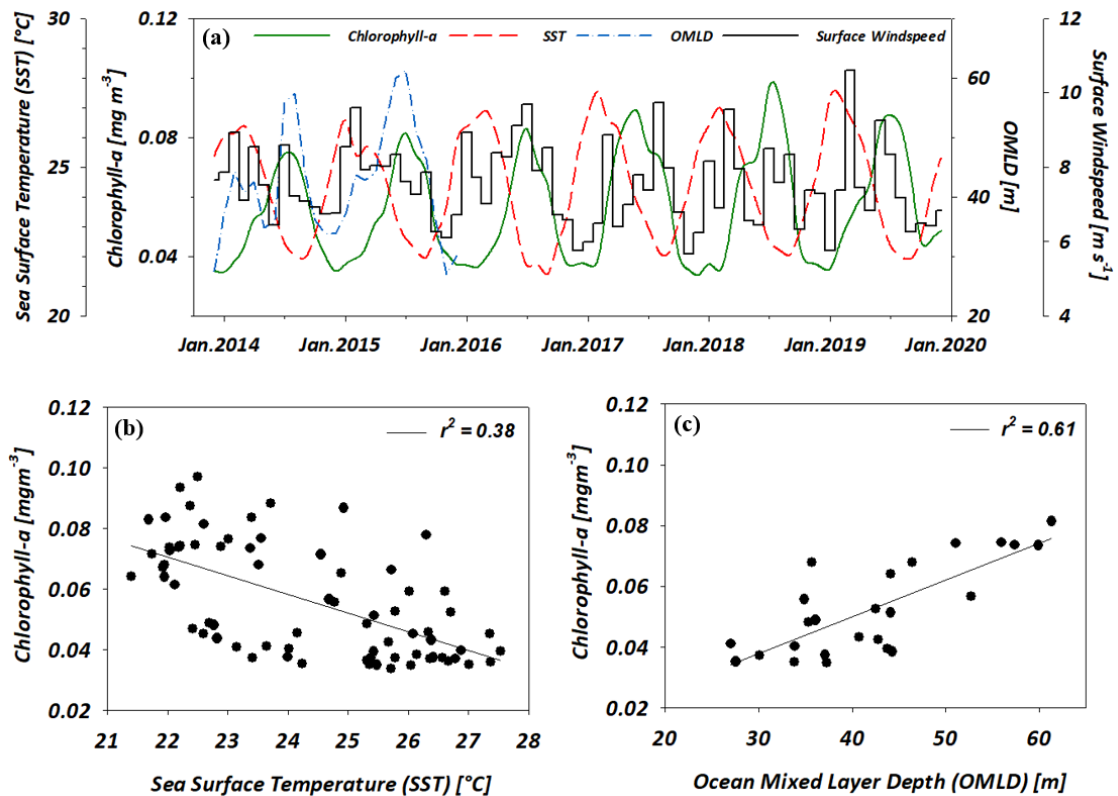


Figure 5.8. Fluctuations in chlorophyll-*a* concentration (in mg m⁻³), sea surface temperature (SST), ocean mixed layer depth (OMLD), and surface wind speed (in m s⁻¹) for the time interval of sediment trap deployments between 2014 and 2019 in the INDEX area (a). Chlorophyll-*a* concentrations are negatively correlated with their SST (b) and positively with the OMLD (c). Chlorophyll-*a* concentrations were taken from MODIS-Aqua (MODISA_L3m_CHL v2018; NASA Earth DataBase Giovanni: <https://giovanni.gsfc.nasa.gov/giovanni/>) as monthly time series, area-averaged over 4 km during 01.12.2013–01.01.2020 within a region of 21°–28°S, 68°–74°E. Data on the OMLD were derived from NOBM model (NORM-MON vR2017 h; NASA Earth DataBase Giovanni) as monthly time series, area-averaged over 0.67×1.25 deg. during 01.12.2013–01.12.2015 within a region of 21°–28°S, 68°–74°E. The SSTs were taken from MODIS-Aqua (MODISA-L3m_SST v2014; NASA Earth DataBase Giovanni) as monthly time series, area-averaged over 9 km during 01.12.2013–01.01.2020 within a region of 21°–28°S, 68°–74°E. Data on the sea surface wind speeds were retrieved from MERRa-2 Model (M2TMNXFLX_5_12_4_SPEED; NASA Earth DataBase Giovanni) as monthly time series, area-averaged over 0.5×0.625 deg. during 01.12.2013–01.01.2020 within a region of 21°–28°S, 68°–74°E.

Elevated SSTs in austral summer reflect strong surface stratification in the IOSG impeding upward nutrient supply to surface waters. This is reflected by a linear anti-correlation between SSTs and chlorophyll-*a* concentrations (Figure 5.8b) and by a positive linear correlation between OMLD and chlorophyll-*a* concentrations

(Figure 5.8c). A deeper OMLD in austral winter may increase the nutrient supply leading to elevated chlorophyll-*a* concentrations in this period. However, our POC flux data do not show a distinct correlation with chlorophyll-*a* concentrations. The POC export must therefore be affected by other processes. A deep OMLD was assumed to intensify degradation and regeneration of organic matter, thus attenuating POC export (Baer *et al.*, 2019). Hence, the increased OMLD significantly reduces POC fluxes during periods of higher primary production (higher chlorophyll-*a* concentrations), leading to a relatively constant rate of POC throughout the year.

Furthermore, physical forcing such as changes in surface wind velocities may influence the export of POC (Delman *et al.*, 2018; Rixen *et al.*, 2019a). At several trap stations, elevated wind speeds correspond to elevated POC fluxes (Harms *et al.*, 2021). Thus, higher-than-average deep vertical mixing may lead to increases in surface nutrient concentrations and trigger regional POC export. Until now, however, little is known about the link between surface wind speed and particulate matter fluxes in the IOSG. Even less is known about the overall seasonal fluctuations in the gyre strength and the volume transport of in- and outflows (McMonigal *et al.*, 2018). Studies on variations in the dynamics of eddies in the IOSG and their effects on biogeochemical processes and particulate matter fluxes are in very early stages. Enhanced cyclonic eddy-activities are observed between Australia and Madagascar in a wide band from ~20°S to 30°S, propagating westwards across our study area (Delman *et al.*, 2018) and might well influence particulate matter export. In the subtropical western North Pacific Ocean, cyclonic eddies are assumed to be an important mechanism for the nutrient supply to the euphotic zone and, thus, might lead to enhanced particulate matter export production (Honda *et al.*, 2018).

5.4 Particulate matter in surface sediments

Marine sediments are considered as the ultimate and final sediment trap of particles descending through the water column. To recognise epigenetic and early diagenetic overprinting and flux attenuation at the sediment-water interface, one needs to compare the particle composition of intercepted particles from the water column with corresponding surface sediments underneath. In our study, we examined 30 short sediment cores (max. 26 cm), retrieved during INDEX expeditions in 2015, 2017, and 2018 (Data on the first centimetre of

sediment cores are presented in Table A6.1 in the Appendix A6). Particle composition of surface sediments for the main components CaCO₃, LM, bOpal, OM, and total sulphur (TS) are shown in Figure 5.9.

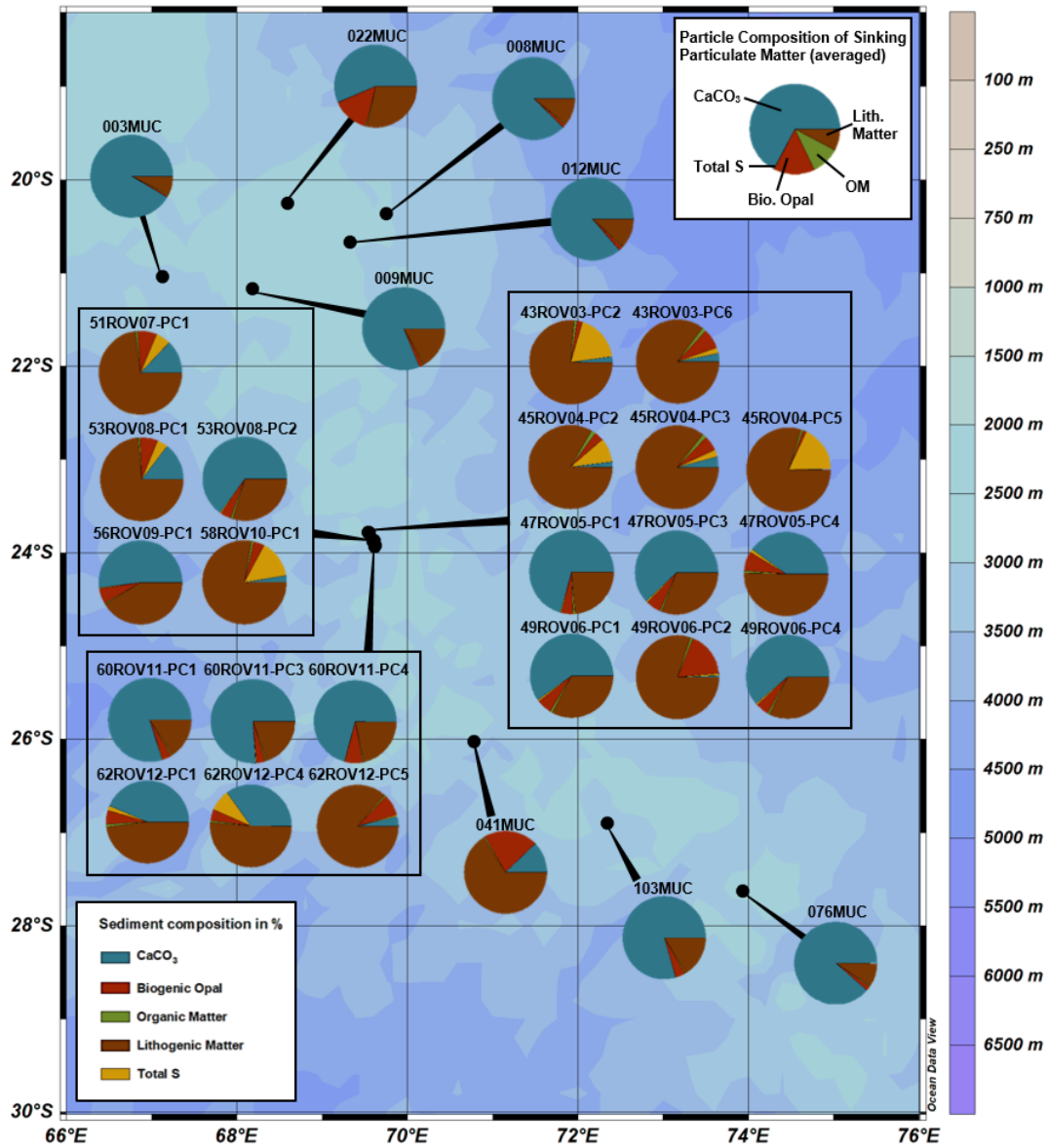


Figure 5.9. Particle compositions in surface sediments (0–1 cm) of push- and multicores taken during 2015, 2017, and 2018 in the INDEX area (see Table A6.1 in the Appendix A6). Diagrams show the individual components CaCO₃ (blue), biogenic opal (red), organic matter (green), lithogenic matter (brown), and total sulphur (yellow). The averaged particle composition of sinking particulate matter from sediment traps is presented for comparison (top right).

Due to hydrothermal activity at the seafloor in the INDEX area, sediments here are much more complex in terms of sedimentation processes and geochemical composition than average deep-sea sediments (Yokoyama *et al.*, 2015). For

example, active vents in the vicinity of mid-ocean ridges, completely change the geochemical environment with respect to pH, temperature, and the concentrations and ratios of most elements (*Urabe et al.*, 2015). This leads to diverse biological and ecological imprints on the biological activity on and within sediments and drives their physical alteration. Furthermore, the seafloor in these regions is not flat, but can be rough and steep. This in turn leads to erosion, sediment resuspension and dynamic particle transport processes. Thus, surface sediments are much more diverse in the vicinity of active and passive hydrothermal vent areas as compared to pelagic sediments elsewhere. This is reflected by surface sediments collected in the working area that reveal highly variable portions of the individual components CaCO₃, LM, bOpal, OM, and total sulphur (TS, Figure 5.9).

In order to compare the average particle composition of surface sediments and sinking particulate matter, we need to identify surface sediments largely unaffected by hydrothermal processes. In the following, we classify surface sediments in the INDEX area into three categories depending on the degree of influence by hydrothermal activity using their specific particle composition:

- Category 1: not affected (background sediment) with >75 % CaCO₃
- Category 2: moderately affected with >20 % LM plus TS
- Category 3: highly affected by hydrothermal activity with >50 % of LM plus TS.

Surface sediments of category 1 (003MUC, 008MUC, 009MUC, 012MUC, 076MUC, 103MUC, 60ROV11-PC1, 60ROV11-PC3; see Figure 5.9) are considered to represent background sedimentation and accumulation rates of POC in the subtropical Indian Ocean.

Throughout the earth's history, almost all preserved organic matter has been incorporated into marine sediments (*Hedges and Keil*, 1995). The most commonly cited preservation rate for organic matter in marine sediments by *Berner* (1982) shows that over 80 % of total organic carbon accumulation occurs in terrigenous delta regions near river mouths, while only ~2–4 % accumulates in pelagic sediments of low productive zones (*Hedges and Keil*, 1995; *Wilson et al.*, 1995). Key variables of final organic carbon storage in pelagic sediments are bulk sedimentation rates at the seabed and processes at the sediment-water interface (*Hedges and Keil*, 1995). The organic carbon from primary production preserved in sediments is positively correlated with bulk sedimentation rates (*Müller and Suess*, 1979; *Hedges and Keil*, 1995). Thus, little organic carbon is stored in the

sediments of open ocean regions that have low sedimentation rates and deep oxygen penetration depths (Müller and Suess, 1979; Hedges and Keil, 1995). In general, bulk sedimentation rates in open ocean regions are between 0.5 to 2 cm per 1000 years (Hüneke and Henrich, 2011), while low productive areas, like the Central Pacific, have even lower sedimentation rates of 0.2–0.6 cm per 1000 years (Müller and Suess, 1979). Accordingly, less than 0.01 % of the primary production becomes fossilized in pelagic sediments (Müller and Suess, 1979). For an assessment in the subtropical Indian Ocean, we first estimate bulk sedimentation rates of particulate matter reaching the seafloor based on our data of sinking particulate matter. In a second step, we estimate the POC potentially accumulating in surface sediments after degradation processes at the sediment-water interface.

Our study on sinking particulate matter fluxes reveals a total average mass flux of $10.6 \text{ mg m}^{-2} \text{ d}^{-1}$ ($0.00039 \text{ g cm}^{-2} \text{ yr}^{-1}$) at ~500–600 m.a.b., composed of 66.2 % CaCO_3 , 14.3 % bOpal, 9.9 % POM, and 9.6 % LM. To calculate the sedimentation rate (SR), we need the total density (ρ) of the accumulated material at the seafloor. Ramaswamy *et al.* (1991) calculated sedimentation rates with densities between 1.15 and 2.0 g cm^{-3} for sinking particulate matter. Regarding the individual densities for CaCO_3 ($\rho = 1.63 \text{ g cm}^{-3}$), bOpal ($\rho = 1.73 \text{ g cm}^{-3}$), POM ($\rho = 0.9 \text{ g cm}^{-3}$), and LM ($\rho = 2.7 \text{ g cm}^{-3}$) mentioned in Rixen *et al.* (2019b), we use an averaged sediment density of $\rho = 1.67 \text{ g cm}^{-3}$ for sinking particulate matter in the IOSG. The sedimentation rate

$$SR = \text{Total flux} / \rho \quad (5.3)$$

depends on the final mass flux and the density of sinking particulate matter ($\rho = 1.66 \text{ g cm}^{-3}$). Following this approach, our calculations suggest that the sedimentation rate is between 0.05 to 0.49 cm (\varnothing 0.23 cm) per 1000 years. This corresponds to the lower limit of sedimentation rates detected in the Central Pacific (0.2–0.6 cm per 1000 years; Müller and Suess, 1979).

However, the sedimentation rate estimated here represents the particulate matter that reaches the seafloor and ignores processes at the sediment-water interface. Because this interface is usually the site of an intense biological activity, a high portion of organic matter and inorganic components (mineralized tests) of the bottom-reaching particulate matter is decomposed/remineralized prior to the final burial in the sediments (Wilson *et al.*, 1985; Lochte *et al.*, 2003). It is assumed

that only 1–10 % of the POM flux arriving at the sediment-water interface is actually being buried in the sediments (*Bender and Heggie, 1984; Emerson et al., 1985; Emerson and Hedges, 1988; Hedges and Keil, 1995*). In our study, only ~4 % of the bottom-reaching POM flux accumulates in surface sediments. This corresponds with an approximate accumulation rate of $<0.001 \text{ mol C m}^{-2} \text{ yr}^{-1}$ in surface sediments. In other words, less than 0.01 % POC of the surface production is stored in pelagic sediments in the IOSG, similar to the estimates of *Müller and Suess (1979)*. Our estimates do not take into account mechanical diagenesis and compaction of the sediments.

5.5 Conclusion and implications

The oligotrophic Indian Ocean subtropical gyre (IOSG) is one of the least explored ocean regions in terms of sinking particulate matter and its final burial in pelagic sediments. It is one of the extensive oligotrophic areas that cover about 75 % of the ocean's surface and are assumed to account for half of the global organic carbon export to the ocean's interior (*Emerson et al., 1997*). These ocean regions are assumed to expand in future warmer climate (*Behrenfeld et al., 2006*) and thus become even more important on a global scale over the next decades.

In general, the IOSG is predominantly influenced by the typical flow-system of subtropical gyres leading to a centered depression of pycnoclines and nutriclines that induce strongly stratified and nutrient-depleted surface waters. As a result, the IOSG is characterized by overall low primary production rates, leading to worldwide lowest POC fluxes ($0.52 \pm 0.18 \text{ mg m}^{-2} \text{ d}^{-1}$ at ~500–600 m.a.b.) and very low POC export efficiency (0.023). Only approximately 0.17 % of the primarily produced POC in surface waters reaches the seafloor (Figure 5.10). The calculated bulk sedimentation rate is about 0.23 cm per 1000 years. Since further decomposition/remineralisation occurs at the sediment-water interface, only 4 % of the POC reaching the seafloor, or in other words less than 0.01 % of the primary production in the photic zone, finally accumulates in surface sediments. Consequently, at primary production rates of $10 \text{ mol C m}^{-2} \text{ yr}^{-1}$ in surface waters in the IOSG, $<0.001 \text{ mol C m}^{-2} \text{ yr}^{-1}$ ($0.02 \text{ mg m}^{-2} \text{ d}^{-1}$ POC) accumulates in surface sediments (Figure 5.10). Figure 5.10 shows a detailed concept of POC export, transfer efficiency, and the final burial rates in surface sediments.

Low primary production rates apparently lead to extremely low POC export and transfer efficiencies and finally to extraordinarily low POC accumulation rates in

surface sediments. Assuming that all subtropical gyres are characterized by these conditions (as has been postulated for the oligotrophic North Atlantic; *Henson et al.*, 2019) and considering an expansion of these areas under climate warming, this might have crucial impacts on the global carbon cycle. However, biogeochemical implications in terms of magnitude and trends are still uncertain. In addition, adaptations of food webs, biological community structure, or potential changes in global or regional circulation patterns to a warmer climate are yet poorly constrained. More interdisciplinary research will help to understand how the oligotrophic ocean gyres will change in times of global warming.

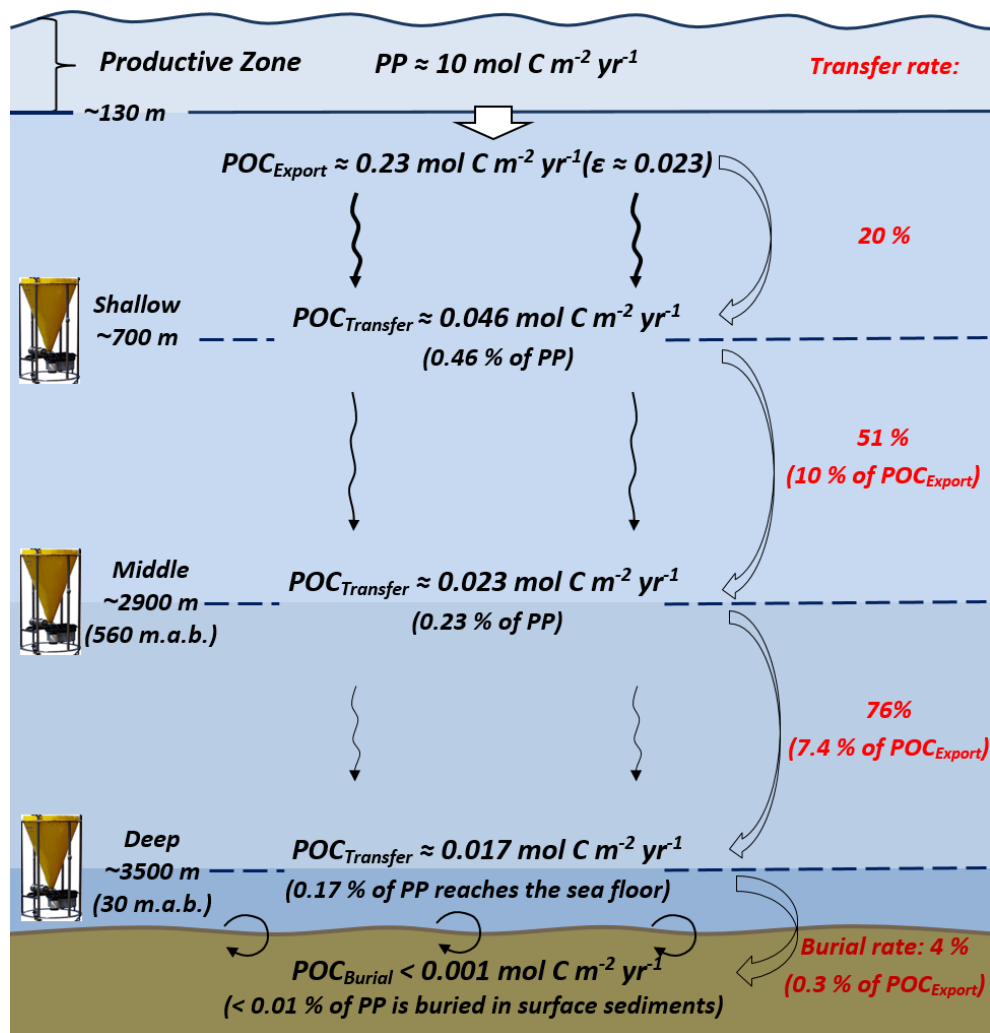


Figure 5.10. Schematic of the particulate organic carbon export (POC_{Export}) below the productive zone, its transfer ($POC_{Transfer}$) across the sediment trap depths of traps *Shallow* (~695 m), *Middle* (~2930 m), and *Deep* (~3465 m) of moorings 04-03 and 04-04, and its final burial (POC_{Burial}) into the deep-sea sediments (first centimeter). The abbreviation m.a.b. stands for meters above bottom. Percentages in red represent the transfer rate of POC between the different depth intervals.

Chapter 6

Conclusion and outlook

6.1 Conclusion

The oligotrophic Indian Ocean subtropical gyre (IOSG) is one of the least explored ocean regions in terms of nitrogen (N) cycle processes, sinking particulate matter, and the final carbon storage in deep-sea sediments. In general, the IOSG is predominantly influenced by the typical flow-system of subtropical gyres leading to a centered depression of pycno- and thermoclines that induce a thick ocean mixed layer with strongly stratified and nutrient-depleted surface waters. To improve the understanding of biogeochemical processes in the marine N and carbon (C) cycle in the IOSG, in this study I have combined investigations on the nutrient distribution and the isotopic composition of nitrate in water masses of the South Indian Ocean, on sediment trap-based sinking particulate matter fluxes, and on surface sediments.

First, my studies revealed that the local biogeochemical setting of the South Indian Ocean is influenced by the influx of preformed nutrients from the adjacent ocean regions. Water masses of Antarctic and subantarctic origin interfinger and converge with water masses of the southern equatorial Indian Ocean and the Arabian Sea. The influx of the Subantarctic Mode Water (SAMW) from the Southern Ocean injects oxygen-saturated waters with preformed nutrients, indicated by increased N and oxygen (O) isotope composition of nitrate ($\delta^{15}\text{N} > 7 \text{ ‰}$; $\delta^{18}\text{O} > 4 \text{ ‰}$) at 400–500 m ($26.6\text{--}26.7 \text{ kg m}^{-3}$) into the subtropical thermocline. These values reflect the partial N assimilation in the Southern Ocean. Moreover, in the northern study area, a residue of nitrate affected by denitrification in the Arabian Sea is imported into intermediate and deep water masses ($> 27.0 \text{ kg m}^{-3}$) of the gyre, indicated by an N deficit ($\text{N}^* \approx -1 \text{ to } -4 \text{ } \mu\text{mol L}^{-1}$) and by elevated isotopic ratios of nitrate ($\delta^{15}\text{N} > 7 \text{ ‰}$; $\delta^{18}\text{O} > 3 \text{ ‰}$). Thus, the

South Indian Ocean is supplied by preformed nutrients from the lateral influx of water masses from regions exhibiting distinctly different N cycle processes. Furthermore, I could show a local external source of nitrogen via dinitrogen (N_2) fixation at 20° – 24° S indicating that at least 32–34 % of the assimilated nitrate is provided from newly fixed N in surface waters. These results are a starting point to track the course of N cycle processes and budgets in a changing climate over the coming years under global warming.

The 5-year time series of sediment trap experiments are the first in the IOSG and give new insights into the POC export and transfer efficiencies down to the seafloor and the final accumulation rates in the surface sediments. My research has shown that the IOSG has the worldwide lowest recorded total mass fluxes and POC fluxes of 9.8 – $10.6 \text{ mg m}^{-2} \text{ day}^{-1}$ and $\sim 0.5 \text{ mg m}^{-2} \text{ day}^{-1}$, respectively, measured at 500–600 m above bottom (2600–3500 m water depth). These low fluxes are the result of the strongly stratified and nutrient-depleted surface waters in the IOSG, leading to low primary production rates and consequently to low sedimentation rates of $\sim 0.23 \text{ cm}$ per 1000 years. Preliminary estimates indicated an extremely low POC export efficiency of $\varepsilon \approx 0.02$ – 0.03 , leading to low accumulation rates of organic carbon in the surface sediments. Here, only 4 % of the POC reaching the seafloor accumulate in surface sediments due to further organic matter degradation at the sediment-water interface. Assuming primary production rates of 7 – $10 \text{ mol C m}^{-2} \text{ year}^{-1}$ in surface waters, only ~ 0.01 % of the initial production in the euphotic zone, or in other words, only $\sim 0.001 \text{ mol C m}^{-2} \text{ year}^{-1}$ (0.02 – $0.03 \text{ mg m}^{-2} \text{ day}^{-1}$ POC) accumulates in surface sediments. This is extremely low by global standards. Moreover, only small regional and temporal variabilities were observed for the IOSG and I have pointed out the lack of seasonality in the POC fluxes that is caused by intense organic matter degradation, variations in the ocean mixed layer depth (OMLD), and impacts by physical mixing (surface wind stress, cyclonic eddies). These investigations contribute to baseline knowledge on C cycle budgets and CO_2 sequestration in the global oceans.

The vast oligotrophic gyres are regions that will most likely expand in future warmer times (*Behrenfeld et al.*, 2006) and there are indications that CO_2 uptake via the organic carbon pump responds to climate change (e.g., *Riebesell et al.*, 2007; *Duce et al.*, 2008; *DeVries and Deutsch*, 2014; *Laufkötter et al.*, 2017). Thus, these areas will become even more important on a global scale during the next decades and are of major importance in terms of N and C cycle processes. Models have

assumed that enhanced stratification in low-latitude oceans lead to a decrease of the already low net primary production under climate warming (*Behrenfeld et al., 2006*). This might also weaken the organic carbon pump and reduce the transfer of carbon to the deep oceans. As yet, the decrease in baseline fluxes and the potential extent of subtropical gyres are unknown and possible adaptations in food webs, biological community structure, or potential adaptations of global or regional circulation patterns to a warmer climate are still under debate. For example, it remains an open question whether primary production will be offset by enhanced N_2 fixation in warmer oceans. Furthermore, the magnitude and even the trends of impacts of changing climate, including its biological carbon pumps, on the biogeochemistry of oligotrophic ocean areas are uncertain (*Passow and Carlson, 2012; Laufkötter et al., 2017; Laufkötter and Gruber, 2018*). Additionally, there is reason to believe that other regions (e.g., the Southern Ocean, the eastern boundary upwelling systems) might compensate for decreasing exports of carbon in the subtropical gyres (*Laufkötter and Gruber, 2018*). Thus, it is unclear how and in which way the changing oligotrophic regions will contribute to global pattern under climate warming. Furthermore, *Yang et al. (2020)* supposed a consistent poleward shift of the major ocean gyres in a warmer climate driven by a systematic poleward displacement of the extratropical atmospheric circulation. This highlights the strong relationship between atmospheric and oceanic circulation patterns and thus both systems are close-coupled and both must be considered in predicting impacts of a changing climate.

6.2 Outlook

More interdisciplinary research is needed in dedicated follow-up studies based on experimental approaches, time series observation, remote sensing, and biogeochemical modelling to understand how the extensive oligotrophic ocean regions will change under global warming and how that affects global N and C budgets. In detail, it is mandatory to raise more observational data on N_2 fixation to quantify the external input of N to the surface ocean, and to establish the magnitude of its contribution to primary and recycled production and thus to total organic matter production and export fluxes. Furthermore, investigation on dissolved organic nitrogen (DON), dissolved organic carbon (DOC), and on suspended matter in the water column are prerequisite to understand how the large pool of organic components (not covered by the collection of sinking

particulate matter) in the ocean responds to warming and putative changes in plankton communities. These aspects beginning to attract increasing scientific attention. Additionally, more data on POC fluxes, its organic matter quality (e.g., by using amino acids), and direct measurements of primary production are necessary to better quantify and make more reliable assumptions on the organic carbon pump and CO₂ sequestration in the IOSG. The impact of variations in the gyre strength and of eddy diffusion processes in the IOSG are uncertain, but may be of major importance for the nutrient supply and thus for the magnitude of primary production that is close-coupled to particulate matter fluxes and organic carbon burial. Thus, interdisciplinary research on geochemical, geophysical, and biological questions is indispensable to understand the complex ecosystem of subtropical gyres in general and the IOSG in particular.

References

- Anderson, L. A., 1995. On the hydrogen and oxygen content of marine phytoplankton. *Deep-Sea Research Part I: Oceanographic Research Papers*, 42, 1675–1680. [https://doi.org/10.1016/0967-0637\(95\)00072-E](https://doi.org/10.1016/0967-0637(95)00072-E).
- Antia, A. N., von Bodungen, B., Peinert, R., 1999. Particle flux across the mid-European continental margin. *Deep-Sea Research Part I: Oceanographic Research Papers*, 46, 1999–2024. [https://doi.org/10.1016/S0967-0637\(99\)00041-2](https://doi.org/10.1016/S0967-0637(99)00041-2).
- Armstrong, R. A., Lee, C., Hedges, J. I., Honjo, S., Wakeham, S. G., 2002. A new, mechanistic model for organic carbon fluxes in the ocean based on the quantitative association of POC with ballast minerals. *Deep-Sea Research Part II: Topical Studies in Oceanography*, 49, 219–236. [https://doi.org/10.1016/S0967-0645\(01\)00101-1](https://doi.org/10.1016/S0967-0645(01)00101-1).
- Asper, V. L., Deuser, W., Knauer, G., Lohrenz, S. E., 1992. Rapid coupling of sinking particle fluxes between surface and deep ocean waters. *Nature*, 357, 670–672. <https://doi.org/10.1038/357670a0>.
- Baer, S. E., Rauschenberg, S., Garcia, C. A., Garcia, N. S., Martiny, A. C., Twining, B. S., Lomas, M. W., 2019. Carbon and nitrogen productivity during spring in the oligotrophic Indian Ocean along the GO-SHIP IO9N transect. *Deep-Sea Research Part II: Topical Studies in Oceanography*, 161, 81–91. <https://doi.org/10.1016/j.dsr2.2018.11.008>.
- Baker, A., Kelly, S., Biswas, K., Witt, M., Jickells, T., 2003. Atmospheric deposition of nutrients to the Atlantic Ocean. *Geophysical Research Letters*, 30, 1–4. <https://doi.org/10.1029/2003GL018518>.
- Bange, H. W., Naqvi, S. W. A., Codispoti, L., 2005. The nitrogen cycle in the Arabian Sea. *Progress in Oceanography*, 65, 145–158. <https://doi.org/10.1016/j.pocean.2005.03.002>.

- Bathmann, U. V., Peinert, R., Noji, T. T., von Bodungen, B., 1990. Pelagic origin and fate of sedimenting particles in the Norwegian Sea. *Progress in Oceanography*, 24, 117–125. [https://doi.org/10.1016/0079-6611\(90\)90024-V](https://doi.org/10.1016/0079-6611(90)90024-V).
- Baumgartner, A., Reichel, E., 1975. The world water balance: Mean annual global, continental and maritime precipitation evaporation and run-off. Elsevier Science Inc, 179 pp.
- Behrenfeld, M. J., Falkowski, P. G., 1997. Photosynthetic rates derived from satellite-based chlorophyll concentration. *Limnology and Oceanography*, 42, 1–20. <https://doi.org/10.4319/lo.1997.42.1.0001>.
- Behrenfeld, M. J., O'Malley, R. T., Siegel, D. A., McClain, C. R., Sarmiento, J. L., Feldman, G. C., Milligan, A. J., Falkowski, P. G., Letelier, R. M., Boss, E. S., 2006. Climate-driven trends in contemporary ocean productivity. *Nature*, 444, 752–755. <https://doi.org/10.1038/nature05317>.
- Bender, M. L., Heggie, D. T., 1984. Fate of organic carbon reaching the sea floor: A status report. *Geochimica Cosmochimica Acta* 48, 977–986. [https://doi.org/10.1016/0016-7037\(84\)90189-3](https://doi.org/10.1016/0016-7037(84)90189-3).
- Berelson, W. M., 2001. Particle settling rates increase with depth in the ocean. *Deep-Sea Research Part II: Topical Studies in Oceanography*, 49, 237–251. [https://doi.org/10.1016/S0967-0645\(01\)00102-3](https://doi.org/10.1016/S0967-0645(01)00102-3).
- Berger, W., 1978. Deep-sea carbonate: pteropod distribution and the aragonite compensation depth. *Deep-Sea Research*, 25, 447–452. [https://doi.org/10.1016/0146-6291\(78\)90552-0](https://doi.org/10.1016/0146-6291(78)90552-0).
- Berger, W., Smetacek, V., Wefer, G., 1989. Ocean productivity and paleoproductivity—an overview, in: W. H. Berger, V. Smetacek, G. Wefer (Eds.), *Productivity of the Ocean: Present and Past*, vol. 44. Wiley New York, pp. 1–34.
- Berman-Frank, I., Cullen, J. T., Shaked, Y., Sherrell, R. M., Falkowski, P. G., 2001. Iron availability, cellular iron quotas, and nitrogen fixation in *Trichodesmium*. *Limnology and Oceanography*, 46, 1249–1260. <https://doi.org/10.4319/lo.2001.46.6.1249>.

- Berner, R. A., 1982. Burial of organic carbon and pyrite sulfur in the modern ocean: its geochemical and environmental significance. *American Journal of Science*, (U.S.A.), 282, 451–473. <https://doi.10.2475/ajs.282.4.451>.
- Betzer, P. R., Showers, W. J., Laws, E. A., Winn, C. D., DiTullio, G. R., Kroopnick, P. M., 1984. Primary productivity and particle fluxes on a transect of the equator at 153°W in the Pacific Ocean. *Deep-Sea Research Part I: Oceanographic Research Papers*, 31, 1–11. [https://doi.org/10.1016/0198-0149\(84\)90068-2](https://doi.org/10.1016/0198-0149(84)90068-2).
- Bianchi, M., Feliatra, F., Tréguer, P., Vincendeau, M.-A., Morvan, J., 1997. Nitrification rates, ammonium and nitrate distribution in upper layers of the water column and in sediments of the Indian sector of the Southern Ocean. *Deep-Sea Research Part II: Topical Studies in Oceanography*, 44, 1017–1032. [https://doi.org/10.1016/S0967-0645\(96\)00109-9](https://doi.org/10.1016/S0967-0645(96)00109-9).
- Bindoff, N. L., McDougall, T. J., 2000. Decadal changes along an Indian Ocean section at 32°S and their interpretation. *Journal of Physical Oceanography*, 30, 1207–1222. [https://doi.org/10.1175/1520-0485\(2000\)030<1207:DCAAIO>2.0.CO;2](https://doi.org/10.1175/1520-0485(2000)030<1207:DCAAIO>2.0.CO;2).
- Böhlke, J. K., Mroczkowski, S. J., Coplen, T. B., 2003. Oxygen isotopes in nitrate: new reference materials for ^{18}O : ^{17}O : ^{16}O measurements and observations on nitrate-water equilibration. *Rapid Communications in Mass Spectrometry*, 17, 1835–1846. <https://doi.org/10.1002/rcm.1123>.
- Bory, A., Jeandel, C., Leblond, N., Vangriesheim, A., Khripounoff, A., Beaufort, L., Rabouille, C., Nicolas, E., Tachikawa, K., Etcheber, H., 2001. Downward particle fluxes within different productivity regimes off the Mauritanian upwelling zone (EUMELI program). *Deep-Sea Research Part I: Oceanographic Research Papers*, 48, 2251–2282. [https://doi.org/10.1016/S0967-0637\(01\)00010-3](https://doi.org/10.1016/S0967-0637(01)00010-3).
- Bourbonnais, A., Lehmann, M. F., Hamme, R. C., Manning, C. C., Juniper, S. K., 2013. Nitrate elimination and regeneration as evidenced by dissolved inorganic nitrogen isotopes in Saanich Inlet, a seasonally anoxic fjord. *Marine Chemistry*, 157, 194–207. <https://doi.org/10.1016/j.marchem.2013.09.006>.

- Bourbonnais, A., Lehmann, M. F., Waniek, J. J., Schulz-Bull, D. E., 2009. Nitrate isotope anomalies reflect N₂ fixation in the Azores Front region (subtropical NE Atlantic). *Journal of Geophysical Research: Oceans*, 114, 1-16. <https://doi.org/10.1029/2007JC004617>.
- Boyd, P. W., Watson, A. J., Law, C. S., Abraham, E. R., Trull, T., Murdoch, R., Bakker, D. C. E., Bowie, A. R., Buesseler, K. O., Chang, H., Charette, M., Croot, P., Downing, K., Frew, R., Gall, M., Hadfield, M., Hall, J., Harvey, M., Jameson, G., LaRoche, J., Liddicoat, M., Ling, R., Maldonado, M. T., McKay, R. M., Nodder, S., Pickmere, S., Pridmore, R., Rintoul, S., Safi, K., Sutton, P., Strzepek, R., Tanneberger, K., Turner, S., Waite, A., Zeldis, J., 2000. A mesoscale phytoplankton bloom in the polar Southern Ocean stimulated by iron fertilization. *Nature*, 407, 695–702. <https://doi.org/10.1038/35037500>.
- Brandes, J. A., Devol, A. H., Yoshinari, T., Jayakumar, D. A., Naqvi, S. W. A., 1998. Isotopic composition of nitrate in the central Arabian Sea and eastern tropical North Pacific: A tracer for mixing and nitrogen cycles. *Limnology and Oceanography*, 43, 1680–1689. <https://doi.org/10.4319/lo.1998.43.7.1680>.
- Breitbarth, E., Oschlies, A., LaRoche, J., 2007. Physiological constraints on the global distribution of *Trichodesmium* - effect of temperature on diazotrophy. *Biogeosciences*, 4, 53–61.
- Buchwald, C., Casciotti, K. L., 2010. Oxygen isotopic fractionation and exchange during bacterial nitrite oxidation. *Limnology and Oceanography*, 55, 1064–1074. <https://doi.org/10.4319/lo.2010.55.3.1064>, 2010.
- Buesseler, K. O., Lamborg, C. H., Boyd, P. W., Lam, P. J., Trull, T. W., Bidigare, R. R., Bishop, J. K. B., Casciotti, K. L., Dehairs, F., Elskens, M., Honda, M., Karl, D. M., Siegel, D. A., Silver, M. W., Steinberg, D. K., Valdes, J., Van Mooy, B., Wilson, S., 2007. Revisiting carbon flux through the ocean's twilight zone. *Science*, 316, 567–570. <https://doi.10.1126/science.1137959>.
- Buesseler, K. O., Steinberg, D. K., Michaels, A. F., Johnson, R. J., Andrews, J. E., Valdes, J. R., Price, J. F., 2000. A comparison of the quantity and composition of material caught in a neutrally buoyant versus surface-tethered sediment trap. *Deep-Sea Research Part I: Oceanographic Research Papers*, 47, 277–294. [https://doi.org/10.1016/S0967-0637\(99\)00056-4](https://doi.org/10.1016/S0967-0637(99)00056-4).

- Capone, D. G., Zehr, J. P., Paerl, H. W., Bergman, B., Carpenter, E. J., 1997. Trichodesmium, a Globally Significant Marine Cyanobacterium. *Science*, 276, 1221-1229. <https://doi.org/10.1126/science.276.5316.1221>.
- Carpenter, E. J., Harvey, H. R., Fry, B., Capone, D. G., 1997. Biogeochemical tracers of the marine cyanobacterium Trichodesmium. *Deep-Sea Research Part I: Oceanographic Research Papers*, 44, 27–38. [https://doi.org/10.1016/S0967-0637\(96\)00091-X](https://doi.org/10.1016/S0967-0637(96)00091-X).
- Casciotti, K. L., McIlvin, M., Buchwald, C., 2010. Oxygen isotopic exchange and fractionation during bacterial ammonia oxidation. *Limnology and Oceanography*, 55, 753–762. <https://doi.org/10.4319/lo.2010.55.2.0753>.
- Casciotti, K. L., Sigman, D. M., Hastings, M. G., Böhlke, J., Hilkert, A., 2002. Measurement of the oxygen isotopic composition of nitrate in seawater and freshwater using the denitrifier method. *Analytical Chemistry*, 74, 4905–4912. <https://doi.org/10.1021/ac020113w>.
- Casciotti, K. L., Trull, T., Glover, D., Davies, D., 2008. Constraints on nitrogen cycling at the subtropical North Pacific Station ALOHA from isotopic measurements of nitrate and particulate nitrogen. *Deep-Sea Research Part II: Topical Studies in Oceanography*, 55, 1661–1672, <https://doi.org/10.1016/j.dsr2.2008.04.017>.
- Clark, D. R., Rees, A. P., Joint, I., 2008. Ammonium regeneration and nitrification rates in the oligotrophic Atlantic Ocean: Implications for new production estimates. *Limnology and Oceanography*, 53, 52–62. <https://doi.org/10.4319/lo.2008.53.1.0052>.
- Cobler, R., Dymond, J., 1980. Sediment trap experiment on the Galapagos spreading center, equatorial Pacific. *Science*, 209, 801–803. <https://doi.org/10.1126/science.209.4458.801>.
- Codispoti, L., Brandes, J. A., Christensen, J., Devol, A., Naqvi, S., Paerl, H. W., Yoshinari, T., 2001. The oceanic fixed nitrogen and nitrous oxide budgets: Moving targets as we enter the anthropocene? *Scientia Marina*, 65, 85–105. <https://doi.org/10.3989/scimar.2001.65s285>.

- Collier, R., Dymond, J., Honjo, S., Manganini, S., Francois, R., Dunbar, R. B., 2000. The vertical flux of biogenic and lithogenic material in the Ross Sea: moored sediment trap observations 1996–1998. *Deep-Sea Research Part II: Topical Studies in Oceanography*, 47, 3491–3520. [https://doi.org/10.1016/S0967-0645\(00\)00076-X](https://doi.org/10.1016/S0967-0645(00)00076-X).
- Conte, M. H., Ralph, N., Ross, E. H., 2001. Seasonal and interannual variability in deep ocean particle fluxes at the Oceanic Flux Program (OFP)/Bermuda Atlantic Time Series (BATS) site in the western Sargasso Sea near Bermuda. *Deep-Sea Research Part II: Topical Studies in Oceanography*, 48, 1471–1505. [https://doi.org/10.1016/S0967-0645\(00\)00150-8](https://doi.org/10.1016/S0967-0645(00)00150-8).
- Cram, J. A., Weber, T., Leung, S. W., McDonnell, A. M., Liang, J. H., Deutsch, C., 2018. The role of particle size, ballast, temperature, and oxygen in the sinking flux to the deep sea. *Global Biogeochemical Cycles*, 32, 858–876. <https://doi.org/10.1029/2017GB005710>.
- Crawford, D. W., Purdie, D. A., 1997. Increase of pCO₂ during blooms of *Emiliana huxleyi*: Theoretical considerations on the asymmetry between acquisition of HCO₃⁻ and respiration of free CO₂. *Limnology and Oceanography*, 42, 365–372. <https://doi.org/10.4319/lo.1997.42.2.0365>.
- Csögör, Z., Melgar, D., Schmidt, K., Posten, C., 1999. Production and particle characterization of the frustules of *Cyclotella cryptica* in comparison with siliceous earth. *Progress in Industrial Microbiology*, 35, 71–75. [https://doi.org/10.1016/S0079-6352\(99\)80100-3](https://doi.org/10.1016/S0079-6352(99)80100-3).
- Deacon, G. E., 1933. A general account of the hydrology of the South Atlantic Ocean. *Discovery Reports*, 7, 171–238.
- Delman, A. S., Lee, T., Qiu, B., 2018. Interannual to Multidecadal Forcing of Mesoscale Eddy Kinetic Energy in the Subtropical Southern Indian Ocean. *Journal of Geophysical Research: Oceans*, 123, 8180–8202. <https://doi.org/10.1029/2018JC013945>.
- DeMaster, D. J., 1981. The supply and accumulation of silica in the marine environment. *Geochimica et Cosmochimica Acta*, 45, 1715–1732. [https://doi.org/10.1016/0016-7037\(81\)90006-5](https://doi.org/10.1016/0016-7037(81)90006-5).

- DeMaster, D. J., 2003. The diagenesis of biogenic silica: Chemical transformations occurring in the water column, seabed, and crust, in: H. D. Holland, K. Karl, (Eds.), *Treatise on Geochemistry*, 7, 407 pp. Pergamon, Oxford, pp. 87–98.
- Deuser, W. G., Ross, E. H., Anderson, R. F., 1981. Seasonality in the supply of sediment to the deep Sargasso Sea and implications for the rapid transfer of matter to the deep ocean. *Deep-Sea Research Part I: Oceanographic Research Papers*, 28, 495–505. [https://doi.org/10.1016/0198-0149\(81\)90140-0](https://doi.org/10.1016/0198-0149(81)90140-0).
- Deutsch, C., Gruber, N., Key, R. M., Sarmiento, J. L., Ganachaud, A., 2001. Denitrification and N₂ fixation in the Pacific Ocean. *Global Biogeochemical Cycles*, 15, 483–506. <https://doi.org/10.1029/2000GB001291>.
- Deutsch, C., Sarmiento, J. L., Sigman, D. M., Gruber, N., Dunne, J. P., 2007. Spatial coupling of nitrogen inputs and losses in the ocean. *Nature*, 445, 163–167, <https://doi.org/10.1038/nature05392>.
- DeVries, T., Deutsch, C., 2014. Large-scale variations in the stoichiometry of marine organic matter respiration. *Nature Geoscience*, 7, 890–894. <https://doi.org/10.1038/ngeo2300>.
- DiFiore, P. J., Sigman D. M., Karsh Kristen, L., Trull Thomas, W., Dunbar Robert, B., Robinson Rebecca, S., 2010. Poleward decrease in the isotope effect of nitrate assimilation across the Southern Ocean. *Geophysical Research Letters*, 37, 1–5. <https://doi.org/10.1029/2010GL044090>.
- DiFiore, P. J., Sigman, D. M., Trull, T. W., Lourey, M. J., Karsh, K., Cane, G., Ho, R., 2006. Nitrogen isotope constraints on subantarctic biogeochemistry. *Journal of Geophysical Research: Oceans*, 111, 1–19. <https://doi.org/10.1029/2005JC003216>.
- Donaghay, P. L., DeManche, J. M., Small, L. F., 1978. On predicting phytoplankton growth rates from carbon: nitrogen ratios. *Limnology and Oceanography*, 23, 359–362. <https://doi.org/10.4319/lo.1978.23.2.0359>.
- Duce, R. A., LaRoche, J., Altieri, K., Arrigo, K., Baker, A., Capone, D., Cornell, S., Dentener, F., Galloway, J., Ganeshram, R., 2008. Impacts of atmospheric anthropogenic nitrogen on the open ocean. *Science*, 320, 893–897. <https://doi.org/10.1126/science.1150369>.

- Duce, R. A., Tindale, N. W., 1991. Atmospheric transport of iron and its deposition in the ocean. *Limnology and Oceanography*, 36, 1715–1726, <https://doi.org/10.4319/lo.1991.36.8.1715>.
- Ducklow, H. W., Steinberg, D. K., Buesseler, K. O., 2001. Upper ocean carbon export and the biological pump. *Oceanography Washington D. C., Oceanography Society*, 14, 50–58. <https://doi.org/10.5670/oceanog.2001.06>.
- Duing, W., 1970. The monsoon regime of the currents in the Indian Ocean: Hawaii institute of Geophysics Honolulu, 68 pp.
- Dunbar, R. B., Leventer, A. R., Mucciarone, D. A., 1998. Water column sediment fluxes in the Ross Sea, Antarctica: atmospheric and sea ice forcing. *Journal of Geophysical Research*, 103, 30741–30759. <https://doi.org/10.1029/1998JC900001>.
- Dunne, J. P., Armstrong, R. A., Gnanadesikan, A., Sarmiento, J. L., 2005. Empirical and mechanistic models for the particle export ratio. *Global Biogeochemical Cycles*, 19, 1–16. <https://doi.org/10.1029/2004GB002390>.
- Duteil, O., Koeve, W., Oschlies, A., Aumont, O., Bianchi, D., Bopp, L., Galbraith, E., Matear, R., Moore, J., Sarmiento, J. L., 2012. Preformed and regenerated phosphate in ocean general circulation models: can right total concentrations be wrong? *Biogeosciences*, 9, 1797–1807. <https://doi.org/10.5194/bg-9-1797-2012>.
- Dymond, J., Collier, R., 1988. Biogenic particle fluxes in the equatorial Pacific: Evidence for both high and low productivity during the 1982–1983 El Niño. *Global Biogeochemical Cycles*, 2, 129–137. <https://doi.org/10.1029/GB002i002p00129>.
- Dymond, J., Lyle, M., 1985. Flux comparisons between sediments and sediment traps in the eastern tropical Pacific: Implications for atmospheric CO₂ variations during the Pleistocene 1. *Limnology and Oceanography*, 30, 699–712. <https://doi.org/10.4319/lo.1985.30.4.0699>.
- Dymond, J., Lyle, M., 1994. Particle fluxes in the ocean and implications for sources and preservation of ocean sediments, in: *Material Fluxes on the Surface of the Earth*, edited by NRC, National Academy Press, D. C., pp 125–142.

- Emerson, S., Fischer, K., Reimers, C., Heggie, D., 1985. Organic carbon dynamics and preservation in deep-sea sediments. *Deep-Sea Research*, 32, 1–21. [https://doi.org/10.1016/0198-0149\(85\)90014-7](https://doi.org/10.1016/0198-0149(85)90014-7).
- Emerson, S., Hedges, J. I., 1988. Processes controlling the organic carbon content of open ocean sediments. *Paleoceanography*, 3, 611–634. <https://doi.org/10.1029/PA003i005p00621>.
- Emerson, S., Mecking, S., Abell, J., 2001. The biological pump in the subtropical North Pacific Ocean: Nutrient sources, Redfield ratios, and recent changes. *Global Biogeochemical Cycles*, 15, 535–554. <https://doi.org/10.1029/2000GB001320>.
- Emerson, S., Quay, P., Karl, D., Winn, C., Tupas, L., Landry, M., 1997. Experimental determination of the organic carbon flux from open-ocean surface waters. *Nature*, 389, 951–954. <https://doi.org/10.1038/40111>.
- Emery, W. J., 2001. Water types and water masses. *Encyclopedia of ocean sciences*, 6, 3179–3187. <https://doi.org/10.1006/rwos.2001.0108>.
- Emery, W. J., Meincke, J., 1986. Global water masses: summary and review. *Oceanologica Acta*, 9, 383–391.
- Engel, A., Szlosek, J., Abramson, L., Liu, Z., Lee, C., 2009. Investigating the effect of ballasting by CaCO₃ in *Emiliana huxleyi*: I. Formation, settling velocities and physical properties of aggregates. *Deep-Sea Research Part II: Topical Studies in Oceanography*, 56, 1396–1407. <https://doi.org/10.1016/j.dsr2.2008.11.027>.
- Eppley, R. W., Peterson, B. J., 1979. Particulate organic matter flux and planktonic new production in the deep ocean. *Nature*, 282, 677–680. <https://doi.org/10.1038/282677a0>.
- Fabres, J., Calafat, A., Sanchez-Vidal, A., Canals, M., Heussner, S., 2002. Composition and spatio-temporal variability of particle fluxes in the Western Alboran Gyre, Mediterranean Sea. *Journal of marine systems*, 33, 431–456. [https://doi.org/10.1016/S0924-7963\(02\)00070-2](https://doi.org/10.1016/S0924-7963(02)00070-2).
- Fine, R. A., 1993. Circulation of Antarctic intermediate water in the South Indian Ocean. *Deep-Sea Research Part I: Oceanographic Research Papers* 40, 2021–2042. [https://doi.org/10.1016/0967-0637\(93\)90043-3](https://doi.org/10.1016/0967-0637(93)90043-3).

- Fischer, G., Donner, B., Ratmeyer, V., Davenport, R., Wefer, G., 1996. Distinct year-to-year particle flux variations off Cape Blanc during 1988–1991: Relation to $\delta^{18}\text{O}$ -deduced sea-surface temperatures and trade winds. *Journal of Marine Research*, 54, 73–98. <https://doi.org/10.1357/0022240963213484>.
- Fischer, G., Ratmeyer, V., Wefer, G., 2000. Organic carbon fluxes in the Atlantic and the Southern Ocean: relationship to primary production compiled from satellite radiometer data. *Deep-Sea Research Part II: Topical Studies in Oceanography*, 47, 1961–1997. [https://doi.org/10.1016/S0967-0645\(00\)00013-8](https://doi.org/10.1016/S0967-0645(00)00013-8).
- Follows, M. J., Ito, T., Marotzke, J., 2002. The wind-driven, subtropical gyres and the solubility pump of CO_2 . *Global biogeochemical cycles*, 16, 1–9. <https://doi.org/10.1029/2001GB001786>.
- Francois, R., Honjo, S., Krishfield, R., Manganini, S., 2002. Factors controlling the flux of organic carbon to the bathypelagic zone of the ocean. *Global Biogeochemical Cycles*, 16, 1–20. <https://doi.org/10.1029/2001GB001722>.
- Fumenia, A., Moutin, T., Bonnet, S., Benavides, M., Petrenko, A., Helias Nunige, S., Maes, C., 2018. Excess nitrogen as a marker of intense dinitrogen fixation in the Western Tropical South Pacific Ocean: impact on the thermocline waters of the South Pacific. *Biogeosciences Discussions*, 10, 1–33. <https://doi.10.5194/bg-2017-557>.
- Gaye, B., Nagel, B., Dähnke, K., Rixen, T., Emeis, K. C., 2013. Evidence of parallel denitrification and nitrite oxidation in the ODZ of the Arabian Sea from paired stable isotopes of nitrate and nitrite. *Global Biogeochemical Cycle*, 27, 1059–1071. <https://doi.org/10.1002/2011GB004115>.
- Gaye-Haake, B., Lahajnar, N., Emeis, K.-C., Unger, D., Rixen, T., Suthhof, A., Ramaswamy, V., Schulz, H., Paropkari, A., Guptha, M., 2005. Stable nitrogen isotopic ratios of sinking particles and sediments from the northern Indian Ocean. *Marine Chemistry*, 96, 243–255, <https://doi.org/10.1016/j.marchem.2005.02.001>.

- Godfrey, J. S., Golding, T. J., 1981. The Sverdrup Relation in the Indian Ocean, and the effect of Pacific-Indian Ocean Throughflow on Indian Ocean Circulation and on the East Australian Current. *Journal of Physical Oceanography*, 11, 771–779. [https://doi.org/10.1175/1520-0485\(1981\)011<0771:TSRITI>2.0.CO;2](https://doi.org/10.1175/1520-0485(1981)011<0771:TSRITI>2.0.CO;2).
- Goldman, J. C., 1980. Physiological processes, nutrient availability, and the concept of relative growth rate in marine phytoplankton ecology, in: P. G. Falkowski (Ed.), *Primary productivity in the sea*, Plenum Press, New York, Springer, pp. 179–194. https://doi.org/10.1007/978-1-4684-3890-1_10.
- Grand, M. M., Measures, C. I., Hatta, M., Hiscock, W. T., Landing, W. M., Morton, P. L., Buck, C. S., Barrett, P. M., Resing, J. A., 2015. Dissolved Fe and Al in the upper 1000 m of the eastern Indian Ocean: A high-resolution transect along 95° E from the Antarctic margin to the Bay of Bengal. *Global Biogeochemical Cycles*, 29, 375–396. <https://doi.org/10.1002/2014GB004920>.
- Granger, J., Sigman D. M., Needoba Joseph, A., Harrison Paul, J., 2004. Coupled nitrogen and oxygen isotope fractionation of nitrate during assimilation by cultures of marine phytoplankton. *Limnology and Oceanography*, 49, 1763–1773. <https://doi.org/10.4319/lo.2004.49.5.1763>.
- Grasshoff, K., Kremling, K., Ehrhardt, M., 2009. *Methods of seawater analysis*: John Wiley and Sons, 419 pp.
- Gregg, W., Rousseaux, C., 2017. NASA Ocean Biogeochemical Model assimilating satellite chlorophyll data global monthly VR2017, in: W. Gregg and C. Rousseaux (Eds.), *Greenbelt, MD, USA, Goddard Earth Sciences Data and Information Services Center (GES DISC)*, (last access: 15.05.2020). <https://10.5067/BHCFDIICIU5>.
- Gruber, N., Sarmiento, J. L., 1997. Global patterns of marine nitrogen fixation and denitrification. *Global Biogeochemical Cycles*, 11, 235–266. <https://doi.org/10.1029/97GB00077>.
- Guidi, L., Legendre, L., Reygondeau, G., Uitz, J., Stemmann, L., Henson, S. A., 2015. A new look at ocean carbon remineralization for estimating deepwater sequestration. *Global Biogeochemical Cycles*, 29, 1044–1059. <https://doi.org/10.1002/2014GB005063>.

- Guieu, C., Roy-Barman, M., Leblond, N., Jeandel, C., Souhaut, M., Le Cann, B., Dufour, A., Bournot, C., 2005. Vertical particle flux in the northeast Atlantic Ocean (POMME experiment). *Journal of Geophysical Research: Oceans*, 110, 1–21. <https://doi.org/10.1029/2004JC002672>.
- Guillen, O., de Mendiola, B. R., de Rondán, R. I., 1973. Primary productivity and phytoplankton in the coastal Peruvian waters. *Oceanography of the South Pacific*. NZ National Commission for UNESCO, 405-418.
- Gupta, L. P., Kawahata, H., 2000. Amino acid and hexosamine composition and flux of sinking particulate matter in the equatorial Pacific at 175°E longitude. *Deep-Sea Research Part I: Oceanographic Research Papers*, 47, 1937–1960. [https://doi.org/10.1016/S0967-0637\(00\)00009-1](https://doi.org/10.1016/S0967-0637(00)00009-1).
- Haake, B., Ittekkot, V., 1990. Die Wind-getriebene “biologische Pumpe” und der Kohlenstoffentzug im Ozean. *Naturwissenschaften*, 77, 75–79. <https://doi.org/10.1007/BF01131777>.
- Haake, B., Ittekkot, V., Rixen, T., Ramaswamy, V., Nair, R. R., Curry, W., 1993. Seasonality and interannual variability of particle fluxes to the deep Arabian Sea. *Deep-Sea Research Part I: Oceanographic Research Papers*, 40, 1323–1344. [https://doi.org/10.1016/0967-0637\(93\)90114-I](https://doi.org/10.1016/0967-0637(93)90114-I).
- Hamm, C. E., 2002. Interactive aggregation and sedimentation of diatoms and clay-sized lithogenic material. *Limnology and Oceanography*, 47, 1790–1795. <https://doi.org/10.4319/lo.2002.47.6.1790>.
- Hargrave, B. T., Walsh, I. D., Murray, D. W., 2002. Seasonal and spatial patterns in mass and organic matter sedimentation in the North Water. *Deep-Sea Research Part II: Topical Studies in Oceanography*, 49, 5227–5244. [https://doi.org/10.1016/S0967-0645\(02\)00187-X](https://doi.org/10.1016/S0967-0645(02)00187-X).
- Harms, N. C., Lahajnar, N., Gaye, B., Rixen, T., Dähnke, K., Ankele, M., Schwarz-Schampera, U., Emeis, K.-C., 2019. Nutrient distribution and nitrogen and oxygen isotopic composition of nitrate in water masses of the subtropical southern Indian Ocean. *Biogeosciences*, 16, 2715–2732. <https://doi.org/10.5194/bg-16-2715-2019>.

- Harms, N. C., Lahajnar, N., Gaye, B., Rixen, T., Schwarz-Schampera, U., Emeis, K.-C., 2021. Sediment trap-derived particulate matter fluxes in the oligotrophic subtropical gyre of the South Indian Ocean. *Deep-Sea Research Part II: Topical Studies in Oceanography*, 104924. <https://doi.org/10.1016/j.dsr2.2020.104924>.
- Harms, N. C., Lahajnar, N., Emeis, K.-C., submitted. Biogeochemistry of particulate matter fluxes and sediment composition in the Indian Ocean subtropical gyre. In: *Marine Metal Exploration: The INDEX Project – Prospecting the Seafloor for Polymetallic Sulphides*, Chapter 20, Springer Nature.
- Hebbeln, D., Marchant, M., Wefer, G., 2000. Seasonal variations of the particle flux in the Peru-Chile current at 30°S under “normal” and El Niño conditions. *Deep-Sea Research Part II: Topical Studies in Oceanography*, 47, 2101–2128. [https://doi.org/10.1016/S0967-0645\(00\)00018-7](https://doi.org/10.1016/S0967-0645(00)00018-7).
- Hedges, J. I., Hu, F. S., Devol, A. H., Hartnett, H. E., Tsamakis, E., Keil, R. G., 1999. Sedimentary organic matter preservation; a test for selective degradation under oxic conditions. *American Journal of Science*, 299, 529–555. <https://doi.org/10.2475/ajs.299.7-9.529>.
- Hedges, J. I., Keil, R. G., 1995. Sedimentary organic matter preservation: an assessment and speculative synthesis. *Marine Chemistry*, 49, 81–115. [https://doi.org/10.1016/0304-4203\(95\)00008-F](https://doi.org/10.1016/0304-4203(95)00008-F).
- Henson, S., Le Moigne, F., Giering, S., 2019. Drivers of carbon export efficiency in the global ocean. *Global Biogeochemical Cycles*, 33, 1–13. <https://doi.org/10.1029/2018GB006158>.
- Herraiz-Borreguero, L., Rintoul, S. R., 2011. Subantarctic mode water: distribution and circulation. *Ocean Dynamics*, 61, 103–126. <https://doi.org/10.1007/s10236-010-0352-9>.
- Heydorn, A. E. F., Bang, N. D., Pearce, A. F., Flemming, B. W., Carter, R. A., Schleyer, M. H., Berry, G. R., Bass, A. J., Wallace, J. H., van der Elst, R. P., Crawford, R. J. M., Shelton P. A., 1978. Ecology of the Agulhas Current region: an assessment of biological responses to environmental parameters in the south-west Indian Ocean. *Transactions of the Royal Society of South Africa*, 43, 151–190. <https://doi.org/10.1080/00359197809520235>.

- Hinga, K., Sieburth, J. M., Heath, G. R., 1979. Supply and use of organic material at the deep-sea floor. *Journal of Marine Research*, 37, 557–579.
- Honda, M. C., 2001. Studies of carbon cycles in the NW Pacific Ocean by sediment trap and C14 data, Ph.D. thesis, D. Hokkaido University, Sapporo, Japan.
- Honda, M. C., Imai, K., Nojiri, Y., Hoshi, F., Sugawara, T., Kusakabe, M., 2002. The biological pump in the northwestern North Pacific based on fluxes and major components of particulate matter obtained by sediment-trap experiments (1997–2000). *Deep-Sea Research Part II: Topical Studies in Oceanography*, 49, 5595–5625. [https://doi.org/10.1016/S0967-0645\(02\)00201-1](https://doi.org/10.1016/S0967-0645(02)00201-1).
- Honda, M. C., Sasai, Y., Siswanto, E., Kuwano-Yoshida, A., Aiki, H., Cronin, M. F., 2018. Impact of cyclonic eddies and typhoons on biogeochemistry in the oligotrophic ocean based on biogeochemical/physical/meteorological time-series at station KEO. *Progress in Earth and Planetary Science* 5, 42, 1–16. <https://doi.org/10.1186/s40645-018-0196-3>.
- Honda, M. C., Watanabe, S., 2010. Importance of biogenic opal as ballast of particulate organic carbon (POC) transport and existence of mineral ballast-associated and residual POC in the Western Pacific Subarctic Gyre. *Geophysical Research Letters*, 37, 1–5. <https://doi.org/10.1029/2009GL041521>.
- Hong, G. H., Choe, S.-M., Suk, M.-S., Na, J.-Y., Sin, I. C., Chung, C. S., Kim, S. H., 1996. Annual biogenic particle fluxes to the interior of the East/Japan Sea, a large marginal sea of the Northwest Pacific, in: S. Tsunogai (Ed.), *Proceedings of the International Marine Science Symposium*, Japan Marine Science Foundation, Mutsu, Aomori, Japan, pp. 300–321.
- Honjo, S., 1980. Material fluxes and modes of sedimentation in the mesopelagic and bathypelagic zones. *Journal of Marine Research*, 38, 53–97.
- Honjo, S., 1982. Seasonality and interaction of biogenic and lithogenic particulate flux at the Panama Basin. *Science*, 218, 883–884. <https://doi.org/10.1126/science.218.4575.883>.
- Honjo, S., 1996. Fluxes of particles to the interior of the open ocean, in: V. Ittekkot, P. Schafer, S. Honjo and P.J. Depetris, *Particle flux in the ocean*, SCOPE, vol. 57, chap. 7, John Wiley Hoboken, New York, pp. 91–154.

- Honjo, S., Dymond, J., Collier, R., Manganini, S. J., 1995. Export production of particles to the interior of the equatorial Pacific Ocean during the 1992 EqPac experiment. *Deep-Sea Research Part II: Topical Studies in Oceanography*, 42, 831–870. [https://doi.org/10.1016/0967-0645\(95\)00034-N](https://doi.org/10.1016/0967-0645(95)00034-N).
- Honjo, S., Dymond, J., Prell, W., Ittekkot, V., 1999. Monsoon-controlled export fluxes to the interior of the Arabian Sea. *Deep-Sea Research Part II: Topical Studies in Oceanography*, 46, 1859–1902. [https://doi.org/10.1016/S0967-0645\(99\)00047-8](https://doi.org/10.1016/S0967-0645(99)00047-8).
- Honjo, S., Manganini, S. J., 1993. Annual biogenic particle fluxes to the interior of the North Atlantic Ocean: studied at 34°N 21°W and 48°N 21°W. *Deep-Sea Research Part II: Topical Studies in Oceanography*, 40, 587–607. [https://doi.org/10.1016/0967-0645\(93\)90034-K](https://doi.org/10.1016/0967-0645(93)90034-K).
- Honjo, S., Manganini, S. J., Karowe, A., Woodward, B. L., 1987. Particle fluxes, North-Eastern Nordic Seas: 1983–1986, in: Woods Hole Oceanographic Institute, technical Report WHOI-87-17, Woods Hole Massachusetts, 84 pp.
- Honjo, S., Manganini, S. J., Krishfield, R. A., Francois, R., 2008. Particulate organic carbon fluxes to the ocean interior and factors controlling the biological pump: A synthesis of global sediment trap programs since 1983. *Progress in Oceanography*, 76, 217–285. <https://doi.org/10.1016/j.pocean.2007.11.003>.
- Hüneke, H., Henrich, R., 2011. Pelagic Sedimentation in modern and ancient oceans, in: Hüneke H. and Mulder T (Eds.), *Deep-Sea Sediments, Deployments in Sedimentology*, Elsevier, Amsterdam, vol. 63, chap. 4, 215–351. <https://doi.org/10.1016/B978-0-444-53000-4.00004-4>.
- Hutchins, D., Sedwick, P., DiTullio, G., Boyd, P., Queguiner, B., Griffiths, F., Crossley, C., 2001. Control of phytoplankton growth by iron and silicic acid availability in the subantarctic Southern Ocean: Experimental results from the SAZ Project. *Journal of Geophysical Research: Oceans*, 106, 31559–31572. <https://doi.org/10.1029/2000JC000333>.
- Ito, T., Follows, M. J., 2005. Preformed phosphate, soft tissue pump and atmospheric CO₂. *Journal of Marine Research*, 63, 813–839. <https://doi.org/10.1357/0022240054663231>.

- Ittekkot, V., Nair, R. R., Honjo, S., Ramaswamy, V., Bartsch, M., Manganini, S. J., Desai, B. N., 1991. Enhanced particle fluxes in Bay of Bengal induced by injection of fresh water. *Nature*, 351, 385–387. <https://doi.org/10.1038/351385a0>.
- Iturriaga, R., 1979. Bacterial activity related to sedimenting particulate matter. *Marine Biology*, 55, 157–169. <https://doi.org/10.1007/BF00396814>.
- Jianfang, C., Lianfu, Z., Wiesner, M. G., Ronghua, C., Yulong, Z., Wong, H. K., 1998. Estimations of primary production and export production in the South China Sea based on sediment trap experiments. *Chinese Science Bulletin*, 43, 585–586. <https://doi.org/10.1007/BF02883645>.
- Jickells, T. D., Newton, P. P., King, P., Lampitt, R. S., Boutle, C., 1996. A comparison of sediment trap records of particle fluxes from 19° to 48°N in the northeast Atlantic and their relation to surface water productivity. *Deep-Sea Research Part I: Oceanographic Research Papers*, 43, 971–986. [https://doi.org/10.1016/0967-0637\(96\)00063-5](https://doi.org/10.1016/0967-0637(96)00063-5).
- Jickells, T. D., Spokes, L. J., 2001. Atmospheric iron inputs to the oceans, in: D. R. Turner, K. Hunter (Eds.), *The Biogeochemistry of Iron in Seawater*, Wiley, Chichester, pp. 85–121.
- Kantha, L., Clayson, C. A., 2003. *Ocean Mixed Layer*, Elsevier, pp. 291–298.
- Karl, D. M., Letelier, R., Hebel, D., Tupas, L., Dore, J., Christian, J., Winn, C., 1995. Ecosystem changes in the North Pacific subtropical gyre attributed to the 1991–92 El Niño. *Nature*, 373, 230–234. <https://doi.org/10.1038/373230a0>.
- Kawahata, H., 2002. Suspended and settling particles in the Pacific. *Deep-Sea Research Part II: Topical Studies in Oceanography*, 49, 5647–5664. [https://doi.org/10.1016/S0967-0645\(02\)00216-3](https://doi.org/10.1016/S0967-0645(02)00216-3).
- Kawahata, H., Nishimura, A., Gagan, M. K., 2002. Seasonal change in foraminiferal production in the western equatorial Pacific warm pool: evidence from sediment trap experiments. *Deep-Sea Research Part II: Topical Studies in Oceanography*, 49, 2783–2800. [https://doi.org/10.1016/S0967-0645\(02\)00058-9](https://doi.org/10.1016/S0967-0645(02)00058-9).

- Kawahata, H., Ohta, H., 2000. Sinking and suspended particles in the South-west Pacific. *Marine and Freshwater research*, 51, 113–126. <https://doi.org/10.1071/MF99057>.
- Kawahata, H., Suzuki, A., Ohta, H., 2000. Export fluxes in the western Pacific warm pool. *Deep-Sea Research Part I: Oceanographic Research Papers*, 47, 2061–2091. [https://doi.org/10.1016/S0967-0637\(00\)00025-X](https://doi.org/10.1016/S0967-0637(00)00025-X).
- Kawahata, H., Yamamuro, M., Ohta, H., 1998. Seasonal and vertical variations of sinking particle fluxes in the West Caroline Basin. *Oceanologica Acta*, 21, 521–532. [https://doi.org/10.1016/S0399-1784\(98\)80035-2](https://doi.org/10.1016/S0399-1784(98)80035-2).
- Kempe, S., Knaack, H., 1996. Vertical Particle Flux in the Western Pacific Below the North Equatorial Current and the Equatorial Counter Current, in: V. Ittekkot, P. Schäfer, S. Honjo and P. J. Depetris, *Particle Flux in the Ocean*, SCOPE, vol. 57, chap. 17, John Wiley, Hoboken, New York, pp. 313–323.
- Klaas, C., Archer, D. E., 2002. Association of sinking organic matter with various types of mineral ballast in the deep sea: Implications for the rain ratio. *Global Biogeochemical Cycles*, 16, 1–14. <https://doi.org/10.1029/2001GB001765>.
- Knapp, A. N., DiFiore, P. J., Deutsch, C., Sigman, D. M., Lipschultz, F., 2008. Nitrate isotopic composition between Bermuda and Puerto Rico: Implications for N₂ fixation in the Atlantic Ocean. *Global Biogeochemical Cycles*, 22, 1–14. <https://doi:10.1029/2007GB003107>.
- Knauer, G. A., Martin, J. H., Bruland, K. W., 1979. Fluxes of particulate carbon, nitrogen, and phosphorus in the upper water column of the northeast Pacific. *Deep-Sea Research Part I: Oceanographic Research Papers*, 26, 97–108. [https://doi.org/10.1016/0198-0149\(79\)90089-X](https://doi.org/10.1016/0198-0149(79)90089-X).
- Knox, F., McElroy, M. B., 1984. Changes in atmospheric CO₂: Influence of the marine biota at high latitude. *Journal of Geophysical Research: Atmospheres*, 89, 4629–4637. <https://doi.org/10.1029/JD089iD03p04629>.
- Koblentz-Mishke, O. J., 1970. Plankton primary production of the world ocean. *Scientific exploration of the South Pacific*, 183–193.

- Kolla, V., Henderson, L., Biscaye, P. E., 1976. Clay mineralogy and sedimentation in the western Indian Ocean. Paper presented at the Deep-Sea Research and Oceanographic Abstracts, 23, 949–961. [https://doi.org/10.1016/0011-7471\(76\)90825-1](https://doi.org/10.1016/0011-7471(76)90825-1).
- Kuss, J., Kremling, K., 1999. Particulate trace element fluxes in the deep northeast Atlantic Ocean. *Deep-Sea Research Part I: Oceanographic Research Papers*, 46, 149–169. [https://doi.org/10.1016/S0967-0637\(98\)00059-4](https://doi.org/10.1016/S0967-0637(98)00059-4).
- Lal, D., Lerman, A., 1975. Size spectra of biogenic particles in ocean water and sediments. *Journal of Geophysical Research*, 80, 423–430. <https://doi.org/10.1029/JC080i003p00423>.
- Lam, P. J., Doney, S. C., Bishop, J. K. B., 2011. The dynamic ocean biological pump: Insights from a global compilation of particulate organic carbon, CaCO₃, and opal concentration profiles from the mesopelagic. *Global Biogeochemical Cycles*, 25, 1–14. <https://doi.org/10.1029/2010GB003868>.
- Lampitt, R. S., 1992. The contribution of deep-sea macroplankton to organic remineralization: results from sediment trap and zooplankton studies over the Madeira Abyssal Plain. *Deep-Sea Research Part I: Oceanographic Research Papers*, 39, 221–233. [https://doi.org/10.1016/0198-0149\(92\)90106-4](https://doi.org/10.1016/0198-0149(92)90106-4).
- Lampitt, R. S., Antia, A. N., 1997. Particle flux in deep seas: regional characteristics and temporal variability. *Deep-Sea Research Part I: Oceanographic Research Papers*, 44, 1377–1403. [https://doi.org/10.1016/S0967-0637\(97\)00020-4](https://doi.org/10.1016/S0967-0637(97)00020-4).
- Lampitt, R. S., Bett, B. J., Kiriakoulakis, K., Popova, E. E., Ragueneau, O., Vangriesheim, A., Wolff, G. A., 2001. Material supply to the abyssal seafloor in the Northeast Atlantic. *Progress in Oceanography*, 50, 27–63. [https://doi.org/10.1016/S0079-6611\(01\)00047-7](https://doi.org/10.1016/S0079-6611(01)00047-7).
- Laufkötter, C., Gruber, N., 2018. Will marine productivity wane? *Science*, 359, 1103–1104. <https://doi.org/10.1126/science.aat0795>.
- Laufkötter, C., John, J. G., Stock, C. A., Dunne, J. P., 2017. Temperature and oxygen dependence of the remineralization of organic matter. *Global Biogeochemical Cycles*, 31, 1038–1050. <https://doi.org/10.1002/2017GB005643>.

- Laws, E. A., Falkowski, P. G., Smith, W. O., Ducklow, H., McCarthy, J. J., 2000. Temperature effects on export production in the open ocean. *Global Biogeochemical Cycles*, 14, 1231–1246. <https://doi.org/10.1029/1999GB001229>.
- Lee, T., 2004. Decadal weakening of the shallow overturning circulation in the South Indian Ocean. *Geophysical Research Letters*, 31, 1–5. <https://doi.org/10.1029/2004GL020884>.
- Lee, Z., Weidemann, A., Kindle, J., Arnone, R., Carder, K. L., Davis, C., 2007. Euphotic zone depth: Its derivation and implication to ocean-color remote sensing. *Journal of Geophysical Research: Oceans*, 112, 1–11. <https://doi.org/10.1029/2006JC003802>.
- Lochte, K., Anderson, R., Francois, R., Jahnke, R., Shimmield, G., Vetrov, A., 2003. Benthic processes and the burial of carbon, in: M. J. R. Fasham (Ed.), *Ocean Biogeochemistry*, Springer, Berlin, Heidelberg, pp. 195–216. https://doi.org/10.1007/978-3-642-55844-3_9.
- Love, C., Allen, R., 1975. EASTROPAC Atlas 10. US Dept. Commerce Circ., 330 pp.
- Lutz, M. J., Caldeira, K., Dunbar, R. B., Behrenfeld, M. J., 2007. Seasonal rhythms of net primary production and particulate organic carbon flux to depth describe the efficiency of biological pump in the global ocean. *Journal of Geophysical Research: Oceans*, 112, 1–26. <https://doi.org/10.1029/2006JC003706>.
- Lyle, M., 2014. Deep-Sea Sediments, *Encyclopedia of Marine Geosciences*, 1–21. https://doi.org/10.1007/978-94-007-6644-0_53-1.
- Mahowald, N. M., Baker, A. R., Bergametti, G., Brooks, N., Duce, R. A., Jickells, T. D., Kubilay, N., Prospero, J. M., Tegen, I., 2005. Atmospheric global dust cycle and iron inputs to the ocean. *Global Biogeochemical Cycles*, 19, 1–15. <https://doi.org/10.1029/2004GB002402>.
- Mantyla, A. W., Reid, J. L., 1995. On the origins of deep and bottom waters of the Indian Ocean. *Journal of Geophysical Research: Oceans*, 100, 2417–2439. <https://doi.org/10.1029/94JC02564>.

- Mariotti, A., Germon, J., Hubert, P., Kaiser, P., Letolle, R., Tardieux, A., Tardieux, P., 1981. Experimental determination of nitrogen kinetic isotope fractionation: some principles; illustration for the denitrification and nitrification processes. *Plant soil*, 62, 413–430. <https://doi.org/10.1007/BF02374138>.
- Marsay, C. M., Sanders, R. J., Henson, S. A., Pabortsava, K., Achterberg, E. P., Lampitt, R. S., 2015. Attenuation of sinking particulate organic carbon flux through the mesopelagic ocean. *Proceedings of the National Academy of Sciences*, 112, 1089–1094. <https://doi.org/10.1073/pnas.1415311112>.
- Martin, J. H., Knauer, G. A., Karl, D. M., Broenkow, W. W., 1987. VERTEX: carbon cycling in the northeast Pacific. *Deep-Sea Research Part I: Oceanographic Research Papers*, 34, 267–285. [https://doi.org/10.1016/0198-0149\(87\)90086-0](https://doi.org/10.1016/0198-0149(87)90086-0).
- Martin, T., Casciotti, K., 2017. Paired N and O isotopic analysis of nitrate and nitrite in the Arabian Sea oxygen deficient zone. *Deep-Sea Research Part I: Oceanographic Research Papers*, 121, 121–131. <https://doi.org/10.1016/j.dsr.2017.01.002>.
- McCartney, M. S., 1977. Subantarctic Mode Water, *A Voyage of Discovery, George Deacon 70th Anniversary Volume* M. Angel, 103–119: Pergamon, New York.
- McCartney, M. S., 1982. The subtropical recirculation of mode waters. *Journal of Marine Research*, 40, 427–464.
- McCave, I. N., 1975. Vertical flux of particles in the ocean. *Deep-Sea Research*, 22, 491–502.
- McClain, C. R., Signorini, S. R., Christian, J. R., 2004. Subtropical gyre variability observed by ocean-color satellites. *Deep-Sea Research Part II: Topical Studies in Oceanography*, 51, 281–301. <https://doi.org/10.1016/j.dsr2.2003.08.002>.
- McDonagh, E. L., Bryden, H. L., King, B. A., Sanders, R. J., Cunningham, S. A., Marsh, R., 2005. Decadal changes in the south Indian Ocean thermocline. *Journal of Climate*, 18, 1575–1590. <https://doi.org/10.1175/JCLI3350.1>.
- McMonigal, K., Beal, L. M., Willis, J. K., 2018. The Seasonal Cycle of the South Indian Ocean Subtropical Gyre Circulation as Revealed by Argo and Satellite Data. *Geophysical Research Letters*, 45, 9034–9041. <https://doi.org/10.1029/2018GL078420>.

- Menzel, D. W., Ryther, J. H., 1960. The annual cycle of primary production in the Sargasso Sea off Bermuda. *Deep-Sea Research*, 6, 351–367. [https://doi.org/10.1016/0146-6313\(59\)90095-4](https://doi.org/10.1016/0146-6313(59)90095-4).
- Michaels, A. F., Bates, N. R., Buesseler, K. O., Carlson, C. A., Knap, A. H., 1994. Carbon-cycle imbalances in the Sargasso Sea. *Nature*, 372, 537–540. <https://doi.org/10.1038/372537a0>.
- Michaels, A., Olson, D., Sarmiento, J., Ammerman, J., Fanning, K., Jahnke, R., Knap, A., Lipschultz, F., Prospero, J., 1996. Inputs, losses and transformations of nitrogen and phosphorus in the pelagic North Atlantic Ocean. *Biogeochemistry*, 35, 181–226. <https://doi.org/10.1007/BF02179827>.
- Miklasz, K. A., Denny, M. W., 2010. Diatom sinkings speeds: Improved predictions and insight from a modified Stokes' law, *Limnology and Oceanography*, 55, 2513–2525. <https://doi.org/10.4319/lo.2010.55.6.2513>.
- Minagawa, M., Wada, E., 1986. Nitrogen isotope ratios of red tide organisms in the East China Sea: A characterization of biological nitrogen fixation. *Marine Chemistry*, 19, 245–259. [https://doi.org/10.1016/0304-4203\(86\)90026-5](https://doi.org/10.1016/0304-4203(86)90026-5).
- Mohiuddin, M. M., Nishimura, A., Tanaka, Y., Shimamoto, A., 2004. Seasonality of biogenic particle and planktonic foraminifera fluxes: response to hydrographic variability in the Kuroshio Extension, northwestern Pacific Ocean. *Deep-Sea Research Part I: Oceanographic Research Papers*, 51, 1659–1683. <https://doi.org/10.1016/j.dsr.2004.06.002>.
- Moisander, P. H., Beinart, R. A., Hewson, I., White, A. E., Johnson, K. S., Carlson, C. A., Montoya, J. P., Zehr, J. P., 2010. Unicellular cyanobacterial distributions broaden the oceanic N₂ fixation domain. *Science*, 327, 1512–1514, <https://doi.org/10.1126/science.1185468>.
- Monteiro, F. M., Follows, M., 2006. Nitrogen fixation and preferential remineralization of phosphorus in the North Atlantic: Model insights. *Eos, Transactions, American Geophysical Union*, 87, 1–36.
- Montoya, J. P., McCarthy, J. J., 1995. Isotopic fractionation during nitrate uptake by phytoplankton grown in continuous culture. *Journal of Plankton Research*, 17, 439–464. <https://doi.org/10.1093/plankt/17.3.439>.

- Montoya, J. P., Carpenter, E. J., Capone, D. G., 2002. Nitrogen fixation and nitrogen isotope abundances in zooplankton of the oligotrophic North Atlantic. *Limnology and Oceanography*, 47, 1617–1628. <https://doi.org/10.4319/lo.2002.47.6.1617>.
- Mortlock, R. A., Froelich, P. N., 1989. A simple method for the rapid determination of biogenic opal in pelagic marine sediments. *Deep-Sea Research Part I: Oceanographic Research Papers*, 36, 1415–1426. [https://doi.org/10.1016/0198-0149\(89\)90092-7](https://doi.org/10.1016/0198-0149(89)90092-7).
- Mouw, C. B., Barnett, A., McKinley, G. A., Gloege, L., Pilcher, D., 2016. Phytoplankton size impact on export flux in the global ocean: Phytoplankton size impact on export flux. *Global Biogeochemical Cycles*, 30, 1542–1562. <https://doi.org/10.1002/2015GB005355>.
- Müller, P. J., Suess, E., 1979. Productivity, sedimentation rate, and sedimentary organic matter in the oceans—I. Organic carbon preservation. *Deep-Sea Research A: Oceanographic Research Papers*, 26, 1347–1362. [https://doi.org/10.1016/0198-0149\(79\)90003-7](https://doi.org/10.1016/0198-0149(79)90003-7).
- Müller-Karger, F., Varela, R., Thunell, R. C., Astor, Y., Zhang, H., Luerssen, R., Hu, C., 2004. Processes of coastal upwelling and carbon flux in the Cariaco Basin. *Deep-Sea Research Part II: Topical Studies in Oceanography*, 51, 927–943. <https://doi.org/10.1016/j.dsr2.2003.10.010>.
- Muromtsev, A., 1959. *Osnovnye cherty gidrologii Indiiskogo okeana (The Main Features of Indian Ocean Hydrology)*. Gidrometeoizdat, Leningrad.
- Murphy, J., Riley, J. P., 1962. A modified single solution method for the determination of phosphate in natural waters. *Analytical Chimica Acta*, 27, 31–36. [https://doi.org/10.1016/S0003-2670\(00\)88444-5](https://doi.org/10.1016/S0003-2670(00)88444-5).
- Murray, J. W., Downs, J. N., Strom, S., Wei, C.-L., Jannasch, H. W., 1989. Nutrient assimilation, export production and ^{234}Th scavenging in the eastern equatorial Pacific. *Deep-Sea Research Part I: Oceanographic Research Papers*, 36, 1471–1489. [https://doi.org/10.1016/0198-0149\(89\)90052-6](https://doi.org/10.1016/0198-0149(89)90052-6).
- Nair, R. R., Ittekkot, V., Manganini, S. J., Ramaswamy, V., Haake, B., Degens, E. T., Desai, B. N., Honjo, S., 1989. Increased particle flux to the deep ocean related to monsoons. *Nature*, 338, 749–751. <https://doi.org/10.1038/338749a0>.

- Neuer, S., Ratmeyer, V., Davenport, R., Fischer, G., Wefer, G. (1997). Deep water particle flux in the Canary Island region: seasonal trends in relation to long-term satellite derived pigment data and lateral sources. *Deep-Sea Research Part I: Oceanographic Research Papers*, 44, 1451–1466. [https://doi.org/10.1016/S0967-0637\(97\)00034-4](https://doi.org/10.1016/S0967-0637(97)00034-4).
- Newton, P. P., Lampitt, R. S., Jickells, T. D., King, P., Boutle, C., 1994. Temporal and spatial variability of biogenic particles fluxes during the JGOFS northeast Atlantic process studies at 47°N, 20°W. *Deep-Sea Research Part I: Oceanographic Research Papers*, 41, 1617–1642. [https://doi.org/10.1016/0967-0637\(94\)90065-5](https://doi.org/10.1016/0967-0637(94)90065-5).
- Nodder, S. D., Northcote, L. C., 2001. Episodic particulate fluxes at southern temperate mid-latitudes (42°–45°S) in the Subtropical Front region, east of New Zealand. *Deep-Sea Research Part I: Oceanographic Research Papers*, 48, 833–864. [https://doi.org/10.1016/S0967-0637\(00\)00062-5](https://doi.org/10.1016/S0967-0637(00)00062-5).
- Noriki, S., Tsunogai, S., 1986. Particulate fluxes and major components of settling particles from sediment trap experiments in the Pacific Ocean. *Deep-Sea Research Part I: Oceanographic Research Papers*, 33, 903–912. [https://doi.org/10.1016/0198-0149\(86\)90005-1](https://doi.org/10.1016/0198-0149(86)90005-1).
- Osipov, V., 2012. Density of clay minerals. *Soil mechanics and foundation engineering*, 48, 231–240. <https://doi.org/10.1007/s11204-012-9153-0>.
- Owen, R. W., 1974. *California Cooperative Oceanic Fisheries Investigations, Atlas No. 20*, State of California, Marine Research Committee, 1974, pp. 98–109.
- Pabortsava, K., Lampitt, R. S., Benson, J., Crowe, C., McLachlan, R., Le Moigne, F. A. C., Mark Moore, C., Pebody, C., Provost, P., Rees, A. P., Tilstone, Gavin H., Woodward, E. M. S., 2017. Carbon sequestration in the deep Atlantic enhanced by Saharan dust. *Nature Geoscience*, 10, 189–194. <https://doi.org/10.1038/ngeo2899>.
- Pace, M. L., Knauer, G. A., Karl, D. M., Martin, J. H., 1987. Primary production, new production and vertical flux in the eastern Pacific Ocean. *Nature*, 325, 803–804. <https://doi.org/10.1038/325803a0>.

- Paerl, H. W., Prufert-Bebout, L. E., Guo, C., 1994. Iron-stimulated N₂ fixation and growth in natural and cultured populations of the planktonic marine cyanobacteria *Trichodesmium* spp. *Applied and Environmental Microbiology*, 60, 1044–1047.
- Passow, U., Carlson, C. A., 2012. The biological pump in a high CO₂ world. *Marine Ecology Progress Series*, 470, 249–271. <https://doi.org/10.3354/meps09985>.
- Paulsen, H., Ilyina, T., Six, K. D., Stemmler, I., 2017. Incorporating a prognostic representation of marine nitrogen fixers into the global ocean biogeochemical model HAMOCC. *Journal of Advances in Modeling Earth Systems*, 9, 438–464. <https://doi.org/10.1002/2016MS000737>.
- Persson, A., 1998. How do we understand the Coriolis force? *Bulletin of the American Meteorological Society*, 79, 1373–1386. [https://doi.org/10.1175/1520-0477\(1998\)079<1373:HDWUTC>2.0.CO;2](https://doi.org/10.1175/1520-0477(1998)079<1373:HDWUTC>2.0.CO;2).
- Pickard, G., Emery, W., 1982. *Descriptive physical Oceanography*, Pergamon, Tanytown, New York, 249 pp.
- Pilskaln, C. H., Manganini, S. J., Trull, T. W., Armand, L., Howard, W., Asper, V. L., Massom, R., 2004. Geochemical particle fluxes in the Southern Indian Ocean seasonal ice zone: Prydz Bay region, East Antarctica. *Deep-Sea Research Part I: Oceanographic Research Papers*, 51, 307–332. <https://doi.org/10.1016/j.dsr.2003.10.010>.
- Pilskaln, C. H., Paduan, J. B., Chavez, F. P., Anderson, R. Y., Berelson, W. M., 1996. Carbon export and regeneration in the coastal upwelling system of Monterey Bay, central California. *Journal of Marine Research*, 54, 1149–1178. <https://doi.org/10.1357/0022240963213772>.
- Piola, A. R., Gordon, A. L., 1989. Intermediate waters in the southwest South Atlantic. *Deep-Sea Research*, 36, 1–16. [https://doi.org/10.1016/0198-0149\(89\)90015-0](https://doi.org/10.1016/0198-0149(89)90015-0).
- Pudsey, C. J., King, P., 1997. Particle fluxes, benthic processes and the palaeoenvironmental record in the Northern Weddell Sea. *Deep-Sea Research Part I: Oceanographic Research Papers*, 44, 1841–1876. [https://doi.org/10.1016/S0967-0637\(97\)00064-2](https://doi.org/10.1016/S0967-0637(97)00064-2).

- Quadfasel, D. R., Schott, F., 1982. Water-mass distributions at intermediate layers off the Somali Coast during the onset of the southwest monsoon, 1979. *Journal of Physical Oceanography*, 12, 1358–1372. [https://doi.org/10.1175/1520-0485\(1982\)012<1358:WMDAIL>2.0.CO;2](https://doi.org/10.1175/1520-0485(1982)012<1358:WMDAIL>2.0.CO;2).
- Rafter, P. A., DiFiore, P. J., Sigman, D. M., 2013. Coupled nitrate nitrogen and oxygen isotopes and organic matter remineralization in the Southern and Pacific Oceans. *Journal of Geophysical Research: Oceans*, 118, 4781–4794. <https://doi.org/10.1002/jgrc.20316>.
- Ramaswamy, V., Nair, R., Manganini, S., Haake, B., Ittekkot, V., 1991. Lithogenic fluxes to the deep Arabian Sea measured by sediment traps. *Deep-Sea Research Part A: Oceanographic Research Papers*, 38, 169–184. [https://doi.org/10.1016/0198-0149\(91\)90078-T](https://doi.org/10.1016/0198-0149(91)90078-T).
- Ramseier, R. O., Garrity, C., Bauerfeind, E., Peinert, R., 1999. Sea-ice impact on long-term particle flux in the Greenland Sea's Is Odden-Nordbukta region, 1985–1996. *Journal of Geophysical Research: Oceans*, 104, 5329–5343. <https://doi.org/10.1029/1998JC900048>.
- Ratmeyer, V., Fischer, G., Wefer, G., 1999. Lithogenic particle fluxes and grain size distributions in the deep ocean off northwest Africa: Implications for seasonal changes of aeolian dust input and downward transport. *Deep-Sea Research I: Oceanographic Research Papers*, 46, 1289–1337. [https://doi.org/10.1016/S0967-0637\(99\)00008-4](https://doi.org/10.1016/S0967-0637(99)00008-4).
- Redfield, A. C., 1934. On the proportions of organic derivatives in sea water and their relation to the composition of plankton. *James Johnstone memorial vol.*, 176–192.
- Redfield, A. C., 1963. The influence of organisms on the composition of seawater. *The Sea*, 2, 26–77.
- Reid, J. L., 1986. On the total geostrophic circulation of the South Pacific Ocean: Flow patterns, tracers and transports. *Progress in Oceanography*, 16, 1–61. [https://doi.org/10.1016/S0079-6611\(97\)00012-8](https://doi.org/10.1016/S0079-6611(97)00012-8).
- Reid, J. L., 1989. On the total geostrophic circulation of the South Atlantic Ocean: Flow patterns, tracers, and transports. *Progress in Oceanography*, 2, 149–244. [https://doi.org/10.1016/0079-6611\(89\)90001-3](https://doi.org/10.1016/0079-6611(89)90001-3).

- Riebesell, U., Schulz, K. G., Bellerby, R., Botros, M., Fritsche, P., Meyerhöfer, M., Neill, C., Nondal, G., Oschlies, A., Wohlers, J., 2007. Enhanced biological carbon consumption in a high CO₂ ocean. *Nature*, 450, 545–548. <https://doi.org/10.1038/nature06267>.
- Rixen, T., Gaye, B., Emeis, K.-C., 2019a. The monsoon, carbon fluxes, and the organic carbon pump in the northern Indian Ocean. *Progress in Oceanography*, 175, 24–39. <https://doi.org/10.1016/j.pocean.2019.03.001>.
- Rixen, T., Gaye, B., Emeis, K.-C., Ramaswamy, V., 2019b. The ballast effect of lithogenic matter and its influences on the carbon fluxes in the Indian Ocean. *Biogeosciences*, 16, 485–503. <http://dx.doi.org/10.5194/bg-16-485-2019>.
- Rixen, T., Ittekkot, V., 2005. Nitrogen deficits in the Arabian Sea, implications from a three component mixing analysis. *Deep-Sea Research Part II: Topical Studies in Oceanography*, 52, 1879–1891. <https://doi.org/10.1016/j.dsr2.2005.06.007>.
- Rowe, G. T., 1979. Symposium on Bio-productivity of Upwelling Ecosystems: Moscow.
- Rowe, G. T., Gardner, W. D., 1979. Sedimentation rates in the slope water of the northwest Atlantic Ocean measured directly with sediment traps. Woods Hole Oceanographic Institution. *Journal of Marine Research*, 37, 581–601.
- Ryther, J. H., 1963. Geographic variations in productivity, in: M. N. Hill (Ed.), *The Sea*, vol. 2, Interscience, Wiley, New York, pp. 347–380.
- Ryther, J. H., 1969. Photosynthesis and fish production in the sea. *Science*, 166, 72–76.
- Ryther, J. H., Menzel, D. W., 1959–1960. The seasonal and geographical range of primary production in the western Sargasso Sea. *Deep-Sea Research*, 6, 235–238. [https://doi.org/10.1016/0146-6313\(59\)90077-2](https://doi.org/10.1016/0146-6313(59)90077-2).
- Ryther, J. H., Yentsch, C. S., 1958. Primary Production of Continental Shelf Waters off New York 1. *Limnology and Oceanography*, 3, 327–335. <https://doi.org/10.4319/lo.1958.3.3.0327>.

- Sanchez-Vidal, A., Calafat, A., Canals, M., Fabres, J., 2004. Particle fluxes in the Almeria-Oran Front: control by coastal upwelling and sea surface circulation. *Journal of marine systems*, 52, 89–106. <https://doi.org/10.1016/j.jmarsys.2004.01.010>.
- Sanudo-Wilhelmy, S. A., Kustka, A. B., Gobler, C. J., Hutchins, D. A., Yang, M., Lwiza, K., Burns, J., Capone, D. G., Raven, J. A., Carpenter, E. J., 2001. Phosphorus limitation of nitrogen fixation by *Trichodesmium* in the central Atlantic Ocean. *Nature*, 411, 66–69. <https://doi.org/10.1038/35075041>.
- Sarmiento, J. L., Gruber, N., 2006. *Ocean biogeochemical dynamics*: Princeton University Press, 503 pp.
- Sarmiento, J. L., Hughes, T. M. C., Stouffer, R. J., Manabe, S., 1998. Simulated response of the ocean carbon cycle to anthropogenic climate warming. *Nature*, 393, 245–249. <https://doi.org/10.1038/30455>.
- Sarmiento, J. L., Toggweiler, J., 1984. A new model for the role of the oceans in determining atmospheric pCO₂. *Nature*, 308, 621–624. <https://doi.org/10.1038/308621a0>.
- Schiebel, R., Barker, S., Lendt, R., Thomas, H., Bollmann, J., 2007. Planktic foraminiferal dissolution in the twilight zone. *Deep-Sea Research Part II: Topical Studies in Oceanography*, 54, 676–686. <https://doi.org/10.1016/j.dsr2.2007.01.009>.
- Schiebel, R., Hemleben, C., 2000. Interannual variability of planktic foraminiferal populations and test flux in the eastern North Atlantic Ocean (JGOFS). *Deep-Sea Research Part II: Topical Studies in Oceanography*, 47, 1809–1852. [https://doi.org/10.1016/S0967-0645\(00\)00008-4](https://doi.org/10.1016/S0967-0645(00)00008-4).
- Schlitzer, R., 2019. Ocean Data View, <https://odv.awi.de> (last access: February 2020).
- Schneider, B., Nagel, K., Struck, U., 2000. Carbon fluxes across the halocline in the eastern Gotland Sea. *Journal of marine systems*, 25, 261–268. [https://doi.org/10.1016/S0924-7963\(00\)00020-8](https://doi.org/10.1016/S0924-7963(00)00020-8).

- Scholten, J. C., Fietzke, J., Vogler, S., Van Der Loeff, M. R., Mangini, A., Koeve, W., Waniek, J., Stoffers, P., Antia, A. N., Kuss, J., 2001. Trapping efficiencies of sediment traps from the deep Eastern North Atlantic: the ^{230}Th calibration. *Deep-Sea Research Part II: Topical Studies in Oceanography*, 48, 2383–2408. [https://doi.org/10.1016/S0967-0645\(00\)00176-4](https://doi.org/10.1016/S0967-0645(00)00176-4).
- Schott, F. A., McCreary, J. P., 2001. The monsoon circulation of the Indian Ocean. *Progress in Oceanography*, 51, 1–123. [https://doi.org/10.1016/S0079-6611\(01\)00083-0](https://doi.org/10.1016/S0079-6611(01)00083-0).
- Schott, F. A., Xie, S.-P., McCreary Jr., J. P., 2009. Indian Ocean circulation and climate variability. *Review of Geophysics*, 47, 1–46. <https://doi:10.1029/2007RG000245>.
- Schrader, H.-J., 1971. Fecal pellets: role in sedimentation of pelagic diatoms. *Science*, 174, 55–57. <https://doi.org/10.1126/science.174.4004.55>.
- Shanks, A. L., Trent, J. D., 1980. Marine snow: sinking rates and potential role in vertical flux. *Deep-Sea Research Part I: Oceanographic Research Papers*, 27, 137–143. [https://doi.org/10.1016/0198-0149\(80\)90092-8](https://doi.org/10.1016/0198-0149(80)90092-8).
- Sharma, G., 1976. Transequatorial movement of water masses in the Indian Ocean. *Journal of Marine Research*, 34, 143–154.
- Siegel, D. A., Granata, T. C., Michaels, A. F., Dickey, T. D., 1990. Mesoscale eddy diffusion, particle sinking, and the interpretation of sediment trap data. *Journal of Geophysical Research: Oceans*, 95, 5305–5311. <https://doi.org/10.1029/JC095iC04p05305>.
- Siegenthaler, U., Wenk, T., 1984. Rapid atmospheric CO_2 variations and ocean circulation. *Nature*, 308, 624–626. <https://doi.org/10.1038/308624a0>.
- Sigman, D. M., Altabet, M. A., McCorkle, D. C., Francois, R., Fischer, G., 1999. The $\delta^{15}\text{N}$ of nitrate in the southern ocean: Consumption of nitrate in surface waters. *Global Biogeochemical Cycles*, 13, 1149–1166. <https://doi.org/10.1029/1999GB900038>.
- Sigman, D. M., Altabet, M. A., McCorkle, D. C., Francois, R., Fischer, G., 2000. The $\delta^{15}\text{N}$ of nitrate in the Southern Ocean: Nitrogen cycling and circulation in the ocean interior. *Journal of Geophysical Research: Oceans*, 105, 19599–19614. <https://doi.org/10.1029/2000JC000265>.

- Sigman, D. M., Casciotti, K. L., 2001. Nitrogen isotopes in the Ocean, in: J. H. Steele, K. K. Turekian and S. A. Thorpe (Eds.), *Encyclopedia of ocean sciences*, New York: Elsevier, pp. 1884–1894.
- Sigman, D. M., Granger, J., DiFiore, P. J., Lehmann, M. M., Ho, R., Cane, G., van Geen, A., 2005. Coupled nitrogen and oxygen isotope measurements of nitrate along the eastern North Pacific margin. *Global Biogeochemical Cycles*, 19, 1–14. <https://doi.org/10.1029/2005GB002458>.
- Sigman, D. M., Karsh, K. L., Casciotti, K. L., 2009. Ocean process tracers: nitrogen isotopes in the ocean, Elsevier Ltd, 4138–4153. <https://doi.org/10.1016/B978-012374473-9.00632-9>.
- Sigman, D. M., Robinson, R., Knapp, A., Van Geen, A., McCorkle, D., Brandes, J., Thunell, R., 2003. Distinguishing between water column and sedimentary denitrification in the Santa Barbara Basin using the stable isotopes of nitrate. *Geochemistry Geophysics Geosystems*, 4, 1–20. <https://doi.org/10.1029/2002GC000384>.
- Signorini, S. R., Franz, B. A. and McClain, C. R., 2015. Chlorophyll variability in the oligotrophic gyres: mechanisms, seasonality and trends. *Frontiers in Marine Science*, 2, 1–11. <https://doi.org/10.3389/fmars.2015.00001>.
- Smetacek, V., von Bröckel, K., Zeitzschel, B., Zenk, W., 1978. Sedimentation of particulate matter during a phytoplankton spring bloom in relation to the hydrographical regime. *Marine Biology*, 47, 211–226. <https://doi.org/10.1007/BF00541000>.
- Stramma, L., 1992. The South Indian Ocean Current. *Journal of Physical Oceanography*, 22, 421–430. [https://doi.org/10.1175/1520-0485\(1992\)022<0421:TSIOC>2.0.CO;2](https://doi.org/10.1175/1520-0485(1992)022<0421:TSIOC>2.0.CO;2).
- Stramma, L., Lutjeharms, J. R., 1997. The flow field of the subtropical gyre of the South Indian Ocean. *Journal of Geophysical Research: Oceans*, 102, 5513–5530. <https://doi.org/10.1029/96JC03455>.
- Suess, E., 1980. Particulate organic carbon flux in the oceans-surface productivity and oxygen utilization. *Nature*, 288, 260–263. <https://doi.org/10.1038/288260a0>.

- Sverdrup, H. U., Johnson, M. W., Fleming, R. H., 1942. *The Oceans: Their Physics, Chemistry, and General Biology*, vol. 7, Prentice Hall NY. <http://ark.cdlib.org/ark:/13030/kt167nb66r>, 1094 pp.
- Takahashi, K., Fujitani, N., Yanada, M., Maita, Y., 2000. Long-term biogenic particle fluxes in the Bering Sea and the central subarctic Pacific Ocean, 1990–1995. *Deep-Sea Research Part I: Oceanographic Research Papers*, 47, 1723–1759. [https://doi.org/10.1016/S0967-0637\(00\)00002-9](https://doi.org/10.1016/S0967-0637(00)00002-9).
- Talley, L. D., 1996. Antarctic intermediate water in the South Atlantic. *The South Atlantic*, Springer, pp. 219–238. <https://doi.org/10.1029/95JC00858>.
- Talley, L. D., 2013. Special Issue on Upper Ocean Processes: Peter Niiler's Contributions and Inspirations. Closure of the Global Overturning Circulation Through the Indian, Pacific, and Southern Oceans - Schematics and Transports. *Oceanography Society*, 26, 80–97. <http://dx.doi.org/10.5670/oceanog.2013.07>.
- Thunell, R. C., 1998. Seasonal and annual variability in particle fluxes in the Gulf of California: A response to climate forcing. *Deep-Sea Research Part I: Oceanographic Research Papers*, 45, 2059–2083. [https://doi.org/10.1016/S0967-0637\(98\)00053-3](https://doi.org/10.1016/S0967-0637(98)00053-3).
- Thunell, R. C., Varela, R., Llano, M., Collister, J., Müller-Karger, F., Bohrer, R., 2000. Organic carbon fluxes, degradation, and accumulation in an anoxic basin: sediment trap results from the Cariaco Basin. *Limnology and Oceanography*, 45, 300–308. <https://doi.org/10.4319/lo.2000.45.2.0300>.
- Toole, J. M., Warren, B. A., 1993. A hydrographic section across the subtropical South Indian Ocean. *Deep-Sea Research Part I: Oceanographic Research Papers*, 40, 1973–2019. [https://doi.org/10.1016/0967-0637\(93\)90042-2](https://doi.org/10.1016/0967-0637(93)90042-2).
- Tréguer (unpublished): http://www.obs-vlfr.fr/cd_rom_dmtt/ANTARES/A3/a3_parameters.htm.
- Trull, T. W., Bray, S., Manganini, S. J., Honjo, S., Francois, R., 2001. Moored sediment trap measurements of carbon export in the Subantarctic and Polar Frontal Zones of the Southern Ocean, south of Australia. *Journal of Geophysical Research: Oceans*, 106, 31489–31509. <https://doi.org/10.1029/2000JC000308>.

- Tsunogai, S., Noriki, S., 1991. Particulate fluxes of carbonate and organic carbon in the ocean. Is the marine biological activity working as a sink of the atmospheric carbon? *Tellus B.* 43, 256–266. <https://doi.org/10.1034/j.1600-0889.1991.00018.x>.
- Tsunogai, S., Uematsu, M., Noriki, S., Tanaka, N., Yamada, M., 1982. Sediment trap experiment in the northern North Pacific: Undulation of settling particles. *Geochemical Journal*, 16, 129–147. <https://doi.org/10.2343/geochemj.16.129>.
- Turner, J. T., 2015. Zooplankton fecal pellets, marine snow, phytodetritus and the ocean's biological pump. *Progress in Oceanography*, 130, 205–248. <https://doi.org/10.1016/j.pocean.2014.08.005>.
- Urabe, T., Ishibashi, J. I., Sunamura, M., Okino, K., Takai, K., Suzuki, K., 2015. Introduction of TAIGA Concept, in: J. Ishibashi, K. Okino, and M. Sunamura (Eds.), *Subseafloor Biosphere Linked to Hydrothermal Systems*, Springer, pp. 3–10. Tokyo. https://doi.org/10.1007/978-4-431-54865-2_1.
- Volk, T., Hoffert, M. I., 1985. Ocean carbon pumps: Analysis of relative strengths and efficiencies in ocean-driven atmospheric CO₂ changes, in: E. T. Sundquist, W. S. Broecker (Eds.), *The carbon cycle and atmospheric CO₂: Natural variations Archean to Present*, Geophysical Monograph Series, vol. 32, AGU. Washington, D. C., pp. 99–110. <https://doi.org/10.1029/GM032p0099>.
- von Bodungen, B., 1975. Thesis, Universität Kiel.
- von Bodungen, B., Antia, A. N., Bauerfeind, E., Haupt, O., Koeve, W., Machado, E., Peeken, I., Peinert, R., Reitmeier, S., Thomsen, C., 1995. Pelagic processes and vertical flux of particles: an overview of a long-term comparative study in the Norwegian Sea and Greenland Sea. *Geologische Rundschau*, 84, 11–27. <https://doi.org/10.1007/BF00192239>.
- von Brökel, K. 1980. Abstract of the international Symposium on Coastal Upwelling, Los Angeles.
- Wada, E., Hattori, A., 1976. Natural abundance of ¹⁵N in particulate organic matter in the North Pacific Ocean. *Geochimica et Cosmochimica Acta*, 40, 249–251, [https://doi.org/10.1016/0016-7037\(76\)90183-6](https://doi.org/10.1016/0016-7037(76)90183-6).

- Wankel, S. D., Kendall, C., Pennington, J. T., Chavez, F. P., Paytan, A., 2007. Nitrification in the euphotic zone as evidenced by nitrate dual isotopic composition: Observations from Monterey Bay, California. *Global Biogeochemical Cycles*, 21, 1–13. <https://doi.org/10.1029/2006GB002723>.
- Ward, B., Devol, A., Rich, J., Chang, B., Bulow, S., Naik, H., Pratihary, A., Jayakumar, A., 2009. Denitrification as the dominant nitrogen loss process in the Arabian Sea. *Nature*, 461, 78–81. <https://doi.org/10.1038/nature08276>.
- Warren, B. A., 1981. Transindian hydrographic section at Lat. 18 S: Property distributions and circulation in the South Indian Ocean. *Deep-Sea Research*, 28, 759–788. [https://doi.org/10.1016/S0198-0149\(81\)80001-5](https://doi.org/10.1016/S0198-0149(81)80001-5).
- Waser, N., Harrison, P., Nielsen, B., Calvert, S., Turpin, D., 1998. Nitrogen isotope fractionation during the uptake and assimilation of nitrate, nitrite, ammonium, and urea by a marine diatom. *Limnology and Oceanography*, 43, 215–224. <https://doi.org/10.4319/lo.1998.43.2.0215>.
- Weber, T., Cram, J. A., Leung, S. W., DeVries, T., Deutsch, C., 2016. Deep ocean nutrients imply large latitudinal variation in particle transfer efficiency. *Proceedings of the National Academy of Sciences*, 113, 8606–8611. <https://doi.org/10.1073/pnas.1604414113>.
- Wefer, G., Fischer, G., 1991. Annual primary production and export flux in the Southern Ocean from sediment trap data. *Marine Chemistry*, 35, 597–613. [https://doi.org/10.1016/S0304-4203\(09\)90045-7](https://doi.org/10.1016/S0304-4203(09)90045-7).
- Wefer, G., Fischer, G., 1993. Seasonal patterns of vertical particle flux in equatorial and coastal upwelling areas of the eastern Atlantic. *Deep-Sea Research Part I: Oceanographic Research Papers*, 40, 1613–1645. [https://doi.org/10.1016/0967-0637\(93\)90019-Y](https://doi.org/10.1016/0967-0637(93)90019-Y).
- Wefer, G., Fischer, G., Fütterer, D., Gersonde, R., 1988. Seasonal particle flux in the Bransfield Strait, Antarctica. *Deep-Sea Research Part A: Oceanographic Research Papers*, 35, 891–898. [https://doi.org/10.1016/0198-0149\(88\)90066-0](https://doi.org/10.1016/0198-0149(88)90066-0).

- Wefer, G., Fischer, G., Fütterer, D., Gersonde, R., Honjo, S., Ostermann, D., 1990. Particle sedimentation and productivity in Antarctic waters of the Atlantic sector, in: U. Bleil, J. Thiede (Eds.), *Geological history of the polar oceans: Arctic versus Antarctic*, Springer, New York, pp. 363–379, https://doi.org/10.1007/978-94-009-2029-3_20.
- Werdell, P.J., Bailey, S.W. 2002. The SeaWiFS Bio-optical Archive and Storage System (SeaBASS), in: G. S. Fargion, C. R. McClain (Eds.), *Current architecture and implementation*, NASA Tech, Memo 2002-211617, NASA Goddard Space Flight Center, Greenbelt, Maryland, p. 45.
- Wiebe, P. H., Boyd, S. H., Winget, C. L., 1976. Particulate matter sinking to the deep-sea floor at 2000 m in the Tongue of the Ocean, Bahamas, with a description of a new sedimentation trap, Woods Hole Oceanographic Institution. *Journal of Marine Research*, 34, 341–354. <https://hdl.handle.net/1912/1792>.
- Wiesner, M. G., Zheng, L., Wong, H. K., Wang, Y., Chen, W., 1996. Fluxes of particulate matter in the South China Sea, in: V. Ittekkot, P. Schäfer, S. Honjo and P. J. Depetris, *Particle Flux in the Ocean*, SCOPE, vol. 57, chap. 16, John Wiley Hoboken, New York, pp. 293–312.
- Williams, P. J. le B., Quay, P. D., Westberry, T. K., Behrenfeld, M. J., 2013. The oligotrophic ocean is autotrophic. *Annual Review of Marine Science*, 5, 535–549. <https://doi.org/10.1146/annurev-marine-121211-172335>.
- Williams, R. G., Follows, M. J., 1998. The Ekman transfer of nutrients and maintenance of new production over the North Atlantic. *Deep-Sea Research Part I: Oceanographic Research Papers*, 45, 461–489. [https://doi.org/10.1016/S0967-0637\(97\)00094-0](https://doi.org/10.1016/S0967-0637(97)00094-0).
- Williams, R. G., Follows, M. J., 2003. Physical transport of nutrients and the maintenance of biological production, in: M. J. R. Fasham (Ed.), *Ocean biogeochemistry*. Springer, Berlin, Heidelberg, pp. 19–51. https://doi.org/10.1007/978-3-642-55844-3_3.

- Wilson, T. R. S., Thomson, J., Colley, S., Hydes, D. J., Higgs, N. C., Sørensen, J., 1985. Early organic diagenesis: the significance of progressive subsurface oxidation fronts in pelagic sediments. *Geochimica Cosmochimica Acta*, 49, 811–822. [https://doi.org/10.1016/0016-7037\(85\)90174-7](https://doi.org/10.1016/0016-7037(85)90174-7).
- Winter, A., Siesser, W. G., 1994. *Composition and morphology of coccolithophore skeletons, Coccolithophores*, Cambridge University Press, New York, pp. 51–62.
- Wong, C. S., Whitney, F. A., Crawford, D. W., Iseki, K., Matear, R. J., Johnson, W. K., Page, J. S., Timothy, D., 1999. Seasonal and interannual variability in particle fluxes of carbon, nitrogen and silicon from time series of sediment traps at Ocean Station P, 1982–1993: relationship to changes in subarctic primary productivity. *Deep-Sea Research Part II: Topical Studies in Oceanography*, 46, 2735–2760. [https://doi.org/10.1016/S0967-0645\(99\)00082-X](https://doi.org/10.1016/S0967-0645(99)00082-X).
- Wong, C. S., Whitney, F. A., Matear, R. J., Iseki, K., 1998. Enhancement of new production in the northeast subarctic Pacific Ocean during negative North Pacific index events. *Limnology and Oceanography*, 43, 1418–1426. <https://doi.org/10.4319/lo.1998.43.7.1418>.
- Woodberry, K. E., Luther, M. E., O'Brien, J. J., 1989. The wind-driven seasonal circulation in the southern tropical Indian Ocean. *Journal of Geophysical Research: Oceans*, 94, 17985–18002. <https://doi.org/10.1029/JC094iC12p17985>.
- Wurl, O., 2009. *Practical guidelines for the analysis of seawater*: CRC press, 408 pp.
- Wüst, G., 1935. Die Stratosphäre. *Wissenschaftliche Ergebnisse der Deutschen Atlantischen Expedition auf dem Vermessungs- und Forschungsschiff "Meteor" 1925–1927*. 6 (1, 2), Jg. S., 109–288.
- Wyrтки, K., 1962. The oxygen minima in relation to ocean circulation. Paper presented at the *Deep-Sea Research and Oceanographic Abstracts*, 9, 11–28. [https://doi.org/10.1016/0011-7471\(62\)90243-7](https://doi.org/10.1016/0011-7471(62)90243-7).
- Wyrтки, K., 1971. *Oceanographic atlas of the international Indian Ocean expedition*: National Science Foundation, 531 pp.

- Wyrтки, K., 1973. Physical oceanography of the Indian Ocean, The biology of the Indian Ocean, Springer, pp. 18–36. https://doi.org/10.1007/978-3-642-65468-8_3.
- Yang, H., Lohman, G., Krebs-Kanzow, U., Ionita, M., Shi, X., Sidorenko, D., Gong, X., Chen, X., Gowan, E. J., 2020. Poleward Shift of the Major Ocean Gyres Detected in a Warming Climate. *Geophysical Research Letters*, 47, 1–10. <https://doi.org/10.1029/2019GL085868>.
- Yokoyama, Y., Takahashi, Y., Miyoshi, Y., Ishibashi, J. I., Kawagucci, S., 2015. Sediment-Pore Water System Associated with Native Sulfur Formation at Jade Hydrothermal Field in Okinawa Trough, in: J. Ishibashi, K. Okino and M. Sunamura (Eds.), *Subseafloor Biosphere Linked to Hydrothermal Systems*, pp. 405–419. Springer, Tokyo, https://doi.org/10.1007/978-4-431-54865-2_31.
- You, Y., 1998. Intermediate water circulation and ventilation of the Indian Ocean derived from water-mass contributions. *Journal of Marine Research*, 56, 1029–1067. <https://doi.org/10.1357/002224098765173455>.
- You, Y., Tomczak, M., 1993. Thermocline circulation and ventilation in the Indian Ocean derived from water mass analysis. *Deep-Sea Research Part I: Oceanographic Research Papers*, 40, 13–56. [https://doi.org/10.1016/0967-0637\(93\)90052-5](https://doi.org/10.1016/0967-0637(93)90052-5).
- Yu, E. F., Francois, R., Bacon, M. P., Honjo, S., Fler, A. P., Manganini, S. J., Rutgers van der Loeff, M. M., Ittekkot, V. 2001. Trapping efficiency of bottom-tethered sediment traps estimated from the intercepted fluxes of ^{230}Th and ^{231}Pa . *Deep-Sea Research Part I: Oceanographic Research Papers*, 48, 865–889. [https://doi.org/10.1016/S0967-0637\(00\)00067-4](https://doi.org/10.1016/S0967-0637(00)00067-4).

Used data and internet sources

Harms et al., 2019a: Physical water properties, nutrient and isotope data of INDEX expedition 2016: <https://doi.pangaea.de/10.1594/PANGAEA.897503>.

Harms et al., 2019b: Physical water properties, nutrient and isotope data of INDEX expedition 2017: <https://doi.pangaea.de/10.1594/PANGAEA.897504>.

NASA Earth DataBase Ocean Color Web:
<https://oceancolor.gsfc.nasa.gov/l3/>

NASA Earth DataBase Giovanni:
<https://giovanni.gsfc.nasa.gov/giovanni/>

NASA Science, by Dr. Mamta Patel Nagaraja (last access 06.07.2020):
<https://science.nasa.gov/earth-science/oceanography/physical-ocean/currents>

Woods Hole Oceanographic Institution:
<https://www.whoi.edu/what-we-do/explore/instruments/instruments-sensors-samplers/sediment-trap/>

Appendix

Appendix A1

Data of water column properties, nutrients, and stable nitrate isotopes collected during INDEX expeditions between 2015 and 2018

Table A1.1. Location of CTD stations during cruises *PE 405* (INDEX 2015), *MSM 59/2* (INDEX 2016), *SO 259* (INDEX 2017), and *PE 446* (INDEX 2018).

	Station ID	Date	Latitude	Longitude
Cruise <i>PE 405</i> in 2015	PS 35	26.11.2015	25°19.81'S	070°28.07'E
	PS 39	27.11.2015	23°51.24'S	069°28.13'E
	PS 42	29.11.2015	23°46.55'S	069°33.58'E
	PS 43	29.11.2015	23°46.97'S	069°32.42'E
	PS 46	05.12.2015	23°32.68'S	069°35.80'E
	PS 48	06.12.2015	23°52.67'S	069°35.81'E
Cruise <i>MSM 59/2</i> in 2016	CTD 03	30.11.2016	23°00.32'S	067°04.10'E
	CTD 14	02.12.2016	23°52.49'S	069°29.73'E
	CTD 22	05.12.2016	22°53.15'S	069°09.82'E
	CTD 32	08.12.2016	21°46.55'S	069°01.03'E
	CTD 35	08.12.2016	21°36.86'S	069°26.64'E
	CTD 52	14.12.2016	21°10.14'S	068°37.32'E
	CTD 67	19.12.2016	21°43.08'S	067°40.45'E
Cruise <i>SO 259</i> in 2017	CTD 01	26.08.2017	02°58.58'S	077°09.50'E
	CTD 03	28.08.2017	08°48.68'S	075°40.34'E
	CTD 05	29.08.2017	15°04.88'S	074°02.86'E
	CTD 07	30.08.2017	20°21.43'S	069°45.07'E
	CTD 11	31.08.2017	20°40.11'S	069°19.47'E
	CTD 15	01.09.2017	20°57.59'S	068°54.99'E
	CTD 45	09.09.2017	23°54.76'S	069°33.35'E
	CTD 49	11.09.2017	26°02.78'S	070°50.39'E
	CTD 60	15.09.2017	27°46.73'S	073°54.98'E
CTD 99	29.09.2017	27°00.38'S	72°24.22'E	
Cruise <i>PE 446</i> in 2018	PS 001	15.10.2018	21°02.17'S	067°07.28'E
	PS 007	16.10.2018	21°09.94'S	068°10.57'E
	PS 029	25.10.2018	25°25.27'S	070°05.36'E
	PS 052	02.11.2018	27°48.23'S	073°53.44'E

Note: CTD water rosette for water sampling equipped with sensors for conductivity (C), temperature (T), and density (D); PS: Plume sled with an on board CTD water rosette; *PE*: Dutch research vessel *Pelagia*; *SO*: German research vessel *Sonne*, *MSM*: German research vessel *Maria S. Merian*.

Table A1.2. Results of CTD casts from cruise *PE 405* (2015).

Cruise <i>PE 405</i> in 2015									
ID	Depth [m]	Sigma-theta [kg m ⁻³]	Salinity [PSU]	Temp [°C]	O ₂ [mL L ⁻¹]	NO ₃ ⁻ [μmol L ⁻¹]	PO ₄ ³⁻ [μmol L ⁻¹]	NO ₃ ⁻ δ ¹⁵ N [‰ ± 1 S.D.] ^a	NO ₃ ⁻ δ ¹⁸ O [‰ ± 1 S.D.] ^b
<i>PS 35</i>	<i>Lat.: 25°19.81'S</i>		<i>Long.: 070°28.07'E</i>			<i>Date: 26 November 2015</i>			
	0	nd.	35.45	24.08	nd.	N/D	0.14	nd.	nd.
	101	nd.	35.69	18.36	nd.	0.07	0.13	nd.	nd.
	2600	nd.	34.72	1.72	nd.	32.52	2.35	4.53	1.67
	3175	nd.	34.72	1.69	nd.	32.61	2.35	4.69	2.27
<i>PS 39</i>	<i>Lat.: 23°51.24'S</i>		<i>Long.: 069°28.13'E</i>			<i>Date: 27 November 2015</i>			
	0	nd.	35.01	24.87	nd.	N/D	0.09	nd.	nd.
	82	nd.	35.34	22.21	nd.	0.04	0.15	nd.	nd.
	2533	nd.	34.72	1.77	nd.	32.68	2.35	5.30	2.34
	3258	nd.	34.72	1.75	nd.	32.80	2.37	4.65	1.98
<i>PS 42</i>	<i>Lat.: 23°46.55'S</i>		<i>Long.: 069°33.58'E</i>			<i>Date: 29 November 2015</i>			
	0	nd.	35.10	25.04	nd.	N/D	0.10	nd.	nd.
	53	nd.	34.72	23.48	nd.	N/D	0.04	nd.	nd.
	100	nd.	34.72	22.15	nd.	N/D	0.05	nd.	nd.
	149	nd.	34.71	20.42	nd.	3.81	0.32	5.19	5.50
	198	nd.	34.62	19.01	nd.	2.76	0.26	4.70	6.71
	502	nd.	34.42	11.49	nd.	11.21	0.82	7.08	4.49
	1004	nd.	34.99	4.87	nd.	31.75	2.18	5.42	3.56
	1500	nd.	35.70	3.07	nd.	23.64	1.57	5.36	1.22
	2000	nd.	35.52	2.08	nd.	32.27	2.33	5.35	2.53
	2884	nd.	35.11	1.77	nd.	25.57	1.74	4.96	0.10
<i>PS 43</i>	<i>Lat.: 23°46.97'S</i>		<i>Long.: 069°32.42'E</i>			<i>Date: 29 November 2015</i>			
	2992	nd.	34.72	1.76	nd.	32.75	2.34	5.37	1.91
<i>PS 46</i>	<i>Lat.: 23°32.68'S</i>		<i>Long.: 069°35.80'E</i>			<i>Date: 05 December 2015</i>			
	3263	nd.	nd.	nd.	nd.	31.86	1.56	5.19	2.40
<i>PS 49</i>	<i>Lat.: 23°52.67'S</i>		<i>Long.: 069°35.81'E</i>			<i>Date: 06 December 2015</i>			
	3252	nd.	34.71	1.83	nd.	31.16	1.71	4.99	1.97

Note. ^a δ¹⁵N in ‰ versus air and ^b δ¹⁸O in ‰ versus VSMOW; S.D. = standard deviation; nd. = no data.

Table A1.3. Results of CTD casts from cruise *MSM 59/2* (2016).

Cruise <i>MSM 59/2</i> in 2016									
ID	Depth [m]	Sigma-theta [kg m ⁻³]	Salinity [PSU]	Temp [°C]	O ₂ [mL L ⁻¹]	NO ₃ ⁻ [μmol L ⁻¹]	PO ₄ ³⁻ [μmol L ⁻¹]	NO ₃ ⁻ δ ¹⁵ N [‰ ± 1 S.D.] ^a	NO ₃ ⁻ δ ¹⁸ O [‰ ± 1 S.D.] ^b
<i>CTD 03</i>	Lat.: 23°00.32'S		Long.: 067°04.10'E			Date: 30 November 2016			
	1	23.47	35.11	24.84	4.21	0.40	0.06	nd.	nd.
	5	23.50	35.10	24.71	4.23	0.36	0.06	nd.	nd.
	10	23.45	35.11	24.91	4.22	0.33	0.02	nd.	nd.
	25	23.55	35.09	24.53	4.24	0.01	0.07	nd.	nd.
	31	23.68	35.06	24.00	4.35	0.00	0.07	nd.	nd.
	51	23.88	35.11	23.48	4.45	0.20	0.09	nd.	nd.
	75	23.95	35.10	23.22	4.45	0.09	0.04	nd.	nd.
	91	24.01	35.11	23.03	4.47	0.25	0.07	nd.	nd.
	100	24.13	35.17	22.80	4.47	0.23	0.06	nd.	nd.
	150	24.83	35.51	21.23	4.18	0.62	0.11	nd.	nd.
	200	25.36	35.64	19.62	3.92	3.02	0.27	5.4 ± 0.0	1.5 ± 0.2
	300	26.15	35.59	16.25	4.20	3.64	0.36	6.6 ± 0.2	2.5 ± 0.4
	400	26.53	35.29	13.48	4.47	7.76	0.62	7.5 ± 0.0	4.4 ± 0.5
	499	26.66	35.07	11.95	4.58	7.32	0.54	7.7 ± 0.1	5.2 ± 1.1
	600	26.74	34.89	10.78	4.60	12.29	0.89	7.3 ± 0.0	4.8 ± 0.2
	799	26.92	34.59	8.27	4.11	19.88	1.40	6.6 ± 0.0	3.4 ± 0.4
	1000	27.19	34.45	5.49	3.36	25.06	1.87	6.0 ± 0.0	1.5 ± 0.1
	1199	27.41	34.58	4.55	2.43	25.22	2.02	6.0 ± 0.1	1.6 ± 0.3
	1599	27.62	34.66	2.99	2.86	35.40	2.46	5.5 ± 0.1	1.1 ± 0.3
	2001	27.74	34.71	2.15	3.21	33.86	2.33	5.2 ± 0.0	1.1 ± 0.3
	2502	27.78	34.72	1.77	3.31	34.13	2.34	5.2 ± 0.1	1.1 ± 0.0
	3000	27.79	34.72	1.70	3.32	27.26	1.83	5.2 ± 0.1	1.4 ± 0.1
	3670	27.80	34.72	1.62	3.33	22.82	1.90	5.1 ± 0.1	1.2 ± 0.1
<i>CTD 14</i>	Lat.: 23°52.49'S		Long.: 069°29.73'E			Date: 02 December 2016			
	3	23.79	35.43	24.60	4.75	0.54	0.11	nd.	nd.
	10	23.98	35.42	23.95	4.80	0.54	0.09	nd.	nd.
	25	24.09	35.44	23.60	4.81	0.56	0.07	nd.	nd.
	35	24.24	35.43	23.06	4.93	0.47	0.05	nd.	nd.
	48	24.54	35.46	22.11	5.02	0.54	0.08	nd.	nd.
	70	24.95	35.57	20.91	4.94	0.54	0.12	nd.	nd.
	90	25.17	35.64	20.29	4.83	0.53	0.12	nd.	nd.
	100	25.26	35.66	20.03	4.79	0.72	0.13	nd.	nd.
	150	25.71	35.69	18.37	4.57	2.47	0.27	4.5 ± 0.1	1.7 ± 0.3
	201	25.97	35.66	17.26	4.62	3.20	0.37	5.8 ± 0.2	2.2 ± 0.1
	301	26.49	35.34	13.85	4.88	6.53	0.53	7.6 ± 0.0	4.0 ± 0.4
	398	26.64	35.12	12.25	5.05	9.71	0.78	7.8 ± 0.0	4.5 ± 0.1
	503	26.73	34.92	10.96	5.15	10.46	0.90	7.3 ± 0.0	4.9 ± 0.1
	602	26.79	34.79	10.08	5.12	10.80	0.93	7.0 ± 0.0	4.8 ± 0.0
	797	26.94	34.55	7.98	4.63	23.37	1.56	6.4 ± 0.4	1.9 ± 0.2
	1001	27.27	34.47	4.93	3.55	34.17	2.31	5.9 ± 0.3	1.6 ± 0.0
	1300	27.49	34.60	3.89	2.98	39.46	2.73	5.8 ± 0.1	1.4 ± 0.2
	1999	27.74	34.72	2.15	3.83	40.22	2.79	5.1 ± 0.1	1.3 ± 0.1
	2496	27.78	34.72	1.78	3.92	30.55	2.24	5.1 ± 0.1	0.6 ± 0.2
	3501	27.79	34.73	1.76	3.93	33.69	2.34	5.0 ± 0.1	0.9 ± 0.5
<i>CTD 22</i>	Lat.: 22°53.15'S		Long.: 069°09.82'E			Date: 05 December 2016			
	3	23.49	35.17	24.95	4.67	0.55	0.08	nd.	nd.
	11	23.49	35.17	24.95	4.69	0.60	0.09	nd.	nd.
	21	23.66	35.28	24.66	4.74	0.53	0.03	nd.	nd.
	30	23.79	35.24	24.12	4.80	0.55	0.02	nd.	nd.
	50	24.05	35.33	23.48	4.94	0.59	0.07	nd.	nd.
	74	24.42	35.35	22.23	4.87	0.58	0.09	nd.	nd.
	100	24.74	35.48	21.46	4.62	0.65	0.11	nd.	nd.
	120	25.04	35.65	20.84	4.87	0.88	0.11	nd.	nd.
	149	25.38	35.67	19.63	4.66	1.79	0.18	4.5 ± 0.2	1.4 ± 0.4
	201	25.74	35.71	18.33	4.57	2.74	0.26	5.7 ± 0.4	2.6 ± 0.5
	300	26.38	35.43	14.68	4.78	6.24	0.55	7.1 ± 0.1	3.8 ± 0.1
	400	26.59	35.20	12.84	4.99	9.47	0.73	7.6 ± 0.2	4.7 ± 0.1
	500	26.71	34.96	11.27	5.12	12.78	0.91	7.0 ± 0.1	5.3 ± 0.5
	600	26.78	34.81	10.21	5.07	15.94	1.09	7.3 ± 0.0	4.3 ± 0.2
	799	26.96	34.54	7.74	4.54	22.98	1.54	6.4 ± 0.4	1.6 ± 0.2
	999	27.24	34.45	5.08	3.71	34.41	2.28	6.1 ± 0.3	1.1 ± 0.1
	1250	27.47	34.62	4.29	2.72	32.65	2.35	5.4 ± 0.2	0.8 ± 0.4
	2000	27.75	34.72	2.03	3.81	35.31	2.32	5.3 ± 0.3	0.6 ± 0.5
	2501	27.78	34.72	1.78	3.86	35.12	2.43	5.3 ± 0.3	0.6 ± 0.2

Table A1.3. (continued)

Cruise MSM 59/2 in 2016									
ID	Depth [m]	Sigma-theta [kg m ⁻³]	Salinity [PSU]	Temp [°C]	O ₂ [mL L ⁻¹]	NO ₃ ⁻ [μmol L ⁻¹]	PO ₄ ³⁻ [μmol L ⁻¹]	NO ₃ ⁻ δ ¹⁵ N [‰ ± 1 S.D.] ^a	NO ₃ ⁻ δ ¹⁸ O [‰ ± 1 S.D.] ^b
CTD 22	Lat.: 22°53.15'S		Long.: 069°09.82'E			Date: 05 December 2016			
	3149	27.79	34.72	1.71	3.86	35.70	2.45	5.3 ± 0.2	0.7 ± 0.4
	3693	27.79	34.72	1.74	3.84	35.53	2.44	5.2 ± 0.3	0.6 ± 0.2
CTD 32	Lat.: 21°46.55'S		Long.: 069°01.03'E			Date: 08 December 2016			
	5	23.14	34.96	25.57	4.61	0.26	0.09	nd.	nd.
	10	23.14	34.96	25.54	4.61	N/D	N/D	nd.	nd.
	20	23.57	35.07	24.43	4.75	0.20	0.02	nd.	nd.
	29	23.64	35.08	24.21	4.78	0.23	0.05	nd.	nd.
	51	23.95	35.11	23.23	4.91	0.19	0.05	nd.	nd.
	75	24.24	35.23	22.57	4.88	0.17	0.07	nd.	nd.
	101	24.49	35.33	21.96	4.75	0.26	0.07	nd.	nd.
	139	24.90	35.50	20.92	4.18	2.64	0.26	5.9 ± 0.3	2.9 ± 0.4
	199	25.53	35.71	19.19	4.24	2.88	0.27	4.9 ± 0.2	0.5 ± 0.3
	293	26.23	35.55	15.81	4.68	3.97	0.39	7.1 ± 0.2	3.2 ± 0.3
	400	26.60	35.19	12.77	4.99	6.74	0.60	7.8 ± 0.2	4.4 ± 0.8
	500	26.71	34.97	11.31	5.14	10.03	0.77	7.2 ± 0.2	5.0 ± 0.5
	601	26.79	34.78	10.03	5.12	15.44	1.07	7.1 ± 0.0	4.5 ± 0.0
	799	26.98	34.54	7.65	4.33	25.15	1.71	6.4 ± 0.4	2.7 ± 0.4
	889	27.11	34.45	6.19	4.08	29.75	2.00	6.2 ± 0.0	1.3 ± 0.1
	1005	27.28	34.47	4.91	3.55	33.97	2.35	6.1 ± 0.0	1.0 ± 0.3
1256	27.49	34.62	4.02	2.84	0.83	0.09	nd.	nd.	
2008	27.75	34.72	2.04	3.83	26.63	1.78	5.3 ± 0.0	0.9 ± 0.2	
2509	27.78	34.72	1.76	3.89	31.23	2.19	5.2 ± 0.0	0.4 ± 0.1	
2731	27.78	34.72	1.76	3.89	34.20	2.37	5.3 ± 0.0	0.5 ± 0.1	
3412	27.79	34.73	1.75	3.91	33.84	2.33	5.1 ± 0.1	1.4 ± 0.1	
CTD 35	Lat.: 21°36.86'S		Long.: 069°26.64'E			Date: 08 December 2016			
	0	n/D	n/D	n/D	n/D	0.05	0.12	nd.	nd.
	10	23.07	34.90	25.62	4.65	0.26	0.02	nd.	nd.
	25	23.33	35.00	25.06	4.70	0.03	0.06	nd.	nd.
	50	23.82	35.05	23.54	4.88	0.05	0.06	nd.	nd.
	75	24.15	35.18	22.72	4.90	0.01	0.01	nd.	nd.
	101	24.44	35.30	22.04	4.88	0.07	0.05	nd.	nd.
	149	24.78	35.47	21.30	4.45	0.85	0.15	nd.	nd.
	200	25.37	35.69	19.73	4.32	2.41	0.25	4.8 ± 0.1	1.7 ± 0.1
	301	26.17	35.59	16.19	4.62	3.74	0.38	6.8 ± 0.3	2.6 ± 0.3
	400	26.56	35.26	13.23	4.97	8.11	0.63	7.9 ± 0.1	4.9 ± 0.8
	501	26.69	35.01	11.55	5.11	11.63	0.84	7.3 ± 0.2	4.9 ± 0.6
	600	26.78	34.81	10.25	5.13	10.99	0.80	7.0 ± 0.2	4.6 ± 0.4
	900	27.16	34.46	5.86	3.80	31.21	2.16	5.9 ± 0.1	2.2 ± 0.2
1400	27.55	34.69	4.00	2.58	37.65	2.70	5.9 ± 0.1	1.7 ± 0.1	
1999	27.75	34.72	2.12	3.77	34.41	2.42	5.2 ± 0.2	1.6 ± 0.7	
3053	27.79	34.73	1.70	3.93	33.51	2.39	5.1 ± 0.3	1.7 ± 0.5	
CTD 32	Lat.: 21°46.55'S		Long.: 069°01.03'E			Date: 08 December 2016			
	5	23.14	34.96	25.57	4.61	0.26	0.09	nd.	nd.
	10	23.14	34.96	25.54	4.61	N/D	N/D	nd.	nd.
	20	23.57	35.07	24.43	4.75	0.20	0.02	nd.	nd.
	29	23.64	35.08	24.21	4.78	0.23	0.05	nd.	nd.
	51	23.95	35.11	23.23	4.91	0.19	0.05	nd.	nd.
	75	24.24	35.23	22.57	4.88	0.17	0.07	nd.	nd.
	101	24.49	35.33	21.96	4.75	0.26	0.07	nd.	nd.
	139	24.90	35.50	20.92	4.18	2.64	0.26	5.9 ± 0.3	2.9 ± 0.4
	199	25.53	35.71	19.19	4.24	2.88	0.27	4.9 ± 0.2	0.5 ± 0.3
	293	26.23	35.55	15.81	4.68	3.97	0.39	7.1 ± 0.2	3.2 ± 0.3
	400	26.60	35.19	12.77	4.99	6.74	0.60	7.8 ± 0.2	4.4 ± 0.8
	500	26.71	34.97	11.31	5.14	10.03	0.77	7.2 ± 0.2	5.0 ± 0.5
	601	26.79	34.78	10.03	5.12	15.44	1.07	7.1 ± 0.0	4.5 ± 0.0
	799	26.98	34.54	7.65	4.33	25.15	1.71	6.4 ± 0.4	2.7 ± 0.4
	889	27.11	34.45	6.19	4.08	29.75	2.00	6.2 ± 0.0	1.3 ± 0.1
	1005	27.28	34.47	4.91	3.55	33.97	2.35	6.1 ± 0.0	1.0 ± 0.3
1256	27.49	34.62	4.02	2.84	0.83	0.09	nd.	nd.	
2008	27.75	34.72	2.04	3.83	26.63	1.78	5.3 ± 0.0	0.9 ± 0.2	
2509	27.78	34.72	1.76	3.89	31.23	2.19	5.2 ± 0.0	0.4 ± 0.1	
2731	27.78	34.72	1.76	3.89	34.20	2.37	5.3 ± 0.0	0.5 ± 0.1	
3412	27.79	34.73	1.75	3.91	33.84	2.33	5.1 ± 0.1	1.4 ± 0.1	

Table A1.3. (continued)

Cruise MSM 59/2 in 2016									
ID	Depth [m]	Sigma-theta [kg m ⁻³]	Salinity [PSU]	Temp [°C]	O ₂ [mL L ⁻¹]	NO ₃ ⁻ [μmol L ⁻¹]	PO ₄ ³⁻ [μmol L ⁻¹]	NO ₃ ⁻ δ ¹⁵ N [‰ ± 1 S.D.] ^a	NO ₃ ⁻ δ ¹⁸ O [‰ ± 1 S.D.] ^b
<i>CTD</i> 35	<i>Lat.: 21°36.86'S</i>		<i>Long.: 069°26.64'E</i>			<i>Date: 08 December 2016</i>			
	0	n/D	n/D	n/D	n/D	0.05	0.12	nd.	nd.
	10	23.07	34.90	25.62	4.65	0.26	0.02	nd.	nd.
	25	23.33	35.00	25.06	4.70	0.03	0.06	nd.	nd.
	50	23.82	35.05	23.54	4.88	0.05	0.06	nd.	nd.
	75	24.15	35.18	22.72	4.90	0.01	0.01	nd.	nd.
	101	24.44	35.30	22.04	4.88	0.07	0.05	nd.	nd.
	149	24.78	35.47	21.30	4.45	0.85	0.15	nd.	nd.
	200	25.37	35.69	19.73	4.32	2.41	0.25	4.8 ± 0.1	1.7 ± 0.1
	301	26.17	35.59	16.19	4.62	3.74	0.38	6.8 ± 0.3	2.6 ± 0.3
	400	26.56	35.26	13.23	4.97	8.11	0.63	7.9 ± 0.1	4.9 ± 0.8
	501	26.69	35.01	11.55	5.11	11.63	0.84	7.3 ± 0.2	4.9 ± 0.6
	600	26.78	34.81	10.25	5.13	10.99	0.80	7.0 ± 0.2	4.6 ± 0.4
	900	27.16	34.46	5.86	3.80	31.21	2.16	5.9 ± 0.1	2.2 ± 0.2
	1400	27.55	34.69	4.00	2.58	37.65	2.70	5.9 ± 0.1	1.7 ± 0.1
	1999	27.75	34.72	2.12	3.77	34.41	2.42	5.2 ± 0.2	1.6 ± 0.7
	3053	27.79	34.73	1.70	3.93	33.51	2.39	5.1 ± 0.3	1.7 ± 0.5
<i>CTD</i> 52	<i>Lat.: 21°10.14'S</i>		<i>Long.: 068°37.32'E</i>			<i>Date: 14 December 2016</i>			
	2	23.00	34.80	25.61	4.62	0.10	0.08	nd.	nd.
	10	23.00	34.80	25.62	4.63	0.11	0.08	nd.	nd.
	21	23.01	34.80	25.61	4.62	0.10	0.08	nd.	nd.
	31	23.01	34.79	25.57	4.61	0.09	0.08	nd.	nd.
	51	23.26	34.87	24.93	4.71	0.09	0.07	nd.	nd.
	75	23.72	34.90	23.49	4.84	0.10	0.07	nd.	nd.
	101	24.12	35.16	22.79	4.82	0.16	0.08	nd.	nd.
	150	24.63	35.41	21.67	4.66	1.00	0.15	nd.	nd.
	201	25.26	35.65	20.03	4.35	1.90	0.21	4.3 ± 0.2	1.0 ± 0.8
	251	25.63	35.73	18.87	4.40	2.49	0.27	4.6 ± 0.1	0.7 ± 0.9
	299	26.07	35.64	16.77	4.54	1.51	0.14	nd.	nd.
	401	26.57	35.24	13.09	4.95	7.62	0.60	7.6 ± 0.1	4.5 ± 0.5
	503	26.69	35.02	11.61	5.11	10.51	0.82	7.1 ± 0.0	4.9 ± 0.2
	600	26.76	34.85	10.49	5.17	8.78	0.79	7.3 ± 0.1	4.4 ± 0.1
	899	27.16	34.47	5.83	3.74	26.05	1.98	6.3 ± 0.2	2.5 ± 0.4
	998	27.28	34.49	4.98	3.36	25.94	2.07	6.2 ± 0.1	2.7 ± 0.3
	1350	27.55	34.69	3.95	2.62	26.54	2.13	6.0 ± 0.1	2.7 ± 0.2
	2001	27.74	34.72	2.15	3.71	26.54	2.11	5.4 ± 0.1	2.0 ± 0.2
	2501	27.78	34.72	1.82	3.83	27.70	2.24	5.3 ± 0.1	2.0 ± 0.4
	2998	27.79	34.73	1.74	3.91	32.21	2.37	5.2 ± 0.3	1.8 ± 0.6
	3712	27.79	34.73	1.81	3.88	27.78	2.22	6.1 ± 0.2	1.8 ± 0.2
<i>CTD</i> 67	<i>Lat.: 21°43.08'S</i>		<i>Long.: 067°40.45'E</i>			<i>Date: 19 December 2016</i>			
	6	23.31	35.11	25.38	4.60	0.10	0.07	nd.	nd.
	10	23.31	35.11	25.37	4.61	0.12	0.06	nd.	nd.
	21	23.37	35.17	25.36	4.60	0.63	0.07	nd.	nd.
	30	23.51	35.24	25.05	4.66	0.80	0.07	nd.	nd.
	50	23.99	35.23	23.41	4.89	0.08	0.06	nd.	nd.
	75	24.37	35.46	22.72	4.89	1.03	0.17	nd.	nd.
	115	24.82	35.48	21.16	4.38	10.97	0.99	nd.	nd.
	150	25.18	35.62	20.22	4.32	2.35	0.25	4.5 ± 0.1	2.6 ± 0.2
	195	25.62	35.69	18.77	4.43	4.06	0.40	5.1 ± 0.2	4.2 ± 0.2
	300	26.24	35.54	15.70	4.63	7.29	0.60	6.7 ± 0.1	4.0 ± 0.1
	401	26.57	35.25	13.16	4.95	10.01	0.77	7.3 ± 0.1	4.5 ± 0.7
	500	26.68	35.04	11.72	5.06	12.28	0.95	7.0 ± 0.3	4.7 ± 0.6
	601	26.77	34.84	10.43	5.05	19.71	1.50	6.8 ± 0.2	4.6 ± 0.3
	801	26.97	34.54	7.72	4.49	25.98	1.94	6.3 ± 0.0	1.8 ± 0.1
	900	27.15	34.46	5.93	3.85	33.81	2.54	6.1 ± 0.0	2.1 ± 0.0
	1300	27.50	34.65	4.21	2.62	26.54	2.15	6.1 ± 0.1	2.8 ± 0.0
	2000	27.73	34.72	2.26	3.60	24.56	2.04	5.6 ± 0.0	2.4 ± 0.3
	3002	27.79	34.73	1.74	3.81	33.17	2.40	5.3 ± 0.0	2.4 ± 0.4
	3459	27.79	34.72	1.76	3.79	27.9	0.23	4.3 ± 0.1	0.3 ± 0.1

Note: ^a δ¹⁵N in ‰ versus air and ^b δ¹⁸O in ‰ versus VSMOW; S.D. = standard deviation; nd. = no data.

Table A1.4. Results of CTD casts from cruise SO 259 (2017).

Cruise SO 259 in 2017									
ID	Depth [m]	Sigma-theta [kg m ⁻³]	Salinity [PSU]	Temp [°C]	O ₂ [mL L ⁻¹]	NO ₃ ⁻ [μmol L ⁻¹]	PO ₄ ³⁻ [μmol L ⁻¹]	NO ₃ ⁻ δ ¹⁵ N [‰ ± 1 S.D.] ^a	NO ₃ ⁻ δ ¹⁸ O [‰ ± 1 S.D.] ^b
<i>CTD 01</i>	<i>Lat.: 02°58.58'S</i>		<i>Long.: 077°09.50'E</i>			<i>Date: 26 August 2017</i>			
	8	22.09	35.18	29.33	3.97	0.40	0.11	nd.	nd.
	28	22.09	35.19	29.33	3.97	0.03	0.12	nd.	nd.
	61	22.91	35.34	27.19	3.76	0.71	0.26	nd.	nd.
	85	24.17	35.33	23.05	2.75	10.09	0.78	7.3 ± 0.1	4.9 ± 0.1
	181	26.18	35.05	14.26	1.42	26.38	1.77	6.3 ± 0.1	3.6 ± 0.2
	302	26.75	34.97	11.04	2.30	26.02	1.74	7.0 ± 0.1	2.5 ± 0.0
	400	26.86	34.92	10.21	1.90	29.84	1.98	7.2 ± 0.0	2.7 ± 0.1
	499	26.98	34.89	9.39	1.53	33.26	2.25	7.2 ± 0.2	3.0 ± 0.2
	600	27.11	34.91	8.67	1.34	35.07	2.45	7.2 ± 0.1	3.0 ± 0.3
	706	27.22	34.95	8.17	1.07	37.17	2.65	7.3 ± 0.0	3.3 ± 0.0
	800	27.29	34.93	7.64	1.04	37.93	2.66	7.2 ± 0.1	2.8 ± 0.3
	910	27.36	34.86	6.68	1.27	32.21	2.40	7.0 ± 0.1	2.6 ± 0.1
	1001	27.40	34.83	6.23	1.37	38.57	2.72	7.1 ± 0.1	3.1 ± 0.2
	1100	27.46	34.81	5.59	1.54	38.66	2.72	6.9 ± 0.0	2.9 ± 0.0
	1201	27.51	34.80	5.15	1.66	38.65	2.73	6.6 ± 0.1	3.4 ± 0.2
	1302	27.56	34.82	4.88	1.71	38.76	2.73	6.6 ± 0.1	2.5 ± 0.1
	1801	27.72	34.78	3.03	2.53	37.52	2.53	6.0 ± 0.1	2.2 ± 0.0
	2998	27.80	34.73	1.68	3.32	36.28	2.45	5.3 ± 0.2	1.8 ± 0.3
	5018	27.82	34.72	1.45	3.72	35.40	2.36	5.3 ± 0.1	2.3 ± 0.1
<i>CTD 03</i>	<i>Lat.: 08°48.68'S</i>		<i>Long.: 075°40.34'E</i>			<i>Date: 28 August 2017</i>			
	3	22.93	35.15	26.67	4.12	0.60	0.16	nd.	nd.
	29	22.93	35.15	26.68	4.11	1.07	0.20	nd.	nd.
	55	23.45	35.08	24.85	3.28	6.35	0.57	7.0 ± 0.1	4.1 ± 0.2
	100	25.51	35.16	17.54	1.40	17.67	1.21	6.2 ± 0.2	3.0 ± 0.2
	200	26.40	34.98	12.91	1.44	27.60	1.80	6.4 ± 0.1	3.0 ± 0.0
	249	26.56	34.96	11.99	1.36	29.24	1.89	6.5 ± 0.0	3.1 ± 0.1
	299	26.68	34.94	11.32	1.62	27.30	1.77	6.7 ± 0.1	3.0 ± 0.2
	399	26.85	34.87	10.06	1.93	22.67	1.65	6.8 ± 0.1	2.9 ± 0.2
	500	26.96	34.83	9.19	1.77	19.60	1.46	7.0 ± 0.0	2.2 ± 0.1
	600	27.07	34.82	8.48	1.68	23.08	1.75	6.9 ± 0.1	2.5 ± 0.4
	700	27.15	34.81	7.88	1.53	35.78	2.44	6.8 ± 0.1	2.7 ± 0.1
	801	27.24	34.79	7.15	1.34	27.57	2.14	6.8 ± 0.1	2.7 ± 0.1
	900	27.31	34.77	6.62	1.41	38.09	2.66	6.7 ± 0.0	3.0 ± 0.2
	1000	27.36	34.74	5.98	1.50	38.59	2.71	6.4 ± 0.2	2.4 ± 0.1
	1100	27.42	34.75	5.59	1.63	26.38	2.04	6.5 ± 0.1	2.6 ± 0.3
	1200	27.47	34.74	5.14	1.74	34.41	2.48	6.5 ± 0.1	3.1 ± 0.3
	1300	27.52	34.74	4.74	1.87	26.72	2.05	6.3 ± 0.0	3.1 ± 0.3
	1399	27.56	34.74	4.30	2.03	19.97	1.73	6.2 ± 0.2	1.9 ± 0.1
	1500	27.61	34.74	3.84	2.24	26.42	2.14	6.0 ± 0.0	2.2 ± 0.1
	1599	27.65	34.75	3.54	2.40	37.76	2.62	6.0 ± 0.1	2.7 ± 0.1
	3000	27.80	34.73	1.64	3.47	35.54	2.40	5.3 ± 0.1	2.0 ± 0.2
	5151	27.82	34.72	1.44	3.78	35.34	2.36	5.0 ± 0.1	2.1 ± 0.2
<i>CTD 05</i>	<i>Lat.: 15°04.88'S</i>		<i>Long.: 074°02.86'E</i>			<i>Date: 29 August 2017</i>			
	8	23.50	35.02	24.52	4.27	0.54	0.24	nd.	nd.
	126	24.10	35.09	23.52	3.72	2.83	0.36	7.2 ± 0.2	nd.
	199	25.47	35.68	20.04	4.07	1.14	0.22	nd.	nd.
	301	26.58	35.34	14.12	4.19	7.69	0.52	7.1 ± 0.1	3.6 ± 0.3
	400	26.73	34.94	11.05	4.66	12.49	0.95	7.6 ± 0.2	4.6 ± 0.1
	499	26.84	34.69	9.31	4.55	17.89	1.28	7.0 ± 0.1	3.9 ± 0.1
	595	27.03	34.55	7.29	3.55	27.44	1.92	6.7 ± 0.0	2.9 ± 0.4
	701	27.23	34.63	6.31	2.43	34.04	2.44	6.6 ± 0.2	3.0 ± 0.1
	799	27.33	34.69	5.92	2.00	36.05	2.21	6.6 ± 0.1	2.6 ± 0.1
	899	27.39	34.71	5.52	1.96	36.00	2.64	6.6 ± 0.1	3.4 ± 0.0
	1000	27.44	34.71	5.17	2.01	36.93	2.70	6.5 ± 0.2	3.5 ± 0.3
	1102	27.48	34.72	4.83	2.06	37.15	2.73	6.4 ± 0.1	3.6 ± 0.0
	1201	27.52	34.73	4.54	2.12	37.20	2.74	6.3 ± 0.0	3.0 ± 0.1
	1299	27.56	34.73	4.22	2.23	37.10	2.57	6.3 ± 0.2	3.4 ± 0.0
	1400	27.59	34.73	3.91	2.38	36.77	2.55	5.9 ± 0.1	2.5 ± 0.2
	1502	27.62	34.72	3.62	2.51	36.63	2.67	6.0 ± 0.0	3.2 ± 0.3
	1800	27.70	34.73	2.79	2.85	36.08	2.62	5.8 ± 0.1	3.2 ± 0.0
	3001	27.80	34.73	1.63	3.56	34.66	2.45	5.3 ± 0.1	3.0 ± 0.1
	5170	27.82	34.72	1.47	3.76	34.56	2.48	5.0 ± 0.0	2.1 ± 0.3

Table A1.4. (continued)

Cruise SO 259 in 2017									
ID	Depth [m]	Sigma-theta [kg m ⁻³]	Salinity [PSU]	Temp [°C]	O ₂ [mL L ⁻¹]	NO ₃ ⁻ [μmol L ⁻¹]	PO ₄ ³⁻ [μmol L ⁻¹]	NO ₃ ⁻ δ ¹⁵ N [‰ ± 1 S.D.] ^a	NO ₃ ⁻ δ ¹⁸ O [‰ ± 1 S.D.] ^b
<i>CTD</i> 15	<i>Lat.: 20°57.59'S</i>		<i>Long.: 068°54.99'E</i>			<i>Date: 01 September 2017</i>			
	4	23.76	35.07	23.78	4.37	0.03	0.10	nd.	nd.
	101	23.86	35.11	23.57	4.35	0.01	0.09	nd.	nd.
	145	24.06	35.24	23.21	4.08	2.38	0.25	5.4 ± 0.1	nd.
	200	25.01	35.53	20.62	3.75	2.41	0.29	5.9 ± 0.1	nd.
	279	25.66	35.70	18.67	3.89	3.01	0.30	5.4 ± 0.1	1.8 ± 0.3
	403	26.49	35.33	13.82	4.51	5.32	0.42	7.5 ± 0.0	4.6 ± 0.1
	500	26.68	35.03	11.74	4.74	10.46	0.68	7.7 ± 0.1	4.9 ± 0.4
	600	26.79	34.78	10.01	4.81	14.88	0.98	7.3 ± 0.1	4.3 ± 0.2
	700	26.87	34.62	8.74	4.56	19.41	1.15	6.9 ± 0.1	3.8 ± 0.2
	801	27.02	34.50	7.11	4.05	25.94	1.71	6.7 ± 0.1	3.1 ± 0.0
	899	27.21	34.44	5.31	3.61	32.00	2.11	6.3 ± 0.0	3.1 ± 0.2
	999	27.35	34.56	4.82	2.73	35.51	2.21	6.4 ± 0.2	2.8 ± 0.1
	1100	27.42	34.59	4.47	2.65	36.13	2.57	6.3 ± 0.0	3.1 ± 0.2
	1199	27.47	34.62	4.18	2.61	35.62	2.52	6.3 ± 0.0	3.0 ± 0.1
	1300	27.53	34.65	3.89	2.60	36.53	2.66	6.2 ± 0.2	2.9 ± 0.0
	1400	27.57	34.69	3.76	2.59	36.50	2.28	6.3 ± 0.0	3.2 ± 0.0
	1499	27.61	34.70	3.51	2.68	36.49	2.74	6.3 ± 0.1	3.1 ± 0.1
	1799	27.71	34.70	2.47	3.41	34.23	2.53	5.8 ± 0.2	2.4 ± 0.4
	2500	27.78	34.72	1.78	3.70	33.83	2.29	5.5 ± 0.1	2.4 ± 0.2
	2999	27.79	34.73	1.74	3.76	33.85	2.18	5.4 ± 0.0	2.4 ± 0.0
	3266	27.79	34.73	1.76	3.77	33.59	2.47	5.4 ± 0.1	2.3 ± 0.3
<i>CTD</i> 45	<i>Lat.: 23°54.76'S</i>		<i>Long.: 069°33.35'E</i>			<i>Date: 09 September 2017</i>			
	5	24.25	35.23	22.50	4.40	0.07	0.01	nd.	nd.
	50	24.27	35.25	22.50	4.40	0.04	0.06	nd.	nd.
	103	24.67	35.55	21.91	4.24	0.02	0.03	nd.	nd.
	201	25.59	35.72	18.94	4.14	1.03	0.15	nd.	nd.
	304	26.30	35.51	15.35	4.40	3.75	0.33	7.4 ± 0.1	2.2 ± 0.2
	405	26.60	35.17	12.70	4.55	8.50	0.62	7.6 ± 0.1	4.4 ± 0.3
	506	26.71	34.94	11.13	4.81	11.68	0.81	7.6 ± 0.0	5.0 ± 0.1
	602	26.79	34.77	9.98	4.82	14.77	0.99	7.2 ± 0.2	4.6 ± 0.2
	707	26.85	34.64	9.01	4.65	N.D	N.D	nd.	nd.
	806	26.96	34.53	7.73	4.23	23.40	1.54	6.6 ± 0.1	3.6 ± 0.1
	904	27.13	34.43	5.91	3.85	28.90	1.91	6.6 ± 0.1	3.7 ± 0.3
	1007	27.26	34.44	4.81	3.49	33.07	2.16	6.3 ± 0.0	2.7 ± 0.2
	1110	27.36	34.51	4.45	3.05	N.D	N.D	6.2 ± 0.0	2.7 ± 0.0
	1209	27.42	34.54	4.09	2.93	35.52	2.46	6.2 ± 0.1	2.6 ± 0.2
	1312	27.48	34.59	3.89	2.77	36.06	2.53	6.1 ± 0.2	2.5 ± 0.4
	1413	27.53	34.62	3.66	2.78	35.99	2.55	6.2 ± 0.1	2.7 ± 0.2
	1516	27.58	34.66	3.44	2.81	35.94	2.54	6.1 ± 0.2	2.5 ± 0.0
	1616	27.62	34.67	3.16	2.96	35.49	2.45	6.0 ± 0.2	2.7 ± 0.3
	1716	27.65	34.69	2.96	3.05	35.00	2.42	6.0 ± 0.0	2.5 ± 0.1
	1818	27.68	34.69	2.72	3.21	34.52	2.35	5.8 ± 0.0	2.4 ± 0.1
	2022	27.73	34.71	2.29	3.51	33.70	2.30	5.5 ± 0.1	2.1 ± 0.2
	3042	27.79	34.72	1.72	3.75	33.15	2.27	5.4 ± 0.1	2.2 ± 0.2
	4291	27.79	34.72	1.85	3.76	33.24	2.23	5.4 ± 0.1	2.2 ± 0.0
<i>CTD</i> 49	<i>Lat.: 26°02.78'S</i>		<i>Long.: 070°50.39'E</i>			<i>Date: 11 September 2017</i>			
	5	25.20	35.72	20.43	4.57	0.10	0.11	nd.	nd.
	102	25.53	35.79	19.38	4.67	0.03	0.10	nd.	nd.
	151	26.00	35.61	16.95	4.73	0.06	0.23	nd.	nd.
	201	26.37	35.44	14.75	4.57	3.94	0.48	7.8 ± 0.0	3.6 ± 0.0
	250	26.49	35.32	13.77	4.72	4.22	0.48	7.8 ± 0.1	3.7 ± 0.1
	303	26.54	35.27	13.33	4.72	4.57	0.52	7.5 ± 0.0	3.3 ± 0.3
	402	26.65	35.11	12.22	4.75	10.01	0.83	7.2 ± 0.0	5.0 ± 0.3
	505	26.70	34.98	11.36	4.78	11.61	0.91	7.2 ± 0.1	4.6 ± 0.2
	602	26.75	34.86	10.61	4.76	13.78	1.05	7.3 ± 0.0	4.4 ± 0.3
	702	26.82	34.72	9.56	4.58	17.00	1.28	6.9 ± 0.1	3.8 ± 0.3
	802	26.93	34.58	8.21	4.32	21.90	1.69	6.5 ± 0.1	3.0 ± 0.3
	903	27.05	34.45	6.60	4.15	26.63	1.99	6.4 ± 0.1	3.6 ± 0.0
	1004	27.22	34.40	4.97	3.87	31.27	2.27	6.3 ± 0.2	2.4 ± 0.2
	1106	27.35	34.45	4.11	3.49	33.91	2.43	6.1 ± 0.1	2.7 ± 0.2
	1205	27.42	34.51	3.93	3.12	34.30	2.49	6.1 ± 0.0	2.4 ± 0.4
	1307	27.48	34.56	3.70	2.98	35.91	2.64	6.2 ± 0.1	2.6 ± 0.2
	1409	27.52	34.59	3.52	2.96	35.75	2.66	6.0 ± 0.2	1.8 ± 0.4
	1507	27.58	34.62	3.14	3.10	35.94	2.58	6.0 ± 0.2	2.4 ± 0.2

Table A1.4. (continued)

Cruise SO 259 in 2017									
ID	Depth [m]	Sigma-theta [kg m ⁻³]	Salinity [PSU]	Temp [°C]	O ₂ [mL L ⁻¹]	NO ₃ ⁻ [μmol L ⁻¹]	PO ₄ ³⁻ [μmol L ⁻¹]	NO ₃ ⁻ δ ¹⁵ N [‰ ± 1 S.D.] ^a	NO ₃ ⁻ δ ¹⁸ O [‰ ± 1 S.D.] ^b
CTD 49	Lat.: 26°02.78'S		Long.: 070°50.39'E			Date: 11 September 2017			
	1609	27.61	34.64	2.93	3.24	34.97	2.54	5.7 ± 0.2	2.1 ± 0.1
	1710	27.65	34.66	2.71	3.36	34.39	2.61	5.7 ± 0.1	2.0 ± 0.0
	1811	27.69	34.69	2.47	3.48	33.84	2.51	5.6 ± 0.0	1.9 ± 0.0
	2011	27.74	34.71	2.17	3.62	33.27	2.39	5.4 ± 0.0	2.2 ± 0.0
	3021	27.79	34.72	1.67	3.73	33.67	2.48	5.3 ± 0.2	1.9 ± 0.4
	4020	27.80	34.73		3.84	33.03	2.47	5.2 ± 0.1	1.8 ± 0.3
CTD 60	Lat.: 27°46.73'S		Long.: 073°54.98'E			Date: 15 September 2017			
	6	25.17	35.73	20.56	4.56	0.06	0.05	nd.	nd.
	51	25.20	35.74	20.46	4.57	0.01	0.05	nd.	nd.
	101	25.61	35.72	18.86	4.62	0.06	0.11	nd.	nd.
	150	26.15	35.59	16.23	4.50	2.05	0.30	6.8 ± 0.1	1.4 ± 0.1
	200	26.34	35.47	15.01	4.56	3.78	0.40	8.0 ± 0.1	3.3 ± 0.1
	301	26.55	35.22	13.10	4.69	7.94	0.64	7.9 ± 0.1	5.0 ± 0.3
	403	26.66	35.06	11.90	4.79	10.72	0.82	7.4 ± 0.1	5.1 ± 0.3
	502	26.71	34.95	11.21	4.82	12.24	0.90	7.3 ± 0.1	4.8 ± 0.1
	604	26.76	34.82	10.36	4.80	14.47	1.01	7.1 ± 0.0	4.5 ± 0.0
	705	26.83	34.68	9.36	4.65	17.95	1.23	6.8 ± 0.1	3.8 ± 0.1
	804	26.95	34.54	7.87	4.29	18.17	1.39	6.4 ± 0.1	3.0 ± 0.2
	905	27.07	34.43	6.33	4.13	27.70	1.88	6.4 ± 0.1	3.3 ± 0.1
	1005	27.19	34.39	5.08	3.98	31.13	2.11	6.2 ± 0.1	2.6 ± 0.0
	1105	27.29	34.41	4.35	3.71	33.34	2.29	6.4 ± 0.1	3.2 ± 0.1
	1207	27.37	34.45	3.89	3.52	34.58	2.38	6.1 ± 0.1	3.2 ± 0.1
	1307	27.44	34.49	3.56	3.33	35.48	2.47	6.0 ± 0.1	3.1 ± 0.1
	1408	27.50	34.54	3.31	3.22	35.71	2.50	6.0 ± 0.0	2.8 ± 0.1
	1508	27.55	34.58	3.05	3.29	35.35	2.47	5.9 ± 0.1	2.8 ± 0.1
	1606	27.61	34.63	2.86	3.31	34.89	2.45	5.4 ± 0.1	1.9 ± 0.1
	1808	27.68	34.68	2.58	3.42	35.08	2.47	5.8 ± 0.1	2.4 ± 0.3
2111	27.75	34.72	2.14	3.78	32.55	2.29	5.4 ± 0.1	2.3 ± 0.3	
3021	27.79	34.72	1.66	3.78	33.84	2.39	5.4 ± 0.0	2.4 ± 0.2	
3216	27.79	34.72	1.64	3.79	33.86	2.40	5.3 ± 0.1	2.5 ± 0.1	
CTD 99	Lat.: 27°00.38'S		Long.: 72°24.22'E			Date: 29 September 2017			
	5	25.23	35.76	20.41	4.56	0.05	0.08	nd.	nd.
	50	25.42	35.77	19.73	4.59	0.36	0.07	nd.	nd.
	99	25.79	35.68	18.03	4.65	0.69	0.16	nd.	nd.
	199	26.45	35.36	14.10	4.54	6.14	0.53	7.6 ± 0.1	4.2 ± 0.2
	300	26.57	35.23	13.03	4.68	8.59	0.67	7.2 ± 0.1	5.0 ± 0.1
	400	26.65	35.09	12.14	4.71	10.48	0.79	7.2 ± 0.1	4.7 ± 0.3
	503	26.71	34.95	11.21	4.74	8.07	0.69	7.1 ± 0.1	3.4 ± 0.1
	602	26.77	34.80	10.20	4.66	15.62	1.10	7.0 ± 0.0	4.4 ± 0.1
	703	26.85	34.66	9.10	4.54	18.63	1.29	6.7 ± 0.1	3.8 ± 0.1
	804	26.96	34.53	7.72	4.22	23.92	1.68	6.7 ± 0.1	3.2 ± 0.2
	904	27.09	34.42	6.10	4.02	28.54	1.95	6.3 ± 0.1	2.8 ± 0.1
	1004	27.22	34.39	4.84	3.89	32.48	2.18	6.4 ± 0.2	3.8 ± 0.1
	1104	27.32	34.43	4.19	3.55	34.12	2.66	6.1 ± 0.1	2.5 ± 0.4
	1205	27.39	34.48	3.85	3.30	33.99	2.33	6.0 ± 0.0	2.4 ± 0.2
	1308	27.46	34.53	3.54	3.16	35.51	2.51	6.0 ± 0.1	2.0 ± 0.2
	1407	27.52	34.57	3.30	3.13	35.73	2.51	6.0 ± 0.1	2.2 ± 0.2
	1507	27.57	34.60	3.04	3.19	35.35	2.47	5.9 ± 0.1	1.9 ± 0.2
	1608	27.62	34.63	2.87	3.24	34.82	2.46	5.7 ± 0.1	1.7 ± 0.0
	1809	27.69	34.68	2.49	3.43	33.57	2.35	5.6 ± 0.0	1.7 ± 0.1
	2111	27.75	34.71	2.02	3.64	33.31	2.33	5.5 ± 0.1	1.8 ± 0.1
3021	27.79	34.72	1.69	3.72	N.D	N.D	nd.	nd.	
4267	27.80	34.72	1.74	3.82	33.19	2.32	5.2 ± 0.0	2.1 ± 0.3	

Note: ^a δ¹⁵N in ‰ versus air and ^b δ¹⁸O in ‰ versus VSMOW; S.D. = standard deviation; nd. = no data.

Table A1.5. Results of CTD casts from cruise *PE 446* (2018).

Cruise <i>PE 446</i> in 2018									
ID	Depth [m]	Sigma-theta [kg m ⁻³]	Salinity [PSU]	Temp [°C]	O ₂ [mL L ⁻¹]	NO ₃ ⁻ [μmol L ⁻¹]	PO ₄ ³⁻ [μmol L ⁻¹]	NO ₃ ⁻ δ ¹⁵ N [‰ ± 1 S.D.] ^a	NO ₃ ⁻ δ ¹⁸ O [‰ ± 1 S.D.] ^b
<i>PS 001</i>		Lat.: 21°02.17'S		Long.: 067°07.28'E			Date: 15 October 2018		
	2	24.03	35.25	23.32	4.59	0.50	0.12	nd.	nd.
	103	24.38	35.39	22.48	4.68	0.93	0.10	nd.	nd.
	200	25.34	35.66	19.75	4.07	3.48	0.29	7.23±0.0	nd.
	300	26.18	35.59	16.14	4.50	3.41	0.35	8.12±0.1	nd.
	401	26.57	35.23	13.09	4.90	8.77	0.56	8.26±0.0	nd.
	502	26.69	35.00	11.54	5.07	12.01	0.79	7.92±0.1	nd.
	703	26.86	34.64	8.95	4.89	20.28	1.32	7.06±0.0	5.66±0.2
	902	27.16	34.46	5.82	3.84	33.68	2.13	6.50±0.1	4.24±0.3
	1201	27.44	34.63	4.56	2.69	40.56	2.63	6.49±0.1	3.62±0.2
	2011	27.74	34.72	2.24	3.72	22.56	1.88	5.74±0.1	3.84±0.4
	2652	27.78	34.73	1.77	3.86	35.74	2.38	5.60±0.0	3.80±0.0
<i>PS 007</i>		Lat.: 21°09.94'S		Long.: 068°10.57'E			Date: 16 October 2018		
	3	23.72	35.04	23.83	4.56	0.44	0.10	nd.	nd.
	48	24.03	35.25	23.32	4.59	0.54	0.08	nd.	nd.
	100	24.24	35.36	22.90	4.52	0.57	0.08	nd.	nd.
	249	25.74	35.68	18.27	4.18	6.35	0.53	7.74±0.0	nd.
	401	26.51	35.29	13.59	4.82	8.67	0.64	8.51±0.0	nd.
	500	26.67	35.05	11.88	4.99	7.68	0.64	8.07±0.0	nd.
	602	26.76	34.84	10.46	5.06	8.09	0.65	7.54±0.1	nd.
	902	27.13	34.47	6.09	3.85	12.37	1.11	6.16±0.1	4.46±0.1
	1202	27.44	34.64	4.60	2.64	23.96	1.80	6.41±0.1	3.14±0.1
	2008	27.74	34.72	2.19	3.75	36.74	2.43	5.72±0.0	3.00±0.3
	2903	27.78	34.72	1.83	3.91	23.67	1.67	5.56±0.1	3.36±0.3
<i>PS 029</i>		Lat.: 25°25.27'S		Long.: 070°05.36'E			Date: 25 October 2018		
	3	24.29	35.42	22.88	4.67	1.14	0.09	nd.	nd.
	123	24.75	35.53	21.56	4.56	1.00	0.11	nd.	nd.
	251	25.80	35.65	17.90	4.37	4.31	0.37	8.75±0.1	nd.
	302	26.19	35.56	15.97	4.51	5.09	0.41	8.34±0.1	nd.
	405	26.52	35.27	13.46	4.85	8.73	0.62	8.73±0.0	nd.
	497	26.63	35.11	12.27	5.01	10.96	0.75	8.37±0.2	nd.
	702	26.77	34.79	10.19	5.07	20.35	1.29	7.88±0.1	nd.
	1105	27.27	34.42	4.60	3.87	N/D	N/D	nd.	nd.
	1408	27.51	34.59	3.61	3.06	38.21	2.51	6.43±0.1	4.81±0.1
	2525	27.78	34.72	1.83	3.84	39.69	2.51	6.07±0.1	3.48±0.0
	3715	27.80	34.72	1.67	3.97	37.45	2.35	5.42±0.3	3.76±0.0
<i>PS 052</i>		Lat.: 27°48.23'S		Long.: 073°53.44'E			Date: 02 November 2018		
	2	24.38	35.59	23.01	4.70	0.84	0.08	nd.	nd.
	100	25.91	35.83	18.02	5.10	1.08	0.10	nd.	nd.
	251	26.45	35.35	14.06	4.83	6.84	0.49	8.78±0.0	nd.
	401	26.66	35.05	11.90	5.10	11.47	0.71	7.84±0.1	nd.
	602	26.78	34.78	10.08	5.10	15.94	0.99	7.59±0.1	nd.
	804	26.92	34.57	8.21	4.63	23.75	1.38	7.04±0.0	nd.
	1003	27.18	34.40	5.30	4.17	33.28	2.09	6.46±0.0	4.32±0.1
	1406	27.51	34.56	3.34	3.40	39.26	2.52	6.02±0.0	3.56±0.1
	2010	27.74	34.71	2.18	3.90	38.27	2.25	5.79±0.0	3.56±0.2
	2515	27.78	34.72	1.78	3.95	37.32	2.38	5.56±0.1	3.50±0.1
	3019	27.79	34.72	1.68	4.00	37.30	2.21	5.52±0.0	3.61±0.1
	3969	27.80	34.72	1.66	4.03	37.72	2.29	5.64±0.0	3.99±0.0

Note: ^a δ¹⁵N in ‰ versus air and ^b δ¹⁸O in ‰ versus VSMOW; S.D. = standard deviation; nd. = no data.

Appendix A2

Data of sinking particulate matter collected during INDEX expeditions between 2015 and 2019

Table A2.1. Sediment trap data of annual mass fluxes ($\text{mg m}^{-2} \text{d}^{-1}$) and percentages (wt.-%) of the particulate matter components TC (total carbon), TN (total nitrogen), particulate organic carbon (POC), particulate organic matter (POM), calcium carbonate (CaCO_3), biogenic opal (bOpal), and lithogenic matter (LM) in the IOSG.

Cup No.	Sampling interval	Duration (days)	Mass fluxes in $\text{mg m}^{-2} \text{d}^{-1}$										Percent (wt.-%) of total						
			Total	TC	TN	POC	POM	CaCO_3	bOpal	LM	TC	TN	POC	POM	CaCO_3	bOpal	LM		
Trap 01-01			<i>Coordinates: 21°14.80'S 068°35.47'E</i>																
			<i>Bottom depth: 3145 m</i>										<i>Trap depth: 2614 m</i>						
1	20.12.16-03.01.17	14	5.70	0.77	0.04	0.35	0.64	3.44	0.80	0.83	13.45	0.69	6.22	11.20	7.23	60.27	14.06	14.47	
2	03.01.17-17.01.17	14	5.64	0.78	0.06	0.33	0.59	3.76	1.22	0.07	13.77	0.99	5.78	10.40	8.00	66.66	21.65	1.30	
3	17.01.17-31.01.17	14	12.75	1.81	0.09	0.78	1.41	8.52	1.97	0.85	14.17	0.71	6.15	11.06	8.02	66.83	15.42	6.69	
4	31.01.17-14.02.17	14	6.81	0.90	0.05	0.53	0.95	3.13	1.28	1.45	13.26	0.71	7.74	13.94	5.52	45.97	18.77	21.33	
5	14.02.17-28.02.17	14	6.19	0.85	0.04	0.38	0.69	3.90	1.44	0.16	13.74	0.72	6.18	11.13	7.56	62.96	23.29	2.62	
6	28.02.17-14.03.17	14	5.10	0.68	0.04	0.30	0.54	3.20	1.01	0.35	13.40	0.74	5.86	10.55	7.54	62.85	19.72	6.88	
7	14.03.17-28.03.17	14	7.56	1.01	0.04	0.36	0.65	5.42	1.05	0.45	13.38	0.59	4.78	8.61	8.60	71.63	13.84	5.92	
8	28.03.17-11.04.17	14	13.94	1.81	0.06	0.54	0.98	10.53	2.17	0.26	12.96	0.47	3.89	7.01	9.07	75.56	15.54	1.89	
9	11.04.17-25.04.17	14	4.58	0.61	0.03	0.24	0.43	3.06	0.76	0.33	13.22	0.64	5.20	9.35	8.02	66.87	16.65	7.13	
10	25.04.17-09.05.17	14	8.17	1.07	0.05	0.39	0.71	5.60	1.33	0.53	13.05	0.62	4.82	8.67	8.23	68.58	16.26	6.50	
11	09.05.17-23.05.17	14	9.09	1.14	0.04	0.33	0.60	6.68	1.30	0.50	12.49	0.43	3.66	6.59	8.83	73.56	14.34	5.51	
12	23.05.17-06.06.17	14	11.23	1.47	0.07	0.49	0.88	8.17	2.00	0.18	13.10	0.60	4.37	7.87	8.73	72.73	17.77	1.62	
13	06.06.17-20.06.17	14	11.67	1.49	0.07	0.54	0.97	7.96	1.91	0.84	12.78	0.60	4.60	8.28	8.18	68.18	16.37	7.17	
14	20.06.17-04.07.17	14	8.44	1.07	0.06	0.36	0.65	5.91	1.70	0.17	12.68	0.67	4.28	7.70	8.40	70.03	20.20	2.07	
15	04.07.17-18.07.17	14	8.89	1.07	0.04	0.34	0.62	6.01	1.55	0.71	11.98	0.43	3.88	6.98	8.11	67.56	17.47	7.99	
16	18.07.17-02.09.17	46	3.06	0.33	0.01	0.04	0.07	2.41	nd.	nd.	10.66	0.16	1.20	2.15	9.46	78.83	nd.	nd.	
Trap 01-02			<i>Coordinates: 21°14.88'S 068°35.33'E</i>																
			<i>Bottom depth: 3145 m</i>										<i>Trap depth: 2614 m</i>						
1	03.10.17-21.10.17	18	15.92	1.95	0.08	0.71	1.28	10.31	2.88	1.45	12.2	0.5	4.5	8.0	7.8	64.8	18.12	9.10	
2	21.10.17-08.11.17	18	13.09	1.64	0.07	0.61	1.09	8.62	2.34	1.03	12.5	0.6	4.6	8.4	7.9	65.9	17.88	7.89	
3	08.11.17-26.11.17	18	11.88	1.35	0.06	0.53	0.95	6.89	1.82	2.22	11.4	0.5	4.4	8.0	7.0	58.0	15.34	18.72	
4	26.11.17-14.12.17	18	9.92	1.07	0.05	0.44	0.79	5.20	1.53	2.40	10.7	0.5	4.4	8.0	6.3	52.4	15.39	24.16	
5	14.12.17-01.01.18	18	2.92	0.49	0.03	0.26	0.47	1.94	0.41	0.11	16.9	1.1	8.9	16.1	8.0	66.3	13.93	3.68	

Table A2.1. (continued)

Cup No.	Sampling interval	Duration (days)	Mass fluxes in mg m ⁻² d ⁻¹										Percent (wt.-%) of total									
			Total	TC	TN	POC	POM	CaCO ₃	bOpal	LM	TC	TN	POC	POM	C _{org}	CaCO ₃	bOpal	LM				
<i>Trap 01-02</i>																						
			<i>Coordinates: 21°14.88'S 068°35.33'E</i>										<i>Bottom depth: 3145 m</i>									
6	01.01.18-19.01.18	18	3.06	0.41	0.02	0.19	0.33	1.83	0.45	0.44	13.3	0.6	6.1	10.9	7.2	59.9	14.70	14.53				
7	19.01.18-06.02.18	18	4.97	0.66	0.04	0.28	0.51	3.16	0.63	0.68	13.3	0.9	5.7	10.2	7.6	63.4	12.62	13.76				
8	06.02.18-24.02.18	18	2.03	0.28	0.01	0.11	0.21	1.37	0.29	0.15	13.8	0.5	5.6	10.2	8.1	67.8	14.55	7.47				
9	24.02.18-14.03.18	18	0.61	nd	nd	nd	nd	nd	nd	nd	nd	nd	nd	nd	nd	nd	nd	nd				
10	14.03.18-01.04.18	18	0.45	nd	nd	nd	nd	nd	nd	nd	nd	nd	nd	nd	nd	nd	nd	nd				
11	01.04.18-19.04.18	18	0.31	nd	nd	nd	nd	nd	nd	nd	nd	nd	nd	nd	nd	nd	nd	nd				
12	19.04.18-07.05.18	18	1.91	0.44	0.03	0.32	0.57	1.08	0.13	0.12	23.3	1.4	16.5	29.8	6.8	56.7	7.04	6.52				
13	07.05.18-25.05.18	18	2.23	0.30	0.01	0.12	0.22	1.46	0.37	0.18	13.4	0.6	5.5	9.9	7.9	65.7	16.46	7.92				
14	25.05.18-12.06.18	18	1.63	0.23	0.01	0.09	0.17	1.09	0.25	0.11	13.9	0.7	5.8	10.5	8.0	66.9	15.57	7.00				
15	12.06.18-30.06.18	18	0.75	0.10	0.00	nd	nd	nd	nd	nd	13.4	0.5	nd	nd	nd	nd	nd	nd				
16	30.06.18-18.07.18	18	8.38	1.06	0.05	0.39	0.71	5.52	1.24	0.91	12.6	0.6	4.7	8.4	7.9	65.9	14.84	10.86				
17	18.07.18-05.08.18	18	0.85	0.12	0.00	nd	nd	nd	nd	nd	14.2	0.3	nd	nd	nd	nd	nd	nd				
18	05.08.18-23.08.18	18	1.96	0.27	0.01	0.12	0.21	1.24	0.24	0.28	13.6	0.6	6.0	10.8	7.6	63.0	12.02	14.14				
<i>Trap ID 01-03</i>																						
			<i>Coordinates: 21°14.88'S 068°35.15'E</i>										<i>Bottom depth: 3145 m</i>									
1	07.11.18-25.11.18	18	7.56	1.07	0.05	0.45	0.81	5.19	1.36	0.19	14.21	0.73	5.97	10.73	8.24	68.69	17.98	2.58				
2	25.11.18-13.12.18	18	7.00	1.00	0.04	0.38	0.69	5.18	1.10	0.02	14.37	0.66	5.48	9.86	8.88	74.03	15.69	0.39				
3	13.12.18-31.12.18	18	4.66	0.67	0.03	0.26	0.48	3.42	0.52	0.23	14.52	0.64	5.71	10.28	8.81	73.42	11.19	5.09				
4	31.12.18-18.01.19	18	3.93	0.62	0.03	0.29	0.52	2.79	0.48	0.12	15.95	0.90	7.42	13.35	8.53	71.09	12.37	3.18				
5	18.01.19-05.02.19	18	2.01	0.34	0.01	0.19	0.34	1.22	0.21	0.23	16.88	0.83	9.61	17.29	7.27	60.60	10.67	11.41				
6	05.02.19-23.02.19	18	2.36	0.41	0.02	0.21	0.39	1.64	0.28	0.04	17.55	1.07	9.23	16.61	8.31	69.31	12.14	1.92				
7	23.02.19-13.03.19	18	1.36	nd.	nd.	0.23	0.43	nd.	nd.	nd.	nd.	nd.	17.49	31.48	nd.	nd.	nd.	nd.				
8	13.03.19-31.03.19	18	1.71	0.28	0.01	0.13	0.23	1.24	0.17	0.06	16.42	0.73	7.74	13.93	8.67	72.32	9.98	3.75				
9	31.03.19-18.04.19	18	4.00	0.60	0.02	0.27	0.48	2.74	0.55	0.21	15.00	0.66	6.76	12.15	8.24	68.66	13.86	5.31				
10	18.04.19-06.05.19	18	1.37	nd.	nd.	0.11	0.19	nd.	nd.	nd.	nd.	nd.	7.99	14.38	nd.	nd.	nd.	nd.				
11	06.05.19-24.05.19	18	1.11	nd.	nd.	0.02	0.05	nd.	nd.	nd.	nd.	nd.	2.48	4.47	nd.	nd.	nd.	nd.				
12	24.05.19-11.06.19	18	1.01	nd.	nd.	0.08	0.15	nd.	nd.	nd.	nd.	nd.	8.44	15.18	nd.	nd.	nd.	nd.				
13	11.06.19-29.06.19	18	0.76	nd.	nd.	0.05	0.09	nd.	nd.	nd.	nd.	nd.	6.52	11.74	nd.	nd.	nd.	nd.				
14	29.06.19-17.07.19	18	0.25	nd.	nd.	nd.	nd.	nd.	nd.	nd.	nd.	nd.	nd.	nd.	nd.	nd.	nd.	nd.				
15	17.07.19-04.08.19	18	0.69	nd.	nd.	nd.	nd.	nd.	nd.	nd.	nd.	nd.	nd.	nd.	nd.	nd.	nd.	nd.				
16	04.08.19-22.08.19	18	0.23	nd.	nd.	nd.	nd.	nd.	nd.	nd.	nd.	nd.	nd.	nd.	nd.	nd.	nd.	nd.				
17	22.08.19-09.09.19	18	0.37	nd.	nd.	nd.	nd.	nd.	nd.	nd.	nd.	nd.	nd.	nd.	nd.	nd.	nd.	nd.				
18	09.09.19-27.09.19	18	0.22	nd.	nd.	nd.	nd.	nd.	nd.	nd.	nd.	nd.	nd.	nd.	nd.	nd.	nd.	nd.				
19	27.09.19-15.10.19	18	2.20	0.39	0.02	0.23	0.42	1.30	0.39	0.07	17.84	1.18	10.72	19.30	7.12	59.33	17.94	3.41				

Table A2.1. (continued)

Cup No.	Sampling interval	Duration (days)	Mass fluxes in mg m ⁻² d ⁻¹										Percent (wt.-%) of total						
			Total	TC	TN	POC	POM	CaCO ₃	bOpal	LM	TC	TN	POC	POM	C _{org}	CaCO ₃	bOpal	LM	
<i>Trap ID 01-03</i>																			
Coordinates: 21°14.88'S 068°35.15'E																			
20	15.10.19-02.11.19	18	2.24	0.36	0.02	0.20	0.37	1.32	0.49	0.05	16.29	0.96	9.20	16.56	7.08	59.02	21.99	2.41	
<i>Trap 03-01</i>																			
Coordinates: 22°53.11'S 069°09.70'E																			
1	20.12.16-03.01.17	14	17.65	2.23	0.08	0.71	1.28	12.68	2.68	1.02	12.65	0.43	4.03	7.25	8.62	71.83	15.16	5.76	
2	03.01.17-17.01.17	14	14.48	1.86	0.07	0.66	1.19	9.99	2.46	0.86	12.82	0.45	4.55	8.18	8.28	68.96	16.95	5.90	
3	17.01.17-31.01.17	14	14.30	1.83	0.08	0.66	1.19	9.73	2.14	1.24	12.79	0.59	4.63	8.33	8.16	68.02	14.99	8.66	
4	31.01.17-03.09.17	215	12.53	1.62	0.06	0.64	1.16	8.16	2.12	1.10	12.94	0.49	5.12	9.22	7.82	65.14	16.89	8.75	
<i>Trap 04-01</i>																			
Coordinates: 23°52.16'S 069°29.75'E																			
1	28.11.15-16.12.15	18	15.10	1.89	0.08	0.68	1.22	10.14	2.92	0.82	12.55	0.52	4.48	8.07	8.06	67.19	19.32	5.42	
2	16.12.15-03.01.16	18	20.17	2.54	0.10	0.78	1.41	14.59	3.15	1.01	12.57	0.49	3.89	7.00	8.68	72.36	15.63	5.02	
3	03.01.16-21.01.16	18	18.07	2.29	0.09	0.81	1.46	12.34	3.06	1.20	12.69	0.52	4.50	8.10	8.19	68.28	16.95	6.67	
4	21.01.16-08.02.16	18	17.99	2.30	0.09	0.72	1.29	13.18	2.69	0.84	12.76	0.50	3.97	7.15	8.79	73.23	14.96	4.66	
5	08.02.16-26.05.16	18	19.09	2.52	0.10	0.90	1.63	13.48	2.73	1.25	13.21	0.54	4.73	8.52	8.47	70.61	14.33	6.55	
6	26.02.16-15.03.16	18	21.07	2.96	0.14	1.03	1.85	16.12	3.00	1.10	14.05	0.67	4.87	8.77	9.18	76.52	14.26	0.46	
7	15.03.16-02.04.16	18	13.26	1.70	0.07	0.69	1.24	8.44	1.75	1.84	12.82	0.52	5.19	9.33	7.63	63.62	13.21	13.84	
8	02.04.16-20.04.16	18	14.40	1.86	0.07	0.60	1.08	10.50	2.17	0.65	12.91	0.47	4.16	7.49	8.75	72.93	15.09	4.49	
9	20.04.16-08.05.16	18	14.25	1.86	0.08	0.72	1.29	9.51	2.25	1.20	13.04	0.53	5.04	9.07	8.01	66.73	15.76	8.44	
10	08.05.16-26.05.16	18	20.39	2.64	0.10	0.81	1.45	15.30	2.86	0.77	12.97	0.50	3.96	7.13	9.01	75.06	14.05	3.76	
11	26.05.16-13.06.16	18	5.23	0.75	0.03	0.23	0.42	4.35	0.40	0.06	14.43	0.49	4.45	8.00	9.98	83.20	7.67	1.12	
12	13.06.16-01.07.16	18	5.96	0.83	0.04	0.33	0.59	4.21	0.59	0.58	13.98	0.64	5.51	9.91	8.47	70.59	9.86	9.64	
13	01.07.16-02.12.16	154	17.74	2.09	0.11	0.81	1.45	10.71	3.45	2.12	11.79	0.59	4.55	8.19	7.25	60.38	19.47	11.97	
<i>Trap 04-03 Shallow</i>																			
Coordinates: 23.51°86'S 069°29.71'E																			
1	03.10.17-21.10.17	18	8.10	1.44	0.12	0.92	1.66	4.26	0.68	1.50	17.72	1.45	11.41	20.54	6.30	52.53	8.43	18.50	
2	21.10.17-08.11.17	18	10.93	1.92	0.15	1.02	1.84	7.53	0.92	0.65	17.60	1.35	9.33	16.80	8.27	68.88	8.41	5.91	
3	08.11.17-26.11.17	18	6.81	1.23	0.09	0.65	1.17	4.87	0.38	0.39	18.10	1.36	9.51	17.12	8.59	71.61	5.58	5.70	
4	26.11.17-14.12.17	18	12.84	2.29	0.18	1.15	2.07	9.54	1.04	1.09	17.86	1.40	8.95	16.10	8.92	74.30	8.11	1.48	
5	14.12.17-01.01.18	18	18.13	3.05	0.23	1.61	2.90	12.01	2.13	1.09	16.84	1.25	8.89	16.00	7.95	66.25	11.75	6.00	
6	01.01.18-19.01.18	18	20.22	3.26	0.23	1.55	2.79	14.26	2.11	1.07	16.12	1.12	7.66	13.78	8.46	70.52	10.41	5.29	
7	19.01.18-06.02.18	18	24.27	3.85	0.24	1.88	3.39	16.44	2.12	2.32	15.88	1.00	7.76	13.96	8.13	67.74	8.75	9.55	
8	06.02.18-24.02.18	18	21.87	3.53	0.26	1.73	3.12	14.95	2.01	1.80	16.12	1.19	7.92	14.26	8.20	68.33	9.19	8.22	
9	24.02.18-14.03.18	18	18.44	3.00	0.22	1.54	2.77	12.15	1.60	1.92	16.26	1.19	8.36	15.04	7.90	65.87	8.70	10.39	

Table A2.1. (continued)

Cup No.	Sampling interval	Duration (days)	Mass fluxes in mg m ⁻² d ⁻¹										Percent (wt.-%) of total									
			Total	TC	TN	POC	POM	CaCO ₃	bOpal	LM	TC	TN	POC	POM	C _{org}	CaCO ₃	bOpal	LM				
<i>Trap 04-03 Shallow</i>			<i>Coordinates: 23.51°86'S 069°29.71'E</i>										<i>Trap depth: 695 m</i>									
10	14.03.18-01.04.18	18	17.72	2.93	0.19	1.40	2.52	12.79	1.28	1.13	16.56	1.07	7.90	14.21	8.66	72.18	7.22	6.40				
11	01.04.18-19.04.18	18	28.09	4.65	0.36	2.49	4.49	18.00	2.79	2.81	16.56	1.28	8.88	15.98	7.69	64.06	9.95	10.02				
12	19.04.18-07.05.18	18	18.95	3.05	0.22	1.29	2.33	14.63	1.51	0.47	16.10	1.14	6.84	12.30	9.27	77.21	7.98	2.51				
13	07.05.18-25.05.18	18	5.32	0.94	0.07	0.51	0.92	3.57	0.44	0.38	17.69	1.31	9.62	17.32	8.07	67.23	8.33	7.12				
14	25.05.18-12.06.18	18	15.71	3.08	0.38	2.11	3.80	8.09	1.30	2.52	19.62	2.44	13.44	24.19	6.18	51.53	8.26	16.02				
15	12.06.18-30.06.18	18	17.83	3.07	0.23	1.68	3.02	11.60	2.43	0.79	17.20	1.27	9.40	16.91	7.80	65.03	13.64	4.43				
16	30.06.18-18.07.18	18	37.59	6.60	0.52	3.76	6.77	23.69	4.61	2.53	17.56	1.39	10.00	18.00	7.56	63.02	12.26	6.73				
17	18.07.18-05.08.18	18	16.44	2.75	0.19	1.43	2.57	11.01	1.78	1.08	16.71	1.18	8.68	15.62	8.04	66.98	10.81	6.59				
18	05.08.18-20.10.18	76	12.40	2.41	0.20	1.45	2.62	7.99	1.35	0.44	19.45	1.63	11.72	21.10	7.73	64.43	10.92	3.55				
<i>Trap 04-03 Middle</i>			<i>Coordinates: 23.51°86'S 069°29.71'E</i>										<i>Trap depth: 2931 m</i>									
1	03.10.17-21.10.17	18	2.64	0.44	0.02	0.25	0.45	1.58	0.33	0.27	16.8	0.9	9.5	17.2	7.2	60.1	12.7 ^a	10.1				
2	21.10.17-08.11.17	18	5.11	0.79	0.05	0.39	0.71	3.32	0.86	0.23	15.5	0.9	7.7	13.9	7.8	64.9	16.7	4.5				
3	08.11.17-26.11.17	18	6.33	0.95	0.05	0.46	0.82	4.11	1.00	0.40	15.0	0.8	7.2	13.0	7.8	64.9	15.9	6.2				
4	26.11.17-14.12.17	18	5.82	0.80	0.04	0.33	0.59	3.97	0.87	0.39	13.8	0.7	5.6	10.2	8.2	68.2	14.9	6.7				
5	14.12.17-01.01.18	18	6.85	0.93	0.04	0.36	0.65	4.76	1.08	0.36	13.6	0.6	5.3	9.5	8.3	69.5	15.7	5.3				
6	01.01.18-19.01.18	18	6.84	0.94	0.05	0.39	0.70	4.58	1.22	0.34	13.7	0.7	5.7	10.3	8.0	66.9	17.9	5.0				
7	19.01.18-06.02.18	18	8.12	1.08	0.04	0.35	0.64	6.03	1.11	0.35	13.3	0.5	4.4	7.8	8.9	74.2	13.6	4.3				
8	06.02.18-24.02.18	18	5.36	0.71	0.04	0.27	0.48	3.67	0.75	0.46	13.2	0.8	5.0	9.0	8.2	68.4	14.0 ^a	8.6				
9	24.02.18-14.03.18	18	1.15	0.16	0.01	0.07	0.13	0.72	nd.	nd.	13.9	0.7	6.4	11.5	7.5	62.3	nd.	nd.				
10	14.03.18-01.04.18	18	0.65	0.11	0.00	0.05	0.09	0.46	nd.	nd.	16.1	0.7	7.8	14.0	8.4	69.7	nd.	nd.				
11	01.04.18-19.04.18	18	3.59	0.44	0.02	0.16	0.29	2.32	0.52	0.46	12.3	0.6	4.6	8.2	7.8	64.6	14.4	12.8				
12	19.04.18-07.05.18	18	2.32	0.32	0.02	0.15	0.26	1.44	0.33	0.29	13.8	1.0	6.3	11.4	7.5	62.2	14.1	12.4				
13	07.05.18-25.05.18	18	13.51	1.62	0.06	0.50	0.90	9.32	2.34	0.95	12.0	0.5	3.7	6.7	8.3	69.0	17.3	7.0				
14	25.05.18-12.06.18	18	5.00	0.72	0.03	0.37	0.66	2.96	0.66	0.71	14.5	0.6	7.4	13.2	7.1	59.3	13.3 ^a	14.2				
15	12.06.18-30.06.18	18	14.06	1.67	0.06	0.54	0.98	9.39	2.29	1.40	11.9	0.5	3.9	6.9	8.0	66.8	16.3	10.0				
16	30.06.18-18.07.18	18	2.99	0.39	0.02	0.14	0.25	2.07	0.46	0.21	12.9	0.6	4.6	8.3	8.3	69.2	15.4	7.1				
17	18.07.18-05.08.18	18	3.48	0.45	0.02	0.16	0.30	2.36	0.51	0.32	12.8	0.5	4.7	8.5	8.1	67.7	14.6	9.2				
18	05.08.18-23.08.18	18	7.98	1.10	0.05	0.49	0.88	5.10	1.22	0.78	13.8	0.7	6.1	11.0	7.7	63.9	15.3	9.8				
19	23.08.18-10.09.18	18	2.31	0.33	0.02	0.16	0.29	1.40	0.35	0.28	14.1	1.0	6.9	12.4	7.3	60.5	15.0	12.1				
20	10.09.18-28.09.18	18	4.12	0.51	0.02	0.21	0.37	2.53	0.62	0.61	12.3	0.5	5.0	9.0	7.4	61.3	15.0	14.8				
<i>Trap 04-03 Deep</i>			<i>Coordinates: 23.51°86'S 069°29.71'E</i>										<i>Trap depth: 3465 m</i>									
1	03.10.17-21.10.17	18	30.39	3.68	0.15	1.27	2.28	20.10	5.17	2.83	12.11	0.49	4.17	7.50	7.94	66.16	17.02	9.31				

Table A2.1. (continued)

Cup No.	Sampling interval	Duration (days)	Mass fluxes in mg m ⁻² d ⁻¹										Percent (wt.-%) of total						
			Total	TC	TN	POC	POM	CaCO ₃	bOpal	LM	TC	TN	POC	POM	C _{org}	CaCO ₃	bOpal	LM	
<i>Trap 04-04 Shallow</i>			<i>Coordinates: 23°51.98'S 069°29.48'E</i>										<i>Trap depth: 694 m</i>						
Mean:			19.14	3.23	0.28	1.82	3.27	11.75	1.39	2.72	16.96	1.48	9.51	17.12	7.45	62.06	6.58	14.24	
<i>Trap 04-04 Middle</i>			<i>Coordinates: 23°51.98'S 069°29.48'E</i>										<i>Trap depth: 2930 m</i>						
1	07.11.18-25.11.18	18	13.41	1.82	0.08	0.65	1.17	9.74	1.77	0.73	13.56	0.56	4.84	8.71	8.72	72.66	13.21	5.43	
2	25.11.18-13.12.18	18	23.07	3.10	0.12	1.13	2.04	16.40	3.05	1.58	13.45	0.54	4.92	8.85	8.53	71.09	13.20	6.85	
3	13.12.18-31.12.18	18	22.33	2.87	0.10	0.91	1.63	16.39	2.59	1.72	12.86	0.46	4.06	7.30	8.81	73.39	11.60	7.71	
4	31.12.18-18.01.19	18	18.47	2.50	0.12	0.88	1.58	13.55	2.26	1.08	13.56	0.64	4.76	8.56	8.80	73.36	12.24	5.85	
5	18.01.19-05.02.19	18	20.44	2.59	0.10	0.80	1.44	14.95	2.83	1.22	12.69	0.50	3.92	7.05	8.78	73.14	13.84	5.97	
6	05.02.19-23.02.19	18	15.41	1.94	0.08	0.61	1.10	11.04	2.02	1.24	12.58	0.50	3.98	7.16	8.60	71.68	13.13	8.04	
7	23.02.19-13.03.19	18	9.83	1.34	0.06	0.48	0.87	7.13	1.31	0.51	13.62	0.57	4.92	8.85	8.71	72.54	13.37	5.24	
8	13.03.19-31.03.19	18	15.51	1.93	0.06	0.80	1.45	9.40	1.94	2.72	12.46	0.42	5.19	9.33	7.27	60.61	12.51	17.55	
9	31.03.19-18.04.19	18	28.16	3.38	0.10	0.86	1.55	20.99	3.29	2.32	12.01	0.36	3.06	5.52	8.95	74.55	11.69	8.25	
10	18.04.19-06.05.19	18	18.92	2.36	0.07	0.67	1.21	14.06	1.76	1.90	12.47	0.36	3.56	6.41	8.91	74.28	9.29	10.02	
11	06.05.19-24.05.19	18	9.27	1.19	0.04	0.37	0.67	6.80	0.97	0.83	12.82	0.44	4.02	7.24	8.80	73.36	10.42	8.99	
12	24.05.19-11.06.19	18	3.01	0.40	0.02	0.13	0.24	2.25	0.35	0.17	13.34	0.50	4.36	7.86	8.97	74.76	11.70	5.69	
13	11.06.19-29.06.19	18	3.29	0.43	0.01	0.13	0.24	2.47	0.42	0.16	13.07	0.45	4.07	7.33	9.00	74.99	12.66	5.01	
14	29.06.19-17.07.19	18	6.71	0.84	0.03	0.27	0.49	4.74	1.02	0.47	12.48	0.44	4.02	7.23	8.47	70.56	15.22	7.00	
15	17.07.19-04.08.19	18	8.58	1.05	0.03	0.31	0.56	6.16	1.01	0.85	12.24	0.40	3.62	6.51	8.62	71.85	11.75	9.90	
16	04.08.19-22.08.19	18	6.68	0.84	0.05	0.31	0.56	4.40	0.88	0.84	12.57	0.71	4.66	8.40	7.90	65.86	13.11	12.63	
17	22.08.19-09.09.19	18	2.45	0.32	0.01	0.11	0.20	1.77	0.32	0.17	13.19	0.49	4.55	8.18	8.65	72.05	12.86	6.91	
18	09.09.19-27.09.19	18	5.06	0.71	0.04	0.32	0.58	3.24	0.68	0.57	14.07	0.82	6.40	11.52	7.67	63.92	13.37	11.19	
19	27.09.19-15.10.19	18	17.91	2.31	0.10	0.83	1.49	12.30	2.74	1.38	12.87	0.55	4.63	8.33	8.24	68.68	15.29	7.69	
20	15.10.19-02.11.19	18	18.96	2.47	0.10	0.85	1.53	13.49	2.75	1.19	13.02	0.55	4.48	8.06	8.54	71.15	14.52	6.27	
<i>Trap 04-04 Deep</i>			<i>Coordinates: 23°51.98'S 069°29.48'E</i>										<i>Trap depth: 3493 m</i>						
1	07.11.18-25.11.18	18	21.78	2.82	0.14	1.38	2.49	11.95	2.96	4.38	12.94	0.62	6.36	11.44	6.59	54.88	13.59	20.09	
2	25.11.18-13.12.18	18	34.26	4.40	0.16	1.39	2.49	25.12	4.15	2.49	12.84	0.44	4.04	7.28	8.80	73.33	12.11	7.27	
3	13.12.18-31.12.18	18	41.26	5.02	0.18	1.50	2.70	29.37	5.10	4.09	12.17	0.44	3.63	6.54	8.54	71.19	12.37	9.90	
4	31.12.18-18.01.19	18	19.32	2.30	0.08	0.67	1.21	13.52	2.58	2.00	11.89	0.42	3.49	6.28	8.40	70.00	13.35	10.38	
5	18.01.19-05.02.19	18	13.44	1.73	0.08	0.71	1.28	8.48	1.99	1.69	12.87	0.58	5.30	9.54	7.57	63.09	14.81	12.56	
6	05.02.19-23.02.19	18	20.35	2.37	0.08	0.72	1.30	13.73	2.52	2.81	11.64	0.41	3.55	6.39	8.10	67.46	12.36	13.79	
7	23.02.19-13.03.19	18	25.53	2.81	0.08	0.68	1.22	17.78	3.03	3.50	11.01	0.32	2.65	4.77	8.36	69.66	11.87	13.70	
8	13.03.19-31.03.19	18	24.24	2.82	0.09	0.72	1.30	17.47	2.70	2.77	11.63	0.36	2.99	5.37	8.65	72.07	11.14	11.42	

Table A2.1. (continued)

Cup No.	Sampling interval	Duration (days)	Mass fluxes in mg m ⁻² d ⁻¹							Percent (wt.-%) of total								
			Total	TC	TN	POC	POM	CaCO ₃	bOpal	LM	TC	TN	POC	POM	C _{carb}	CaCO ₃	bOpal	LM
<i>Trap 04-04 Deep</i>																		
<i>Coordinates: 23°51.98'S 069°29.48'E</i>																		
<i>Bottom depth: 3493 m</i>																		
<i>Trap depth: 3465 m</i>																		
9	31.03.19-18.04.19	18	21.72	2.58	0.10	0.75	1.35	15.25	2.96	2.16	11.89	0.44	3.46	6.23	8.42	70.20	13.61	9.96
10	18.04.19-06.05.19	18	18.51	2.18	0.09	0.60	1.09	13.09	2.39	1.93	11.76	0.46	3.27	5.88	8.49	70.76	12.92	10.45
11	06.05.19-24.05.19	18	23.34	2.66	0.08	0.70	1.26	16.36	2.98	2.73	11.42	0.36	3.00	5.41	8.42	70.13	12.76	11.71
12	24.05.19-11.06.19	18	29.14	3.39	0.11	0.91	1.63	20.68	3.86	2.97	11.63	0.38	3.11	5.61	8.52	70.97	13.25	10.18
13	11.06.19-29.06.19	18	7.08	0.85	0.03	0.23	0.42	5.14	0.88	0.64	12.02	0.42	3.31	5.95	8.71	72.62	12.37	9.06
14	29.06.19-17.07.19	18	4.43	0.59	0.03	0.24	0.43	2.95	0.56	0.50	13.36	0.75	5.37	9.66	7.99	66.59	12.57	11.18
15	17.07.19-04.08.19	18	2.37	0.36	0.02	0.17	0.31	1.52	0.32	0.22	14.97	0.74	7.30	13.14	7.67	63.94	13.45	9.47
16	04.08.19-22.08.19	18	7.54	0.92	0.05	0.38	0.68	4.49	0.98	1.38	12.17	0.61	5.03	9.05	7.15	59.58	13.06	18.32
17	22.08.19-10.11.19	80	3.49	0.17	0.01	0.08	0.15	0.70	0.20	2.44	4.78	0.26	2.38	4.28	2.40	20.03	5.77	69.91
<i>Trap 05-01</i>																		
<i>Coordinates: 25°18.81'S 070°59.99'E</i>																		
<i>Bottom depth: 3110 m</i>																		
<i>Trap depth: 2579 m</i>																		
1	10.11.14-29.11.14	19	12.08	1.73	0.09	0.74	1.32	8.32	1.80	0.63	14.36	0.71	6.09	10.97	8.26	68.87	14.92	5.24
2	29.11.14-18.12.14	19	10.27	1.39	0.06	0.50	0.90	7.42	1.02	0.92	13.56	0.56	4.88	8.79	8.68	72.32	9.95	8.94
3	18.12.14-06.01.15	19	14.52	1.98	0.08	0.68	1.22	10.87	1.47	0.96	13.64	0.54	4.66	8.38	8.99	74.88	10.12	6.62
4	06.01.15-25.01.15	19	14.02	1.91	0.08	0.69	1.24	10.21	1.78	0.79	13.66	0.56	4.92	8.86	8.74	72.81	12.69	5.64
5	25.01.15-13.02.15	19	24.35	3.24	0.09	0.88	1.58	19.70	1.82	1.25	13.32	0.37	3.62	6.51	9.71	80.90	7.46	5.14
6	13.02.15-04.03.15	19	10.71	1.44	0.05	0.48	0.86	8.05	1.16	0.65	13.46	0.48	4.44	8.00	9.02	75.17	10.80	6.04
7	04.03.15-23.03.15	19	7.60	1.04	0.04	0.33	0.59	5.92	0.73	0.35	13.70	0.50	4.35	7.82	9.35	77.95	9.57	4.66
8	23.03.15-11.04.15	19	10.89	1.56	0.07	0.64	1.16	7.64	1.10	0.99	14.32	0.64	5.90	10.63	8.42	70.14	10.13	9.10
9	11.04.15-30.04.15	19	3.34	0.48	0.02	0.18	0.33	2.45	0.35	0.20	14.33	0.63	5.52	9.93	8.82	73.46	10.53	6.07
10	30.04.15-19.05.15	19	4.90	0.65	0.02	0.21	0.38	3.70	0.60	0.23	13.35	0.50	4.30	7.73	9.05	75.44	12.20	4.63
11	19.05.15-07.06.15	19	8.21	1.06	0.05	0.35	0.63	5.95	0.84	0.79	12.96	0.59	4.27	7.68	8.69	72.45	10.22	9.64
12	07.06.15-26.06.15	19	7.23	0.92	0.03	0.29	0.52	5.26	0.80	0.65	12.73	0.45	4.00	7.19	8.73	72.74	11.03	9.04
13	26.06.15-15.07.15	19	5.51	0.70	0.02	0.21	0.37	4.14	0.56	0.44	12.77	0.44	3.74	6.73	9.03	75.25	10.11	7.91
14	15.07.15-03.08.15	19	7.86	1.01	0.04	0.32	0.57	5.79	0.94	0.55	12.88	0.50	4.04	7.27	8.84	73.67	12.01	7.06
15	03.08.15-26.11.15	115	9.57	1.33	0.07	0.54	0.98	6.56	1.29	0.74	13.91	0.74	5.68	10.23	8.22	68.53	13.51	7.74
<i>Trap 07-01</i>																		
<i>Coordinates: 26°02.78'S 070°50.67'E</i>																		
<i>Bottom depth: 4010 m</i>																		
<i>Trap depth: 3479 m</i>																		
1	03.10.17-21.10.17	18	16.81	1.94	0.08	0.53	0.95	11.76	3.05	1.05	11.55	0.50	3.15	5.68	8.40	69.97	18.13	6.22
2	21.10.17-08.11.17	18	18.33	2.18	0.10	0.92	1.66	10.48	3.50	2.69	11.89	0.54	5.04	9.07	6.86	57.14	19.11	14.68
3	08.11.17-26.11.17	18	15.50	1.95	0.09	0.81	1.46	9.45	2.46	2.12	12.56	0.57	5.24	9.44	7.32	61.00	15.86	13.70
4	26.11.17-14.12.17	18	12.70	1.57	0.07	0.60	1.08	8.08	1.98	1.55	12.37	0.54	4.73	8.52	7.64	63.64	15.62	12.22
5	14.12.17-01.01.18	18	11.00	1.39	0.06	0.50	0.91	7.35	1.69	1.06	12.59	0.53	4.58	8.25	8.01	66.75	15.40	9.60

Table A2.1. (continued)

Cup No.	Sampling interval	Duration (days)	Mass fluxes in mg m ⁻² d ⁻¹						Percent (wt.-%) of total									
			Total	TC	TN	POC	POM	CaCO ₃	bOpal	LM	TC	TN	POC	POM	C _{org}	CaCO ₃	bOpal	LM
Trap 07-02			<i>Coordinates: 26°02.68'S 070°50.53'E</i>			<i>Bottom depth: 4010 m</i>			<i>Trap depth: 3479 m</i>									
17	22.08.19-09.09.19	18	1.69	0.22	0.01	0.11	0.19	0.96	0.20	0.34	13.13	0.46	6.32	11.37	6.82	56.83	11.95	19.86
18	09.09.19-27.09.19	18	2.36	0.33	0.02	0.20	0.35	1.11	0.31	0.58	13.98	0.82	8.35	15.02	5.64	46.98	13.26	24.74
19	27.09.19-15.10.19	18	5.82	0.75	0.03	0.39	0.70	3.01	0.59	1.51	12.93	0.56	6.71	12.08	6.22	51.79	10.19	25.94
20	15.10.19-02.11.19	18	4.29	0.56	0.02	0.23	0.42	2.73	0.48	0.66	13.10	0.53	5.45	9.81	7.65	63.78	11.11	15.30
Trap 10-01			<i>Coordinates: 26°53.95'S 072°20.48'E</i>			<i>Bottom depth: 3400 m</i>			<i>Trap depth: 2869 m</i>									
1	03.10.17-21.10.17	18	6.68	0.91	0.04	0.41	0.74	4.19	0.96	0.80	13.6	0.7	6.1	11.0	7.5	62.7	14.3	12.0
Trap 10-02			<i>Coordinates: 26°53.72'S 072°20.37'E</i>			<i>Bottom depth: 3400 m</i>			<i>Trap depth: 2869 m</i>									
1	07.11.18-25.11.18	18	15.06	2.13	0.10	0.86	1.55	10.62	1.83	1.06	14.17	0.69	5.71	10.27	8.47	70.56	12.14	7.03
2	25.11.18-13.12.18	18	21.71	3.07	0.17	1.33	2.39	14.48	1.99	2.83	14.13	0.77	6.13	11.03	8.01	66.72	9.19	13.06
3	13.12.18-31.12.18	18	13.87	1.91	0.08	0.61	1.10	10.83	1.40	0.54	13.77	0.58	4.40	7.92	9.37	78.08	10.08	3.91
4	31.12.18-18.01.19	18	10.82	1.48	0.07	0.47	0.85	8.39	1.46	0.12	13.68	0.63	4.38	7.89	9.30	77.52	13.47	1.13
5	18.01.19-05.02.19	18	17.72	2.44	0.10	0.87	1.57	13.09	2.32	0.74	13.80	0.56	4.93	8.88	8.86	73.86	13.09	4.17
6	05.02.19-23.02.19	18	15.99	2.21	0.08	0.73	1.31	12.38	1.77	0.53	13.85	0.53	4.56	8.21	9.29	77.41	11.09	3.30
7	23.02.19-13.03.19	18	17.58	2.53	0.11	0.96	1.73	13.11	2.73	0.02	14.41	0.65	5.46	9.82	8.95	74.58	15.51	0.10
8	13.03.19-31.03.19	18	23.40	3.28	0.13	1.15	2.07	17.76	3.44	0.13	14.02	0.57	4.91	8.84	9.11	75.89	14.70	0.57
9	31.03.19-18.04.19	18	18.80	2.39	0.08	0.68	1.23	14.27	2.56	0.75	12.73	0.42	3.62	6.52	9.11	75.90	13.60	3.99
10	18.04.19-06.05.19	18	14.81	1.95	0.07	0.55	0.98	11.72	1.59	0.51	13.18	0.48	3.69	6.64	9.50	79.15	10.74	3.48
11	06.05.19-24.05.19	18	6.61	0.90	0.03	0.28	0.51	5.15	0.59	0.37	13.60	0.51	4.26	7.67	9.34	77.84	8.91	5.58
12	24.05.19-11.06.19	18	5.83	0.81	0.03	0.27	0.48	4.50	0.47	0.36	13.89	0.56	4.61	8.30	9.28	77.30	8.14	6.26
13	11.06.19-29.06.19	18	10.63	1.39	0.05	0.37	0.67	8.46	1.06	0.44	13.05	0.49	3.51	6.31	9.55	79.56	9.96	4.17
14	29.06.19-17.07.19	18	5.56	0.76	0.03	0.26	0.47	4.18	0.60	0.31	13.69	0.58	4.65	8.38	9.03	75.27	10.85	5.51
15	17.07.19-04.08.19	18	4.21	0.57	0.02	0.19	0.34	3.18	0.46	0.22	13.61	0.53	4.54	8.17	9.07	75.56	10.99	5.28
16	04.08.19-22.08.19	18	4.10	0.59	0.03	0.22	0.39	3.08	0.47	0.15	14.30	0.73	5.27	9.49	9.02	75.19	11.55	3.77
17	22.08.19-04.12.19	104	3.68	0.59	0.03	0.26	0.46	2.76	0.44	0.01	15.97	0.88	6.96	12.52	9.02	75.13	12.06	0.28
Trap ID 12-01			<i>Coordinates: 27°48.24'S 073°53.35'E</i>			<i>Bottom depth: 3970 m</i>			<i>Trap depth: 3439 m</i>									
1	03.10.17-21.10.17	18	13.55	1.67	0.07	0.62	1.11	8.80	2.01	1.63	12.35	0.55	4.56	8.20	7.79	64.95	14.84	12.01
2	21.10.17-08.11.17	18	11.68	1.40	0.06	0.45	0.82	7.89	1.69	1.28	12.00	0.47	3.89	7.00	8.11	67.59	14.46	10.95
3	08.11.17-26.11.17	18	10.26	1.21	0.04	0.39	0.70	6.89	1.37	1.30	11.84	0.43	3.78	6.80	8.06	67.13	13.37	12.70
4	26.11.17-02.11.18	341	12.26	1.55	0.07	0.63	1.14	7.67	1.56	1.89	12.66	0.59	5.15	9.27	7.51	62.60	12.69	15.44

Table A2.1. (continued)

Cup No.	Sampling interval	Duration (days)	Mass fluxes in mg m ⁻² d ⁻¹										Percent (wt.-%) of total					
			Total	TC	TN	POC	POM	CaCO ₃	bOpal	LM	TC	TN	POC	POM	C _{carb}	CaCO ₃	bOpal	LM
			<i>Coordinates: 27°48.50'S 073°53.33'E</i>															
			<i>Bottom depth: 3820 m</i>					<i>Trap depth: 3289 m</i>										
1	07.11.18-25.11.18	18	6.09	0.87	0.03	0.28	0.51	4.86	0.57	0.15	14.23	0.54	4.64	8.36	9.59	79.88	9.34	2.43
2	25.11.18-13.12.18	18	4.26	0.60	0.03	0.22	0.40	3.15	0.44	0.26	14.09	0.59	5.22	9.39	8.88	73.99	10.44	6.19
3	13.12.18-31.12.18	18	7.14	0.99	0.05	0.37	0.67	5.15	0.70	0.62	13.86	0.64	5.21	9.37	8.66	72.14	9.80	8.69
4	31.12.18-18.01.19	18	10.33	1.30	0.05	0.41	0.74	7.43	1.06	1.10	12.61	0.46	3.98	7.17	8.63	71.92	10.27	10.64
5	18.01.19-05.02.19	18	8.64	1.10	0.04	0.36	0.64	6.17	1.13	0.70	12.68	0.50	4.12	7.41	8.57	71.40	13.09	8.10
6	05.02.19-23.02.19	18	7.38	0.93	0.03	0.28	0.50	5.45	0.84	0.60	12.59	0.46	3.73	6.71	8.86	73.87	11.33	8.09
7	23.02.19-05.12.19	267	8.87	1.14	0.05	0.50	0.90	5.56	1.19	1.42	12.87	0.59	5.62	10.11	7.25	60.40	13.45	16.04

Note: nd.: no data; ^aStandard deviation is <16 %; ^bStandard deviation is >10 %; <17 %; ^cStandard deviation is >10 %; <12 %; ^dStandard deviation is >10 %; <11 %; ^eStandard deviation is >10 %; <12 %.

Appendix A3

Global data of sinking particulate organic carbon (POC) collected by sediment traps

Table A3.1. Data on global sediment trap-based particulate organic carbon (POC) fluxes to depth and normalized to 2000 m water depth.

Region	Trap ID	Lat. [°N]	Long. [°E]	Water depth [m]	Trap depth [m]	POC flux [mg m ⁻² d ⁻¹]	POC ₂₀₀₀ flux [mg m ⁻² d ⁻¹]*	Reference
Pacific Ocean								
Central Bering Sea		58.00	179.00	3783	3137	5.53	8.14	Honjo (1996) ^a
Bering Sea, Aluetian Basin	AB	53.50	-177.00	3788	3198	6.96	10.41	Takahashi et al. (2000) ^b
Central Okhotsk Sea	OS	53.00	149.00	1170	258	8.58	1.48	Honjo (1996) ^a
Central Okhotsk Sea	OS	53.00	149.00	1170	1061	4.08	2.37	Honjo (1996) ^a
South of Kamchatka Peninsula	GD	51.10	165.00	4960	4500	4.38	8.78	Wong et al. (1999)
West Pacific Subarctic Gyre	50N	50.00	165.00	5500	1227	4.60	3.02	Honda (2001); Honda et al. (2002) ^{b,b}
West Pacific Subarctic Gyre	50N	50.00	165.00	5500	3260	3.10	4.71	Honda (2001); Honda et al. (2002) ^{b,b}
West Pacific Subarctic Gyre	50N	50.00	165.00	5500	5090	2.30	5.13	Honda (2001); Honda et al. (2002) ^{b,b}
Subarctic Pacific	OSP	50.00	-145.00	4240	200	18.20	2.52	Wong et al. (1999) ^b
Subarctic Pacific	OSP	50.00	-145.00	4240	1000	7.42	4.09	Wong et al. (1999) ^b
Subarctic Pacific	OSP	50.00	-145.00	4240	3800	3.10	5.38	Wong et al. (1999) ^b
Subarctic Pacific	SA	49.00	-173.90	5406	4806	3.93	8.34	Takahashi et al. (2000) ^b
Juan de Fuca Ridge	JDF	48.00	-128.10	nd.	2200	2.99	3.24	Dymond and Lyle (1994)
North Central Pacific	NP3	48.00	178.00	3870	1040	38.50	21.97	Tsunogai et al. (1982); Noriki and Tsunogai (1986)
North Central Pacific	NP3	48.00	178.00	3870	2160	31.60	33.76	Tsunogai et al. (1982); Noriki and Tsunogai (1986)
North Central Pacific	NP3	48.00	178.00	3870	4380	18.90	37.03	Tsunogai et al. (1982); Noriki and Tsunogai (1986)
North Central Pacific	NP-B	46.80	162.10	5670	700	33.70	13.69	Tsunogai and Noriki (1991)
North Central Pacific	NP-B	46.80	162.10	5670	5200	5.10	11.58	Tsunogai and Noriki (1991)
Subarctic Front	Site 8	46.10	175.00	5435	1412	8.11	6.02	Kawahata (2002) ^b
East of Kurile Is.	GA	45.00	165.00	5830	5300	3.01	6.95	Wong et al. (1999)
South of Aleutian Is.	GB	45.00	-177.00	6100	5600	1.37	3.31	Wong et al. (1999)
West Pacific Subarctic Gyre	KNOT	44.00	155.00	5500	924	9.10	4.69	Honda et al. (2002) ^b
West Pacific Subarctic Gyre	KNOT	44.00	155.00	5500	2960	6.10	8.54	Honda et al. (2002) ^b
West Pacific Subarctic Gyre	KNOT	44.00	155.00	5500	4989	4.20	9.20	Honda et al. (2002) ^b
California Current, Midway	MW	42.20	-127.60	nd.	2830	6.02	8.11	Dymond and Lyle (1994)
California Current, Nearshore	NS	42.10	-125.80	nd.	2829	13.40	18.04	Dymond and Lyle (1994)
California Current, Gyre	G	41.60	-132.00	nd.	3664	2.46	4.14	Dymond and Lyle (1994)
Northwest Pacific	WP	41.50	146.50	5160	1330	99.00	69.76	Noriki and Tsunogai (1986)
Northwest Pacific	WP	41.50	146.50	5160	1650	84.00	71.22	Noriki and Tsunogai (1986)
Northwest Pacific	WP	41.50	146.50	5160	3250	46.00	69.77	Noriki and Tsunogai (1986)
Northwest Pacific	EM	40.90	142.00	5370	5000	12.80	28.10	Tsunogai and Noriki (1991)
Subarctic boundary	40N	40.00	165.00	5500	953	4.90	2.59	Honda (2001); Honda et al. (2002) ^{b,b}

Table A3.1. (continued)

Region	Trap ID	Lat. [°N]	Long. [°E]	Water depth [m]	Trap depth [m]	POC flux [mg m ⁻² d ⁻¹]	POC ₂₀₀ flux [mg m ⁻² d ⁻¹]*	Reference
Subarctic boundary	40N	40.00	165.00	5500	2986	3.90	5.50	Honda (2001), Honda et al. (2002) ^{a, b}
Subarctic boundary	40N	40.00	165.00	5500	5016	3.40	7.48	Honda (2001), Honda et al. (2002) ^{a, b}
East Japan Sea	Sta. T	39.70	132.40	3300	2800	8.10	10.81	Hong et al. (1996)
California Current	MF2	39.50	-127.70	nd.	4230	3.48	6.62	Dymond and Lyle (1994)
Subarctic Front	Site 7	37.40	174.90	5105	1482	6.44	4.98	Karathada (2002) ^a
Subarctic Front	Site 7	37.40	174.90	5105	4588	3.06	6.24	Karathada (2002) ^a
Northeast Pacific	EP5	37.00	-127.60	4750	510	30.00	9.29	Noriki and Tsunogai (1986)
Northeast Pacific	EP5	37.00	-127.60	4750	720	31.20	12.99	Noriki and Tsunogai (1986)
Northeast Pacific	EP5	37.00	-127.60	4750	1250	26.00	17.37	Noriki and Tsunogai (1986)
Northeast Pacific	EP5	37.00	-127.60	4750	3370	18.40	28.79	Noriki and Tsunogai (1986)
Northeast Pacific	EP5	37.00	-127.60	4750	4220	13.40	25.43	Noriki and Tsunogai (1986)
Monteary Bay	51	36.80	-122.00	700	450	39.50	10.98	Piskahn et al. (1996) ^b
Northeast Pacific		36.70	-122.22	nd.	50	432.88	18.27	Krumer et al. (1979); Oruen (1974); Ryther (1969)
Northeast Pacific		36.70	-122.22	nd.	250	252.05	42.33	Krumer et al. (1979); Oruen (1974); Ryther (1969)
Northeast Pacific		36.70	-122.22	nd.	700	115.07	46.75	Krumer et al. (1979); Oruen (1974); Ryther (1969)
Northeast Pacific		36.70	-122.22	nd.	50	90.41	3.82	Krumer et al. (1979); Oruen (1974); Ryther (1969)
Northeast Pacific		36.70	-122.22	nd.	250	52.05	8.74	Krumer et al. (1979); Oruen (1974); Ryther (1969)
Northeast Pacific		36.70	-122.22	nd.	700	46.58	18.92	Krumer et al. (1979); Oruen (1974); Ryther (1969)
Kuroshio Extension	WCT-7-s	36.70	154.90	5578	1191	4.44	2.85	Mohiuddin et al. (2004)
Kuroshio Extension	WCT-7-d	36.70	154.90	5578	5034	3.83	8.46	Mohiuddin et al. (2004)
Kuroshio Extension	WCT-3-s	36.00	147.00	5615	1108	2.50	1.51	Mohiuddin et al. (2004)
Kuroshio Extension	WCT-3-d	36.00	147.00	5615	5081	4.06	9.04	Mohiuddin et al. (2004)
Subtropical Front	Site 5	34.40	177.70	3365	1342	2.89	2.05	Karathada (2002) ^a
Subtropical Front	Site 5	34.40	177.70	3365	2848	4.28	5.80	Karathada (2002) ^a
Santa Barbara Basin		34.20	-120.00	590	540	12.30	4.00	Thunell (1998) ^b
North Pacific		32.70	-144.43	nd.	575	14.52	4.98	Krumer et al. (1979); Oruen (1974); Ryther (1969)
North Pacific		32.70	-144.43	nd.	1050	12.05	6.94	Krumer et al. (1979); Oruen (1974); Ryther (1969)
North Pacific		32.70	-144.43	nd.	75	68.49	4.09	Krumer et al. (1979); Oruen (1974); Ryther (1969)
Northeast Pacific	EP7	31.70	-124.60	4200	500	8.28	2.52	Noriki and Tsunogai (1986)
Northeast Pacific	EP7	31.70	-124.60	4200	4200	4.89	2.04	Noriki and Tsunogai (1986)
Northeast Pacific	EP7	31.70	-124.60	4200	1250	3.20	2.14	Noriki and Tsunogai (1986)
Northeast Pacific	EP7	31.70	-124.60	4200	3380	4.00	6.27	Noriki and Tsunogai (1986)
Northeast Pacific	EP7	31.70	-124.60	4200	3800	2.74	4.75	Noriki and Tsunogai (1986)
Northeast Pacific	EP7	31.70	-124.60	4200	3873	2.67	4.71	Karathada (2002) ^a
Subtropical Front	Site 6	30.00	175.00	5390	3873	18.90	5.75	Thunell (1998) ^b
Gulf of California	Gayamas Basin	27.90	-111.70	700	500	6.23	3.47	Honda (2001) ^{a, b}
Okinawa Trough	JAST01	27.20	126.40	1650	1010	4.11	3.30	Honda (2001) ^{a, b}
Okinawa Trough	JAST01	27.20	126.40	1650	1547	4.11	3.30	Honda (2001) ^{a, b}
Ryukyu Trench	JAST03	25.10	127.40	3771	3175	1.23	1.83	Honda (2001) ^{a, b}
South China Sea	SCS-N	18.50	116.00	3750	3350	3.92	2.16	Wiesner et al. (1996); Jianfang et al. (1998)
South China Sea	SCS-N	18.50	116.00	3750	3350	2.02	3.14	Wiesner et al. (1996); Jianfang et al. (1998)
East Pacific	EP11	17.50	-117.00	3870	470	9.45	2.73	Noriki and Tsunogai (1986)
East Pacific	EP11	17.50	-117.00	3870	690	10.10	4.05	Noriki and Tsunogai (1986)
East Pacific	EP11	17.50	-117.00	3870	1220	7.38	4.83	Noriki and Tsunogai (1986)
East Pacific	EP11	17.50	-117.00	3870	3340	6.00	9.32	Noriki and Tsunogai (1986)

Table A3.1. (continued)

Region	Trap ID	Lat.	Long.	Water depth [m]	Trap depth [m]	POC flux [mg m ⁻² d ⁻¹]	POC ₂₀₀₀ flux [mg m ⁻² d ⁻¹] ^a	Reference
East Pacific	EP11	17.50	-117.00	3870	3660	4.11	6.90	Noriki and Tsunogai (1986)
Central Pacific		15.35	-151.48	nd.	378	3.56	0.85	Horjio (1980); Koblenz-Mishke et al. (1970)
Central Pacific		15.35	-151.48	nd.	978	0.55	0.30	Horjio (1980); Koblenz-Mishke et al. (1970)
Central Pacific		15.35	-151.48	nd.	2778	1.10	1.45	Horjio (1980); Koblenz-Mishke et al. (1970)
Central Pacific		15.35	-151.48	nd.	4280	0.88	1.68	Horjio (1980); Koblenz-Mishke et al. (1970)
Central Pacific		15.35	-151.48	nd.	5582	0.66	1.59	Horjio (1980); Koblenz-Mishke et al. (1970)
South China Sea	SCS-C	14.60	115.10	4310	1200	4.20	2.71	Wiesner et al. (1996); Jianfang et al. (1998) ^b
South China Sea	SCS-C	14.60	115.10	4310	2240	3.51	3.87	Wiesner et al. (1996); Jianfang et al. (1998) ^b
South China Sea	SCS-C	14.60	115.10	4310	3770	2.52	4.34	Wiesner et al. (1996); Jianfang et al. (1998) ^b
North Equatorial Current	NEC	12.00	134.20	5300	1200	0.38	0.25	Kempe and Knaack (1996)
North Equatorial Current	MANOP-S	12.00	134.30	5300	4300	0.43	0.83	Kempe and Knaack (1996)
North Equatorial Counter	MANOP-S	11.00	-140.00	nd.	700	3.12	1.27	Dymond and Collier (1988) ^b
North Equatorial Counter	MANOP-S	11.00	-140.00	nd.	1600	2.33	1.92	Dymond and Collier (1988) ^b
North Equatorial Counter	MANOP-S	11.00	-140.00	nd.	3400	1.61	2.54	Dymond and Collier (1988) ^b
North Equatorial Counter	MANOP-S	11.10	-140.10	nd.	4620	0.82	1.68	Dymond and Lyle (1994)
Equatorial Pacific	JGOFs-EqPac-9N	9.00	-140.00	5100	2150	1.51	1.61	Horjio et al. (1995)
Equatorial Pacific	JGOFs-EqPac-9N	9.00	-140.00	5100	2250	1.52	1.68	Horjio et al. (1995)
Equatorial Pacific	JGOFs-EqPac-9N	9.00	-140.00	5100	4400	1.09	2.14	Horjio et al. (1995)
East Tropical Pacific	MANOP-M	8.80	-104.00	nd.	3150	3.78	5.58	Dymond and Lyle (1985); Dymond and Lyle (1994)
Equatorial Counter Current	Site 4	7.90	175.00	5260	4743	0.78	1.64	Dymond and Lyle (2002) ^c
East Tropical Pacific	MANOP-H	6.60	-92.80	nd.	3565	2.44	4.01	Kawahata et al. (1998); Dymond and Lyle (1994)
Panama Basin	PB2	5.40	-85.60	3860	890	9.00	4.49	Horjio (1982)
Panama Basin	PB2	5.40	-85.60	3860	2590	11.00	13.73	Horjio (1982)
Panama Basin	PB2	5.40	-85.60	3860	3560	14.00	22.96	Horjio (1982)
Equatorial Pacific	JGOFs-EqPac-5N	5.00	-140.00	4493	1191	6.02	3.86	Horjio (1982)
Equatorial Pacific	JGOFs-EqPac-5N	5.00	-140.00	4493	2091	4.50	4.68	Horjio (1982)
Equatorial Pacific	JGOFs-EqPac-5N	5.00	-140.00	4493	3793	3.69	6.39	Horjio (1982)
Equatorial Counter Current	ECC	5.00	138.80	4130	1130	1.78	1.09	Kempe and Knaack (1996)
Equatorial Counter Current	ECC	5.00	138.30	4130	3130	0.67	0.98	Kempe and Knaack (1996)
Equatorial Counter Current	Site 2	4.10	136.30	4888	1769	6.72	6.05	Kawahata et al. (2000); Kawahata et al. (2002) ^c
Equatorial Counter Current	Site 2	4.10	136.30	4888	4574	6.06	12.32	Kawahata et al. (2000) ^c
Equatorial Counter Current	Site 1	3.00	135.00	4402	1592	9.33	7.67	Kawahata et al. (1998); Kawahata et al. (2002) ^c
Equatorial Counter Current	Site 1	3.00	135.00	4402	3902	7.83	13.89	Kawahata et al. (1998) ^c
Equatorial Pacific	JGOFs-EqPac-2N	2.00	-140.00	4397	2203	4.02	4.37	Kawahata et al. (1998)
Equatorial Pacific	Site 10	1.22	160.60	3180	1164	1.94	1.22	Horjio et al. (1995)
South Equatorial Current	C	1.04	-138.90	nd.	4445	3.56	7.06	Kawahata et al. (2000)
South Equatorial Current	MANOP-C	1.00	-139.00	nd.	1089	4.17	2.48	Dymond and Lyle (1994) ^b
South Equatorial Current	MANOP-C	1.00	-139.00	nd.	1889	5.52	5.26	Dymond and Collier (1988) ^b
South Equatorial Current	MANOP-C	1.00	-139.00	nd.	2908	5.18	7.14	Dymond and Collier (1988)
South Equatorial Current	MANOP-C	1.00	-139.00	nd.	3495	3.26	5.26	Dymond and Collier (1988)
East equatorial Pacific		0.60	-86.20	nd.	2570	5.48	6.79	Cobler and Dymond (1980); Love and Allen (1975)
Equatorial Pacific	JGOFs-EqPac-Eq	0.00	-140.00	4358	880	4.65	5.03	Horjio et al. (1995)
Equatorial Pacific	JGOFs-EqPac-Eq	0.00	-140.00	4358	2284	4.49	5.00	Horjio et al. (1995)
Equatorial Pacific	JGOFs-EqPac-Eq	0.00	-140.00	4358	3618	4.37	7.27	Horjio et al. (1995)

Table A3.1. (continued)

Region	Trap ID	Lat.	Long.	Water depth	Trap depth	POC flux	POC ₂₀₀₀ flux	Reference
		[°N]	[°E]	[m]	[m]	[mg m ⁻² d ⁻¹]	[mg m ⁻² d ⁻¹ *]	
South Equatorial Current	Site 3	0.00	175.20	4880	1357	2.44	1.75	<i>Gupta and Karavathra</i> (2000) ^c
South Equatorial Current	Site 3	0.00	175.20	4880	4363	1.50	2.93	<i>Gupta and Karavathra</i> (2000) ^c ; <i>Karavathra et al.</i> (2000) ^c
Equatorial Pacific	JGOFS-EqPac-25	-2.00	-140.00	4293	3593	3.61	5.97	<i>Honjo et al.</i> (1995)
Equatorial Pacific	JGOFS-EqPac-55	-5.00	-140.00	4198	2099	2.73	2.85	<i>Honjo et al.</i> (1995)
Equatorial Pacific	JGOFS-EqPac-55	-5.00	-140.00	4198	2209	2.72	2.96	<i>Honjo et al.</i> (1995)
Equatorial Pacific	JGOFS-EqPac-55	-5.00	-140.00	4198	2316	2.79	3.16	<i>Honjo et al.</i> (1995)
Southeast Pacific		-7.66	-79.53	nd.	22	1035.62	21.61	<i>Roze</i> (1979); <i>Guillem et al.</i> (1973)
Southeast Pacific		-10.07	-78.19	nd.	19	1013.70	18.66	<i>Roze</i> (1979); <i>Guillem et al.</i> (1973)
Equatorial Pacific	JGOFS-EqPac-12S	-11.98	-77.18	nd.	20	693.15	13.33	<i>Roze</i> (1979); <i>Guillem et al.</i> (1973)
Equatorial Pacific	JGOFS-EqPac-12S	-12.00	-135.00	4294	1292	1.52	1.04	<i>Honjo et al.</i> (1995)
Tropical Convergence: Coral	Site 11	-13.00	156.00	1832	1315	0.71	1.17	<i>Honjo et al.</i> (1995)
Southeast Pacific		-13.67	-76.29	nd.	13	457.53	1.05	<i>Karavathra and Ohia</i> (2000) ^c
Southeast Pacific		-15.09	-75.47	nd.	50	657.53	6.08	<i>Roze</i> (1979); <i>Guillem et al.</i> (1973)
Southeast Pacific		-15.09	-75.47	nd.	70	356.16	20.07	<i>von Bröckel</i> (1980); <i>Roze</i> (1979); <i>Guillem et al.</i> (1973)
Tropical Convergence: Coral	Site 12	-17.80	154.80	2821	2304	0.56	0.63	<i>Roze</i> (1979); <i>Guillem et al.</i> (1973)
Peru-Chile current	CH3, CH4	-29.50	-73.20	4360	2333	7.69	23.06	<i>Roze</i> (1979); <i>Guillem et al.</i> (1973)
Peru-Chile current	CH1, CH3	-29.50	-73.20	4360	3687	7.56	12.78	<i>Hebbeln et al.</i> (2000) ^b
Tasman Front	Site 13	-35.50	161.00	3174	1161	2.50	1.57	<i>Karavathra and Ohia</i> (2000) ^c
Subtrop. Front: North	NCR	-42.70	178.60	1500	300	10.10	1.98	<i>Nodder and Northcote</i> (2001)
Subtrop. Front: North	NCR	-42.70	178.60	1500	1000	20.60	11.37	<i>Nodder and Northcote</i> (2001)
Subtrop. Front: South	SCR	-44.60	178.60	1500	300	4.11	0.81	<i>Nodder and Northcote</i> (2001)
Subtrop. Front: South	SCR	-44.60	178.60	1500	1000	4.93	2.72	<i>Nodder and Northcote</i> (2001)
Subantarctic Zone	JGOFS-AESOPS-MS1	-53.00	-174.70	5441	986	1.25	0.68	<i>Honjo et al.</i> (1995) ^a
Polar Frontal Zone	JGOFS-AESOPS-MS2	-56.90	-170.20	4924	4224	4.92	2.67	<i>Honjo et al.</i> (1995) ^a
Polar Frontal Zone	JGOFS-AESOPS-MS2	-60.30	-170.20	4924	520	1.71	3.25	<i>Honjo et al.</i> (1995) ^a
South Pacific	AO	-61.50	150.50	3580	770	176.00	54.46	<i>Noriki and Tsunogai</i> (1986)
South Pacific	AO	-61.50	150.50	3580	1200	143.00	77.60	<i>Noriki and Tsunogai</i> (1986)
South Pacific	AO	-61.50	150.50	3580	2260	120.00	92.25	<i>Noriki and Tsunogai</i> (1986)
South Pacific	AO	-61.50	150.50	3580	3110	138.00	133.27	<i>Noriki and Tsunogai</i> (1986)
South Pacific	AO	-61.50	150.50	3580	3110	138.00	201.55	<i>Noriki and Tsunogai</i> (1986)
Antarctic Circumpolar	JGOFS-AESOPS-MS3	-63.10	-170.10	3958	1003	6.40	3.54	<i>Honjo et al.</i> (1995) ^a
Antarctic Circumpolar	JGOFS-AESOPS-MS4	-66.20	-169.90	2886	1031	6.03	3.42	<i>Honjo et al.</i> (1995) ^a
Antarctic Zone	JGOFS-AESOPS-MS5	-66.20	-168.70	3016	1842	2.82	2.63	<i>Honjo et al.</i> (1995) ^a
Antarctic Zone	JGOFS-AESOPS-MS5	-72.50	-168.70	3016	937	5.31	2.77	<i>Honjo et al.</i> (1995) ^a
Ross Sea polynya	C bot	-72.50	-172.50	493	230	10.80	1.69	<i>Dunbar et al.</i> (1998) ^b
Ross Sea polynya	C bot	-73.50	-172.50	493	443	2.78	0.76	<i>Dunbar et al.</i> (1998) ^b
Ross Sea polynya	JGOFS-AESOPS-MS6	-76.50	176.90	565	200	5.23	0.73	<i>Collier et al.</i> (2000)
Ross Sea polynya	JGOFS-AESOPS-MS7b	-76.50	-178.00	581	206	13.60	1.93	<i>Collier et al.</i> (2000) ^d
Ross Sea polynya	JGOFS-AESOPS-MS7a	-76.50	-178.00	581	465	28.90	8.27	<i>Collier et al.</i> (2000) ^d
Ross Sea polynya	JGOFS-AESOPS-MS7b	-76.50	-178.00	581	481	33.40	9.83	<i>Collier et al.</i> (2000) ^{d,e}
Ross Sea polynya	A top	-76.50	167.50	719	230	13.70	2.14	<i>Dunbar et al.</i> (1998)
Ross Sea polynya	A bot	-76.50	167.50	719	669	11.10	4.34	<i>Dunbar et al.</i> (1998) ^b

Table A3.1. (continued)

Region	Trap ID	Lat.	Long.	Water depth [m]	Trap depth [m]	POC flux [mg m ⁻² d ⁻¹]	POC ₃₀₀₀ flux [mg m ⁻² d ⁻¹]*	Reference
Ross Sea polynya	B top	-76.50	-175.00	519	230	19.20	3.00	Dunbar et al. (1998) ^{b,d,f}
Ross Sea polynya	B bot	-76.50	-175.00	519	469	11.20	3.23	Dunbar et al. (1998) ^{b,d,f}
Atlantic Ocean								
Central Fram Strait	FS-1	78.90	1.40	2823	2442	0.65	0.77	Honjo et al. (1987)
East Fram Strait	SP-2, Sp-3	78.90	6.70	1669	1118	19.70	11.96	Hebbeln (2000) ^b
North Water polynya, Baifin	S5A	76.00	-78.00	365	258	26.90	4.64	Hargrave et al. (2002) ^b
North Water polynya, Baifin	S2B	76.00	-73.00	561	511	30.00	9.30	Hargrave et al. (2002) ^b
North Norwegian Sea	BI-1	75.90	11.50	2123	1700	4.60	4.00	Honjo et al. (1987)
Greenland Basin	GB-23	75.60	-6.70	3445	2823	0.88	1.18	Honjo et al. (1987)
East Greenland Sea	OG7 75N	75.00	-10.60	3073	500	10.70	3.26	Ramsøer et al. (1999)
Greenland Sea	OG	72.50	-7.70	2700	500	7.83	2.38	von Bodungen et al. (1995) ^b
Greenland Sea	OG	72.50	-7.70	2700	1000	3.16	1.74	von Bodungen et al. (1995) ^b
Greenland Sea	OG	72.50	-7.70	2700	2200	0.95	1.03	von Bodungen et al. (1995) ^b
Norwegian Basin	NB	70.00	0.40	3350	500	9.81	2.99	von Bodungen et al. (1995) ^b
Norwegian Basin	NB	70.00	0.40	3350	1000	6.03	3.33	von Bodungen et al. (1995) ^b
East Lofoten Basin	LB-1	69.50	10.00	3161	2760	2.21	2.91	Honjo et al. (1987)
Vøring Plateau	VP	67.80	5.50	1300	525	6.66	2.11	Bathmann et al. (1990)
Aegir Ridge	NA-1	65.50	1.00	3058	2630	1.62	2.05	Honjo et al. (1987)
East Gotland Sea		57.30	20.00	nd.	140	16.80	1.72	Schneider et al. (2000)
Baltic Sea		55.64	15.38	nd.	55	178.08	8.16	Smetacek et al. (1978)
Northeast Atlantic	L3	54.60	-21.20	3027	2200	2.15	2.33	Kuss and Krenmling (1999) ^b
Northeast Atlantic	L3	54.50	-21.10	2979	2880	2.03	2.78	Kuss and Krenmling (1999)
Baltic Sea		53.50	10.03	nd.	20	82.19	1.58	Iurriaga (1979); von Bodungen (1975)
Mid-European cont. Mar.	OMEX-2	49.20	-12.80	1450	600	5.75	2.05	Antia et al. (1999)
Mid-European cont. Mar.	OMEX-2	49.20	-12.80	1450	1050	6.30	3.62	Antia et al. (1999)
Mid-European cont. Mar.	OMEX-3	49.10	-13.40	3660	580	6.03	2.08	Antia et al. (1999)
Mid-European cont. Mar.	OMEX-3	49.10	-13.40	3660	1450	10.10	7.66	Antia et al. (1999)
Mid-European cont. Mar.	OMEX-3	49.10	-13.40	3660	3260	5.75	8.74	Antia et al. (1999)
Madeira Abyssal Plain	PAP	48.80	-16.50	4850	1000	2.60	1.43	Lampitt et al. (2001) ^b
Madeira Abyssal Plain	PAP	48.80	-16.50	4850	3000	3.32	4.70	Lampitt et al. (2001) ^b
Madeira Abyssal Plain	PAP	48.80	-16.50	4850	4700	3.18	6.62	Lampitt et al. (2001) ^b
Northeast Atlantic	L2	47.80	-19.70	4553	500	2.96	0.90	Scholten et al. (2001)
Northeast Atlantic	L2	47.80	-19.80	4551	1033	3.56	2.02	Kuss and Krenmling (1999); Scholten et al. (2001) ^b
Northeast Atlantic	L2	47.80	-19.80	4551	2017	5.11	5.15	Kuss and Krenmling (1999); Scholten et al. (2001) ^b
Northeast Atlantic	L2	47.80	-19.80	4553	3515	2.35	3.81	Kuss and Krenmling (1999); Scholten et al. (2001) ^b
North Atlantic Drift	JGOFs-NABE-48N	47.70	-20.90	4435	1110	4.05	2.44	Honjo and Mangarini (1993) ^c
North Atlantic Drift	JGOFs-NABE-48N	47.70	-20.90	4435	2109	3.78	3.96	Honjo and Mangarini (1993) ^c
North Atlantic Drift	JGOFs-NABE-48N	47.70	-20.90	4435	3734	2.74	4.68	Honjo and Mangarini (1993)
North Atlantic Drift	BOFS-48N	47.30	-19.50	4435	3100	5.19	7.56	Newton et al. (1994); Jickells et al. (1996)
Northeast Atlantic	POMME-NE	43.50	-17.30	3760	400	3.29	0.83	Gutew et al. (2005)
Northeast Atlantic	POMME-NE	43.50	-17.30	3760	1000	4.93	2.72	Gutew et al. (2005)
Northeast Atlantic	POMME-NE	39.50	-17.30	4940	400	6.30	1.58	Gutew et al. (2005)

Table A3.1. (continued)

Region	Trap ID	Lat. [°N]	Long. [°E]	Water depth [m]	Trap depth [m]	POC flux [mg m ⁻² d ⁻¹]	POC ₂₀₀₀ flux [mg m ⁻² d ⁻¹] ^a	Reference
Mauritanian upwelling zone	EUMELI-M	18.50	-21.00	3100	3000	5.30	7.51	Borje <i>et al.</i> (2001)
Northwest Atlantic		13.50	-54.00	nd.	389	6.74	1.65	Honjo (1980); Koblenitz-Mishke <i>et al.</i> (1970)
Northwest Atlantic		13.50	-54.00	nd.	988	3.95	2.15	Honjo (1980); Koblenitz-Mishke <i>et al.</i> (1970)
Northwest Atlantic		13.50	-54.00	nd.	3755	1.73	2.96	Honjo (1980); Koblenitz-Mishke <i>et al.</i> (1970)
Northwest Atlantic		13.50	-54.00	nd.	5068	1.70	3.77	Honjo (1980); Koblenitz-Mishke <i>et al.</i> (1970)
Cabe Verde	CV1, CV2	11.50	-21.00	4971	989	4.52	2.47	Fischer <i>et al.</i> (2000) ^b
Cariaco Basin	A	10.50	-64.70	1400	275	72.10	13.14	Thunell <i>et al.</i> (2000); Müller-Karger <i>et al.</i> (2004) ^{b, h}
Cariaco Basin	B	10.50	-64.70	1400	440	53.60	14.62	Thunell <i>et al.</i> (2000); Müller-Karger <i>et al.</i> (2004) ^{b, h}
Cariaco Basin	C	10.50	-64.70	1400	840	37.30	17.72	Thunell <i>et al.</i> (2000); Müller-Karger <i>et al.</i> (2004) ^{b, h}
Cariaco Basin	D	10.50	-64.70	1400	1255	30.60	20.52	Thunell <i>et al.</i> (2000); Müller-Karger <i>et al.</i> (2004) ^{b, h}
East Equatorial Atlantic	GB2, GBN3, GBN6,	1.80	-11.20	4314	853	5.97	2.87	Fischer <i>et al.</i> (2000) ^b
Guinea Basin	GBN3-1, GBN6-1	1.80	-11.10	4502	3921	5.48	9.76	Fischer and Wefer (1996) ^b
West Equatorial Atlantic	WA8	0.00	-23.50	3744	718	6.82	2.83	Fischer <i>et al.</i> (2000)
East Equatorial Atlantic	EA3c, EA7, EA9, EA10	0.00	-10.80	4385	1138	4.35	2.68	Fischer <i>et al.</i> (2000) ^b
East Equatorial Atlantic	GB54, GB55	-2.20	-9.90	3916	696	5.62	2.27	Fischer <i>et al.</i> (2000) ^b
Guinea Basin	GBZ5-1	-2.20	-9.90	3920	3382	5.75	9.02	Fischer and Wefer (1996)
West Equatorial Atlantic	WA1, WA4, WA7	-4.00	-25.70	5552	771	4.61	2.03	Fischer <i>et al.</i> (2000)
East Equatorial Atlantic	EA5	-4.30	-10.30	3490	947	2.16	1.14	Fischer <i>et al.</i> (2000)
East Equatorial Atlantic	EA8	-5.80	-9.40	3450	598	6.05	2.15	Fischer <i>et al.</i> (2000)
West Equatorial Atlantic	WA2, WA3, WA6	-7.50	-28.00	5363	602	2.57	0.92	Fischer <i>et al.</i> (2000) ^b
South Subtropical Gyre	SOG	-18.70	-25.00	nd.	3000	0.49	0.69	Paborisara <i>et al.</i> (2017)
Walvis Ridge	WR1, WR2, WR3, WR4- WR2-u	-20.00	9.20	2221	1663	10.10	8.62	Fischer <i>et al.</i> (2000) ^b
Namibia Upwelling	NU2	-20.00	9.20	2196	599	14.00	4.98	Wefer and Fischer (1993)
Polar Front	PF3, PF5, PF7, PF8	-50.10	5.87	3795	3145	4.41	5.37	Fischer <i>et al.</i> (2000) ^b
Polar Front	PF1, PF3, PF5, PF7, PF8	-28.90	14.60	3055	2516	4.41	5.37	Fischer <i>et al.</i> (2000) ^b
Bovert Island	BO1-BO5	-54.30	-3.34	3787	658	3.84	1.48	Fischer <i>et al.</i> (2000) ^b
Bovert Island	BO1, BO2, BO5	-54.30	-3.34	2728	487	2.19	0.65	Fischer <i>et al.</i> (2000) ^b
North Weddell Sea Gyre	VIII-u	-62.10	-40.60	2729	2209	1.10	1.20	Fischer <i>et al.</i> (2000) ^b
Bransfield St., King George Is.	KG1	-62.30	-57.50	3280	2453	0.61	0.73	Pudsey and King (1997)
Bransfield St., King George Is.	KG1	-62.30	-57.50	1952	1588	8.20	6.73	Wefer <i>et al.</i> (1988); Wefer and Fischer (1991)
Bransfield St., King George Is.	KG2, KG3	-62.40	-57.70	1992	687	3.01	1.20	Wefer <i>et al.</i> (1988); Wefer and Fischer (1991)
North Weddell Sea Gyre	I-u	-63.20	-42.70	3798	2971	0.24	0.34	Pudsey and King (1997)
North Weddell Sea	WS1	-62.44	-34.76	380	863	0.06	0.03	Wefer and Fischer (1991)
Weddell Sea	WS2	-64.90	-2.50	5000	4456	0.47	0.93	Wefer <i>et al.</i> (1990); Wefer and Fischer (1991)
Weddell Sea	WS3	-64.90	-2.60	5053	360	6.25	1.44	Wefer and Fischer (1991)
Maud Rise	WS4	-64.93	-2.59	5044	352	0.44	0.10	Wefer and Fischer (1991)
Indian Ocean								
Arabian Sea	MS-1	17.70	57.90	1447	808	10.50	4.82	Honjo <i>et al.</i> (1999) ^{a, b}
Arabian Sea	MS-1	17.70	57.90	1447	999	10.50	5.79	Honjo <i>et al.</i> (1999) ^{a, b}
Bay of Bengal	North-s	17.40	89.60	2263	809	9.84	4.53	Ittekkot <i>et al.</i> (1991)
Bay of Bengal	North-d	17.40	89.60	2263	1727	7.26	6.40	Ittekkot <i>et al.</i> (1991)

Table A3.1. (continued)

Region	Trap ID	Lat	Long.	Water depth	Trap depth	POC flux	POC _{3000}} flux	Reference
		[°N]	[°E]	[m]	[m]	[mg m ⁻² d ⁻¹]	[mg m ⁻² d ⁻¹]*	
Arabian Sea	MS-2	17.40	58.80	1447	839	13.50	6.41	<i>Horjio et al. (1999)^{a,b}</i>
Arabian Sea	MS-2	17.40	58.80	1447	914	17.20	8.78	<i>Horjio et al. (1999)^{a,b}</i>
Arabian Sea	MS-2	17.40	58.80	3642	1985	17.40	17.29	<i>Horjio et al. (1999)^{a,b}</i>
Arabian Sea	MS-2	17.40	58.80	3642	3150	13.20	19.49	<i>Horjio et al. (1999)^{a,b}</i>
Arabian Sea	MS-3	17.20	59.60	3465	778	13.20	5.87	<i>Horjio et al. (1999)^{a,b}</i>
Arabian Sea	MS-3	17.20	59.60	3465	873	17.50	8.59	<i>Horjio et al. (1999)^{a,b}</i>
Arabian Sea	MS-3	17.20	59.60	3465	1870	16.30	15.39	<i>Horjio et al. (1999)^{a,b}</i>
Arabian Sea	MS-3	17.20	59.60	3465	2979	12.80	18.02	<i>Horjio et al. (1999)^{a,b}</i>
Arabian Sea	WAST	16.50	60.50	4016	3027	8.77	12.51	<i>Haake et al. (1993)</i>
Arabian Sea	WAST	16.00	60.00	nd.	3020	4.93	7.02	<i>Nair (1989)</i>
Arabian Sea	EAST	15.50	68.70	3785	2830	5.75	7.74	<i>Haake et al. (1993)</i>
Arabian Sea	MS-4	15.30	61.50	3974	814	8.90	4.12	<i>Horjio et al. (1999)^{a,b}</i>
Arabian Sea	MS-4	15.30	61.50	3974	2222	11.10	12.15	<i>Horjio et al. (1999)^{a,b}</i>
Arabian Sea	MS-4	15.30	61.50	3974	3484	8.90	14.33	<i>Horjio et al. (1999)^{a,b}</i>
Arabian Sea	MS-4	15.00	68.50	nd.	2770	4.27	5.65	<i>Nair (1989)</i>
Arabian Sea	MS-4	14.00	64.00	nd.	2900	4.19	5.77	<i>Nair (1989)</i>
Arabian Sea	CAST	14.90	64.10	3904	2954	5.21	7.28	<i>Haake et al. (1993)</i>
Bay of Bengal	Central-s	13.20	84.40	3259	906	7.23	3.66	<i>Hekkot et al. (1991)</i>
Bay of Bengal	Central-d	13.20	84.40	3259	2282	7.15	8.01	<i>Hekkot et al. (1991)</i>
Arabian Sea	MS-5	10.00	65.00	4411	2363	3.80	4.38	<i>Horjio et al. (1999)^a</i>
Arabian Sea	MS-5	10.00	65.00	4411	3915	3.30	5.87	<i>Horjio et al. (1999)^a</i>
Bay of Bengal	South-s	4.43	87.30	4017	1040	6.49	3.70	<i>Hekkot et al. (1991)</i>
Bay of Bengal	South-d	4.43	87.30	4017	3006	5.59	7.93	<i>Hekkot et al. (1991)</i>
Southern subtrop. gyre	01-01	-21.25	68.59	3145	2614	0.42	0.53	<i>Harns et al., 2021</i>
Southern subtrop. gyre	01-02	-21.25	68.59	3145	2614	0.29	0.36	<i>Harns et al., 2021</i>
Southern subtrop. gyre	01-03	-21.25	68.59	3145	2614	0.21	0.27	<i>Harns et al., submitted</i>
Southern subtrop. gyre	03-01	-22.89	69.16	3700	3169	0.65	0.96	<i>Harns et al., (2021)</i>
Southern subtrop. gyre	04-03 <i>Shallow</i>	-23.86	69.50	3493	695	1.55	0.63	<i>Harns et al., (2021)</i>
Southern subtrop. gyre	04-03 <i>Deep</i>	-23.86	69.50	3493	2931	0.29	0.40	<i>Harns et al., (2021)</i>
Southern subtrop. gyre	04-03 <i>Middle</i>	-23.87	69.49	3493	3465	0.59	0.94	<i>Harns et al., (2021)</i>
Southern subtrop. gyre	04-04 <i>Shallow</i>	-23.87	69.49	3493	694	1.82	0.73	<i>Harns et al., submitted</i>
Southern subtrop. gyre	04-04 <i>Middle</i>	-23.87	69.49	3493	2930	0.57	0.79	<i>Harns et al., submitted</i>
Southern subtrop. gyre	04-04 <i>Deep</i>	-23.87	69.49	3493	3465	0.70	1.12	<i>Harns et al., submitted</i>
Southern subtrop. gyre	04-01	-23.87	69.50	3493	2962	0.74	1.04	<i>Harns et al., (2021)</i>
Southern subtrop. gyre	05-01	-25.33	70.00	3110	2579	0.49	0.61	<i>Harns et al., (2021)</i>
Southern subtrop. gyre	07-01	-26.05	70.84	4010	3479	0.53	0.85	<i>Harns et al., (2021)</i>
Southern subtrop. gyre	07-02	-26.04	70.84	4010	3479	0.90	1.44	<i>Harns et al., submitted</i>
Southern subtrop. gyre	10-01	-26.90	72.34	3400	2869	0.41	0.56	<i>Harns et al., (2021)</i>
Southern subtrop. gyre	10-02	-26.90	72.34	3400	2869	0.59	0.81	<i>Harns et al., submitted</i>
Southern subtrop. gyre	12-01	-27.80	73.89	3970	3439	0.61	0.97	<i>Harns et al., (2021)</i>
Southern subtrop. gyre	12-02	-27.81	73.89	3820	3289	0.51	0.78	<i>Harns et al., submitted</i>

Table 3.1. (continued)

Region	Trap ID	Lat.	Long.	Water depth [m]	Trap depth [m]	POC flux [mg m ⁻² d ⁻¹]	POC ₀₀₀ flux [mg m ⁻² d ⁻¹]*	Reference
Southern Ocean	ANTARES-M2	-52.00	61.50	4600	1300	2.88	1.99	Tréguer, unpub. ¹
Southern Ocean	ANTARES-M2	-52.00	61.50	4600	4025	1.56	2.84	Tréguer, unpub. ¹
Polar Frontal Zone	PFZ54	-53.80	141.80	2280	830	2.19	1.03	Trull <i>et al.</i> (2001)
Polar Frontal Zone	PFZ54	-53.80	141.80	2280	1580	1.37	1.12	Trull <i>et al.</i> (2001)
Prydz Bay	PZB-1	-62.40	73.00	4000	1400	2.47	1.82	Piiskahn <i>et al.</i> (2004)
Southern Ocean	ANTARES-M3	-63.00	71.00	4020	1300	0.30	0.21	Tréguer, unpub. ¹
Southern Ocean	ANTARES-M3	-63.00	71.00	4020	3445	0.44	0.70	Tréguer, unpub. ¹

Notes:

* POC fluxes are normalized using Eq. 3.1 in the main text.

nd.: no data.

^aData available online (https://usjgofs.whoi.edu/mzweb/data/Honjo/sed_traps.html); S. Honjo and R. Francois.

^bMultiple trap deployment flux estimates are combined.

^cOrganic carbon (POC) calculated as 1.8*POC = Organic matter following Kawahata *et al.* (1998).

^dDue to local cloud cover remote sensing data used are from ~2770 m north of location, for details see Lutz *et al.* (2007).

^eLutz *et al.* (2007) corrected POC flux for a component potentially associated with pteropod 'swimmers' following Collier *et al.* (2000).

^fOverlapping deployment intervals are excluded by Lutz *et al.* (2007) to avoid attenuating seasonality.

^gData available online (<https://www.whoi.edu/OFF>); M. Conte.

^hData available online (<https://www.imars.usf.edu/CAR>); F. Müller-Karger, R. Varela, R. Thunell, M. Scranton and others.

ⁱData available online (https://www.obs-vlfr.fr/cd_rom_dmtt/ANTARES/A3/a3_parameters.htm); P. Tréguer.

Appendix A4

The use of a Multiple Linear Regression Analysis (MLRA) to calculate the major ballast material enhancing the sinking speed of particles in the IOSG

We use a multiple linear regression analysis (MLRA) to identify relevant ballast materials in the IOSG. Therefore, we characterize the POC fractions associated with or transported by the particulate matter components CaCO_3 ($\text{POC}_{\text{CaCO}_3}$), biogenic Opal (POC_{Opal}), and lithogenic matter (POC_{LM}) using the formula:

$$\begin{aligned} \text{POC}_{\text{total}} &= \text{POC}_{\text{CaCO}_3} + \text{POC}_{\text{Opal}} + \text{POC}_{\text{LM}} \\ &= a \times \text{CaCO}_3 \text{ flux} + b \times \text{Opal flux} + c \times \text{Lithogenic matter flux}, \end{aligned} \quad (\text{A4.1})$$

where a , b and c are defined as the “carrying coefficients” (CCs) that represent the proportional contribution of each potential ballast material to the total POC flux and the sum of the CCs become 1 (unity) (Klaas and Archer, 2002; Honda and Watanabe, 2010). For this analysis, we used the relative fluxes of the individual components to the respective averages of particulate matter fluxes of sediment traps deployed at 2600–3500 m water depth (500–600 m above bottom). The following Table A4.1 summarizes the CCs for the individual components, indicating that 48 %, 39 %, and 12 % of POC in the deep-sea were transported by CaCO_3 , biogenic Opal and lithogenic matter, respectively. Thus, CaCO_3 and biogenic opal play the most important role as ballast material. Considering that CaCO_3 contributes with ~62–74 % to the total mass flux, CaCO_3 is the most relevant ballast material in the IOSG that triggers the effective transfer of POC to the deep-sea.

Table A4.1. Statistical data of a Multiple Linear Regression Analysis (MLRA) of sediment trap data in the IOSG.

Depth [m]	Sample number [n]	$\text{POC} = a \times \text{CaCO}_3 + b \times \text{Opal} + c \times \text{Lithogenic matter}$ Carrying Coefficients (CCs) and Significance (Sig)			Correlation Coefficient R^2
		a	b	c	
2600–3500	100	0.484 (Sig < 0.001)	0.387 (Sig < 0.001)	0.116 (Sig = 0.027)	0.92

Appendix A5

Calculation of the sinking speed of particulate matter to the deep IOSG

The sinking speed of particles descending through the water column can be quantified by its cumulative density (ρ_{solids}) that bases on the specific densities of the individual components that contribute to the total mass flux and can be expressed by the following equation:

$$\rho_{\text{solids}} = \frac{(\text{CaCO}_3\% \times \rho_{\text{CaCO}_3} + \text{Opal}\% \times \rho_{\text{Opal}} + \text{LM}\% \times \rho_{\text{LM}} + \text{POM}\% \times \rho_{\text{POM}})}{100}, \quad (\text{A5.1})$$

where $\text{CaCO}_3\%$, $\text{Opal}\%$, $\text{LM}\%$, and $\text{POM}\%$ ($= \text{POC} \times 1.8$) are the percentages of the individual components and ρ_{CaCO_3} , ρ_{Opal} , ρ_{LM} , and ρ_{POM} are their specific densities in g cm^{-3} (Table A5.1). Using particulate matter data of sediment traps deployed at 2600–3500 m water depth (500–600 m above bottom), we calculated a density of $\rho_{\text{solids}} = 1.68 \pm 0.01 \text{ g cm}^{-3}$. The density of the sinking material is changing during descending through the water column and taking into account sinking particulate matter at 2600–3500 m water depth leads to an overestimation of sinking speeds in the upper ocean. Sinking particulate matter at 700 m water depth (trap 04-03 *Shallow*) indicates a density of $1.59 \pm 0.01 \text{ g cm}^{-3}$, which is slightly lower. As a first approximation, we calculate sinking velocities in our study area by using trap data of both, traps deployed at 500–600 m.a.b. (*) and trap 04-03 *Shallow* deployed at 700 m water depth (°), knowing that sinking velocities can be lower above 700 m.

Table A5.1. Percentages and densities of the individual components CaCO₃, biogenic opal, lithogenic matter, and particulate organic matter (POM) that contribute to the total mass flux of particulate matter collected by sediment traps deployed at 500–600 m above bottom in the IOSG.

Percentages and densities of the individual components contributing to the total mass flux			
	[%]	[%]	[g cm ⁻³]
	For traps at 500–600 m.a.b.	For trap 04-03 <i>Shallow</i>	(after Rixen et al., 2019b)
CaCO ₃	65.7 ± 2.7	66.2 ± 6.3	1.63 ± 0.08
Biogenic Opal	14.9 ± 1.6	9.6 ± 1.9	1.73 ± 0.27
Lithogenic Matter	10.0 ± 2.4	6.9 ± 4.2	2.70 ± 0.05
POM	9.6 ± 1.1	17.3 ± 2.8	0.90 ± 0.20

The Stokes' law is derived from the Navier-Stokes equation and is commonly used to calculate sinking velocities (U) of particles (e.g., *Lal and Lerman, 1975; McCave, 1975; Engel et al., 2009; Miklasz and Denny, 2010; Rixen et al., 2019b*) by the formula:

$$U = (2 \times g \times \Delta\rho \times radius^2) / 9\eta, \quad (A5.2)$$

where g is the gravitational acceleration, $radius$ defines the radius of sinking particles, η is the viscosity and $\Delta\rho$ represents the difference between the density of the particles ($\rho_{particle}$) and the density of the seawater (ρ_{water}).

$$\Delta\rho = \rho_{particle} - \rho_{seawater} \quad (A5.3)$$

The density of sinking particles ($\rho_{particle}$) is the result from its pore water content and the density of the solids (ρ_{solids}).

$$\rho_{particle} = (porosity \times \rho_{seawater}) + (1 - porosity) \times \rho_{solids} \quad (A5.4)$$

By using the Eq. A.5.1–A5.4, we can calculate a sinking speed of 179 ± 33 m per day based on seawater properties shown in Table A5.2 and on our data of sinking particulate matter at 2600–3500 m water depth in the IOSG (Table A5.1). For a water depth of 700 m (trap 04-03 *Shallow*), we calculate a sinking speed of 153 ± 65 m per day.

Table A5.2. Values used to calculate sinking speeds and the intermediate results of Eq. A2.2–A2.4.

Important parameters to calculate the sinking speed of particulate matter (^a parameters from Rixen et al., 2019b)		
	Value	Unit
$\rho_{\text{seawater}}^{\text{a}}$	1.03	g cm^{-3}
ρ_{solids} (our calculation*)	1.69 ± 0.15	g cm^{-3}
ρ_{solids} (our calculation ^o)	1.59 ± 0.14	g cm^{-3}
Porosity ^a	0.917	(dimensionless)
ρ_{particle} (our calculation*)	1.09 ± 0.01	g cm^{-3}
ρ_{particle} (our calculation ^o)	1.08 ± 0.02	g cm^{-3}
$\Delta\rho$ (our calculation*)	0.054 ± 0.01	g cm^{-3}
$\Delta\rho$ (our calculation ^o)	0.047 ± 0.02	g cm^{-3}
Viscosity η^{a}	~ 0.0013	$\text{kg m}^{-1} \text{s}^{-1}$
Radius ^a	0.150	mm
Gravitational acceleration g	9.81	m s^{-2}

Note: *traps deployed at 500-600 m.a.b.; ^otrap 04-03 *Shallow* deployed at 700 m water depth.

Appendix A6

Data on surface sediments collected during INDEX expeditions between 2015 and 2018

Table A6.1. Data on the composition of surface sediments consisting of total nitrogen (TN), total carbon (TC), particulate organic carbon (POC), particulate organic matter (POM), calcium carbonate (CaCO₃), total sulfur (TS), biogenic opal (bOpal), and lithogenic matter (LM) collected during INDEX expeditions in 2015, 2017, and 2018.

Station	Core ID	Sediment depth [cm]	TN	TC	POC	POM	CaCO ₃	TS	bOpal	LM
INDEX cruise PE 405 in 2015										
43ROV03	PC2	0-1	0.086	0.863	0.597	1.07	2.22	18.27	2.142	94.57
43ROV03	PC6	0-1	0.121	1.256	0.879	1.582	3.14	2.23	7.800	87.48
45ROV04	PC2	0-1	0.134	1.208	0.967	1.741	2.01	9.36	3.575	92.68
45ROV04	PC3	0-1	0.115	1.394	0.900	1.620	4.12	2.77	5.830	88.43
45ROV04	PC5	0-1	0.075	0.507	0.461	0.830	0.38	17.71	1.294	97.49
47ROV05	PC1	0-1	0.044	8.891	0.406	0.731	70.71	0.418	4.466	24.09
47ROV05	PC3	0-1	0.043	7.816	0.375	0.675	62.01	0.623	5.811	31.51
47ROV05	PC4	0-1	0.061	5.292	0.488	0.878	40.03	1.24	7.464	51.62
49ROV06	PC1	0-1	0.060	7.687	0.508	0.914	59.83	0.649	5.840	33.42
49ROV06	PC2	0-1	0.062	0.603	0.521	0.938	0.68	0.808	17.443	80.94
49ROV06	PC4	0-1	0.055	7.798	0.455	0.819	61.19	0.618	5.119	32.87
51ROV07	PC1	0-1	0.058	1.989	0.440	0.792	12.91	5.74	7.508	78.79
53ROV08	PC1	0-1	0.041	2.124	0.371	0.668	14.61	4.16	6.977	77.75
53ROV08	PC2	0-1	0.050	8.230	0.433	0.779	64.98	0.450	4.050	30.20
56ROV09	PC1	0-1	0.033	6.452	0.208	0.374	52.03	0.333	5.965	41.63
58ROV10	PC1	0-1	0.067	0.792	0.482	0.868	2.58	14.63	4.181	92.37
60ROV11	PC1	0-1	0.050	9.827	0.247	0.445	79.83	0.281	3.537	16.19
60ROV11	PC3	0-1	0.042	9.377	0.255	0.459	76.02	0.294	3.515	20.01
60ROV11	PC4	0-1	0.032	8.704	0.219	0.394	70.71	0.227	7.057	21.84
62ROV12	PC1	0-1	0.066	5.796	0.559	1.006	43.64	1.82	5.455	49.90
62ROV12	PC4	0-1	0.053	4.585	0.384	0.691	35.01	8.43	4.468	59.83
62ROV12	PC5	0-1	0.041	0.794	0.328	0.590	3.88	0.592	8.396	87.13
INDEX cruise SO 259 in 2017										
008MUC	7	0-1	0.018	10.683	0.170	0.306	87.61	0.094	1.355	10.64
012MUC	7	0-1	0.034	10.541	0.172	0.310	86.41	0.123	1.650	11.51
022MUC	7	0-1	0.026	6.967	0.196	0.353	56.43	0.105	14.591	28.53
076MUC	8	0-1	0.024	10.800	0.174	0.313	88.55	0.017	1.776	9.34
103MUC	7	0-1	0.040	9.742	0.213	0.383	79.40	0.017	3.871	16.32
INDEX cruise PE 446 in 2018										
003MUC	5	0-1	0.023	11.181	0.202	0.364	91.49	0.050	0.751	7.34
009MUC	3	0-1	0.028	9.937	0.184	0.331	81.28	nd.	1.613	16.78
041MUC	6	0-1	0.019	1.745	0.280	0.504	12.21	nd.	21.130	66.16

Note: nd.: no data.

Acknowledgement

First, I would like to thank my supervisor Prof. Dr. Kay-Christian Emeis for his support during my PhD with respect to several constructive meetings, as well as his help on revising manuscripts and conference abstracts.

A great thanks goes to my co-supervisor Dr. Niko Lahajnar for his continuous support and guidance during my PhD, especially during the instructive ship cruises and for giving me the freedom and time to explore on my own and at the same time being always there if assistance was needed. Thanks, for the tireless revision of numerous research reports in the INDEX program, journal manuscripts, and conference abstracts and presentations.

I also thank Dr. Birgit Gaye for her continues support during writing manuscripts, research reports and conference abstracts, as well as for several constructive discussions on scientific issues and for the participation at the panel meetings that were part of the structured program of the graduate school SICSS. I thank Dr. Tim Rixen for the helpful comments to improve my journal manuscripts. Overall, I thank the whole Biogeochemistry working group, especially Frauke Langenberg, Peggy Bartsch and Marc Metzke for the assistance during the laboratory work, for the nice working atmosphere, for enjoyable group lunches, and nice conversations.

I thank Dr. Andreas Lückge for being my panel chair during the meeting of the SICSS structured program and for giving helpful advice on the chosen path of research during the thesis and during the BGR ship cruises.

I further thank Dr. Kirstin Dähnke, Dpl.-Ing. Markus Ankele, and Dr. Tina Sanders for the instructions and support during my analyses of nutrients and stable isotopes of nitrate at the Helmholtz Institute in Geesthacht (Germany).

A special thank goes to Dr. Ulrich Schwarz-Schampera, who gave me the chance to participate at four BGR ship cruises within the INDEX program, for

constructive discussions on scientific issues, for the revision of journal manuscripts, and for great non-scientific conversations during ship expeditions. I also like to thank all scientific members of the ship cruises INDEX 2016, 2017, 2018, and 2019 for the nice company. Furthermore, many thanks goes to the ship crews of the German research vessels *Maria S. Merian* and *Sonne* and the crew of the Dutch research vessel *Pelagia* for their outstanding support of my work on board.

I thank the School for Integrated Climate System Sciences (SICSS), especially Dr. Berit Hachfeld and Dr. Ingo Harms for their excellent management and organization of SICSS retreats and courses.

Finally, I would like to thank my family for their support and the relaxing times at home with several encouraging talks and being always there for me. A special thank goes to Lasse for always being at my side and for tolerating my long ship expeditions.

Aus dieser Disserstation hervorgegangene Veröffentlichungen

List of Publications

Harms, N. C., Lahajnar, N., Gaye, B., Rixen, T., Dähnke, K., Ankele, M., Schwarz-Schampera, U., Emeis, K.-C., 2019. Nutrient distribution and nitrogen and oxygen isotopic composition of nitrate in water masses of the subtropical southern Indian Ocean. *Biogeosciences*, 16, 2715-2732.

Harms, N. C., Lahajnar, N., Gaye, B., Rixen, T., Schwarz-Schampera, U., Emeis, K.-C., 2021. Sediment trap-derived particulate matter fluxes in the oligotrophic subtropical gyre of the South Indian Ocean. *Deep-Sea Research Part II: Topical Studies in Oceanography*, 104924.

Harms, N. C., Lahajnar, N., Gaye, B., Emeis, K.-C., submitted. Water masses and nutrient cycling in the subtropical southern Indian Ocean. In: *Marine Metal Exploration: The INDEX Project – Prospecting the Seafloor for Polymetallic Sulphides*, Chapter 19, Springer Nature.

Harms, N. C., Lahajnar, N., Emeis, K.-C., submitted. Biogeochemistry of particulate matter fluxes and sediment composition in the Indian Ocean subtropical gyre. In: *Marine Metal Exploration: The INDEX Project – Prospecting the Seafloor for Polymetallic Sulphides*, Chapter 20, Springer Nature.